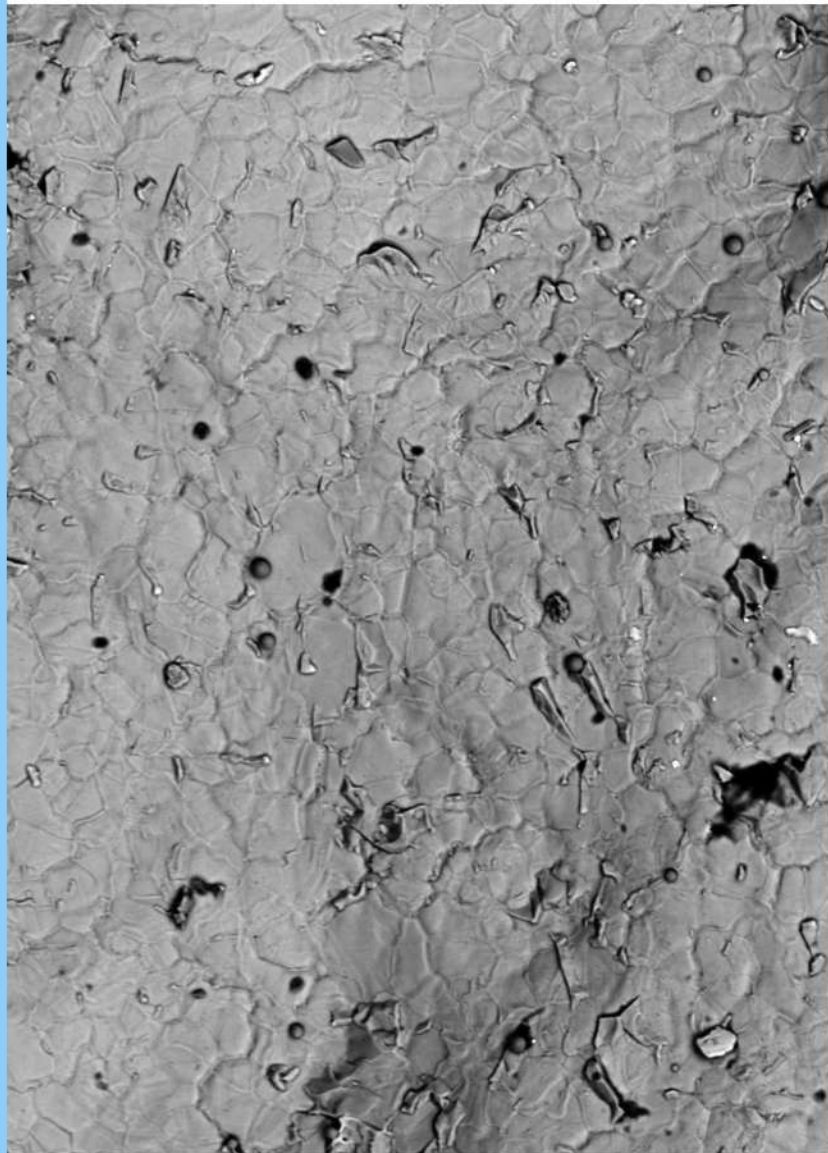


ISSN 2782-4039 (Print)
ISSN 2782-6074 (Online)

Frontier Materials & Technologies



2025
Nº 1

Frontier Materials & Technologies

Founded in 2008

No. 1
2025

16+

Quarterly
Scientific Journal

The Founder is
Togliatti State University

Editor-in-Chief

Mikhail M. Krishtal, DSc (Physics and Mathematics), Professor

Deputy Editor-in-Chief

for Metallurgy and Materials Science

Dmitry L. Merson, DSc (Physics and Mathematics), Professor

Deputy Editor-in-Chief

for Mechanical Engineering and Machine Science

Aleksandr P. Shaikin, DSc (Engineering), Professor

Deputy Editor-in-Chief

for Welding and Allied Processes and Technologies

Aleksandr I. Kovtunov, DSc (Engineering), Associate Professor

Editors:

Petr Yu. Bochkarev, DSc (Engineering), Professor

Boris M. Brzhozovskiy, DSc (Engineering), Professor

Aleksandr F. Denisenko, DSc (Engineering), Professor

Yuri Z. Estrin, DSc (Physics and Mathematics), Professor

Sergey S. Gavryushin, DSc (Engineering), Professor

Gregory Gerstein, DSc (Engineering)

Fedor V. Grechnikov, Academician of the Russian Academy of Sciences, DSc (Engineering), Professor

Mikhail I. Karpov, Corresponding Member of the Russian Academy of Sciences, DSc (Engineering), Professor

Aleksandr V. Katsman, PhD (Physics and Mathematics)

Aleksandr A. Kazakov, DSc (Engineering), Professor

Aleksandr V. Kudrya, DSc (Engineering), Professor

Sergey V. Kuzmin, Corresponding Member of the Russian Academy of Sciences, DSc (Engineering), Professor

Aleksey V. Makarov, Corresponding Member of the Russian Academy of Sciences, DSc (Engineering)

Radik R. Mulyukov, Corresponding Member of the Russian Academy of Sciences,

DSc (Physics and Mathematics), Professor

Oleg B. Naimark, DSc (Physics and Mathematics), Professor

Nikolay V. Nosov, DSc (Engineering), Professor

Aleksandr V. Pilinsky, PhD (Engineering), Associate Professor

Aleksey E. Romanov, DSc (Physics and Mathematics), Professor

Vasili V. Rubanik, Corresponding Member of the National Academy of Sciences of Belarus, DSc (Engineering)

Vladimir A. Shishkov, DSc (Engineering)

Tushar Madhukar Sonar, PhD (Engineering)

Ramasubbu Sunder, Fellow of the Indian Academy of Sciences, PhD (Engineering)

Vladimir P. Tabakov, DSc (Engineering), Professor

Alexey Yu. Vinogradov, DSc (Engineering), PhD (Physics and Mathematics), Professor

Until December 2021,
the journal was published under
the title
**“Science Vector
of Togliatti State University”**.

Indexed in Scopus.
Included in the List of HAC,
RSCI core, DOAJ,
“White List”.
Available in Crossref,
Google Scholar.

Registered by the Federal
Service for Supervision
of Communications,
Information Technology
and Mass Media
(Registration Certificate
ПИ No. ФС77-83040
dated March 31, 2022).

Subscription index
in the Russian Press catalogue:
13088.

Desktop publishing:

Natalya A. Nikitenko

*Responsible/technical
editor:*

Natalya A. Nikitenko

Mailing Address:

14, Belorusskaya St.,

Togliatti,

Russia, 445020

Phone: **(8482) 44-91-74**

E-mail:

vektornaukitgu@yandex.ru

Website:

<https://vektornaukitech.ru>

Passed for printing
27.03.2025.
Published 31.03.2025.
Format 60×84 1/8.
Digital printing.
Conventional printed sheets 13.5.
Circulation is 30 copies.
Order 3-86-25.
The price is free.

EDITORIAL BOARD INFORMATION

Editor-in-Chief

Mikhail M. Krishtal, Doctor of Sciences (Physics and Mathematics), Professor, Rector (Togliatti State University, Togliatti, Russia).
Scopus AuthorID: [14634063100](#)
ResearcherID: [AAD-7707-2019](#)
ORCID: <https://orcid.org/0000-0001-7189-0002>

Deputy Editor-in-Chief for Metallurgy and Materials Science

Dmitry L. Merson, Doctor of Sciences (Physics and Mathematics), Professor, Director of the Research and Development Institute of Advanced Technologies (Togliatti State University, Togliatti, Russia).
Scopus AuthorID: [6603449333](#)
ResearcherID: [M-7210-2016](#)
ORCID: <https://orcid.org/0000-0001-5006-4115>

Deputy Editor-in-Chief for Mechanical Engineering and Machine Science

Aleksandr P. Shaikin, Doctor of Sciences (Engineering), Professor, Professor of Chair “Energy-Converting Machines and Control Systems” (Togliatti State University, Togliatti, Russia).
Scopus AuthorID: [6602779899](#)
ORCID: <https://orcid.org/0000-0002-9832-4753>

Deputy Editor-in-Chief for Welding and Allied Processes and Technologies

Aleksandr I. Kovtunov, Doctor of Sciences (Engineering), Associate Professor, Professor of Chair “Welding, Pressure Treatment of Materials and Allied Processes” (Togliatti State University, Togliatti, Russia).
Scopus AuthorID: [36761987000](#)
ResearcherID: [B-4545-2016](#)
ORCID: <https://orcid.org/0000-0002-7705-7377>

Editorial board:

Petr Yu. Bochkarev, Doctor of Sciences (Engineering), Professor, Professor of Chair “Mechanical Engineering Technology and Applied Mechanics” (Kamyshin Technological Institute (Branch) of Volgograd State Technical University, Kamyshin, Russia), Professor of Chair “Technical Support of Agro-Industrial Complex” (Saratov State Vavilov Agrarian University, Saratov, Russia).
Scopus AuthorID: [57189893110](#)

Boris M. Brzhozovskiy, Doctor of Sciences (Engineering), Professor, chief researcher of Laboratory of Theory of Mechanisms and Machine Structure (Institute of Machines Science named after A.A. Blagonravov of the Russian Academy of Sciences, Moscow, Russia).
Scopus AuthorID: [55683317200](#)

Alexander F. Denisenko, Doctor of Sciences (Engineering), Professor, Professor of Chair “Technology of Mechanical Engineering, Machines and Tools” (Samara State Technical University, Samara, Russia).
Scopus AuthorID: [36131150100](#)

Yuri Z. Estrin, Doctor of Sciences (Physics and Mathematics), Professor, Professor of Chair of Engineering Materials (Monash University, Melbourne, Australia).
Scopus AuthorID: [7005031984](#)

Sergey S. Gavryushin, Doctor of Sciences (Engineering), Professor, Head of Chair “Computer Systems of Production Automation”, Head of the Theory & Machines Structure Laboratory (Bauman Moscow State Technical University, Moscow, Russia; Mechanical Engineering Research Institute of the Russian Academy of Sciences, Moscow, Russia).
Scopus AuthorID: [6507067486](#)
ResearcherID: [AAT-8610-2020](#)
ORCID: <https://orcid.org/0000-0002-6547-1351>

Gregory Gerstein, Doctor of Sciences (Engineering), Laboratory Head (Leibniz University Hannover, Hanover, Germany).
Scopus AuthorID: [55001912200](#)

Fedor V. Grechnikov, Academician of the Russian Academy of Sciences, Doctor of Sciences (Engineering), Professor, Head of the Chair of Forming Processes (Samara National Research University, Samara, Russia).
Scopus AuthorID: [6506174877](#)
ResearcherID: [P-2319-2016](#)
ORCID: <https://orcid.org/0000-0002-3767-4004>

Mikhail I. Karpov, Corresponding Member of the Russian Academy of Sciences, Doctor of Sciences (Engineering), Professor, Head of the Laboratory of Materials Science (Institute of Solid State Physics of the Russian Academy of Sciences, Chernogolovka, Russia).
Scopus AuthorID: [7004130343](#)
ResearcherID: [Q-9288-2016](#)

Aleksandr V. Katsman, PhD (Physics and Mathematics), Senior Research Associate (Technion – Israel Institute of Technology, Haifa, Israel).
Scopus AuthorID: [7004225554](#)

Aleksandr A. Kazakov, Doctor of Sciences (Engineering), Professor, Professor of Chair “Metallurgy and Casting Technologies”, Head of the Metallurgy Expertise Laboratory (Peter the Great Saint-Petersburg Polytechnic University, St. Petersburg, Russia).
Scopus AuthorID: [56037035400](#)
ResearcherID: [E-6090-2014](#)
ORCID: <https://orcid.org/0000-0001-6511-1228>

Aleksandr V. Kudrya, Doctor of Sciences (Engineering), Professor, Professor of Chair of Physical Metallurgy and Physics of Strength (National University of Science and Technology MISiS, Moscow, Russia).

Scopus AuthorID: [6603628218](#)

Sergey V. Kuzmin, Corresponding Member of the Russian Academy of Sciences, Doctor of Sciences (Engineering), Professor, First Prorector, Professor of Chair “Equipment and Technology of Welding Production” (Volgograd State Technical University, Volgograd, Russia).

Scopus AuthorID: [57217278342](#)

ResearcherID: [I-7424-2012](#)

ORCID: <https://orcid.org/0000-0003-2802-8497>

Aleksey V. Makarov, Corresponding Member of the Russian Academy of Sciences, Doctor of Sciences (Engineering), Chief Research Associate, Head of Chair of Materials Science, Head of the Laboratory of Mechanical Properties (M.N. Mikheev Institute of Metal Physics of Ural Branch of Russian Academy of Sciences, Ekaterinburg, Russia).

Scopus AuthorID: [57195590138](#)

ResearcherID: [D-5663-2016](#)

ORCID: <https://orcid.org/0000-0002-2228-0643>

Radik R. Mulyukov, Corresponding Member of the Russian Academy of Sciences, Doctor of Sciences (Physics and Mathematics), Professor, Director (Institute for Metals Superplasticity Problems of the Russian Academy of Sciences, Ufa, Russia).

Scopus AuthorID: [7003520439](#)

ResearcherID: [B-3800-2016](#)

ORCID: <https://orcid.org/0000-0002-0452-3816>

Oleg B. Naimark, Doctor of Sciences (Physics and Mathematics), Professor, Head of the Laboratory of Physical Foundations of Strength (Institute of Continuous Media Mechanics of Ural Branch of Russian Academy of Sciences, Perm, Russia).

Scopus AuthorID: [6701720806](#)

Nikolay V. Nosov, Doctor of Sciences (Engineering), Professor, Professor of Chair “Technology of Mechanical Engineering, Machines and Tools” (Samara State Technical University, Samara, Russia).

Scopus AuthorID: [6602506825](#)

Aleksandr V. Pilinsky, PhD (Engineering), Associate Professor, MSME (Master of Science in Mechanical Engineering), Los Angeles, USA.

ORCID: <https://orcid.org/0009-0009-8933-195X>

Aleksey E. Romanov, Doctor of Sciences (Physics and Mathematics), Professor, Professor of the Institute of Advanced Data Transfer Systems (ITMO University, St. Petersburg, Russia).

Scopus AuthorID: [7202768874](#)

Vasili V. Rubanik, Corresponding Member of the National Academy of Sciences of Belarus, Doctor of Sciences (Engineering), Head of the Laboratory of Metal Physics (Institute of Technical Acoustics of the National Academy of Sciences of Belarus, Vitebsk, Belarus).

Scopus AuthorID: [57215218253](#)

Vladimir A. Shishkov, Doctor of Sciences (Engineering), Head of the Technical Department (Palladio LLC, Togliatti, Russia).

RSCI AuthorID: [596086](#)

SPIN-code: [9504-4454](#)

Tushar Madhukar Sonar, PhD (Engineering), Senior Research Scientist of Chair “Welding Engineering”

(South Ural State University, Chelyabinsk, Russia).

Scopus AuthorID: [57200800257](#)

ResearcherID: [AAS-6037-2021](#)

ORCID: <https://orcid.org/0000-0002-3997-5337>

Ramasubbu Sunder, Fellow of the Indian Academy of Sciences, PhD (Engineering), Director (BISS (P) Ltd, Bangalore, India).

Scopus AuthorID: [7003530245](#)

ResearcherID: [H-6740-2016](#)

ORCID: <https://orcid.org/0000-0001-6143-0723>

Vladimir P. Tabakov, Doctor of Sciences (Engineering), Professor, Head of Chair “Innovative Technologies in Mechanical Engineering” (Ulyanovsk State Technical University, Ulyanovsk, Russia).

Scopus AuthorID: [6701501345](#)

ResearcherID: [E-1832-2017](#)

ORCID: <https://orcid.org/0000-0002-2568-9401>

Alexey Yu. Vinogradov, Doctor of Sciences (Engineering), PhD (Physics and Mathematics), Professor, Professor of Faculty of Mechanical and Industrial Engineering (Norwegian University of Science and Technology, Trondheim, Norway).

Scopus AuthorID: [7402889776](#)

ResearcherID: [A-7175-2009](#)

ORCID: <https://orcid.org/0000-0001-9585-2801>

СВЕДЕНИЯ О ЧЛЕНАХ РЕДКОЛЛЕГИИ

Главный редактор

Кристал Михаил Михайлович, доктор физико-математических наук, профессор, ректор (Тольяттинский государственный университет, Тольятти, Россия).

Scopus AuthorID: [14634063100](#)

ResearcherID: [AAD-7707-2019](#)

ORCID: <https://orcid.org/0000-0001-7189-0002>

Заместитель главного редактора по направлению «Металлургия и материаловедение»

Мерсон Дмитрий Львович, доктор физико-математических наук, профессор, директор Научно-исследовательского института перспективных технологий (Тольяттинский государственный университет, Тольятти, Россия).

Scopus AuthorID: [6603449333](#)

ResearcherID: [M-7210-2016](#)

ORCID: <https://orcid.org/0000-0001-5006-4115>

Заместитель главного редактора по направлению «Машиностроение и машиноведение»

Шайкин Александр Петрович, доктор технических наук, профессор, профессор кафедры «Энергетические машины и системы управления» (Тольяттинский государственный университет, Тольятти, Россия).

Scopus AuthorID: [6602779899](#)

ORCID: <https://orcid.org/0000-0002-9832-4753>

Заместитель главного редактора по направлению «Сварка, родственные процессы и технологии»

Ковтунов Александр Иванович, доктор технических наук, доцент, профессор кафедры «Сварка, обработка материалов давлением и родственные процессы» (Тольяттинский государственный университет, Тольятти, Россия).

Scopus AuthorID: [36761987000](#)

ResearcherID: [B-4545-2016](#)

ORCID: <https://orcid.org/0000-0002-7705-7377>

Редакционная коллегия:

Бочкарев Петр Юрьевич, доктор технических наук, профессор, профессор кафедры «Технология машиностроения и прикладная механика» (Камышинский технологический институт (филиал) Волгоградского государственного технического университета, Камышин, Россия), профессор кафедры «Техническое обеспечение АПК» (Саратовский государственный аграрный университет имени Н.И. Вавилова, Саратов, Россия).

Scopus AuthorID: [57189893110](#)

Бржозовский Борис Максевич, доктор технических наук, профессор главный научный сотрудник лаборатории теории механизмов и структуры машин (Институт машиноведения им. А.А. Благонравова РАН, Москва, Россия).

Scopus AuthorID: [55683317200](#)

Виноградов Алексей Юрьевич, доктор технических наук, кандидат физико-математических наук, профессор факультета механической и промышленной инженерии (Норвежский университет науки и технологии, Тронхейм, Норвегия).

Scopus AuthorID: [7402889776](#)

ResearcherID: [A-7175-2009](#)

ORCID: <https://orcid.org/0000-0001-9585-2801>

Гаврюшин Сергей Сергеевич, доктор технических наук, профессор, заведующий кафедрой «Компьютерные системы автоматизации производства», заведующий лабораторией компьютерных систем автоматизации производства и цифровых технологий (Московский государственный технический университет имени Н.Э. Баумана (национальный исследовательский университет), Москва, Россия; Институт машиноведения им. А.А. Благонравова Российской академии наук, Москва, Россия).

Scopus AuthorID: [6507067486](#)

ResearcherID: [AAT-8610-2020](#)

ORCID: <https://orcid.org/0000-0002-6547-1351>

Герштейн Григорий, доктор технических наук, заведующий лабораторией (Ганноверский университет имени Готфрида Вильгельма Лейбница, Ганновер, Германия).

Scopus AuthorID: [55001912200](#)

Гречников Федор Васильевич, академик РАН, доктор технических наук, профессор, заведующий кафедрой обработки металлов давлением (Самарский национальный исследовательский университет имени академика С.П. Королева, Самара, Россия).

Scopus AuthorID: [6506174877](#)

ResearcherID: [P-2319-2016](#)

ORCID: <https://orcid.org/0000-0002-3767-4004>

Денисенко Александр Федорович, доктор технических наук, профессор, профессор кафедры «Технология машиностроения, станки и инструменты» (Самарский государственный технический университет, Самара, Россия).

Scopus AuthorID: [36131150100](#)

Казаков Александр Анатольевич, доктор технических наук, профессор, профессор кафедры «Металлургические и литейные технологии», руководитель научно-испытательной лаборатории «Металлургическая экспертиза» (Санкт-Петербургский политехнический университет Петра Великого, Санкт-Петербург, Россия).

Scopus AuthorID: [56037035400](#)

ResearcherID: [E-6090-2014](#)

ORCID: <https://orcid.org/0000-0001-6511-1228>

Карнов Михаил Иванович, член-корреспондент РАН, доктор технических наук, профессор, заведующий лабораторией материаловедения (Институт физики твердого тела Российской академии наук, Черноголовка, Россия).

Scopus AuthorID: [7004130343](#)

ResearcherID: [Q-9288-2016](#)

Кацман Александр Владимирович, кандидат физико-математических наук, PhD, старший научный сотрудник (Технион – Израильский технологический институт, Хайфа, Израиль).

Scopus AuthorID: [7004225554](#)

Кудря Александр Викторович, доктор технических наук, профессор, заместитель заведующего кафедрой металловедения и физики прочности (Национальный исследовательский технологический университет «МИСиС», Москва, Россия).

Scopus AuthorID: [6603628218](#)

Кузьмин Сергей Викторович, член-корреспондент РАН, доктор технических наук, профессор, первый проректор, профессор кафедры «Оборудование и технология сварочного производства» (Волгоградский государственный технический университет, Волгоград, Россия).

Scopus AuthorID: [57217278342](#)

ResearcherID: [I-7424-2012](#)

ORCID: <https://orcid.org/0000-0003-2802-8497>

Макаров Алексей Викторович, член-корреспондент РАН, доктор технических наук, главный научный сотрудник, заведующий отделом материаловедения и лабораторией механических свойств (Институт физики металлов имени М.Н. Михеева Уральского отделения Российской академии наук, Екатеринбург, Россия).

Scopus AuthorID: [57195590138](#)

ResearcherID: [D-5663-2016](#)

ORCID: <https://orcid.org/0000-0002-2228-0643>

Мулюков Радик Рафикович, член-корреспондент РАН, доктор физико-математических наук, профессор, директор (Институт проблем сверхпластичности металлов Российской академии наук, Уфа, Россия).

Scopus AuthorID: [7003520439](#)

ResearcherID: [B-3800-2016](#)

ORCID: <https://orcid.org/0000-0002-0452-3816>

Наймарк Олег Борисович, доктор физико-математических наук, профессор, заведующий лабораторией «Физические основы прочности» (Институт механики сплошных сред Уральского отделения Российской академии наук, Пермь, Россия).

Scopus AuthorID: [6701720806](#)

Носов Николай Васильевич, доктор технических наук, профессор, профессор кафедры «Технология машиностроения, станки и инструменты» (Самарский государственный технический университет, Самара, Россия).

Scopus AuthorID: [6602506825](#)

Пилинский Александр Вениаминович, кандидат технических наук, доцент, MSME (Master of Science in Mechanical Engineering), Лос-Анджелес, США.

ORCID: <https://orcid.org/0009-0009-8933-195X>

Романов Алексей Евгеньевич, доктор физико-математических наук, профессор Института перспективных систем передачи данных, руководитель научно-исследовательского центра перспективных функциональных материалов и лазерных коммуникационных систем (Национальный исследовательский университет ИТМО, Санкт-Петербург, Россия).

Scopus AuthorID: [7202768874](#)

Рубаник Василий Васильевич, член-корреспондент Национальной академии наук Беларуси, доктор технических наук, заведующий лабораторией физики металлов (Институт технической акустики Национальной академии наук Беларуси, Витебск, Республика Беларусь).

Scopus AuthorID: [57215218253](#)

Сонар Тушар Мадхукар, кандидат технических наук, старший научный сотрудник кафедры «Оборудование и технология сварочного производства» (Южно-Уральский государственный университет, Челябинск, Россия).

Scopus AuthorID: [57200800257](#)

ResearcherID: [AAS-6037-2021](#)

ORCID: <https://orcid.org/0000-0002-3997-5337>

Сундер Рамасуббу, член Индийской академии наук, кандидат технических наук, директор (“BISS (P) Ltd”, Бангалор, Индия).

Scopus AuthorID: [7003530245](#)

ResearcherID: [H-6740-2016](#)

ORCID: <https://orcid.org/0000-0001-6143-0723>

Табakov Владимир Петрович, доктор технических наук, профессор, заведующий кафедрой «Инновационные технологии в машиностроении» (Ульяновский государственный технический университет, Ульяновск, Россия).

Scopus AuthorID: [6701501345](#)

ResearcherID: [E-1832-2017](#)

ORCID: <https://orcid.org/0000-0002-2568-9401>

Шишков Владимир Александрович, доктор технических наук, начальник технического отдела (ООО «Палладио», Тольятти, Россия).

AuthorID РИНЦ: [596086](#)

SPIN-код: [9504-4454](#)

Эстрин Юрий Захарович, доктор физико-математических наук, профессор, профессор кафедры инженерных материалов (Университет им. Монаша, Мельбурн, Австралия).

Scopus AuthorID: [7005031984](#)

CONTENT

Development of a laboratory tribotechnical facility for testing PDC cutters for wear Kolibasov V.A., Ibatullin I.D., Novikov V.A.	9
Structure and mechanical properties of high-entropy alloys of the CoCrZrMnNi system with different Zr and Mn contents produced by vacuum-induction melting Konovalov S.V., Drobyshev V.K., Panchenko I.A., Li Haixin	21
Cutting ceramics for turning of specialised stainless hard-to-machine steel Mokritskiy B.Ya., Sablin P.A., Kosmynin A.V.	35
The influence of silicon content on the structure of Cu55Ni6Mn4Zn brazing alloy and on the structure and properties of brazed joints Pashkov I.N., Gadzhiev M.R., Tavolzhanskiy S.A., Bazlova T.A., Bazhenov V.E., Katanaeva D.A.	47
Calculation of the effective solidification range and its relationship with hot brittleness of alloys based on Mg–Al and Mg–Zn systems Pozdniakov A.V.	59
Effect of erbium and hafnium microalloying on the formation of Al₃Sc particles in aluminium alloy with a high magnesium content Ragazin A.A., Aryshenskiy E.V., Aryshenskiy V.Yu., Rasposienko D.Yu., Konovalov S.V., Bakhtegareev I.D.	69
Influence of crystallographic texture on the strength and electrical conductivity of ultrafine-grained copper Tarov D.V., Nesterov K.M., Islamgaliev R.K., Korznikova E.A.	81
Mathematical modelling to predict the tensile strength of additively manufactured AlSi10Mg alloy using artificial neural networks Srivastava S.K., Mathivanan N.R.	93
OUR AUTHORS	111

СОДЕРЖАНИЕ

Разработка лабораторного триботехнического комплекса для испытаний PDC-резцов на изнашивание Колибасов В.А., Ибатуллин И.Д., Новиков В.А.	9
Структура и механические свойства высокоэнтропийных сплавов системы CoCrZrMnNi, полученных вакуумно-индукционной плавкой, с разным содержанием Zr и Mn Коновалов С.В., Дробышев В.К., Панченко И.А., Ли Хайсинь	21
Режущая керамика для точения специализированной нержавеющей труднообрабатываемой стали Мокрицкий Б.Я., Саблин П.А., Космынин А.В.	35
Влияние количественного содержания кремния на структуру припоя Cu55Ni6Mn4Zn и на структуру и свойства паяных соединений Пашков И.Н., Гаджиев М.Р., Таволжанский С.А., Базлова Т.А., Баженов В.Е., Катанаева Д.А.	47
Расчет эффективного интервала кристаллизации и его связь с горячеломкостью сплавов на основе систем Mg–Al и Mg–Zn Поздняков А.В.	59
Влияние микролегирования эрбием и гафнием на формирование частиц Al₃Sc в алюминиевом сплаве с высоким содержанием магния Рагазин А.А., Арышенский Е.В., Арышенский В.Ю., Распосиенко Д.Ю., Коновалов С.В., Бахтегареев И.Д.	69
Влияние кристаллографической текстуры на прочность и электропроводность ультрамелкозернистой меди Таров Д.В., Нестеров К.М., Исламгалиев Р.К., Корзникова Е.А.	81
Математическая модель прогнозирования предела прочности сплава AlSi10Mg, изготовленного аддитивным способом, с использованием искусственных нейронных сетей Шривастава С.К., Мативанан Н.Р.	93
OUR AUTHORS.....	111

Development of a laboratory tribotechnical facility for testing PDC cutters for wear

*Vladimir A. Kolibasov**¹, postgraduate student,

assistant of Chair “Machinery and Equipment of Petroleum and Chemical Production”

Ildar D. Ibatullin, Doctor of Sciences (Engineering), Professor,

Head “Chair of Machinery and Equipment of Petroleum and Chemical Production”

*Vladislav A. Novikov*², PhD (Engineering),

assistant professor of Chair “Metal Science, Powder Metallurgy, Nanomaterials”,

senior researcher of the Laboratory of X-ray Diffractometry, Electron and Probe Microscopy

Samara State Technical University, Samara (Russia)

*E-mail: mahp@samgtu.ru,
csstea@yandex.ru

¹ORCID: <https://orcid.org/0000-0002-0503-2533>

²ORCID: <https://orcid.org/0000-0002-8052-305X>

Received 10.02.2025

Revised 25.02.2025

Accepted 11.03.2025

Abstract: In the practice of drilling oil and gas wells with diamond bits equipped with PDC cutters, cutter quality non-compliance with the declared class occurs. At the same time, the currently used methods of full-scale testing, when granite stone is used as a counterbody, are time-consuming and expensive, which complicates their use for prompt incoming inspection of new batches of PDC cutters arriving for assembly of diamond bits. This necessitated the development of a laboratory tribotechnical facility for quantitative assessment of the ability of PDC cutters to resist abrasion against abrasive materials. The study covers the development of a specialized tribotechnical facility that allows testing PDC cutters of various sizes for wear during friction against a diamond-containing metal work face, for which it is proposed to use diamond cutting wheels. The developed laboratory tribotechnical facility includes: an electromechanical rotary drive (a drilling-and-milling machine); a measuring unit with sensors for normal loads, friction force and temperature of cutter self-heating during testing; a lever loading mechanism; a set of mandrels for the possibility of installing PDC cutters of various sizes; a data collection system and licensed software. The results of practical evaluation of the developed laboratory tribotechnical facility on PDC cutters of various batches showed that testing on the new equipment allows for quick collection of data on the wear rate of the working edges of PDC cutters. The developed methods, equipment and criteria can be used to certify the wear resistance of PDC cutters.

Keywords: diamond bit; PDC cutter; tribotechnical facility; diamond-containing metal work face.

For citation: Kolibasov V.A., Ibatullin I.D., Novikov V.A. Development of a laboratory tribotechnical facility for testing PDC cutters for wear. *Frontier Materials & Technologies*, 2025, no. 1, pp. 9–19. DOI: 10.18323/2782-4039-2025-1-71-1.

INTRODUCTION

Currently, the most popular drilling tools for drilling oil and gas wells in soft rocks with interlayers of hard rocks and medium-hard rocks are bits with PDC (Polycrystalline Diamond Compact) cutters [1]. It is known that rock-destructing PDC cutters are the most loaded and least reliable elements of the design of diamond drill bits [2; 3]. When used at the work face, they have a chipping, crushing and abrasive effect on the rock being drilled. In turn, the rock has a destructive effect on the cutters: their working edge wears out when dragging against the rock, which leads to a gradual decrease in the aggressiveness of the cutters and, accordingly, a decrease in the drilling speed. In most cases, the durability of the PDC cutters limits the repair-to-repair period of the diamond bit, and therefore the efficiency of drilling wells [4; 5].

When drilling prospecting, exploratory and producing wells, the drilling tool passes through shale, limestone, sandstones, quartzites and other rocks of different strength and

abrasiveness. To determine the degree of wear of the bits (crowns), it is necessary to bring the tool to the surface. The duration of the process of pulling and running operations significantly increases the cost of well construction [6].

PDC cutters are a superhard monolithic composite material produced by sintering a hard-alloy tungsten carbide base on a cobalt bond and a polycrystalline diamond insert [7]. The sintering process is carried out in cubic presses at ultra-high pressures (6...8 GPa) and temperatures (1400...1500 °C) in a liquid medium of a metal catalyst (cobalt) [8]. Despite the existing multi-stage control system in the production of PDC cutters, including control of raw materials, sintering pressure, visual inspection, defect analysis and laboratory impact and wear tests, studies have shown that changes in the wear resistance of PDC cutters occur from batch to batch [9]. Therefore, the introduction of incoming quality control of cutters arriving for assembly of diamond bits should be an integral part of the implementation of a quality

system in bit production. The problem is complicated by the fact that, currently, there are no international norms and standards for assessing the quality of PDC cutters. Until recently, each company with diamond production developed its own testing methods and criteria for analyzing their reliability. Now, one can see a trend towards conducting seminatural tests, when the tested PDC cutters (in real design) are worn out on a rotating natural stone (Fig. 1) simulating a work face [10].

For example, the general technical requirements of the Institute of Oil and Gas Technology Initiatives for cutting action blade bits equipped with cutters with a diamond polycrystalline insert¹ propose to test PDC cutters for abrasive resistance on the basis of a turning-and-boring lathe, including a mandrel for installing the test cutter in the cutter holder installed at a given angle to the cylindrical granite stone surface. The lathe ensures cutting of the rock with a constant angular velocity (40...80 rpm) and axial load. The tensile strength of granite is set in the range of 150...250 MPa. A standard system for supplying lubricating and cooling liquid is used to cool the cutter. The cutting depth during tests is 0.25...1.0 mm. The cutting stroke is from the centre to the periphery. The return stroke is carried out without contact with the surface of the stone. After each cycle, the friction surface of the cutter is photographed to assess the volumetric wear, and then the cycles are repeated.

A similar method for assessing the wear resistance of PDC cutters was described in the Laboratory of Ultra-hard Materials at MISiS. It involves drilling granite on a vertical turret lathe under high load. The wear rate is defined as the change in the weight of the cutter before the start of the experiment and after a certain number of passes in the granite [10]. Similar equipment for testing PDC cutters was used by LANDS Superabrasives, Element Six (E6), Drilling Industrial Systems (LLC), Volgaburmash (OJSC), and others. For example, Element Six (E6) tests cutters for wear resistance by turning a granite sample of fine-grained or medium-grained structure with a strength of at least 220 MPa at a rotation speed of 54 rpm (40–160 m/min), a cutting depth of 0.25 mm, and a feed rate of 4.5 mm/rev with water-cooling [4]. The Ufa State Petroleum Technological University has proposed a technique for testing cutters for wear during friction against granite, taking into account the work face profile [11]. Test modes: six levels of penetration per one cutter revolution $\delta=0.28, 0.4, 0.56, 0.8, 1.12, 1.6$ mm at a rotation frequency of 90 min^{-1} . Flushing is carried out with technical water.

The considered tests are attractive because they create conditions that are as similar as possible to operational ones. However, some unaccounted factors, such as the flow of abrasive-containing drill fluid acting on the cutter, can lead to hydroerosive wear of the carbide base under the polycrystalline diamond insert, depriving it of support (Fig. 2). Moreover, during the drilling process, a specified

axial load is maintained on the bit and on the cutters in particular [12; 13]. If the tests are carried out at a constant penetration depth, this leads to constant changes in axial loads, which creates uncertainty in the modes of loading the cutters during tests. The choice of granite or marble as the work face material is caused by the fact that these materials, due to their high abrasiveness and hardness, allow assessing the wear of the cutters in a relatively short time. However, natural materials have a heterogeneous (layered) structure in depth, which, taking into account the long duration of the tests, can lead to an error in the measurements depending on the location of the abraded layer of the work face [14; 15]. To solve this problem, it was proposed to use artificial abrasive materials – 64C (silicon carbide) grinding wheels, as a counterbody during testing, which due to their increased hardness, accelerate the wear process [10].

Despite the general test scheme, one can state that currently, there is no generally accepted technique for wear tests of cutters, which does not allow comparing the results of different researchers and confirming the declared quality of products. To move to the possibility of certifying the quality of cutters according to the wear resistance criterion, it is necessary to determine the list of confirmed indicators and their ranges or limit values, observing the unity of the conditions for conducting tests and measurements. At the same time, it is advisable to supplement the arsenal of full-scale methods for testing cutters with simpler and more efficient methods of laboratory testing. Their purpose is not to determine the wear rate of cutters during operation, but only to give a comparative assessment of the wear resistance of polycrystalline diamond inserts on the edges of cutters while maintaining the test scheme, acceptable forcing of mechanical stresses and increasing the aggressiveness of the counterbody for the quickest possible comparative analysis. All other factors – the value of the load on the cutter, the cutter angle to the counterbody, the speed of rotation of the work face, etc. – are chosen constant so that the wear rate of the PDC insert depends only on the properties of the insert on the tested cutter.

The purpose of the study is to develop a laboratory tribotechnical facility and a method for testing PDC cutters for wear.

METHODS

Development of a methodology for wear test of PDC cutters

When developing equipment for laboratory wear tests of cutters, the following assumptions were made. The design of the bit provides for an angular (usually at angles from 5 to 30°) position of the cutters relative to the work face, in which not the entire cutter surface contacts the rock, but only the protruding edge of the diamond polycrystalline insert (working edge). In this respect, it was decided to set an angle close to the average in the specified range equal to 15°, due to the geometry of the equipment.

To accelerate wear tests, the authors proposed using a metal-diamond "work face" in the form of a diamond-

¹ *Cutting action blade bits equipped with cutters with a diamond polycrystalline insert. General technical requirements. St. Petersburg, Institute of Oil and Gas Technology Initiatives, 2022. 81 p.*

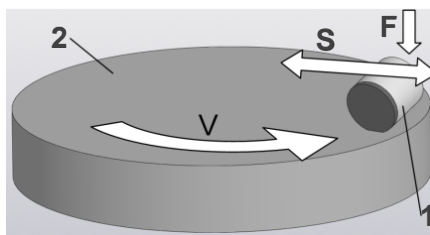


Fig. 1. Scheme of PDC cutter wear tests:
 1 – tested cutter; 2 – counterbody (granite stone);
 F – normal load; S – transverse feed; V – rotation speed of the movable counterbody

Рис. 1. Схема испытаний PDC-резцов на изнашивание:
 1 – испытуемый резец; 2 – контртело (гранитный камень);
 F – нормальная нагрузка; S – поперечная подача;
 V – скорость вращения подвижного контртела

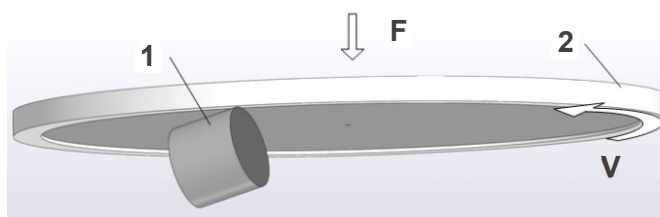


Fig. 2. The proposed scheme for wear tests of the PDC cutters:
 1 – tested cutter; 2 – counterbody (diamond cutting wheel);
 F – fixed normal load; V – wheel rotation speed

Рис. 2. Предлагаемая схема испытаний PDC-резцов на изнашивание:
 1 – испытуемый резец; 2 – контртело (алмазный отрезной диск);
 F – фиксированная нормальная нагрузка;
 V – скорость вращения диска

containing rim of a diamond cutoff disk as a counterbody. Unlike the use of natural rocks (granite stone), which can have significant differences in hardness (6.5–7 units on the Mohs scale) and tensile strength (from 40 to 80 MPa), artificially created diamond tools are manufactured according to accepted technical specifications and have a regulated range of properties. To test PDC cutters, it is recommended to take wheels with a hard bond (6600 MPa on the Vickers scale). This will reduce the wear rate of the diamond rim and allow using one disk twice: first from one end, then from the other. In this case, there is no disk clogging. The tested edge of the PDC cutter effectively removes the metal layer and reveals new diamond grains. Moreover, with an increase in the hardness of the counterbody, the pressure at the point of contact of the cutter with the metal-diamond work face during friction increases. This creates conditions for a significant acceleration of wear tests.

The recommended load on the friction contact is 20 kgf (196.2 N). Higher loads lead to the appearance of areas of adhesion of the PDC cutter with the diamond rim, strong heating of the contact (over 300 °C), and rapid failure of the diamond wheel without the possibility of its secondary use. For the same reasons, the speed of rotation of

the wheel was limited to 200 rpm. Lower loads lead to the necessity of increasing the test duration to form noticeable wear. Studies have shown that the characteristic values of the force of friction between the cutter and the diamond rim at the selected normal load are about 60...70 N, which with a cutting wheel diameter of 115 mm corresponds to a friction torque of 3.6...4.2 N·m. To implement such an effort, it is recommended to use a drive with a power of at least 400 W. Modernized vertical drilling machines equipped with a lever loading system can be used as such a drive.

The PDC cutters were tested for abrasive wear resistance under the following test conditions:

- friction pattern: “tooth edge – diamond wheel”;
- rotation frequency of the metal “work face” – 200 rpm;
- counter sample (“work face”) – diamond cutting wheel (125 mm);
- samples – two PDC cutters with the same service life;
- sample mounting angle relative to the “work face” – 15°;
- test time – 30 min;
- friction without lubrication (dry);
- continuous collection of data on the normal load applied to the contact and the friction force, and periodic temperature monitoring.

Development of equipment for laboratory wear tests of PDC cutters

Taking into account the above, a laboratory software and hardware complex (Fig. 2, 3) was developed at the Chair of Machinery and Equipment of Petroleum and Chemical Production of Samara State Technical University. The scheme of the friction unit (Fig. 2) of this facility is generally similar to the scheme of full-scale tests shown in Fig. 1. The model work face is also rotating relative to the fixed cutter inclined relative to the work face at an operating angle and cutting into it with the edge of the polycrystalline diamond insert. The difference is that the work face is inverted relative to the cutter, which creates conditions for the spontaneous removal (shedding) of wear particles from the friction zone. Moreover, such a mutual arrangement allows free loading of the cutter from above with a fixed load and rotation of the work face using standard and relatively inexpensive equipment – desktop drilling or drilling-and-milling machines as a drive. The edge of the cutter is pressed into the diamond rim for an amount determined by a fixed normal load and relatively stable strength properties of the rim. This creates identical friction conditions when testing various cutters and more closely matches the loading pattern of cutters during drilling.

The design of the device for testing PDC cutters for abrasive wear is shown in Fig. 3. The main components of the test facility are:

1) a drive consisting of an electric motor, a spindle unit, a rack, a base and a console table. Drilling or drilling-and-milling machines can be used as a drive. The modification of the machine includes the installation of a lever loading system allowing the creation of an axial load of up to 200 N. It is preferable to use machines with the ability to move axially the console table along the toothed rack;

2) a system for monitoring experimental data consisting of a measuring unit (Fig. 4), an E14-140 data collection system and PowerGraph software. The measuring unit is equipped with sensors for the average self-heating temperature of the PDC cutter, normal load and tangential load. In the lower part of the monoblock, there is a shank end for fixing in a vice on the console table. In the upper part, there is a vertical hole with a clamp allowing the fixation of the mandrel with the tested cutter. The range of measured values of the sensors: temperature T – up to 600 °C, normal load F_n – up to 1000 N, friction force F_{fr} – up to 500 N. The software allows calibrating the sensors and building diagrams of the measured values in real time with the adopted data collection frequency of 100 Hz. Since the PDC cutter materials (polycrystalline diamond insert and hard alloy) have good thermal conductivity, the process hole for measuring its average temperature is located directly under the PDC cutter;

3) a mandrel for the PDC cutter. The mandrel provides its reliable fixation on the monoblock and a specified angle

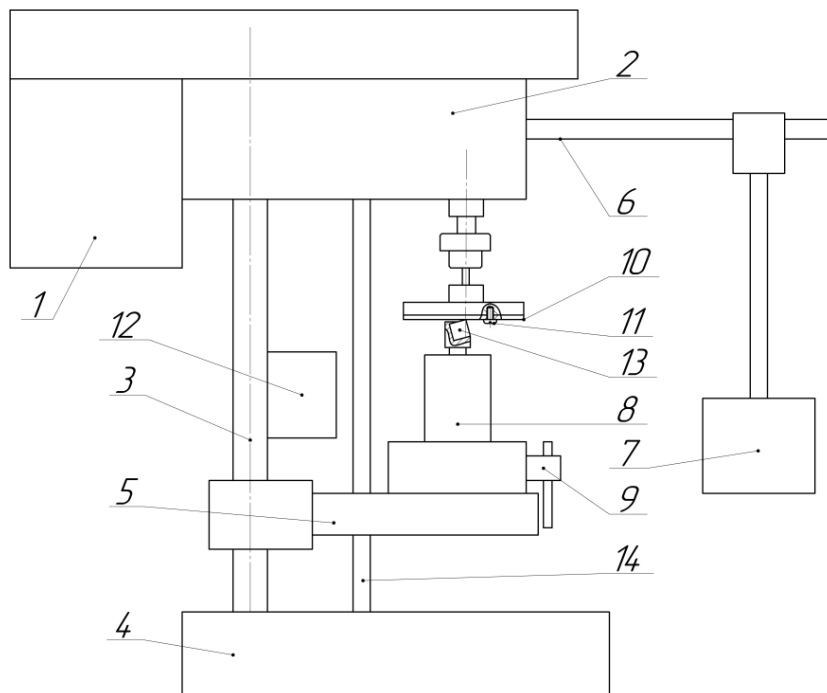


Fig. 3. Device for abrasive wear tests of the PDC cutters:

1 – electric motor; 2 – spindle unit; 3 – rack; 4 – base; 5 – console table; 6 – lever; 7 – load; 8 – data collection system; 9 – vise;

10 – diamond cutting wheel; 11 – lock; 12 – cooler; 13 – PDC cutter; 14 – screw coupling

Рис. 3. Устройство для испытания PDC-резцов на абразивное изнашивание:

1 – электродвигатель; 2 – шпиндельный узел; 3 – стойка; 4 – основание;

5 – консольный стол; 6 – рычаг; 7 – груз; 8 – система сбора данных; 9 – тиски;

10 – алмазный отрезной диск; 11 – фиксатор; 12 – охладитель; 13 – резец PDC; 14 – стяжка

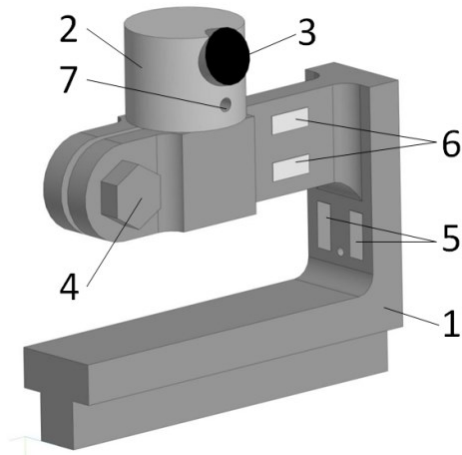


Fig. 4. Measuring unit without housing:

1 – monoblock; 2 – mandrel; 3 – PDC cutter; 4 – clamp bolt; 5 – axial load sensors;
6 – friction force sensors (tangential load); 7 – process hole for thermocouple

Рис. 4. Измерительный блок без корпуса:

1 – моноблок; 2 – оправка; 3 – PDC-резец; 4 – болт хомута; 5 – датчики осевой нагрузки;
6 – датчики силы трения (тангенциальной нагрузки); 7 – технологическое отверстие для термопары

of the cutter location. To unify the tests, a single angle of 15° was accepted for all cutters;

4) a mandrel for a counter-sample (Fig. 5). It allows fixing the diamond cutting wheel in the drive chuck and eliminates the possibility of bending the diamond cutting wheel under the action of axial load. Moreover, the diamond cutting wheel mandrel is additionally equipped with a lock that prevents the diamond cutting wheel from rotating around the rotation axis at high friction torques during tests, thus ensuring the same friction path when testing different PDC cutters and, accordingly, increasing the reliability of the results obtained.

RESULTS

The typical diagram of wear tests according to the "tooth edge – diamond wheel" scheme given in Fig. 6 shows that as the cutter wears, the friction torque increases. In this case, axial and torsional vibrations occur. Axial vibrations lead to the formation of a wave-like profile on the surface of the counter sample. Upon completion of the tests, a flat similar in shape to the worn surface is formed on the working edge of the cutter (Fig. 7).

Fractographic analysis of the surfaces of PDC cutters worn during operation (Fig. 8) and during laboratory tests showed a similar damage pattern in the form of a stepped

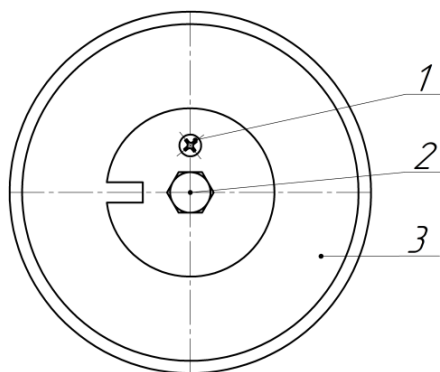


Fig. 5. Mandrel for counter sample.

Diamond cutting wheel mandrel:

1 – hole for the lock; 2 – installed lock; 3 – diamond cutting wheel

Рис. 5. Оправка для контробразца.

Оправка алмазного отрезного диска:

1 – отверстие под фиксатор; 2 – установленный фиксатор; 3 – алмазный отрезной диск

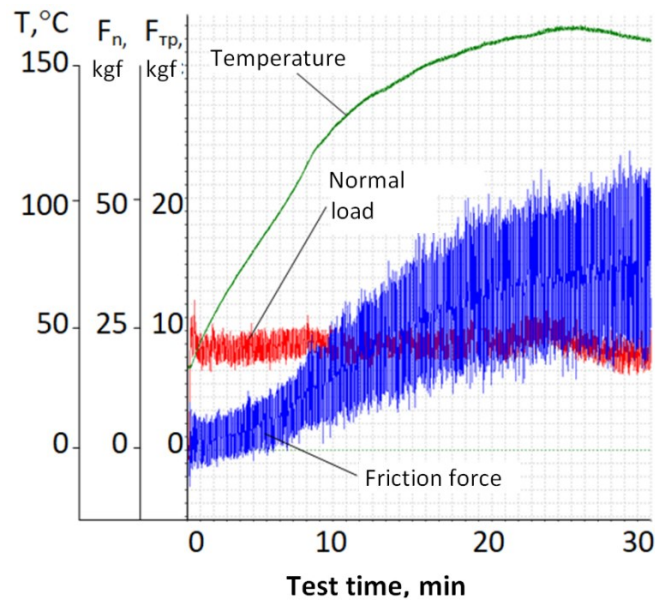


Fig. 6. Typical view of the PDC cutter test diagram
Рис. 6. Характерный вид эюры испытаний PDC-резцов



Fig. 7. View of the worn surface of a polycrystalline diamond insert
Рис. 7. Вид изношенной поверхности поликристаллической алмазной пластины

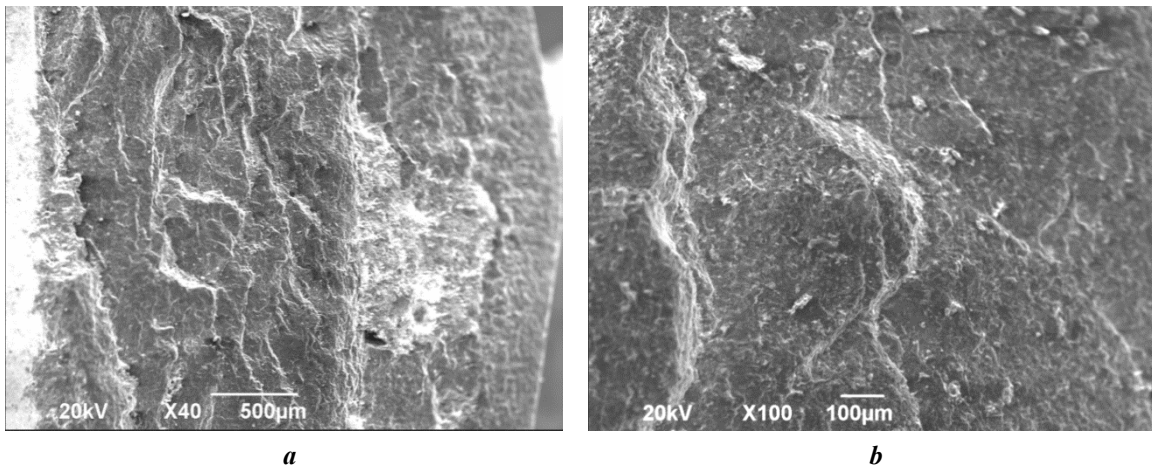


Fig. 8. Stepped structure of the wear surface of the polycrystalline diamond insert of PDC cutters: at magnification $\times 40$ (a) and $\times 100$ (b)
Рис. 8. Ступенчатая структура поверхности изнашивания поликристаллической алмазной пластины PDC-резцов: при увеличении $\times 40$ (a) и $\times 100$ (b)

structure characteristic of fatigue wear. The studies of PDC cutters of different batches and quality classes for wear showed that the range of wear rates is from 1 to 11 mg/h, and the wear rate of the work face is from 0.8 to 8 g/h.

The wear rate of the counterbody characterizes the degree of aggressiveness of the cutter in relation to the work face. Cutters with a lower content of plastic cobalt binder turned out to be more aggressive to the metal work face.

A complex parameter characterizing the efficiency of the cutter during friction – the amount of removed work face (in mg) per 1 mg of weight wear of the cutting edge of the cutter is also of interest.

Based on the conducted studies, the authors proposed a criterion that allows classifying cutters into one of four groups of operational properties by wear resistance, which is given in Table 1.

DISCUSSION

The results of testing the developed laboratory tribotechnical facility on PDC cutters of different batches showed that tests on the new equipment allow obtaining data on the wear rate of the working edges of PDC cutters quite quickly. At the same time, the fact that grinding wheels are manufactured using a specific technology regulated by technical requirements creates prerequisites for improving the reproducibility of test results. Since diamond inserts are superhard materials, artificial diamond-containing materials manufactured using a specific technology can have the greatest abrasive effect on them. Such metal-diamond composites are used as a working layer in diamond grinding wheels and diamond cutting wheels, the use of the latter has a significant advantage in terms of economy.

The experimental equipment developed for conducting abrasive tests has a wide potential for application both in the field of well drilling and in other areas where it is necessary to assess the wear resistance of materials when exposed to abrasive media.

Studying the processing of materials using diamond cutting wheels often requires the development of specialized devices for optimal tool operation. One of the key elements of such a device is a mandrel that ensures reliable fixation of the diamond cutting wheel and PDC cutter. It is important to take into account that the mandrel design should

prevent the wheel from bending under the influence of axial load and ensure the correct angle of the cutter.

The obtained results show that the developed methods for testing PDC cutters for wear and equipment can be used to differentiate cutters by wear resistance.

The quality management system for diamond and matrix bits requires improving the methods of incoming inspection of PDC cutter resistance to operational destructive factors. For effective incoming inspection of PDC cutter wear resistance, it is necessary to ensure both the adequacy of test results and the efficiency of testing without unnecessary costs. For this purpose, special laboratory equipment was developed at Samara State Technical University. To accelerate wear tests, it was proposed to use a metal-diamond work face in the form of a diamond-containing rim of a diamond cutting wheel as a counterbody. Unlike the use of natural rocks (granite stone), which can have significant differences in hardness (6.5–7 units on the Mohs scale) and tensile strength (from 40 to 80 MPa), artificially created diamond tools are manufactured according to accepted technical requirements and have a regulated range of properties. To test PDC cutters, it is recommended to take wheels with a hard bond (6600 MPa on the Vickers scale). This will reduce the wear rate of the diamond rim and allow using one disk twice: first from one end, then from the other. In this case, there is no disk clogging. The tested edge of the PDC cutter effectively removes the metal layer and reveals new diamond grains. Moreover, with an increase in the hardness of the counterbody, the pressure at the point of contact of the cutter with the metal-diamond face during friction increases. This creates conditions for forcing wear tests.

The recommended load on the friction contact is 20 kgf (196.2 N). Higher loads lead to the appearance of areas of adhesion of the PDC cutter with the diamond rim, strong heating of the contact (over 300 °C), and rapid failure of the diamond wheel without the possibility of its secondary use. For the same reasons, the rotation speed of the wheel was limited to 200 rpm. Lower loads lead to the necessity of increasing the test duration to form noticeable wear. The studies have shown that the characteristic values of the force of friction between the cutter and the diamond rim under the selected normal load are about 60...70 N, which, with a cutting wheel diameter of 115 mm, corresponds to a friction torque of 3.6...4.2 N·m. To implement such

Table 1. Classification of PDC cutters by abrasion resistance
Таблица 1. Классификация PDC-резов по стойкости к абразивному истиранию

Group of cutter operational properties according to wear resistance	Cutter wear rate, mg/h
1	<2
2	2...4
3	4...6
4	>6

an effort, it is recommended to use a drive with a power of at least 400 W. For testing, the drive can be implemented on the basis of vertical drilling machines equipping them additionally with a lever loading system.

Similarly, OAO Volgaburmash (OJSC) practiced methods for assessing the abrasion resistance of teeth, in which a granite blank was installed on a turning lathe and turned with a special cutter, where instead of a replaceable cutting plate, the test tooth was installed so that its cutting edge was located at the place of the cutting edge of the cutter. Thus, the operation of the tooth at the work face was simulated. The disadvantages of this method are the duration and high cost of tests. One test requires time from several hours to several days. The use of granite stone both leads to economic expenditures and creates certain difficulties in terms of standardizing its characteristics: natural stone is heterogeneous, has strength that varies several times and may contain an unregulated number of defects. Moreover, during these tests, a large amount of stone dust is created, and since this has a negative impact on human health and safety, a separate room is required. In addition, dust can settle on production lines, equipment and finished products, which leads to defects, quality deterioration, and the need for additional cleaning and, as a result, to increased costs.

The manual developed by OOO PetroEngineering (LLC) proposes a technology for determining the feasibility of further operation of a PDC bit in field conditions. The technology is based on observations of the wear of hundreds of bits in Western Siberian fields and an analysis of maintenance documentation (flaw detection reports, bit run cards, repair cost estimates), as well as expert opinions from specialized professionals from various companies². This technology is quite comprehensive and suggests assessing both the bit suitability for further work as intended and, based on economic calculations, the profitability of its repair (if the repair expenses do not exceed 20...30 % of the new bit cost) or the need for disposal (if the repair expenses reach 70...80 % of the new bit cost). The analysis of the bit condition is based on a visual inspection and wear assessment of five main elements that have the greatest impact on the bit condition: PDC cutters, cavities, flushing elements, bit diameter and thread condition. When counting the cutters that require replacement, all cutting elements with noticeable damage, regardless of their size and nature, are considered as such. It is believed that if the share of damaged cutters on a bit is more than 60 % of all rock-destroying cutters, then the bit operation should be finished before a decision is made on the advisability of its restoration or disposal. One should note that this guide is practical and economically feasible, but not every cutter damage should be considered a reason for its replacement, taking into account that this is the most expensive repair item. At the same time,

the features of the geological section are not always taken into account.

The methodology adopted by the Burintekh Scientific and Production Enterprise considers bits unsuitable and subjected to rejection in the following cases: the diameter of the bit has decreased by 2...3 mm (depending on the size); wear of the cutters has caused a noticeable decrease in the mechanical drilling speed; overheating of the cutters is observed over the entire surface; with significant destruction of one or several cutters³. These recommendations are also not unambiguously clear for an operator using them with insufficient experience.

The considered approaches to the analysis of tool wear are based on the study of existing damage, but how to approach the prediction of the performance of the drill bit tool? To answer this question, there are various prediction models [16; 17], including methods based on the use of artificial intelligence. Thus, in the work [18] a two-stage neural network model is proposed, which at the first stage estimates the drilling speed, and at the second – predicts the percentage of PDC cutter breakdowns.

CONCLUSIONS

Conducting tests on a laboratory tribotechnical facility for PDC cutters of different batches allowed obtaining important data on the wear rate of working edges. Testing results showed that the range of wear rates varies from 1 to 11 mg/h. It is important to note that the wear rate of the work face fluctuates from 0.8 to 8 g/h. These results indicate the effectiveness of the new equipment for quick and accurate measurement of PDC cutter wear during operation.

The authors have developed methods and equipment for laboratory testing of PDC cutters for wear during friction against a diamond-containing metal work face, which can be used for incoming quality control of a batch of PDC cutters arriving for assembly of diamond drill bits. Research conducted based on the obtained data allowed developing a criterion for classifying cutters by their wear resistance. The proposed criterion allows determining more accurately the wear resistance category of cutters, which, in turn, helps to increase the efficiency of production processes. Except for the wear of PDC cutters, it is recommended to evaluate also the wear of the counterbody, which characterizes the performance of the cutter.

REFERENCES

1. Neskoromnykh V.V., Popova M.S., Parakhonko E.V. Development of rock cutting tool with PDC cutters. *Bulletin of the Tomsk Polytechnic University. Geo Assets Engineering*, 2020, vol. 331, no. 2, pp. 131–138. DOI: [10.18799/24131830/2020/2/2499](https://doi.org/10.18799/24131830/2020/2/2499).

² Myasnikov Ya.V., Ionenko A.V., Gadzhiev S.G., Lipatnikov A.A., Leonov E.G. *How to assess properly the wear of PDC bits in the field? Sphere. Oil and Gas: official website.* URL: <https://сферанефтегаз.рф/iscpetro-2014-5/>.

³ *Recommendations for assessing wear of PDC bits. Burintekh Scientific and Production Enterprise: official website.* URL: <https://burintekh.ru/upload/iblock/871/r817xkl9kjc04qjl3qtt25rfp3pmtf8lh.pdf>.

2. Nenashev M.V., Ibatullin I.D., Zhuravlev A.N., Kosulin S.I. Engineering tools and methods of PDC bits entrance quality control. *Izvestiya Samarskogo nauchnogo tsentra Rossiyskoy akademii nauk*, 2011, vol. 13, no. 4-3, pp. 835–838. EDN: [PCLSTT](#).
3. Konyashin I., Zaitsev A.A., Sidorenko D. et al. On the mechanism of obtaining functionally graded hard-metals. *Materials Letters*, 2017, vol. 186, pp. 142–145. DOI: [10.1016/j.matlet.2016.09.130](#).
4. Bogomolov R.M., Serikov D.Yu. Improvement of the cutting structures of the rolling cutter drill bits. *Obo-rudovanie i tekhnologii dlya neftegazovogo kompleksa*, 2018, no. 5, pp. 24–28. DOI: [10.30713/1999-6934-2018-5-24-28](#).
5. Vasilev A.A., Serikov D.Yu., Bliznyukov V.Yu. Improvement of drill bits of different types. *Stroitelstvo neftyanykh i gazovykh skvazhin na sushe i na more*, 2019, no. 6, pp. 28–31. DOI: [10.30713/0130-3872-2019-6-28-31](#).
6. Neskormnykh V.V., Popova M.S., Komarovskiy I.A., Bao-chang L. Concave PDC cutter. *Bulletin of the Tomsk Polytechnic University. Geo Assets Engineering*, 2022, vol. 333, no. 4, pp. 181–192. DOI: [10.18799/24131830/2022/4/3488](#).
7. Tretyak A.A., Krivosheev K.V. Winning combination of PDC cutter arrangement on a rock-destructing tool. *Delovoy zhurnal Neftegaz.RU*, 2025, no. 3, pp. 36–40. EDN: [NCPITK](#).
8. Bellin F., Dourfaye A., King W., Thigpen M. The current state of PDC bit technology. Part 1 of 3: Development and application of polycrystalline diamond compact bits have overcome complex challenges from the difficulty of reliably mounting PDC cutters in bit bodies to accelerated thermal wear. *World Oil*, 2010, pp. 41–46.
9. Kolibasov V.A., Ibatullin I.D., Parfenov K.V., Gordeeva E.S. Development of procedure and device for abrasion test of PDC cutters. *Neftegazovoe delo*, 2024, vol. 22, no. 6, pp. 53–62. DOI: [10.17122/ngdelo-2024-6-53-62](#).
10. Kuftyrev R.Y., Polushin N.I., Kotel'nikova O.S., Laptev A.I., Sorokin M.N. Wear resistance of polycrystalline diamond cutters for drill bits. *Steel in Translation*, 2017, vol. 47, no. 9, pp. 594–598. DOI: [10.3103/S096709121709008X](#).
11. Trushkin O.B., Akchurin Kh.I. PDC cutter pressure on plastic-brittle rock in the process of its destruction. *Journal of Mining institute*, 2020, vol. 244, pp. 448–453. DOI: [10.31897/PMI.2020.4.7](#).
12. Kanyanta V., Ozbayraktar S., Maweja K. Effect of manufacturing parameters on polycrystalline diamond compact cutting tool stress-state. *International Journal of Refractory Metals and Hard Materials*, 2014, vol. 45, pp. 147–152. DOI: [10.1016/j.ijrmhm.2014.03.009](#).
13. Moseley S.G., Bohn K.P., Goedickemeier M. Core drilling in reinforced concrete using polycrystalline diamond (PDC) cutters: wear and fracture mechanisms. *International Journal of Refractory Metals and Hard Materials*, 2009, vol. 27, no. 2, pp. 394–402. DOI: [10.1016/j.ijrmhm.2008.11.014](#).
14. Borisov K.I., Rubtsov V.L. Analytical investigation of rock temporal strength property at PDC cutting. *Izvestiya Tomskogo politekhnicheskogo universiteta*, 2014, vol. 325, no. 1, pp. 172–178. EDN: [SITAEP](#).
15. Yahiaoui M., Gerbaud L., Paris J.-Y., Denape J., Dourfaye A. A study on PDC drill bits quality. *Wear*, 2013, vol. 298–299, pp. 32–41. DOI: [10.1016/j.wear.2012.12.026](#).
16. Ahmed O.S., Adeniran A.A., Samsuri A. Computational intelligence based prediction of drilling rate of penetration: a comparative study. *Journal of Petroleum Science and Engineering*, 2019, vol. 172, pp. 1–12. DOI: [10.1016/j.petrol.2018.09.027](#).
17. Zhao Y., Noorbakhsh A., Koopialipoor M., Azizi A., Tahir M.M. A new methodology for optimization and prediction of rate of penetration during drilling operations. *Engineering with Computers*, 2019, vol. 3, pp. 587–595. DOI: [10.1007/s00366-019-00715-2](#).
18. Tretyak A.Ya., Kuznetsova A.V., Borisov K.A. Determination of PDC cutter breakdowns using regression and neural network modeling. *Bulletin of the Tomsk Polytechnic University. Geo Assets Engineering*, 2019, vol. 330, no. 5, pp. 169–177. DOI: [10.18799/24131830/2019/5/275](#).

СПИСОК ЛИТЕРАТУРЫ

1. Нескоромных В.В., Попова М.С., Парахонько Е.В. Разработка породоразрушающего инструмента с режущими PDC // Известия Томского политехнического университета. Инжиниринг георесурсов. 2020. Т. 331. № 2. С. 131–138. DOI: [10.18799/24131830/2020/2/2499](#).
2. Ненашев М.В., Ибатуллин И.Д., Журавлев А.Н., Косулин С.И. Технические средства и методики входного контроля качества PDC зубков алмазных буровых долот // Известия Самарского научного центра Российской академии наук. 2011. Т. 13. № 4-3. С. 835–838. EDN: [PCLSTT](#).
3. Konyashin I., Zaitsev A.A., Sidorenko D. et al. On the mechanism of obtaining functionally graded hard-metals // *Materials Letters*. 2017. Vol. 186. P. 142–145. DOI: [10.1016/j.matlet.2016.09.130](#).
4. Богомоллов Р.М., Сериков Д.Ю. Совершенствование вооружения шарошечного бурового долота // Оборудование и технологии для нефтегазового комплекса. 2018. № 5. С. 24–28. DOI: [10.30713/1999-6934-2018-5-24-28](#).
5. Васильев А.А., Сериков Д.Ю., Близиюков В.Ю. Совершенствование буровых долот различных типов // Строительство нефтяных и газовых скважин на суше и на море. 2019. № 6. С. 28–31. DOI: [10.30713/0130-3872-2019-6-28-31](#).
6. Нескоромных В.В., Попова М.С., Комаровский И.А., Баочанг Л. Резцы PDC с вогнутой поверхностью режущей грани // Известия Томского политехнического университета. Инжиниринг георесурсов. 2022. Т. 333. № 4. С. 181–192. DOI: [10.18799/24131830/2022/4/3488](#).
7. Третьяк А.А., Кривошеев К.В. Выигрышная комбинация расположения резов PDC на породоразрушающем инструменте // Деловой журнал Neftegaz.RU. 2025. № 3. С. 36–40. EDN: [NCPITK](#).
8. Bellin F., Dourfaye A., King W., Thigpen M. The current state of PDC bit technology. Part 1 of 3: Develop-

- ment and application of polycrystalline diamond compact bits have overcome complex challenges from the difficulty of reliably mounting PDC cutters in bit bodies to accelerated thermal wear // *World Oil*. 2010. P. 41–46.
9. Колибасов В.А., Ибатуллин И.Д., Парфенов К.В., Гордеева Е.С. Разработка методики и устройства для испытания PDC резцов на абразивное изнашивание // *Нефтегазовое дело*. 2024. Т. 22. № 6. С. 53–62. DOI: [10.17122/ngdelo-2024-6-53-62](https://doi.org/10.17122/ngdelo-2024-6-53-62).
 10. Куфтырев Р.Ю., Полушин Н.И., Котельникова О.С., Лаптев А.И., Сорокин М.Н. Износостойкость PDC режущих элементов, применяемых для комплектации PDC буровых долот // *Известия высших учебных заведений. Черная металлургия*. 2017. Т. 60. № 9. С. 745–751. DOI: [10.17073/0368-0797-2017-9-745-751](https://doi.org/10.17073/0368-0797-2017-9-745-751).
 11. Трушкин О.Б., Акчурин Х.И. Давление резцов PDC на пластично-хрупкую горную породу в процессе ее разрушения // *Записки Горного института*. 2020. Т. 244. С. 448–453. DOI: [10.31897/PMI.2020.4.7](https://doi.org/10.31897/PMI.2020.4.7).
 12. Kanyanta V., Ozbayraktar S., Mawaja K. Effect of manufacturing parameters on polycrystalline diamond compact cutting tool stress-state // *International Journal of Refractory Metals and Hard Materials*. 2014. Vol. 45. P. 147–152. DOI: [10.1016/j.ijrmhm.2014.03.009](https://doi.org/10.1016/j.ijrmhm.2014.03.009).
 13. Moseley S.G., Bohn K.P., Goedickemeier M. Core drilling in reinforced concrete using polycrystalline diamond (PDC) cutters: wear and fracture mechanisms // *International Journal of Refractory Metals and Hard Materials*. 2009. Vol. 27. № 2. P. 394–402. DOI: [10.1016/j.ijrmhm.2008.11.014](https://doi.org/10.1016/j.ijrmhm.2008.11.014).
 14. Борисов К.И., Рубцов В.Л. Аналитическое исследование временной прочностной характеристики горной породы при резании-скальвании резцами PDC // *Известия Томского политехнического университета*. 2014. Т. 325. № 1. С. 172–178. EDN: [SITAEP](https://www.edn.ru/SITAEP).
 15. Yahiaoui M., Gerbaud L., Paris J.-Y., Denape J., Dourfaye A. A study on PDC drill bits quality // *Wear*. 2013. Vol. 298–299. P. 32–41. DOI: [10.1016/j.wear.2012.12.026](https://doi.org/10.1016/j.wear.2012.12.026).
 16. Ahmed O.S., Adeniran A.A., Samsuri A. Computational intelligence based prediction of drilling rate of penetration: a comparative study // *Journal of Petroleum Science and Engineering*. 2019. Vol. 172. P. 1–12. DOI: [10.1016/j.petrol.2018.09.027](https://doi.org/10.1016/j.petrol.2018.09.027).
 17. Zhao Y., Noorbakhsh A., Koopialipoor M., Azizi A., Tahir M.M. A new methodology for optimization and prediction of rate of penetration during drilling operations // *Engineering with Computers*. 2019. Vol. 3. P. 587–595. DOI: [10.1007/s00366-019-00715-2](https://doi.org/10.1007/s00366-019-00715-2).
 18. Третьяк А.Я., Кузнецова А.В., Борисов К.А. Определение поломок резцов PDC с помощью регрессионного и нейросетевого моделирования // *Известия Томского политехнического университета. Инжиниринг георесурсов*. 2019. Т. 330. № 5. С. 169–177. DOI: [10.18799/24131830/2019/5/275](https://doi.org/10.18799/24131830/2019/5/275).

Разработка лабораторного триботехнического комплекса для испытаний PDC-резцов на изнашивание

*Колибасов Владимир Александрович**¹, аспирант,

ассистент кафедры «Машины и оборудование нефтегазовых и химических производств»

Ибатуллин Ильдар Дугласович, доктор технических наук, профессор,

заведующий кафедрой «Машины и оборудование нефтегазовых и химических производств»

*Новиков Владислав Александрович*², кандидат технических наук,

доцент кафедры «Металловедение, порошковая металлургия, наноматериалы»,

старший научный сотрудник лаборатории рентгеновской дифрактометрии, электронной и зондовой микроскопии

Самарский государственный технический университет, Самара (Россия)

*E-mail: mahp@samgtu.ru,
csstea@yandex.ru

¹ORCID: <https://orcid.org/0000-0002-0503-2533>

²ORCID: <https://orcid.org/0000-0002-8052-305X>

Поступила в редакцию 10.02.2025

Пересмотрена 25.02.2025

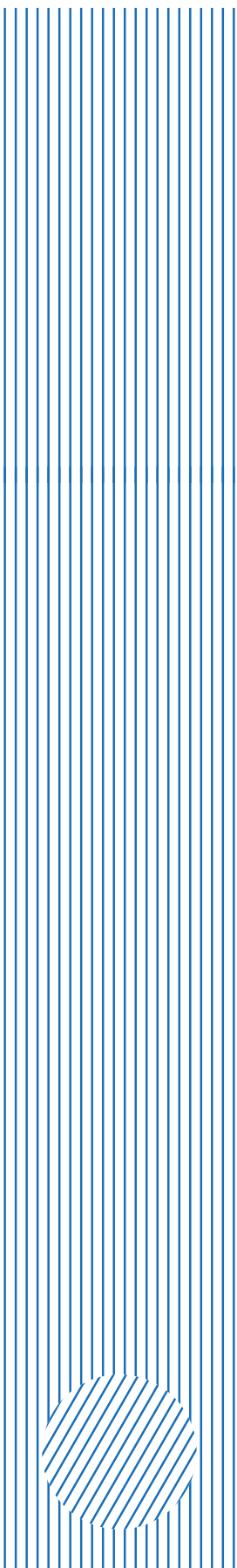
Принята к публикации 11.03.2025

Аннотация: В практике бурения нефтегазовых скважин алмазными долотами, вооруженными PDC-резцами, имеют место случаи несоответствия качества резцов заявленному классу. При этом применяемые в настоящее время методы натуральных испытаний, когда в качестве контртела используют гранитный камень, являются длительными и дорогостоящими, что затрудняет их применение для оперативного входного контроля новых партий PDC-резцов, поступающих на сборку алмазных долот. Это обусловило необходимость разработки лабораторного триботехнического комплекса для количественной оценки способности PDC-резцов противостоять истиранию об абразивные материалы. Исследование посвящено разработке специализированного триботехнического комплекса, позволяющего проводить испытания на изнашивание PDC-резцов различных типоразмеров при трении об алмазосодержащий металлический забой, в качестве которого предложено использовать алмазные отрезные диски. В состав разработанного лабораторного триботехнического комплекса входят: электромеханический привод вращения (станок сверлильно-фрезерной группы); измерительный блок с датчиками нормальных нагрузок, силы трения и температуры саморазогрева резца при испытаниях; рычажный механизм нагружения; набор оправок для возможности установки PDC-резцов различных типоразмеров; система сбора данных и лицензионное программное обеспечение. Результаты апробации разработанного лабораторного трибо-

технического комплекса на PDC-резцах различных партий показали, что испытания на новом оборудовании позволяют достаточно быстро получать данные о скорости изнашивания рабочих кромок PDC-резцов. Разработанные методики, оборудование и критерии можно использовать для возможности сертификации износостойкости PDC-резцов.

Ключевые слова: алмазное долото; PDC-резец; триботехнический комплекс; алмазосодержащий металлический забой.

Для цитирования: Колибасов В.А., Ибатуллин И.Д., Новиков В.А. Разработка лабораторного триботехнического комплекса для испытаний PDC-резцов на изнашивание // Frontier Materials & Technologies. 2025. № 1. С. 9–19. DOI: 10.18323/2782-4039-2025-1-71-1.



Togliatti State University is a participant in the Priority-2030 program of strategic academic leadership, a flagship university in the Samara region, a center for innovative and technological development of the region.

Togliatti State University was created in 2001 by merging Togliatti Polytechnic Institute (founded in 1951 as a branch of Kuibyshev Industrial Institute) and Togliatti branch of Samara State Pedagogical University (founded in 1987).

Togliatti State University today

- More than 22,000 students of all modes of study.
- Ten institutes implementing more than 170 higher education programs for 25 integrated groups of training areas, advanced technologies research institute, Zhiguli Valley Institute of Additional Education, military training center.
- 38 resource centers with up-to-date facilities and equipment created since 2011.
- Accreditation in eight systems for standard testing, research, and engineering.
- Main areas: advanced digital, intelligent manufacturing technologies, robotic systems, advanced materials and design methods, environmentally friendly and resource-saving energy engineering, personalized medicine, countering industrial threats.

University main achievements

- Ongoing project and professional practical activity was introduced for 100 % of full-time undergraduate/specialist students.
- Four mega-grants were implemented according to the Resolutions of the Government of the Russian Federation dated April 9, 2010 No. 219 and No. 220 – three laboratories in the field of physical materials science and nanotechnology (with the invitation of leading scientists), as well as an innovation technology center were created. The latter was transformed into a university innovation technopark.
- A member of the extraterritorial scientific and educational center “Engineering of the Future”.
- An initiator of the formation of eight consortiums, which brought together 69 organizations, including 36 universities, six scientific partners, among which there are three organizations of the Russian Academy of Sciences.
- A twice winner of the RF Government award in the field of quality (2009, 2019).
- An Online Higher Education System promoted under the Rosdistant brand was created. The project is the winner of the Project Olympus competition of the Analytical Center under the Government of the Russian Federation in the Project Management in the System of Higher Education and Science nomination (2019).

Structure and mechanical properties of high-entropy alloys of the CoCrZrMnNi system with different Zr and Mn contents produced by vacuum-induction melting

Sergey V. Konovalov^{*1,2,3}, Doctor of Sciences (Engineering), Professor,
Vice-Rector for Research and Innovation Activities

Vladislav K. Drobyshev^{1,4}, postgraduate student of Chair of Metal Forming and Materials Science of EVRAZ ZSMK,
researcher of the Laboratory of Electron Microscopy and Image Processing

Irina A. Panchenko^{1,5}, PhD (Engineering), assistant professor of Chair of Quality Management and Innovation,
Head of the Laboratory of Electron Microscopy and Image Processing

Li Haixin^{2,6}, PhD, associate professor of Yantai Research Institute

¹Siberian State Industrial University, Novokuznetsk (Russia)

²Harbin Engineering University, Yantai (China)

*E-mail: konovalov@sibsiu.ru

³ORCID: <https://orcid.org/0000-0003-4809-8660>

⁴ORCID: <https://orcid.org/0000-0002-1532-9226>

⁵ORCID: <https://orcid.org/0000-0002-1631-9644>

⁶ORCID: <https://orcid.org/0000-0002-3444-115X>

Received 29.11.2024

Revised 30.01.2025

Accepted 19.02.2025

Abstract: The mechanical properties and microstructure of high-entropy alloys (HEA) of the CoCrZrMnNi system produced by vacuum-induction melting are studied depending on the change in the Zr and Mn content. The effect of the Zr and Mn percentage on the microstructure and mechanical properties (Young's modulus, nanohardness, microhardness) of the high-entropy alloys of the CoCrZrMnNi system is estimated. The relationship between varying the percentage of Zr and Mn and changing the grain size and mechanical properties of high-entropy alloys is studied. The structure, chemical composition and distribution of the intensity of characteristic X-ray radiation of atoms are studied using scanning electron microscopy. The study by scanning electron microscopy methods has demonstrated that in CoCrZrMnNi alloys, with an increase in the zirconium content and a decrease in the manganese content closer to the equiatomic composition, the material structure became more homogeneous. Changing the percentage of zirconium from 8 to 28 at. % contributed to the grain size reduction from 30 to 5 μm and a more uniform elemental distribution. The $\text{Co}_{19.8}\text{Cr}_{17.5}\text{Zr}_{15.3}\text{Mn}_{27.7}\text{Ni}_{19.7}$ alloy demonstrated the highest nanohardness (10 GPa) and Young's modulus (161 GPa) during instrumental indentation with an indenter load of 50 mN. The $\text{Co}_{20.4}\text{Cr}_{18.0}\text{Zr}_{7.9}\text{Mn}_{33.3}\text{Ni}_{20.3}$ alloy has the lowest nanohardness, Young's modulus, and microhardness among other alloys, which may be related to the coarse-grained structure with a grain size of up to 30 μm . As the indenter load increased to 5 N, the microhardness of the $\text{Co}_{19.8}\text{Cr}_{17.5}\text{Zr}_{15.3}\text{Mn}_{27.7}\text{Ni}_{19.7}$ alloy decreased compared to the $\text{Co}_{18.7}\text{Cr}_{16.5}\text{Zr}_{28.9}\text{Mn}_{17.4}\text{Ni}_{18.6}$ alloy, which may indicate more universal mechanical properties of alloys with equiatomic zirconium content.

Keywords: structure; mechanical properties; high-entropy alloy; vacuum-induction melting; scanning electron microscopy; Young's modulus; nanohardness; microhardness.

Acknowledgments: The study was supported by the grant of the Russian Science Foundation No. 23-49-00015, <https://rscf.ru/project/23-49-00015/>.

For citation: Konovalov S.V., Drobyshev V.K., Panchenko I.A., Li Haixin. Structure and mechanical properties of high-entropy alloys of the CoCrZrMnNi system with different Zr and Mn contents produced by vacuum-induction melting. *Frontier Materials & Technologies*, 2025, no. 1, pp. 21–34. DOI: 10.18323/2782-4039-2025-1-71-2.

INTRODUCTION

A new class of metallic materials, high-entropy alloys (HEAs), possessing the necessary physical, mechanical and operational characteristics, are materials consisting of five or more elements in equal or similar concentrations [1–3]. An increase in the number of elements improves mutual solubility, facilitating the formation of a single-phase solid solution [4]. Some promising technological features of HEAs include high hardness [5], good wear resistance [6], excellent strength at both high and low temperatures [7; 8],

and good resistance to oxidation and corrosion [9; 10]. The unique characteristics of these alloys are due to the intrinsic properties of a multicomponent solid solution, such as a distorted lattice structure [11], a cocktail effect [12], slow diffusion [5], and nanoscale twinning [9].

Among the HEAs, a comprehensively studied and promising material is the equiatomic CoCrFeMnNi composition called the Cantor alloy [13]. Although this material has a multicomponent chemical structure, it forms a single-phase solid solution with a face-centered cubic

lattice [14]. Due to this structure, the material demonstrates high plasticity at room temperature with a relative elongation before failure of $\sim 71\%$. However, the key disadvantage of the Cantor alloy remains the relatively low values of yield strength of ≈ 220 MPa and tensile strength of ≈ 491 MPa, which significantly narrows the area of their practical application [15]. In this regard, an urgent task in the development of the HEA of this system is to find methods for improving the strength characteristics without compromising on the reduction of plasticity.

In recent years, much work has been focused on the development of new HEA compositions with good mechanical characteristics [16]. A promising direction for improving the mechanical and functional properties of alloys is alloying with well-studied elements, for example, by adding zirconium [17]. Zirconium alloying has been studied to improve the mechanical properties of both light alloys [18] and steels [19], but the influence of zirconium on the mechanical properties of high-entropy Cantor alloys with Zr content up to 30 at. % has not yet been studied. The expected strengthening mechanism associated with Zr modifications in HEA is pinning of dislocations, which can be caused by a strong lattice distortion. This distortion, in turn, can be caused by substitution defects, vacancies, or phase mismatch [20]. Based on the study of the CoCrFeNiZr system alloy, the work [17] discusses the effect of zirconium on changes in the alloy microstructure, but does not investigate the dependence of changes in mechanical properties and structure with an increase in the zirconium content with a simultaneous decrease in the content of another component.

In this study, the authors study three compositions of high-entropy alloys of the CoCrZrMnNi system with a change in the concentration of zirconium and manganese in the alloy from ≈ 5 to ≈ 30 at. %.

The aim of this research is a detailed study of the microstructure and homogeneity of the distribution of elements in the produced alloys depending on the increase in the Zr content with a simultaneous decrease in Mn; analysis of the effect of zirconium additives on the change in microhardness, nanohardness, and Young's modulus of CoCrZrMnNi alloys; and selection of a composition with optimal mechanical properties.

METHODS

In this work, the authors investigated as-cast high-entropy CoCrZrMnNi system alloys with different zirconium and manganese contents (Table 1) produced by vacuum-induction melting.

Samples were cut from the produced ingots on a DK7732 M11 jet-type electrical discharge machine. To obtain a high-quality microsection surface for research, during grinding the authors successively moved from one sandpaper to another with continuously decreasing sizes of abrasive particles and then polished the sample using a special cloth and paste. To identify the microstructure of the samples, etching in a reagent

consisting of HNO₃ and HCl in a ratio of 1:3 was carried out; the etching time was 10–30 s.

The structure and elemental composition of the samples were studied using scanning electron microscopy (SEM) (KYKY EM-6900 device (China) equipped with an Oxford Xplore energy-dispersive analyzer (UK)) with an accelerating voltage of 30 kV, a filament current of 2.20 A, and an emission current of $150 \cdot 10^{-6}$ A. The distribution of the intensity of the characteristic X-ray radiation of atoms was obtained by scanning along the line using X-ray microanalysis to determine the concentration heterogeneity of the alloys. This analysis was carried out on etched areas ranging from 80 to 600 μm in length.

The microhardness study was carried out using an HVS-1000A microhardness tester. The load was constant for all processing modes and was 5 N. The nanohardness and elastic modulus were measured using a NanoScan-4D nanohardness tester. The measurement method is indenting a diamond pyramid (indenter) with recording the force and depth of loading and subsequent calculation of hardness and modulus of elasticity in accordance with GOST 8.748-2011 (ISO 14577). Measurement procedure parameters: indenter is a triangular Berkovich pyramid; loading time is 10 s; unloading time is 10 s; maximum load maintenance time is 10 s; applied load is 50 mN.

RESULTS

The microstructure of the as-cast Co_{19.8}Cr_{17.5}Zr_{15.3}Mn_{27.7}Ni_{19.7} high-entropy alloy produced by vacuum-induction remelting is shown in Fig. 1 and demonstrates a dendritic structure. The distribution of Co, Cr, Zr, Mn, and Ni was identified by mapping techniques. According to the data of conducted X-ray microanalysis, the content of elements presented in Table 2 was identified in the interdendritic (Fig. 1, spectra 1, 2) and dendritic regions (Fig. 1, spectra 3, 4) of the Co_{19.8}Cr_{17.5}Zr_{15.3}Mn_{27.7}Ni_{19.7} alloy. The dendritic region is enriched in chromium and manganese, reaching 42 and 29 at. %, respectively, but is depleted in zirconium (≈ 1 at. %). The grain size of the chromium-enriched dendritic "islands" was 30 μm . Based on the distribution of the intensity of characteristic X-ray radiation of atoms shown in Fig. 2, one can conclude that the distribution of chromium, manganese and zirconium atoms is non-uniform.

In the alloy with a Zr content of 7.9 % and Mn content of 33.3 %, a quasi-uniform distribution of manganese, cobalt and nickel was identified (Fig. 3). The rest Zr and Cr elements demonstrate large-scale non-uniformities. The dendrites consist of an equimolar solid solution of Mn, Cr, Ni (Fig. 3, spectra 2–4), with the absolute amount of each component slightly higher than the nominal. Zirconium is mainly concentrated in the interdendritic regions (Fig. 3, spectrum 1, Table 3); these regions are also enriched in Ni and depleted in Cr. The interdendritic phase of the Zr-free alloy contains grains consisting of Mn and Cr. Based on the graph (Fig. 4), one can conclude that two compounds are formed in the 16–36 μm and 56–68 μm regions. In these regions, the concentration of manganese and nickel varies from 6 to 46 at. %.

Table 1. Chemical composition of the studied samples of as-cast high-entropy alloys based on the CoCrZrMnNi system produced by the method of vacuum-induction melting
Таблица 1. Химический состав исследуемых образцов высокоэнтропийных сплавов в литом состоянии на основе системы CoCrZrMnNi, полученных методом вакуумной индукционной плавки

Co, at. %	Cr, at. %	Zr, at. %	Mn, at. %	Ni, at. %
19.8	17.5	15.3	27.7	19.7
20.4	18.0	7.9	33.3	20.3
18.7	16.5	28.9	17.4	18.6

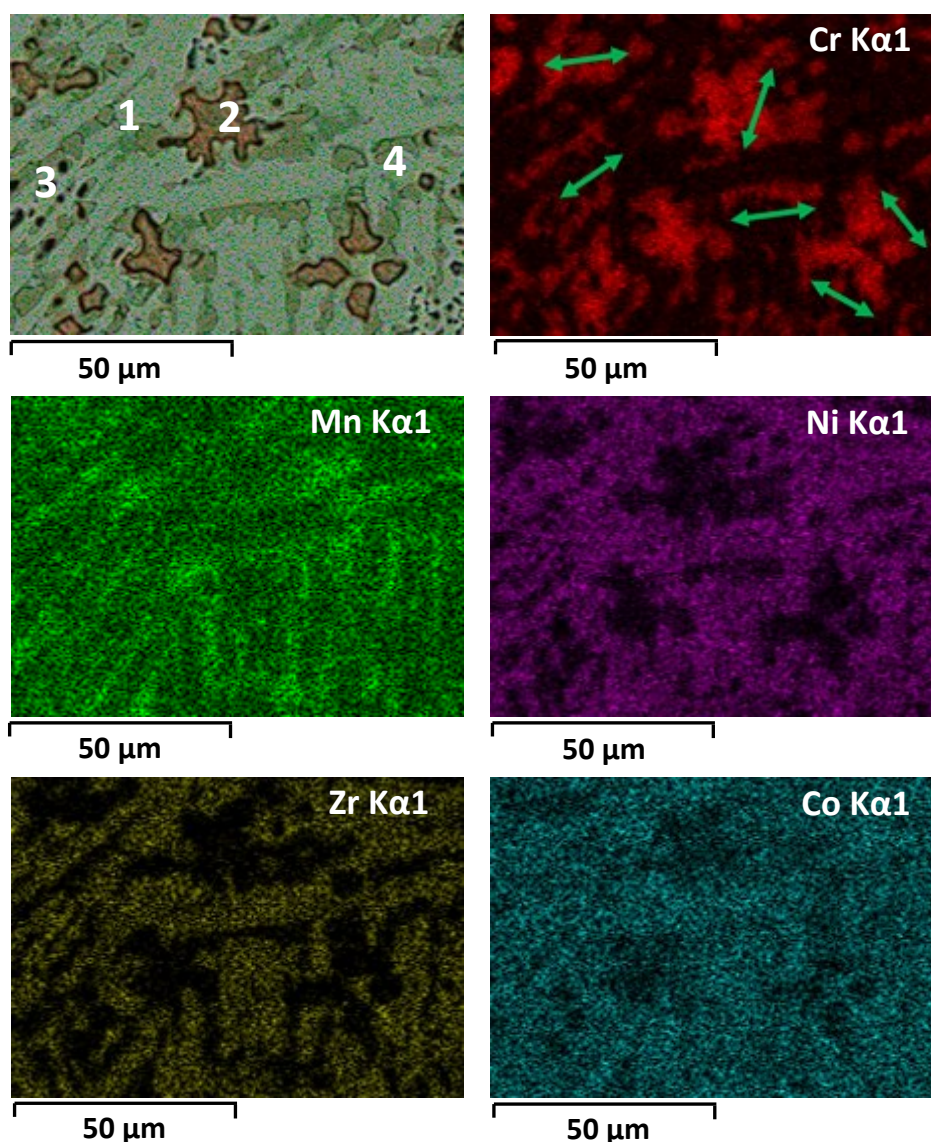


Fig. 1. Elemental mapping of the $Co_{19.8}Cr_{17.5}Zr_{15.3}Mn_{27.7}Ni_{19.7}$ alloy.
 1–4 are sections of X-ray spectral microscanning. The arrows indicate the areas of dendrites measured in diameter
Рис. 1. Элементное картирование сплава $Co_{19.8}Cr_{17.5}Zr_{15.3}Mn_{27.7}Ni_{19.7}$.
 1–4 – участки микрорентгеноспектрального сканирования.
 Стрелками показаны области измеряемых дендритов по диаметру

Table 2. The results of X-ray spectral microanalysis of the HEA presented in Fig. 1
Таблица 2. Результаты микрорентгеноспектрального анализа ВЭС по спектрам, представленного на рис. 1

Spectrum	Element, at. %					
	Cr	Mn	Zr	Co	Ni	O
1	10.27	25.29	16.26	25.43	22.75	–
2	39.21	26.94	0.92	15.83	9.64	7.45
3	42.33	29.06	1.00	17.16	10.44	–
4	33.63	29.45	4.08	18.96	13.88	–

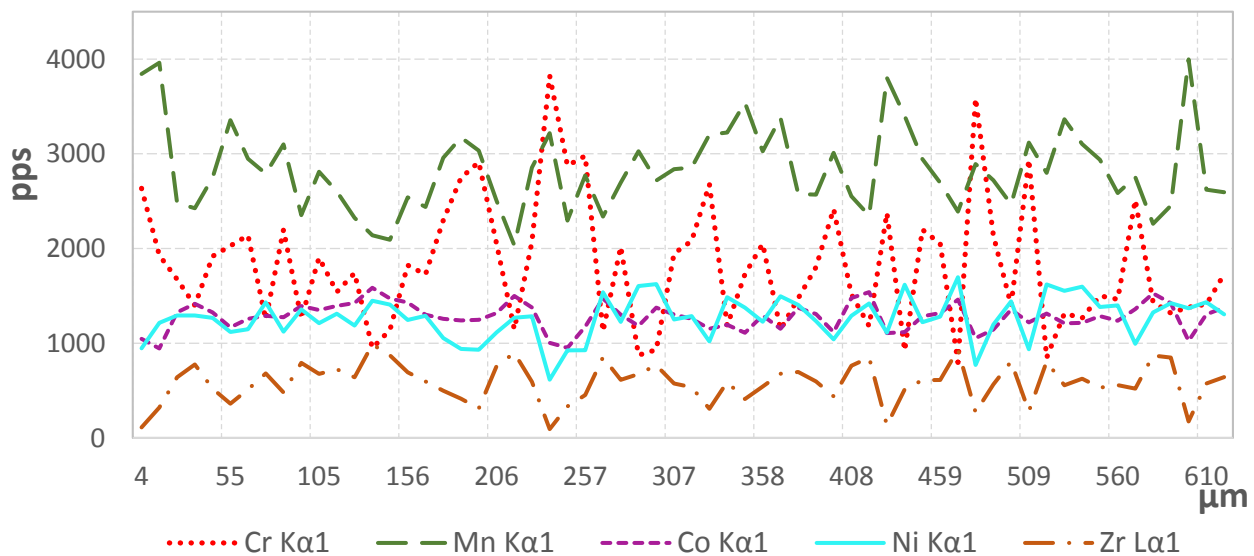
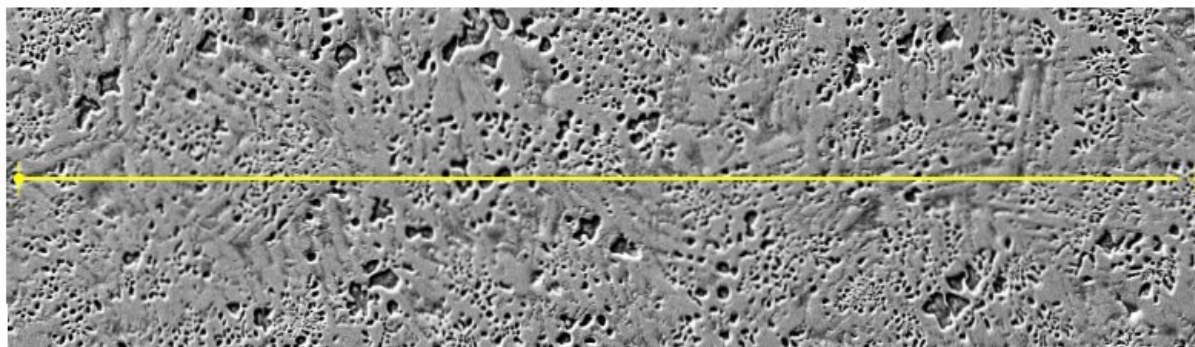


Fig. 2. Analysis of concentration heterogeneity of the $Co_{19.8}Cr_{17.5}Zr_{15.3}Mn_{27.7}Ni_{19.7}$ alloy a line length of 600 μm

Рис. 2. Анализ концентрационной неоднородности сплава $Co_{19.8}Cr_{17.5}Zr_{15.3}Mn_{27.7}Ni_{19.7}$ вдоль линии протяженностью 600 мкм

Analysis of the images obtained using SEM demonstrates the presence of elongated grains in the microstructure of the alloy (Fig. 5, spectrum 1). Despite the fact that the resulting high-entropy alloy has a non-equiatomic ratio of elements, among which Zr is predominant (Fig. 5, spectrum 1), its content in different regions decreases to 3 at. % (Fig. 5, spectrum 2) simultaneously with an increase in the content of Mn (30 at. %) and Ni (32 at. %). Elemental mapping demonstrated a uniform distribution of nickel, manganese, and

cobalt (Fig. 5, spectrum 3). The microstructure analysis performed using SEM and a built-in EDS detector confirmed the non-uniform distribution of zirconium and chromium (Table 4), as well as the formation of globular inclusions containing Zr (Fig. 5).

Based on the distribution of the intensity of characteristic X-ray radiation of atoms shown in Fig. 6, it is possible to conclude about the non-uniform distribution of chromium, manganese and zirconium atoms. The size of

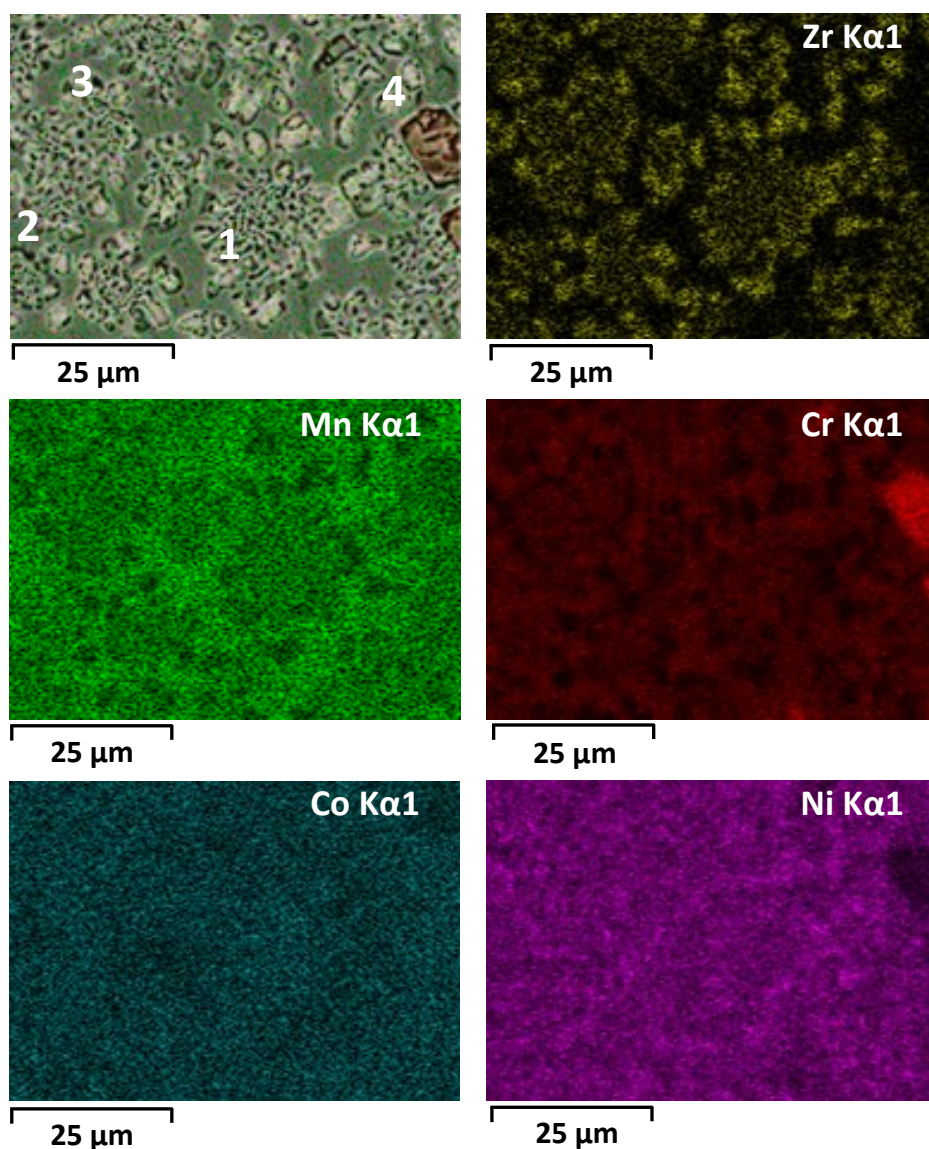


Fig. 3. Elemental mapping of the $Co_{20.4}Cr_{18.0}Zr_{7.9}Mn_{33.3}Ni_{20.3}$ alloy.
 1–4 are sections of X-ray spectral microscanning
Рис. 3. Элементное картирование сплава $Co_{20.4}Cr_{18.0}Zr_{7.9}Mn_{33.3}Ni_{20.3}$.
 1–4 – участки микрорентгеноспектрального сканирования

Table 3. The results of X-ray spectral microanalysis of the HEA presented in Fig. 3
Таблица 3. Результаты микрорентгеноспектрального анализа ВЭС по спектрам, представленного на рис. 3

Spectrum	Element, at. %				
	Cr	Mn	Zr	Co	Ni
1	5.98	26.24	14.00	20.65	33.14
2	45.92	21.78	1.00	21.75	10.55
3	16.33	40.62	1.46	17.69	23.91
4	45.92	21.78	1.00	21.75	10.55

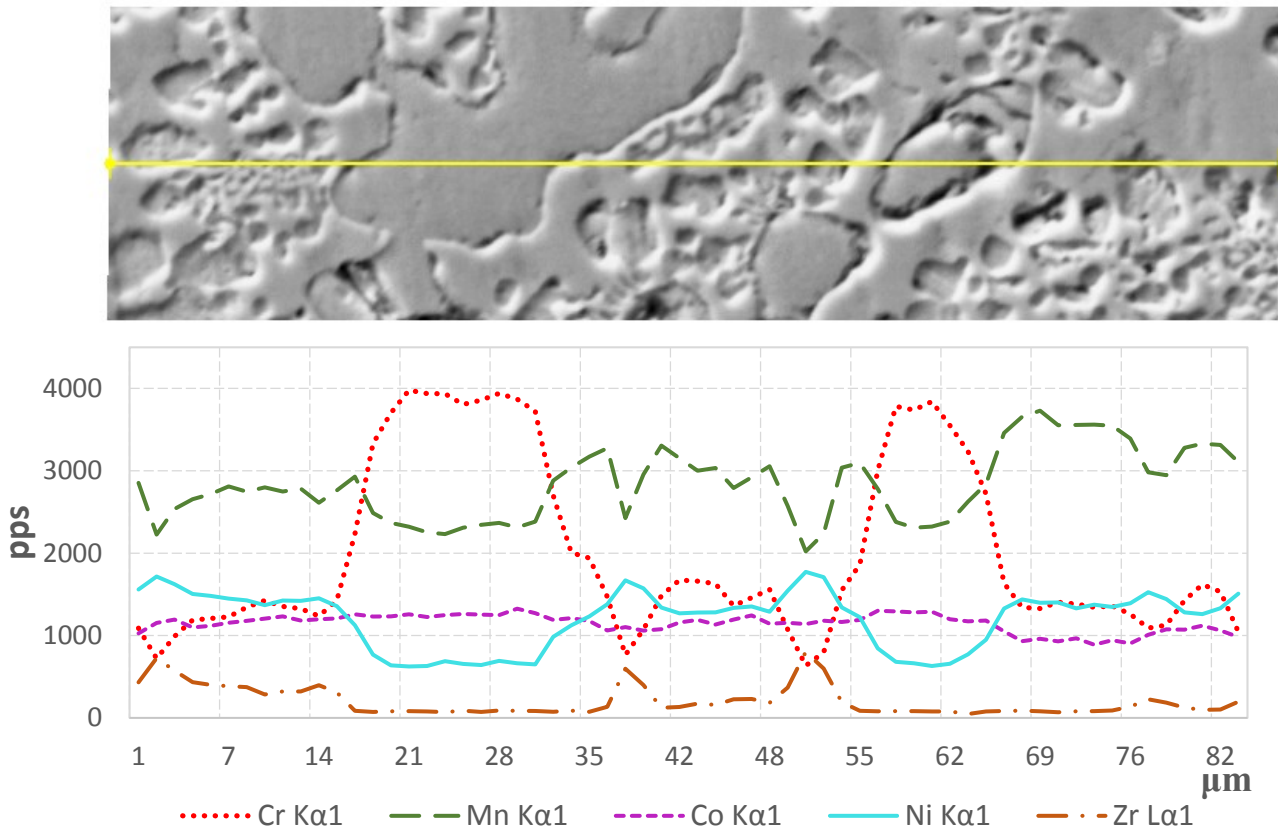


Fig. 4. Determination of concentration heterogeneity of the $Co_{20.4}Cr_{18.0}Zr_{7.9}Mn_{33.3}Ni_{20.3}$ alloy a line length of 90 μm
Рис. 4. Определение концентрационной неоднородности сплава $Co_{20.4}Cr_{18.0}Zr_{7.9}Mn_{33.3}Ni_{20.3}$ вдоль линии протяженностью 90 мкм

Table 4. The results of X-ray spectral microanalysis of the HEA presented in Fig. 5
Таблица 4. Результаты микрорентгеноспектрального анализа ВЭС по спектрам, представленного на рис. 5

Spectrum	Element, at. %				
	Cr	Mn	Zr	Co	Ni
1	18.31	16.27	24.26	23.21	17.95
2	10.74	30.21	3.87	23.18	32.00
3	12.76	22.28	19.65	20.98	24.32

the areas of non-uniform distribution of elements is up to 10 μm (Fig. 6).

The change in nanohardness and microhardness in CoCrZrMnNi alloys with an increase in the zirconium content and a decrease in the manganese content is distributed non-linearly. Thus, in the $Co_{19.8}Cr_{17.5}Zr_{15.3}Mn_{27.7}Ni_{19.7}$ alloy, the nanohardness values obtained in the interdendritic phase enriched with zirconium were 11 GPa, which is higher compared to the measurements carried out in the dendritic region equal to 9 GPa. These nanohardness values are the best among the other alloys studied. With an increase in

the indenter load from 50 mN to 5 N, the microhardness of the $Co_{19.8}Cr_{17.5}Zr_{15.3}Mn_{27.7}Ni_{19.7}$ alloy decreases compared to the $Co_{18.7}Cr_{16.5}Zr_{28.9}Mn_{17.4}Ni_{18.6}$ alloy by 10%. In general, the trend of increasing zirconium content has a positive effect on the increase in the microhardness of the material changing from 295 to 553 HV_{0.5} (Fig. 7, Table 5). Thus, the alloy with the element content close to equimolar $Co_{18.7}Cr_{16.5}Zr_{28.9}Mn_{17.4}Ni_{18.6}$ alloy demonstrates better hardening ability compared to alloys with a nominal zirconium content of 7 and 15%. Mechanically (elastic modulus), the $Co_{20.4}Cr_{18.0}Zr_{7.9}Mn_{33.3}Ni_{20.3}$ and $Co_{18.7}Cr_{16.5}Zr_{28.9}Mn_{17.4}Ni_{18.6}$

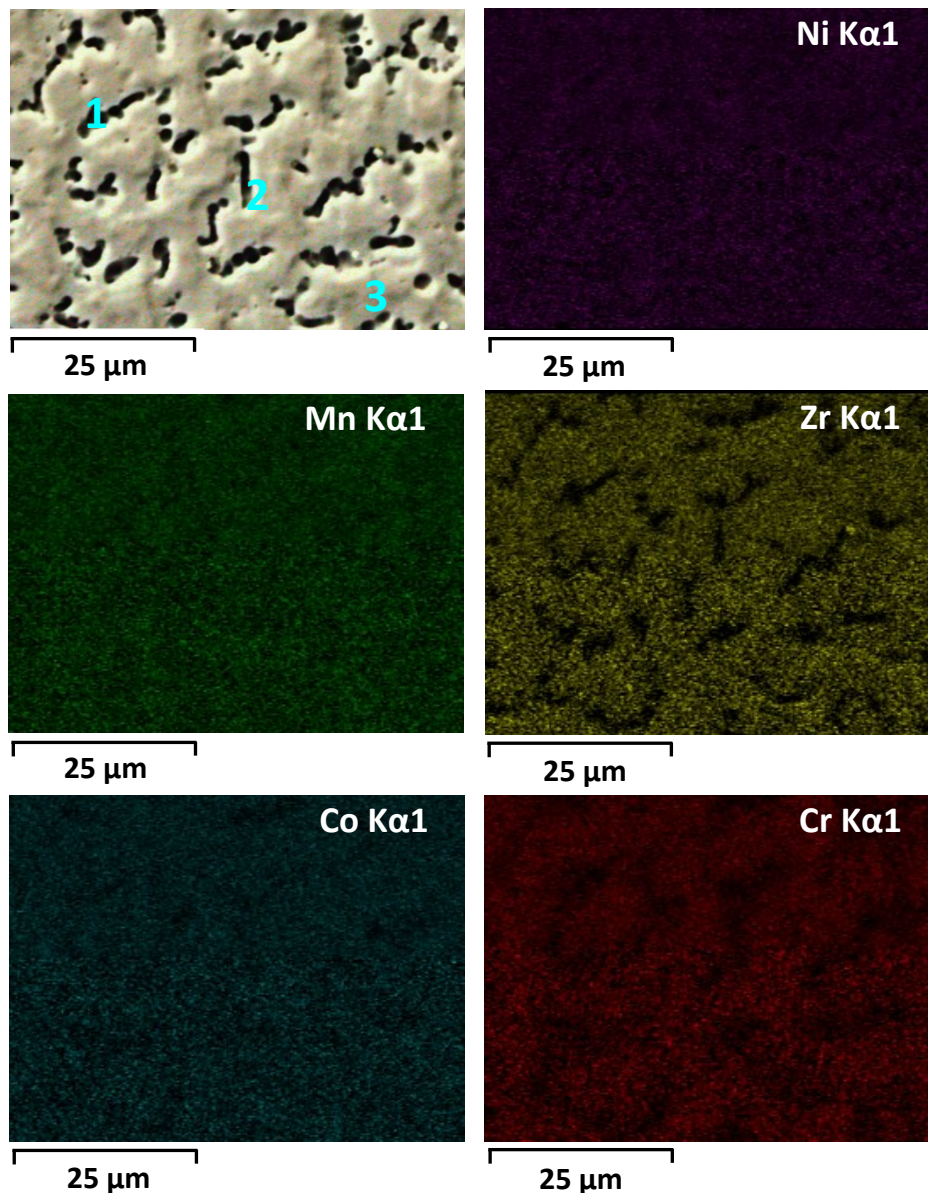


Fig. 5. Elemental mapping of the $Co_{18.7}Cr_{16.5}Zr_{28.9}Mn_{17.4}Ni_{18.6}$ alloy.
1–3 are sections of X-ray spectral microscanning

Рис. 5. Элементное картирование сплава $Co_{18.7}Cr_{16.5}Zr_{28.9}Mn_{17.4}Ni_{18.6}$.
1–3 – участки микрорентгеноспектрального сканирования

alloys differ little, demonstrating very similar values – 122.73 ± 10.37 and 109 ± 10.41 GPa, respectively.

The microstructure of the as-cast CoCrZrMnNi alloy with nonequimolar Zr (8 at. %) and Mn (33 at. %) contents (Fig. 8 c, 8 d) consists predominantly of large dendrites with an increased chromium content of up to 46 % (Table 3). An increase in the zirconium content in the interdendritic regions of the $Co_{20.4}Cr_{18.0}Zr_{7.9}Mn_{33.3}Ni_{20.3}$ alloy reached 14 at. %. With an increase in the Zr content and a decrease in the Mn content closer to the equiatomic composition, the structure of the material became more uniform and the grain size decreased from 30 (Fig. 8 a, 8 b) to 5 μm (Fig. 8 e, 8 f). The smallest dendritic grains are found in the $Co_{18.7}Cr_{16.5}Zr_{28.9}Mn_{17.4}Ni_{18.6}$ alloy, located from the edge of the sample to the center.

DISCUSSION

In Fig. 1, the interdendritic phase of the Zr-free alloy contains small spherical inclusions (10 μm in diameter) consisting of Mn and Cr oxides. The formation of such inclusions has been previously noted by several authors. Apparently, inclusions are difficult to avoid when producing materials melted in a vacuum-induction furnace [21]. The reason for their presence is partial oxidation of the charge material, as evidenced by the data in Table 2 obtained by the X-ray microanalysis method.

Probably, the alignment of dendritic grains is associated with the direction of heat flow during solidification. In all the studied alloys, a quasi-homogeneous distribution of cobalt atoms was noted in elemental mapping (Figs. 1, 3, 5), thereby the percentage content of cobalt corresponds to

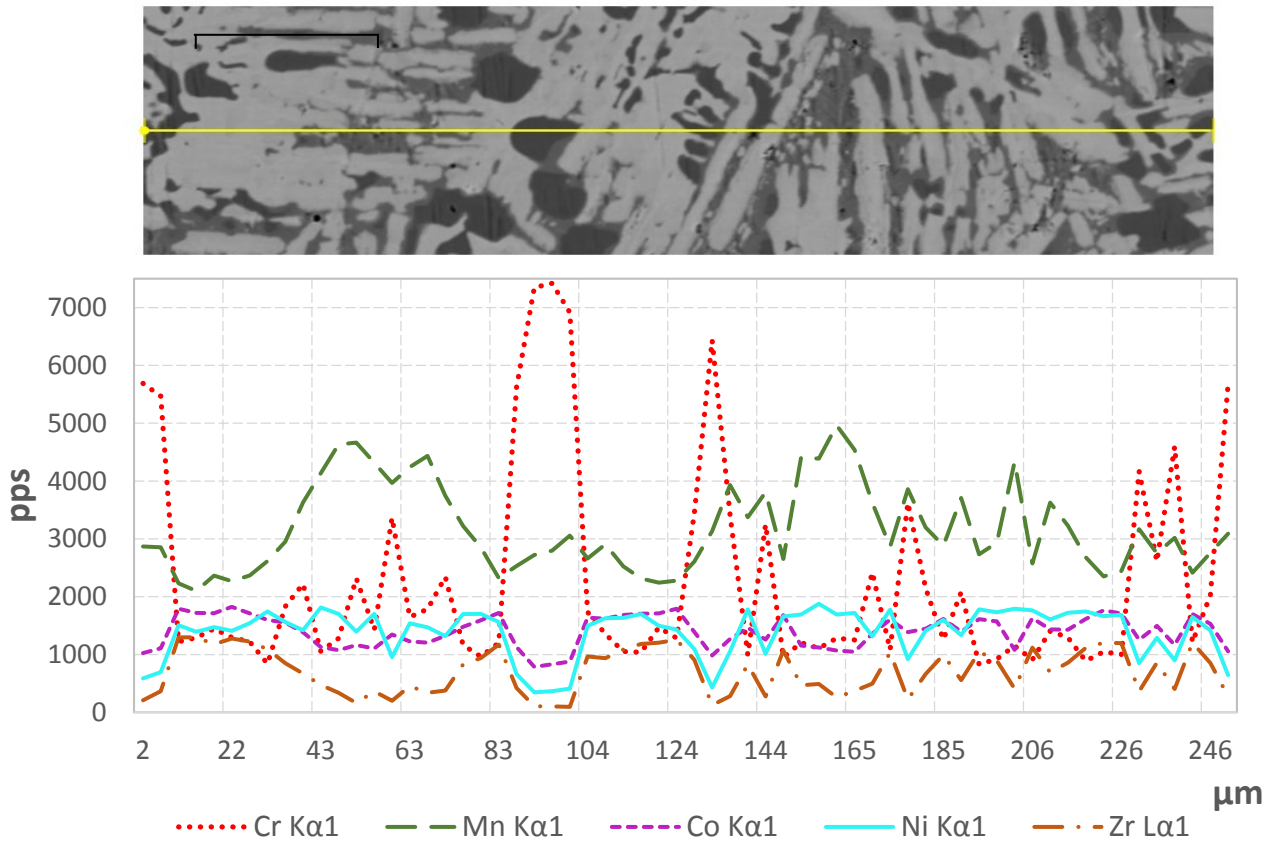


Fig. 6. Determination of concentration heterogeneity of the $Co_{18.7}Cr_{16.5}Zr_{28.9}Mn_{17.4}Ni_{18.6}$ alloy along a line length of 246 μm
Рис. 6. Определение концентрационной неоднородности сплава $Co_{18.7}Cr_{16.5}Zr_{28.9}Mn_{17.4}Ni_{18.6}$ вдоль линии протяженностью 246 мкм

Table 5. Changes in the mechanical properties of CoCrZrMnNi alloys depending on changes in the zirconium and manganese content
Таблица 5. Изменение механических свойств сплавов CoCrZrMnNi в зависимости от изменения содержания циркония и марганца

Average value			
Indenter penetration depth, nm	Nanohardness, GPa	Young's modulus, GPa	Microhardness, HV0.5
$Co_{19.8}Cr_{17.5}Zr_{15.3}Mn_{27.7}Ni_{19.7}$			
425.41±0.28	10.05±1.03	161.67±20.57	484±58
$Co_{20.4}Cr_{18.0}Zr_{7.9}Mn_{33.3}Ni_{20.3}$			
745.22±43.63	3.48±0.38	122.73±10.37	334±35
$Co_{18.7}Cr_{16.5}Zr_{28.9}Mn_{17.4}Ni_{18.6}$			
454.30±23.45	8.95±0.83	109.96±10.41	537±57

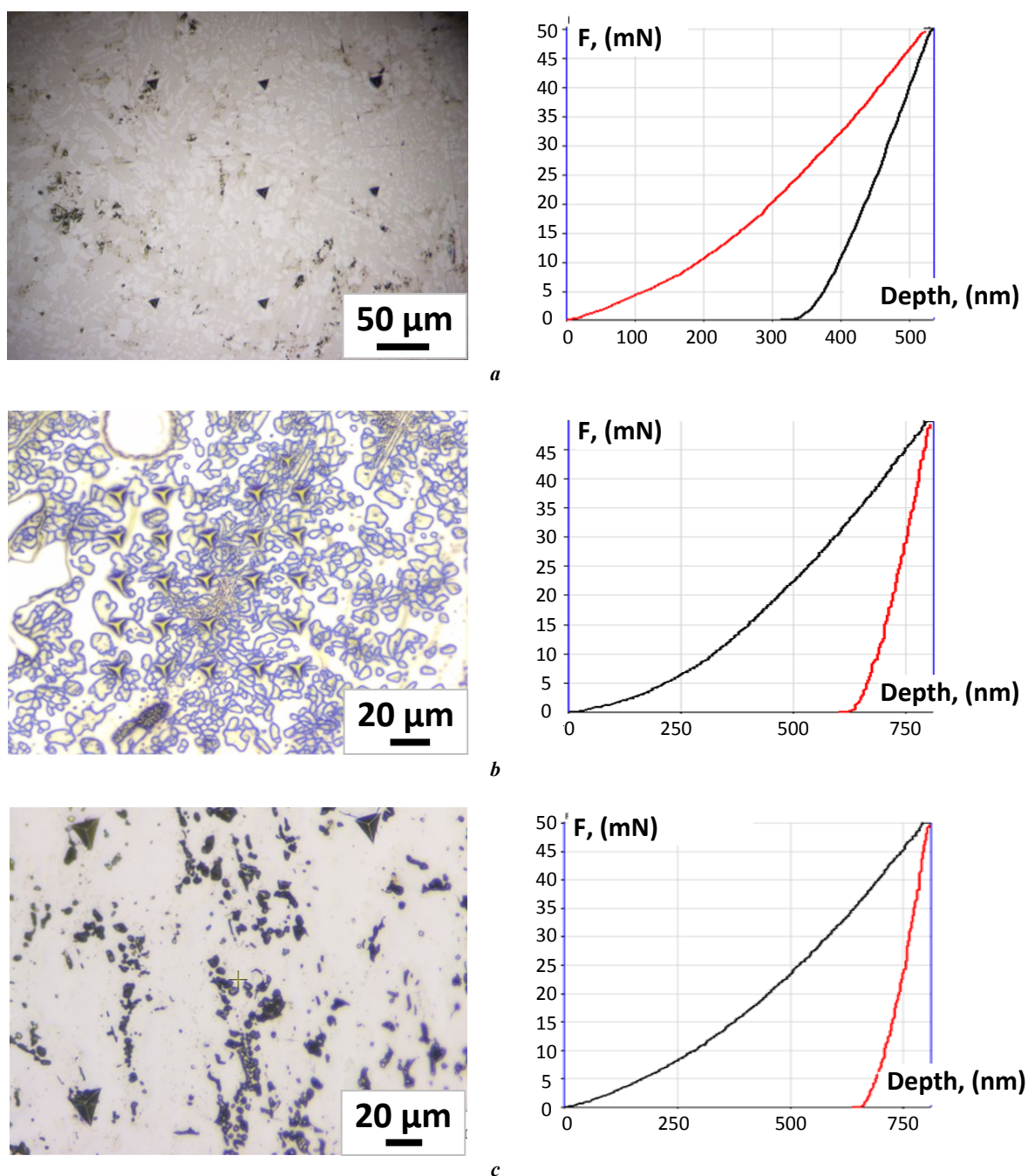


Fig. 7. Optical image and loading–unloading graph of instrumental indentation of CoCrZrMnNi alloys:

a – $Co_{19.8}Cr_{17.5}Zr_{15.3}Mn_{27.7}Ni_{19.7}$; **b** – $Co_{20.4}Cr_{18.0}Zr_{7.9}Mn_{33.3}Ni_{20.3}$; **c** – $Co_{18.7}Cr_{16.5}Zr_{28.9}Mn_{17.4}Ni_{18.6}$

Рис. 7. Оптическое изображение и график разгрузки – нагрузки инструментального индентирования сплавов CoCrZrMnNi:

a – $Co_{19.8}Cr_{17.5}Zr_{15.3}Mn_{27.7}Ni_{19.7}$; **b** – $Co_{20.4}Cr_{18.0}Zr_{7.9}Mn_{33.3}Ni_{20.3}$; **c** – $Co_{18.7}Cr_{16.5}Zr_{28.9}Mn_{17.4}Ni_{18.6}$

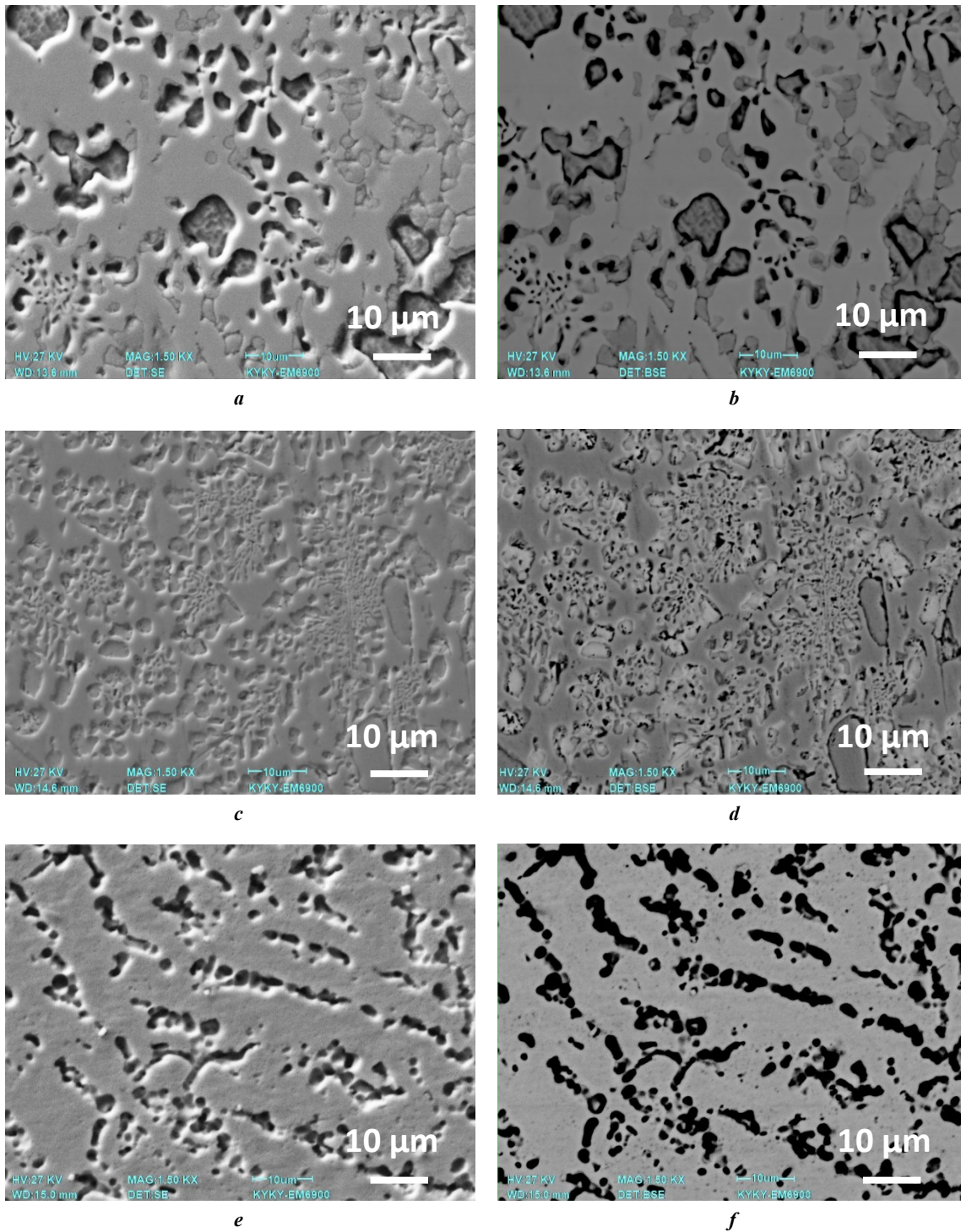


Fig. 8. Microstructure of CoCrZrMnNi alloys with different zirconium and manganese contents:
a, b – SEM of the $Co_{19.8}Cr_{17.5}Zr_{15.3}Mn_{27.7}Ni_{19.7}$ alloy using SE and BSE detector;
c, d – SEM of the $Co_{20.4}Cr_{18.0}Zr_{7.9}Mn_{33.3}Ni_{20.3}$ alloy using SE and BSE detector;
e, f – SEM of the $Co_{18.7}Cr_{16.5}Zr_{28.9}Mn_{17.4}Ni_{18.6}$ alloy using SE and BSE detector

Рис. 8. Микроструктура сплавов CoCrZrMnNi с разным содержанием циркония и марганца:
a, b – СЭМ сплава $Co_{19.8}Cr_{17.5}Zr_{15.3}Mn_{27.7}Ni_{19.7}$ с использованием SE и BSE детектора;
c, d – СЭМ сплава $Co_{20.4}Cr_{18.0}Zr_{7.9}Mn_{33.3}Ni_{20.3}$ с использованием SE и BSE детектора;
e, f – СЭМ сплава $Co_{18.7}Cr_{16.5}Zr_{28.9}Mn_{17.4}Ni_{18.6}$ с использованием SE и BSE детектора

the nominal one in the studied alloys, which is consistent with the data of [22].

It is worth noting that the microhardness of the nonequiatomic $\text{Co}_{18.7}\text{Cr}_{16.5}\text{Zr}_{28.9}\text{Mn}_{17.4}\text{Ni}_{18.6}$ alloy ($537 \pm 57 \text{ HV}_{0.5}$) (Table 5) exceeds the value for the $\text{Co}_{19.8}\text{Cr}_{17.5}\text{Zr}_{15.3}\text{Mn}_{27.7}\text{Ni}_{19.7}$ composition close to equiatomic ($484 \pm 58 \text{ HV}_{0.5}$) [29], and the lowest values are observed in the alloy with a Zr content of 7.9 at. % and a Mn content of 33.3 at. %. This may be due to a finer grain structure reaching a size of about $5 \mu\text{m}$ and a more uniform distribution of elements in the $\text{Co}_{18.7}\text{Cr}_{16.5}\text{Zr}_{28.9}\text{Mn}_{17.4}\text{Ni}_{18.6}$ alloy compared to the $\text{Co}_{19.8}\text{Cr}_{17.5}\text{Zr}_{15.3}\text{Mn}_{27.7}\text{Ni}_{19.7}$ и $\text{Co}_{20.4}\text{Cr}_{18.0}\text{Zr}_{7.9}\text{Mn}_{33.3}\text{Ni}_{20.3}$ alloys. A similar pattern of changes in mechanical properties at nonequiatomic concentrations of Fe and Mn leading to an increase in the micro- and nanohardness of CoCrFeMnNi alloys is observed in [15].

Dark particles are present in the electron microscopic images shown in Fig. 7. This may be due to contamination of the material mainly by particles coming from metal oxides during sample preparation using jet-type electrical discharge equipment. Thus, in the work [23], a similar phenomenon was observed after milling the alloy of the CoCrFeNi system.

Changing the zirconium and manganese content has a significant effect on the nanohardness, microhardness, and Young's modulus of the CoCrZrMnNi alloys, which can lead to various structural transformations and mechanical characteristics. Thus, in the study [16], a similar effect was observed from varying the percentage content of Fe and Mn from 5 to 35 at. %, which led to a nonlinear change in the strength properties of these materials, which are decisive for the use of HEA in modern structural materials. The conducted studies confirm the assumption about the strengthening effect of HEA with an increased zirconium content.

CONCLUSIONS

It was found that the production of high-entropy alloys of the CoCrZrMnNi system by vacuum-induction melting contributes to the production of alloys with a heterogeneous structure and various mechanical properties:

1. An increase in the zirconium content in the CoCrZrMnNi alloys from 8 to 28 at. % contributed to the formation of a fine-grained structure and a more uniform elemental distribution.

2. The $\text{Co}_{19.8}\text{Cr}_{17.5}\text{Zr}_{15.3}\text{Mn}_{27.7}\text{Ni}_{19.7}$ alloy demonstrated the highest nanohardness (10 GPa) and Young's modulus (161 GPa) during instrumental indentation. At the same time, the $\text{Co}_{20.4}\text{Cr}_{18.0}\text{Zr}_{7.9}\text{Mn}_{33.3}\text{Ni}_{20.3}$ alloy has the lowest mechanical properties (nanohardness, Young's modulus, and microhardness) among other alloys, which may be due to the coarse-grained structure. As the indenter load increased (5 N), the microhardness of the $\text{Co}_{19.8}\text{Cr}_{17.5}\text{Zr}_{15.3}\text{Mn}_{27.7}\text{Ni}_{19.7}$ alloy decreased compared to the $\text{Co}_{18.7}\text{Cr}_{16.5}\text{Zr}_{28.9}\text{Mn}_{17.4}\text{Ni}_{18.6}$ alloy, which may indicate more universal mechanical properties of alloys with a zirconium content of 20 at. %.

REFERENCES

1. Pandey V., Seetharam R., Chelladurai H. A comprehensive review: Discussed the effect of high-entropy alloys

as reinforcement on metal matrix composite properties, fabrication techniques, and applications. *Journal of Alloys and Compounds*, 2024, vol. 1002, article number 175095. DOI: [10.1016/j.jallcom.2024.175095](https://doi.org/10.1016/j.jallcom.2024.175095).

2. Zosu S.J., Amaghionyeodiwe C.A., Adedeji K.A. Optimization of high-entropy alloys (HEAs) for lightweight automotive components: Design, fabrication, and performance enhancement. *Global Journal of Engineering and Technology Advances*, 2024, vol. 21, no. 1, pp. 064–072. DOI: [10.30574/gjeta.2024.21.1.0182](https://doi.org/10.30574/gjeta.2024.21.1.0182).
3. Ahmadvkhaniha D., Zanella C. High Entropy Alloy Deposition from an Aqueous Bath. *Meeting abstracts*, 2023, vol. MA2023-02, article number 1263. DOI: [10.1149/ma2023-02201263mtgabs](https://doi.org/10.1149/ma2023-02201263mtgabs).
4. Rogachev A.S. Structure, stability, and properties of high-entropy alloys. *Physics of Metals and Metallography*, 2020, vol. 121, no. 8, pp. 733–764. DOI: [10.1134/S0031918X20080098](https://doi.org/10.1134/S0031918X20080098).
5. Kao Yih-Farn, Chen Ting-Jie, Chen Swe-Kai, Yeh Jien-Wei. Microstructure and mechanical property of as-cast, homogenized and deformed $\text{Al}_x\text{CoCrFeNi}$ ($0 \leq x \leq 2$) high-entropy alloys. *Journal of Alloys and Compounds*, 2009, vol. 488, pp. 57–64. DOI: [10.1016/j.jallcom.2009.08.090](https://doi.org/10.1016/j.jallcom.2009.08.090).
6. Poletti M.G., Fiore G., Gili F., Mangherini D., Battezzati L. Development of a new high entropy alloy for wear resistance: $\text{FeCoCrNiW}_{0.3}$ and $\text{FeCoCrNiW}_{0.3} + 5 \text{ at.}\%$ of C. *Materials and Design*, 2017, vol. 115, pp. 247–254. DOI: [10.1016/j.matdes.2016.11.027](https://doi.org/10.1016/j.matdes.2016.11.027).
7. Tabachnikova E.D., Podolskiy A.V., Laktionova M.O., Bereznaiya N.A., Tikhonovsky M.A., Tortika A.S. Mechanical properties of the CoCrFeNiMnV_x high entropy alloys in temperature range 4.2–300 K. *Journal of Alloys and Compounds*, 2017, vol. 698, pp. 501–509. DOI: [10.1016/j.jallcom.2016.12.154](https://doi.org/10.1016/j.jallcom.2016.12.154).
8. Gludovatz B., Hohenwarter A., Catoor D., Chang E.H., George E.P., Ritchie R.O. A fracture-resistant high entropy alloy for cryogenic applications. *Science*, 2014, vol. 345, pp. 1153–1158. DOI: [10.1126/science.1254581](https://doi.org/10.1126/science.1254581).
9. Kim Han-Eol, Kim Jae-Hyun, Jeong Ho-In, Cho Young-Tae, Salem O., Jung Dong-Won, Lee Choon-Man. Effects of Mo Addition on Microstructure and Corrosion Resistance of $\text{Cr}_{25-x}\text{Co}_{25}\text{Ni}_{25}\text{Fe}_{25}\text{Mo}_x$ High-Entropy Alloys via Directed Energy Deposition. *Micromachines*, 2024, vol. 15, no. 10, article number 1196. DOI: [10.3390/mi15101196](https://doi.org/10.3390/mi15101196).
10. Nesterov K.M., Farrakhov R.G., Aubakirova V.R., Islamgaliev R.K., Sirazeeva A.R., Abuayyash A. Thermal stability and corrosion resistance of ultrafine-grained high-entropy $\text{Fe}_{30}\text{Ni}_{30}\text{Mn}_{30}\text{Cr}_{10}$ alloy. *Frontier Materials & Technologies*, 2022, no. 4, pp. 81–89. DOI: [10.18323/2782-4039-2022-4-81-89](https://doi.org/10.18323/2782-4039-2022-4-81-89).
11. Yeh Jien-Wei. Alloy Design Strategies and Future Trends in High-Entropy Alloys. *JOM*, 2013, vol. 65, pp. 1759–1771. DOI: [10.1007/s11837-013-0761-6](https://doi.org/10.1007/s11837-013-0761-6).
12. Yong Zhang, Ting Ting Zuo, Zhi Tang, Michael C. Gao, Dahmen K.A., Liaw P.K., Zhao Ping Lu. Microstructures and properties of high-entropy alloys. *Progress in Materials Science*, 2014, vol. 61, pp. 1–93. DOI: [10.1016/j.pmatsci.2013.10.001](https://doi.org/10.1016/j.pmatsci.2013.10.001).
13. Cantor B., Chang I.T.H., Knight P., Vincent A.J.B. Microstructural development in equiatomic multi-

- component alloys. *Materials Science and Engineering: A*, 2004, vol. 375–377, pp. 213–218. DOI: [10.1016/j.msea.2003.10.257](https://doi.org/10.1016/j.msea.2003.10.257).
14. Gromov V.E., Kononov S.V., Chen X., Efimov M.O., Panchenko I.A., Shlyarov V.V. Development vector for enhancement of Cantor HEA properties. *Bulletin of the Siberian State Industrial University*, 2023, no. 2, pp. 3–12. DOI: [10.57070/2304-4497-2023-2\(44\)-3-12](https://doi.org/10.57070/2304-4497-2023-2(44)-3-12).
 15. Drobyshev V.K., Panchenko I.A., Kononov S.V. Mechanical properties and microstructure of alloys of the CoCrFeMnNi system. *Polzunovskiy vestnik*, 2024, no. 2, pp. 249–254. DOI: [10.25712/ASTU.2072-8921.2024.02.033](https://doi.org/10.25712/ASTU.2072-8921.2024.02.033).
 16. Panchenko I.A., Drobyshev V.K., Kononov S.V., Bessonov D.A. Structural Change in Co–Cr–Fe–Mn–Ni Alloys upon Variation in Mn and Fe Concentrations. *Technical Physics Letters*, 2024, no. 7. DOI: [10.1134/S1063785024700391](https://doi.org/10.1134/S1063785024700391).
 17. Huo Wenyi, Zhou Hui, Fang Feng, Xie Zonghan, Jiang Jianqing. Microstructure and mechanical properties of CoCrFeNiZr_x eutectic high-entropy alloys. *Materials and Design*, 2017, vol. 134, pp. 226–233. DOI: [10.1016/j.matdes.2017.08.030](https://doi.org/10.1016/j.matdes.2017.08.030).
 18. Polunina A.O., Polunin A.V., Krishtal M.M. The influence of addition of ZrO₂ nanoparticles to the electrolyte on the structure and anticorrosion properties of oxide layers formed by plasma electrolytic oxidation on the Mg₉₇Y₂Zn₁ alloy. *Frontier Materials & Technologies*, 2023, no. 4, pp. 87–98. DOI: [10.18323/2782-4039-2023-4-66-8](https://doi.org/10.18323/2782-4039-2023-4-66-8).
 19. Xu Haijian, Lu Zheng, Wang Dongmei, Liu Chunming. Microstructure Refinement and Strengthening Mechanisms of a 9Cr Oxide Dispersion Strengthened Steel by Zirconium Addition. *Nuclear Engineering and Technology*, 2017, vol. 49, no. 1, pp. 178–188. DOI: [10.1016/j.net.2017.01.002](https://doi.org/10.1016/j.net.2017.01.002).
 20. He J.Y., Wang H., Huang H.L. et al. A precipitation-hardened high-entropy alloy with outstanding tensile properties. *Acta Materialia*, 2016, vol. 102, pp. 187–196. DOI: [10.1016/j.actamat.2015.08.076](https://doi.org/10.1016/j.actamat.2015.08.076).
 21. Otto F., Hanold N.L., George E.P. Microstructural evolution after thermomechanical processing in an equiatomic, single-phase CoCrFeMnNi high-entropy alloy with special focus on twin boundaries. *Intermetallics*, 2014, vol. 54, pp. 39–48. DOI: [10.1016/j.intermet.2014.05.014](https://doi.org/10.1016/j.intermet.2014.05.014).
 22. Campari E.G., Casagrande A., Colombini E., Gualtieri M.L., Veronesi P. The effect of Zr addition on melting temperature, microstructure, recrystallization and mechanical properties of a Cantor high entropy alloy. *Materials*, 2021, vol. 14, no. 20, article number 5994. DOI: [10.3390/ma14205994](https://doi.org/10.3390/ma14205994).
 23. Moravcik I., Kubicek A., Moravcikova-Gouvea L., Ondrej A., Kana V., Pouchly V., Zadera A., Dlouhy I. The Origins of High-Entropy Alloy Contamination Induced by Mechanical Alloying and Sintering. *Metals*, 2020, vol. 10, no. 9, article number 1186. DOI: [10.3390/met10091186](https://doi.org/10.3390/met10091186).
 - loys and Compounds. 2024. Vol. 1002. Article number 175095. DOI: [10.1016/j.jallcom.2024.175095](https://doi.org/10.1016/j.jallcom.2024.175095).
 2. Zosu S.J., Amaghionyeodiwe C.A., Adedeji K.A. Optimization of high-entropy alloys (HEAs) for lightweight automotive components: Design, fabrication, and performance enhancement // *Global Journal of Engineering and Technology Advances*. 2024. Vol. 21. № 1. P. 064–072. DOI: [10.30574/gjeta.2024.21.1.0182](https://doi.org/10.30574/gjeta.2024.21.1.0182).
 3. Ahmadkhaniha D., Zanella C. High Entropy Alloy Deposition from an Aqueous Bath // Meeting abstracts. 2023. Vol. MA2023-02. Article number 1263. DOI: [10.1149/ma2023-02201263mtgabs](https://doi.org/10.1149/ma2023-02201263mtgabs).
 4. Rogachev A.S. Structure, stability, and properties of high-entropy alloys // *Physics of Metals and Metallography*. 2020. Vol. 121. № 8. P. 733–764. DOI: [10.1134/S0031918X20080098](https://doi.org/10.1134/S0031918X20080098).
 5. Kao Yih-Farn, Chen Ting-Jie, Chen Swe-Kai, Yeh Jien-Wei. Microstructure and mechanical property of as-cast, homogenized and deformed Al_xCoCrFeNi (0 ≤ x ≤ 2) high-entropy alloys // *Journal of Alloys and Compounds*. 2009. Vol. 488. P. 57–64. DOI: [10.1016/j.jallcom.2009.08.090](https://doi.org/10.1016/j.jallcom.2009.08.090).
 6. Poletti M.G., Fiore G., Gili F., Mangherini D., Battezzati L. Development of a new high entropy alloy for wear resistance: FeCoCrNiW_{0.3} and FeCoCrNiW_{0.3} + 5 at. % of C // *Materials and Design*. 2017. Vol. 115. P. 247–254. DOI: [10.1016/j.matdes.2016.11.027](https://doi.org/10.1016/j.matdes.2016.11.027).
 7. Tabachnikova E.D., Podolskiy A.V., Laktionova M.O., Bereznaiya N.A., Tikhonovsky M.A., Tortika A.S. Mechanical properties of the CoCrFeNiMnV_x high entropy alloys in temperature range 4.2–300 K // *Journal of Alloys and Compounds*. 2017. Vol. 698. P. 501–509. DOI: [10.1016/j.jallcom.2016.12.154](https://doi.org/10.1016/j.jallcom.2016.12.154).
 8. Gludovatz B., Hohenwarter A., Catoor D., Chang E.H., George E.P., Ritchie R.O. A fracture-resistant high entropy alloy for cryogenic applications // *Science*. 2014. Vol. 345. P. 1153–1158. DOI: [10.1126/science.1254581](https://doi.org/10.1126/science.1254581).
 9. Kim Han-Eol, Kim Jae-Hyun, Jeong Ho-In, Cho Young-Tae, Salem O., Jung Dong-Won, Lee Choon-Man. Effects of Mo Addition on Microstructure and Corrosion Resistance of Cr_{25-x}Co₂₅Ni₂₅Fe₂₅Mo_x High-Entropy Alloys via Directed Energy Deposition // *Micro-machines*. 2024. Vol. 15. № 10. Article number 1196. DOI: [10.3390/mi15101196](https://doi.org/10.3390/mi15101196).
 10. Нестеров К.М., Фаррахов Р.Г., Аубакирова В.Р., Исламгалиев Р.К., Сиразеева А.Р., Абуайяш А. Термическая стабильность и коррозионная стойкость ультрамелкозернистого высокоэнтروпийного сплава Fe₃₀Ni₃₀Mn₃₀Cr₁₀ // *Frontier Materials & Technologies*. 2022. № 4. С. 81–89. DOI: [10.18323/2782-4039-2022-4-81-89](https://doi.org/10.18323/2782-4039-2022-4-81-89).
 11. Yeh Jien-Wei. Alloy Design Strategies and Future Trends in High-Entropy Alloys // *JOM*. 2013. Vol. 65. P. 1759–1771. DOI: [10.1007/s11837-013-0761-6](https://doi.org/10.1007/s11837-013-0761-6).
 12. Yong Zhang, Ting Ting Zuo, Zhi Tang, Michael C. Gao, Dahmen K.A., Liaw P.K., Zhao Ping Lu. Microstructures and properties of high-entropy alloys // *Progress in Materials Science*. 2014. Vol. 61. P. 1–93. DOI: [10.1016/j.pmatsci.2013.10.001](https://doi.org/10.1016/j.pmatsci.2013.10.001).
 13. Cantor B., Chang I.T.H., Knight P., Vincent A.J.B. Microstructural development in equiatomic multi-component alloys // *Materials Science and Engineering: A*. 2004. Vol. 375–377. P. 213–218. DOI: [10.1016/j.msea.2003.10.257](https://doi.org/10.1016/j.msea.2003.10.257).

СПИСОК ЛИТЕРАТУРЫ

1. Pandey V., Seetharam R., Chelladurai H. A comprehensive review: Discussed the effect of high-entropy alloys as reinforcement on metal matrix composite properties, fabrication techniques, and applications // *Journal of Al-*

14. Громов В.Е., Коновалов С.В., Чен С., Ефимов М.О., Панченко И.А., Шляров В.В. Вектор развития улучшения свойств ВЭС Кантора // Вестник Сибирского государственного индустриального университета. 2023. № 2. С. 3–12. DOI: [10.57070/2304-4497-2023-2\(44\)-3-12](https://doi.org/10.57070/2304-4497-2023-2(44)-3-12).
15. Дробышев В.К., Панченко И.А., Коновалов С.В. Механические свойства и микроструктура сплавов системы CoCrFeMnNi // Ползуновский вестник. 2024. № 2. С. 249–254. DOI: [10.25712/ASTU.2072-8921.2024.02.033](https://doi.org/10.25712/ASTU.2072-8921.2024.02.033).
16. Panchenko I.A., Drobyshev V.K., Konovalov S.V., Bessonov D.A. Structural Change in Co–Cr–Fe–Mn–Ni Alloys upon Variation in Mn and Fe Concentrations // Technical Physics Letters. 2024. № 7. DOI: [10.1134/S1063785024700391](https://doi.org/10.1134/S1063785024700391).
17. Huo Wenyi, Zhou Hui, Fang Feng, Xie Zonghan, Jiang Jianqing. Microstructure and mechanical properties of CoCrFeNiZr_x eutectic high-entropy alloys // Materials and Design. 2017. Vol. 134. P. 226–233. DOI: [10.1016/j.matdes.2017.08.030](https://doi.org/10.1016/j.matdes.2017.08.030).
18. Полунина А.О., Полунин А.В., Криштал М.М. Влияние добавки наночастиц ZrO₂ в электролит на структуру и антикоррозионные свойства оксидных слоев, формируемых плазменно-электролитическим окислением на сплаве Mg₉₇Y₂Zn₁ // Frontier Materials & Technologies. 2023. № 4. С. 87–98. DOI: [10.18323/2782-4039-2023-4-66-8](https://doi.org/10.18323/2782-4039-2023-4-66-8).
19. Xu Haijian, Lu Zheng, Wang Dongmei, Liu Chunming. Microstructure Refinement and Strengthening Mechanisms of a 9Cr Oxide Dispersion Strengthened Steel by Zirconium Addition // Nuclear Engineering and Technology. 2017. Vol. 49. № 1. P. 178–188. DOI: [10.1016/j.net.2017.01.002](https://doi.org/10.1016/j.net.2017.01.002).
20. He J.Y., Wang H., Huang H.L. et al. A precipitation-hardened high-entropy alloy with outstanding tensile properties // Acta Materialia. 2016. Vol. 102. P. 187–196. DOI: [10.1016/j.actamat.2015.08.076](https://doi.org/10.1016/j.actamat.2015.08.076).
21. Otto F., Hanold N.L., George E.P. Microstructural evolution after thermomechanical processing in an equiatomic, single-phase CoCrFeMnNi high-entropy alloy with special focus on twin boundaries // Intermetallics. 2014. Vol. 54. P. 39–48. DOI: [10.1016/j.intermet.2014.05.014](https://doi.org/10.1016/j.intermet.2014.05.014).
22. Campari E.G., Casagrande A., Colombini E., Gualtieri M.L., Veronesi P. The effect of Zr addition on melting temperature, microstructure, recrystallization and mechanical properties of a Cantor high entropy alloy // Materials. 2021. Vol. 14. № 20. Article number 5994. DOI: [10.3390/ma14205994](https://doi.org/10.3390/ma14205994).
23. Moravcik I., Kubicek A., Moravcikova-Gouvea L., Ondrej A., Kana V., Pouchly V., Zadera A., Dlouhy I. The Origins of High-Entropy Alloy Contamination Induced by Mechanical Alloying and Sintering // Metals. 2020. Vol. 10. № 9. Article number 1186. DOI: [10.3390/met10091186](https://doi.org/10.3390/met10091186).

Структура и механические свойства высокоэнтروпийных сплавов системы CoCrZrMnNi, полученных вакуумно-индукционной плавкой, с разным содержанием Zr и Mn

Коновалов Сергей Валерьевич^{*1,2,3}, доктор технических наук, профессор,
проректор по научной и инновационной деятельности

Дробышев Владислав Константинович^{1,4}, аспирант кафедры обработки металлов давлением и материаловедения
ЕВРАЗ ЗСМК, научный сотрудник лаборатории электронной микроскопии и обработки изображений

Панченко Ирина Алексеевна^{1,5}, кандидат технических наук, доцент кафедры менеджмента качества и инноваций,
заведующий лабораторией электронной микроскопии и обработки изображений

Ли Хайсинь^{2,6}, кандидат наук, доцент Научно-исследовательского института в Яньтае

¹Сибирский государственный индустриальный университет, Новокузнецк (Россия)

²Харбинский инженерный университет, Яньтай (Китай)

*E-mail: konovalov@sibsiiu.ru

³ORCID: <https://orcid.org/0000-0003-4809-8660>

⁴ORCID: <https://orcid.org/0000-0002-1532-9226>

⁵ORCID: <https://orcid.org/0000-0002-1631-9644>

⁶ORCID: <https://orcid.org/0000-0002-3444-115X>

Поступила в редакцию 29.11.2024

Пересмотрена 30.01.2025

Принята к публикации 19.02.2025

Аннотация: Изучены механические свойства и микроструктура высокоэнтропийных сплавов (ВЭС) системы CoCrZrMnNi, полученных вакуумно-индукционной плавкой, в зависимости от изменения содержания Zr и Mn. Оценивается влияние процентного содержания Zr и Mn на микроструктуру и механические свойства (модуль Юнга, нанотвердость, микротвердость) ВЭС системы CoCrZrMnNi. Изучена связь варьирования процентного содержания Zr и Mn с изменением размера зерен и механических свойств ВЭС. Исследования структуры, химического состава и распределения интенсивности характеристического рентгеновского излучения атомов выполнены с использованием сканирующей электронной микроскопии. Методами сканирующей электронной микроскопии продемонстрировано, что в сплавах CoCrZrMnNi при увеличении содержания циркония и уменьшении содержания марганца ближе к эквиаtomному составу структура материала становилась более однородной. Изменение процентного содержания циркония с 8 до 28 ат. % способствовало уменьшению зерна с 30 до 5 мкм и более однородному элементному распределению. Сплав Co_{19,8}Cr_{17,5}Zr_{15,3}Mn_{27,7}Ni_{19,7} в ходе инструментального индентирования

с нагрузкой на индентор 50 мН продемонстрировал наибольшее значение нанотвердости (10 ГПа) и модуля Юнга (161 ГПа). Сплав $\text{Co}_{20,4}\text{Cr}_{18,0}\text{Zr}_{7,9}\text{Mn}_{33,3}\text{Ni}_{20,3}$ обладает наименьшими параметрами нанотвердости, модуля Юнга, микротвердости среди других сплавов, что может быть связано с крупнозернистой структурой с размером зерна до 30 мкм. По мере увеличения нагрузки на индентор до 5 Н микротвердость сплава $\text{Co}_{19,8}\text{Cr}_{17,5}\text{Zr}_{15,3}\text{Mn}_{27,7}\text{Ni}_{19,7}$ снижалась по сравнению со сплавом $\text{Co}_{18,7}\text{Cr}_{16,5}\text{Zr}_{28,9}\text{Mn}_{17,4}\text{Ni}_{18,6}$, что может указывать на более универсальные механические свойства сплавов с эквивалентным содержанием циркония.

Ключевые слова: структура; механические свойства; высокоэнтропийный сплав; вакуумная индукционная плавка; сканирующая электронная микроскопия; модуль Юнга; нанотвердость; микротвердость.

Благодарности: Исследование выполнено за счет гранта Российского научного фонда № 23-49-00015, <https://rscf.ru/project/23-49-00015/>.

Для цитирования: Коновалов С.В., Дробышев В.К., Панченко И.А., Ли Хайсинь. Структура и механические свойства высокоэнтропийных сплавов системы CoCrZrMnNi, полученных вакуумно-индукционной плавкой, с разным содержанием Zr и Mn // Frontier Materials & Technologies. 2025. № 1. С. 21–34. DOI: 10.18323/2782-4039-2025-1-71-2.

Cutting ceramics for turning of specialised stainless hard-to-machine steel

Boris Ya. Mokritskiy¹, Doctor of Sciences (Engineering), Professor, professor of Chair “Machine Engineering”

Pavel A. Sablin*², PhD (Engineering), Associate Professor, assistant professor of Chair “Machine Engineering”

Aleksandr V. Kosmynin³, Doctor of Sciences (Engineering), Professor, professor of Chair “Shipbuilding and Computing Engineering”

Komsomolsk-na-Amure State University, Komsomolsk-on-Amur (Russia)

*E-mail: ikpmt0@knastu.ru

¹ORCID: <https://orcid.org/0000-0003-4727-9873>

²ORCID: <https://orcid.org/0000-0001-5950-9010>

³ORCID: <https://orcid.org/0000-0002-3200-0190>

Received 08.09.2023

Revised 23.01.2024

Accepted 20.02.2025

Abstract: This study shows the possibility of using cutting ceramics as a turning tool. Replaceable standard cutting plates made of VOK-60 and VOK-71 cutting ceramics are used. In the work, based on simulation modelling in the DEFORM software environment, the possibility of high-speed processing with the specified cutting ceramics is substantiated and then experimentally confirmed. Additionally, the authors propose to apply hardening coatings by condensation with ion bombardment, which ensures an increase in the cutting speed to 100 m/min and more with an increase in the service life of the cutting ceramics from 3 to 3.8 times. The maximum stresses in the tool material and the deformation rate of the process material are studied. To select rational solutions in simulation modelling, the authors used the “temperature in the cutting zone”, “stresses in the tool material”, and “tool wear” parameters, which characterise the combined tension of the tool material. The transition from these parameters to the predictive design of cutting ceramics was performed by measuring the cutting force during natural cutting. The measured values of the cutting force components were used to calculate the stresses in the tool material. The study confirmed the hypothesis that the cutting ceramics is capable of operating under the conditions of processing viscous hard-to-machine corrosion-resistant specialised stainless steels such as 09H17N7Yu (C-0.09; Cr-17; Ni-7; Al-1) grade (EU 1.4568, X7CrNiAl17-7), which have a high content of chromium (16–17.5 %) and nickel (7–8 %). The authors propose original technological methods to improve the performance of the cutting ceramics through special heat treatment and coating deposition. In particular, heat treatment in a vacuum at a temperature of 1100–1400 °C for 20–40 min increased the bulk strength of the ceramics, and additional thermochemical treatment by ion nitriding performed at the final stage of heat treatment made it possible to alloy the bond.

Keywords: cutting ceramics; turning of stainless steel; turning process modelling; cutting speed.

Acknowledgments: The research was supported by the grant of the Russian Science Foundation No. 23-29-00393, <https://rscf.ru/project/23-29-00393/>.

For citation: Mokritskiy B.Ya., Sablin P.A., Kosmynin A.V. Cutting ceramics for turning of specialised stainless hard-to-machine steel. *Frontier Materials & Technologies*, 2025, no. 1, pp. 35–45. DOI: 10.18323/2782-4039-2025-1-71-3.

INTRODUCTION

Mechanical processing of hard-to-machine corrosion-resistant stainless steels, such as 09H17N7Yu (C-0.09; Cr-17; Ni-7; Al-1) steel, is a problem for many mechanical engineering industries. This is due to the high content of chromium (16–17.5 %) and nickel (7–8 %) in the 09H17N7Yu steel. The scope of application of this steel is growing: it is used in shipbuilding, marine structures, chemical and food industries, and space and defence industries. Accordingly, the share of tool costs in the cost of manufactured products is growing. Traditionally, such stainless steels are processed with hard-alloy metal-cutting tools. In this case, the cutting speed cannot exceed 50 m/min; extra measures can increase it to

60 m/min. This situation slows down the growth of processing productivity. Major measures are needed.

In the Russian literature, the authors did not find any publications dealing with solving this problem. Publications on the use of cutting ceramics under other conditions are available [1; 2], but they do not solve the problems of increasing the productivity of processing the specified stainless steel. Foreign publications [3–6] consider the issues of applying cutting ceramics in a general sense, i. e., to all grades of stainless steels. They do not refer to the 09H17N7Yu steel grade or similar foreign steels. In the catalogues of the world’s leading tool companies – Walter (Germany), Sandvik Coromant (Sweden),

© Mokritskiy B.Ya., Sablin P.A., Kosmynin A.V., 2025

Mitsubishi (Japan), ISCAR (Israel), the recommendations for processing special stainless steels are of a general nature, without specifying steel grades, i. e., all hard-to-machine stainless steels are combined into one conditional group. Testing of their recommendations on Russian 09H17N7Yu steel showed that VOK-60 and VOK-71 cutting ceramics are destroyed in the first minutes of cutting [1; 2]. This allows concluding that the recommendations are inconsistent and do not solve the issue of increasing the processing productivity in relation to turning of 09H17N7Yu steel.

The authors have their own experience in processing hard-to-machine stainless steels with hard-alloy metal-cutting tools. Thus, the works [1; 2] show that milling with monolithic hard-alloy end-milling cutters is possible, but not promising due to the limited period of their service life. The use of interlocking side mills with mechanical fastening of hard-alloy cutting plates is more promising. The indicated works present the results of using different interlocking side mills and recommendations on the parameters of their cutting mode.

The efficiency of using hard-alloy tools is limited in terms of processing productivity due to the low cutting speed. Therefore, this paper considers the experience of more highly productive processing due to the use of cutting ceramics. The work is performed on the example of turning Russian 09H17N7Yu steel and similar hard-to-machine 12H18N10T, 13H15N5 AM-3 stainless steels. The DEFORM software environment was used for simulation modelling of operational properties [7] and physical and technical characteristics of the most rational tool materials. The study was aimed at determining the necessary (input and output) variables in simulation modelling. The authors assessed the possibility of using VOK-60 and VOK-71 black cutting ceramics for high-performance turning of 09H17N7Yu steel grade and similar 12Kh18N10T, 13Kh15N5 and AM-3 steel grades. At the same time, the possibility of increasing the cutting speed to 100 m/min or more by using wear-resistant coatings on the cutting ceramics was assessed.

The aim of this work is to study the possibility of high-performance turning of blanks made of hard-to-machine 09H17N7Yu steel with a cutting speed of more than 50 m/min by applying nanostructured coatings to the VOK-60 and VOK-71 cutting ceramics and by means of preliminary heat treatment.

METHODS

Methodological approach to solving the problem and its tasks

The work uses a methodological approach to the development of turning cutting plates made of tool cutting ceramics, based on the simulation modelling of the cutting tool in the DEFORM software environment [7] equipped with a large number of applications in the form of different libraries. This allowed selecting new modelling options and designing different operating conditions for the cutting tool. The authors considered a flat orthogonal free cutting scheme representing the penetration of a prismatic cutting

wedge into the material of the blank. The cutting wedge was taken as a solid body fully corresponding to the shape and geometry of a standard replaceable plate. The following restrictions were specified: preventing the coating destruction according to the brittle mechanism; preventing plastic deformation of the coating and substrate due to excess temperatures in the cutting zone. For the simulation modelling of turning with cutting ceramics, an approach known from work [7] was used, but with a significant revision of the approach.

The mathematical framework of the DEFORM software environment is based on the calculation of internal stresses in the material. The stress tensor was used to describe them. The equation and characteristics of the stress tensor are given below, they use the notations adopted in work [7] with their dimensions:

$$\sigma = \begin{bmatrix} \sigma_x & \tau_{xy} & \tau_{xz} \\ \tau_{xy} & \sigma_y & \tau_{yz} \\ \tau_{zx} & \tau_{zy} & \sigma_z \end{bmatrix}.$$

Here, normal stresses σ and shear stresses τ are considered along the corresponding X , Y and Z coordinate axes. One of the main characteristics of the stress tensor is its quadratic invariant, which is usually called the effective stress:

$$\sigma_i = \sqrt{\frac{1}{2}[(\sigma_x - \sigma_y)^2 + (\sigma_y - \sigma_z)^2 + (\sigma_z - \sigma_x)^2] + 3(\tau_{xy}^2 + \tau_{yz}^2 + \tau_{zx}^2)}.$$

The element deformation is described by the ε_x , ε_y , ε_z , γ_{xy} , γ_{yz} , and γ_{zx} components, which are determined by the displacements of the u , v , ω element in the direction of the x , y , z coordinates, respectively:

$$\begin{aligned} \varepsilon_x &= \frac{\partial u}{\partial x}; & \gamma_{xy} &= \frac{\partial v}{\partial x} + \frac{\partial u}{\partial y}; \\ \varepsilon_y &= \frac{\partial v}{\partial y}; & \gamma_{yz} &= \frac{\partial \omega}{\partial y} + \frac{\partial v}{\partial z}; \\ \varepsilon_z &= \frac{\partial \omega}{\partial z}; & \gamma_{zx} &= \frac{\partial u}{\partial z} + \frac{\partial \omega}{\partial x}. \end{aligned}$$

It is accepted that it is sufficient to introduce the following input parameters and conditions: the physical and mechanical characteristics of the materials being processed and the architecture (features of the design, composition, and application technology) of the tool coatings. It is accepted that it is sufficient to obtain the output predicted results for the "temperature in the cutting zone", "stresses in the tool material", and "tool wear" parameters. If necessary, the "tool material deformation" and "tool material deformation rate" parameters were additionally used. This allowed characterising the combined tension state of the tool. The transition from these parameters to the predictive design of the coating architecture was carried out by monitoring the cutting force

during natural cutting. The values of the cutting force components were used to calculate the stresses in the tool material according to the professor S.I. Petrushin's well-known dependence [6; 7].

Predictive design of cutting ceramics was carried out by measuring the cutting force during natural cutting. All three cutting force components were measured during cutting. The transition from the values of the cutting force components to the stresses in the tool material was carried out, according to the dependencies given in works [6–9]:

$$\sigma_{\max} = 2 \cdot \frac{P_y \cdot [\cos \gamma \cdot \sin(\gamma + \Theta) - \sin \alpha \cdot \cos(\alpha - \Theta) + \beta \cdot \cos \Theta]}{r \cdot [(\sin^2 \alpha - \cos^2 \gamma) - \beta^2 + (\sin \alpha \cdot \cos \alpha - \sin \gamma \cdot \cos \gamma)]} + \frac{P_z \cdot [\sin \alpha \cdot \sin(\alpha - \Theta) - \cos \gamma \cdot \cos(\gamma + \Theta) - \beta \cdot \sin \Theta]}{r \cdot [(\sin^2 \alpha - \cos^2 \gamma) - \beta^2 + (\sin \alpha \cdot \cos \alpha - \sin \gamma \cdot \cos \gamma)]}$$

where P_y is the radial component of the cutting force;
 P_z is the main component of the cutting force;
 α is the main back angle;
 γ is the rake angle;
 r and Θ are the polar coordinates in the main secant cutting plane.

Based on the results of the experimental tests, graphs showing the dependence of the wear value on the coatings used were constructed. According to the rate of wear for an equal processing time, the most rational coatings were selected, based on the fact that the lower is the rate of wear, the more rational is the coating. Metals of groups 4–8 of the Mendeleev's periodic table (Ti+TiN+(NbZrTiAl)N, Ti+Zr+ZrN+(ZrAlNb)N, and Ti+Zr+TiCN+(TiZrAl)CN) were used as coatings. A nitride or carbonitride coating layer was applied over the metal coating layer to reduce interaction with the blank.

The model shown in Fig. 1 was used to develop (virtual design in the DEFORM software environment) rational options for cutting ceramic tools, and consequently, to design the architecture of their coatings. The model took into account options in which the durability period (it is called the service life P in the model) should increase by 2–4 times, productivity N and quality K of processing should increase in comparison with the original option, and tool costs Q should decrease.

Within the specified approach, it is accepted that it is possible to apply coatings to the tool material as a measure to improve the tool performance. This method has proven itself in the processing of basic structural materials with a hard-alloy tool. The proposed approach borrows this methodology to improve the performance of cutting ceramics, developing and adapting it to specific tool operating conditions.

The authors considered it methodologically necessary to compare the manufacturing technologies of ceramic tools and hard-alloy tools with coatings. For ceramic tools, the recommendations of work [10] were used; for hard-alloy tools, the recommendations of work [11] were used.

Comparison of special aspects of technological processes for manufacturing ceramic and hard-alloy tools

The technological process (TP) for manufacturing ceramic and hard-alloy tools is generally presented in Fig. 2. Block A shows what exactly is taken into account – the base of the tool material, for example, VOK-60 cutting ceramics or VK8 tool hard alloy. This is considered the first stage of tool production. The next stage of the technological process of tool production is coating deposition (block B). This sequence of stages allowed obtaining technological processes called the TP1 group. Technological processes in the TP1 group include the use of a particular tool base material, a particular coating deposition process, etc.

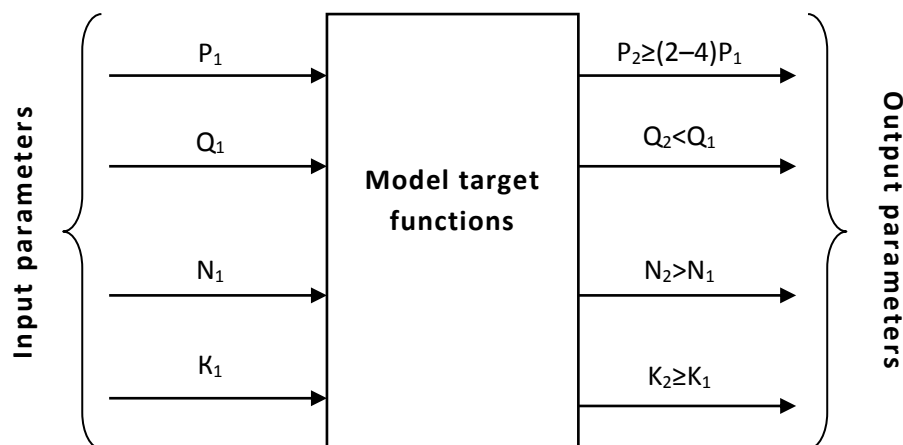


Fig. 1. A model for the implementation of simulation (virtual) design of tool materials:

P – service life; Q – tool costs; N – productivity; K – quality of treatment

Рис. 1. Модель реализации имитационного (виртуального) проектирования инструментальных материалов:

P – период стойкости; Q – затраты на инструмент; N – производительность; K – качество обработки

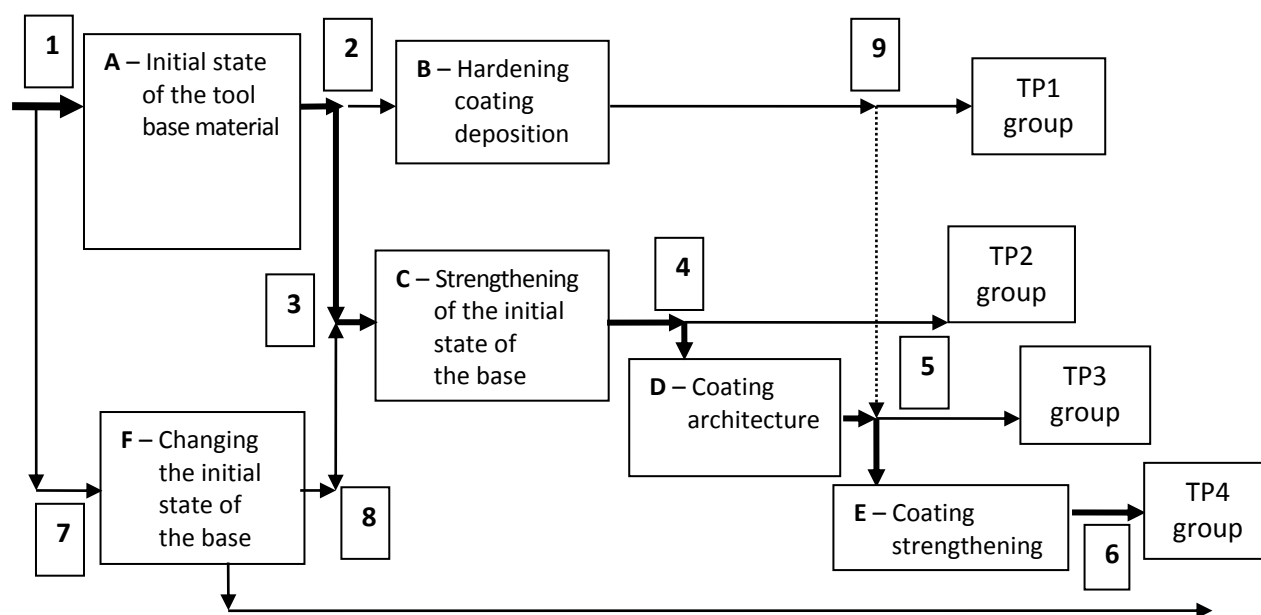


Fig. 2. Generalized scheme of technological processes for manufacturing hard-alloy and ceramic tools: TP1, TP2, TP3, TP4 – technological processes; 1, 2...9 – nodal points of technological process branching
Рис. 2. Обобщенная схема технологических процессов изготовления твердосплавного и керамического инструмента: TP1, TP2, TP3, TP4 – технологические процессы; 1, 2...9 – узловые точки разветвления технологических процессов

If it was necessary to apply strengthening effects on the tool base material (for example, ion nitriding of the base, i. e. VK8 alloy), a chain of actions by branches at points 2 and 3 is formed. This sequence of stages allowed obtaining technological processes called the TP2 group. TP2 were developed and applied in order to improve the operational performance of the cutting tool. However, TP1 are simpler to be implemented and cheaper.

If after implementing TP1 or TP2, the tool performance or processing productivity turned out to be insufficient, then there is a need for a TP3 group of technological processes. This can be achieved by coating architecture (block D). Architecture is understood as the creation of a particular coating (single-layer, multi-layer, nitride, carbide, carbonitride, with the same or different layer thicknesses, using the same or different coating deposition methods, etc.).

If this is not enough, then by the coating strengthening (block E) it is possible to implement the TP4 group of technological processes. The coating strengthening is understood as extra measures to improve the performance properties of the coating as a whole or its particular layers. For example, when applying the first coating layer with a thickness of less than 1 μm , the coating may contain discontinuities, i. e. uncovered areas of the base of the tool material. This is undesirable. Discontinuities can provoke the seizure of the base material of the tool material with the material being processed or reduce the adhesion strength of this layer to the next one. To "heal" such discontinuities, extra effects can be used, for

example, ion nitriding [11] of the layer with discontinuities before applying the next layer.

Technologically, TP4 is more complex than TP3, and TP3 is more complex than TP2 and TP1. Accordingly, the cost of implementing these technological processes is different: for TP4 it is higher than for TP3, etc. However, the performance of the tool manufactured according to TP4 is higher than that of TP3, etc.

If it turns out that the performance of the tool manufactured according to TP4 is still insufficient for specific conditions of processing blanks of parts, then it is possible to influence purposefully the base of the tool material in order to improve its operational properties. We are talking about minimising or eliminating those defects on the base of the tool material that formed during its manufacture, for example, microcracks of mechanical or thermal origin formed during grinding of cutting plates or when sharpening the required edges, fillets, and radii on them. Such cracks are present both on hard-alloy plates [11] and on cutting ceramics [10]. In these cases, it is possible to change the initial state of the tool material base (block F), for example, to heal these microcracks by applying [11], one or another coating before applying the main coating or subject the tool base to "etching" by ion nitriding [11].

Thus, a group of technological processes is implemented (we will conventionally designate it as TP i , it is not shown in Fig. 2), which is more complex than TP4. Such a technological process is more expensive, but it can be the most effective in terms of increasing

the cutting tool performance and increasing the processing productivity.

Materials and methods

In this work, VOK-60 and VOK-71 cutting ceramics (GOST 19043-80, 25003-81) were used as the material for the cutting tool.

The authors used hard-to-machine 09H17N7Yu (EI 973) stainless steel (old designation is 0H17N7Yu (analogues in the European Union – 1.4568, in the USA – 631.S17700, in England – 301 S81)). It is produced in accordance with GOST 19904-90 (cold-rolled sheet metal products) and GOST 7350-77 (Standard ST SEV6434-88).

For comparison and generalisation of the results, the authors also used less durable 12H18N10T and 13H15N AM-3 stainless steels. 13H15N AM-3 steel was accepted for analysis as the base one (ordinary steel that does not present any particular difficulties during blade processing). 12H18N10T steel was chosen as the hard-to-machine one. This steel is unique because its tensile strength is significantly affected by heat treatment conditions.

12H18N10T steel is manufactured according to GOST 5362-2014 "Stainless steels and corrosion-resistant, heat-resistant and heat-proof alloys", position 6-42. It contains 17–19 % of chromium and 9–11 % of nickel. Its Brinell hardness HB is 179 MPa. Impact toughness KCU is 285 kJ/cm². Information on the strength of this steel varies, for example, the ultimate strength is $\sigma_{-1}=279$ MPa, $\sigma_B=610$ MPa, $\sigma_{0.2}=196$ –236 MPa. The closest substitutes are 08H18G8N2T and 12H18N9T steels. The analogues in the USA are 321, 321H, S32109 steels, in Germany – X12CrNiNi8-9.

13H15N5 AM-3 steel (other designations – EP310, VNS-5) is produced according to the industry standard OST 1 90005-91 and according to the technical specifications TU14-1-1271-75 of the manufacturer. Its closest substitutes are 07H16N6 (EP-288), 18H14N4 AM-3 steels. It has a good combination of strength, impact toughness and ductility. The difficulty of its processing is caused by the significant amount of chromium (14–16 %) and nickel (4–6 %). Its hardness depends on many parameters, primarily on the conditions of its strengthening. A small tensile strength (500–800 MPa) of this steel is noted during its heat treatment under normal conditions. During cold hardening, the tensile strength increases to 1200–1700 MPa.

Heat treatment and coating deposition were carried out in a Bulat installation (Russia) operating using the condensation method with ion bombardment. Heat treatment in a vacuum was carried out by heating to 1100–1400 °C for 20–40 min. Metals of groups 4–8 of the periodic table were used as coatings. The use of evaporable cathodes made of metals from groups 4–8 of the periodic table in the Bulat installation allowed producing various coatings. The following coatings were considered as the most rational:

a) the lower layer is made of titanium, a titanium nitride layer is deposited on it, then a Ti+TiN+(NbZrTiAl)N ni-

tride of a combination of niobium, zirconium, titanium, and aluminium is deposited;

b) the lower layer is made of titanium, a zirconium layer is deposited on it, a zirconium nitride layer is deposited on it, and then a Ti+Zr+ZrN+(ZrAlNb)N nitride of a combination of zirconium, aluminium, and niobium is deposited;

c) the lower layer is made of titanium, a zirconium layer is deposited on it, then a titanium carbonitride layer is deposited and then a Ti+Zr+TiCN+(TiZrAl)CN carbonitride of a combination of titanium, zirconium, and aluminium is applied.

Cutting plates made of VOK-60 and VOK-71 cutting ceramics were tested in their different states, namely:

a) in the as-delivered condition supplied from the manufacturer (OOO Technical Ceramics Plant, Aprelevka, Moscow Region);

b) after additional heat treatment (in a vacuum at a temperature of 1100–1400 °C for 20–40 min), which allowed for the relaxation of internal stresses in the plate; this increased the strength of the ceramics;

c) after the plates were subjected to additional heat treatment followed by ion nitriding in a Bulat-type installation, ion bombardment allowed alloying the bond, which increased the strength of the grain boundaries of the cutting ceramics;

d) after the plates were subjected to the application of hardening coatings in a Bulat-type installation.

In each type of these tests, ten (or more if necessary) square tetrahedral plates were used, i. e. at least 40 tests (ten plates with four cutting edges). Since there were four types of tests (listed above as a, b, c, and d), the total number of tests was 160. Since the cutting plates were double-sided (i. e. they could be both rotated and turned over with the backside), 320 final tests were conducted.

The operating time of each cutting edge was monitored until 0.5 mm wear along the back face or until the cutting edge chipped.

RESULTS

When using the technological processes for manufacturing hard-alloy and ceramic tools according to the scheme shown in Fig. 2, the following was experimentally identified:

a) the tool life period before 0.5 mm wear on the rear face when turning a blank made of 09H17N7Yu steel, in the case of using VOK-60 and VOK-71 cutting ceramics, is up to 7–10 times higher for TP1 and TP4 in comparison with a tool made of VK8 hard-alloy material;

b) in this case, the processing productivity of VOK-60 cutting ceramics in comparison with VK8 hard-alloy cutting tool increases up to 1.4–1.6 times with the same cutting mode parameters, and it increases more than 2 times for VOK-71 cutting ceramics. This makes it possible to consider that an arsenal of technological processes has been developed that allows choosing the most rational technological process for the tool life period for specific processing conditions.

Table 1 shows the results of applying cutting ceramics using the VOK-71 grade as an example. The table indicates the operating time (service life) of the cutting plate for external turning of a 09H17N7Yu steel blank until the plate wears out to 0.5 mm or until the cutting edge breaks. VOK-71 ceramics in its initial state had a service life of 5 min. VOK-71 ceramics that was thermally treated had a service life of 9 min, which is 1.8 times higher than the ceramics in its initial state. The reason for such an increase in the service life is the relaxation of internal stresses in the cutting ceramics after heat treatment. VOK-71 ceramics after heat treatment and ion nitriding had a wear life of 14 min. This is 2.8 times higher in comparison with the ceramics in the initial state and 1.5 times higher than that of the ceramics after heat treatment. Such a positive result in terms of the service life of cutting ceramics is accompanied by a significant increase in processing productivity, compared to the use of a hard-alloy cutting tool due to the increased cutting speed (120–140 m/min for cutting ceramics and 50 m/min for a hard alloy, i. e. by 2.6 times).

Examples of implementing simulation modelling in the DEFORM environment are shown in Fig. 3 in the form of screenshots for VOK-71 ceramics (Fig. 3 a, 3 b), and VOK-71 ceramics with a Ti+TiN+(NbZrTiAl)N coating (Fig. 3 c, 3 d), where a and b are the maximum primary stresses, c and d are the resulting strain rates. From the comparison of screenshots using the VOK-71 example, it is clear that the maximum primary stresses and resulting strain rates are preferable in the case of using a coating, in this case the Ti+TiN+(NbZrTiAl)N coating.

The numerical values of the longitudinal, radial and vertical components of the cutting forces are given in Table 2. From the table data, it follows:

a) the highest values of the cutting force components occur when turning 09H17N7Yu steel in comparison with 12H18N10T and 13H15N AM-3 steels, i. e. this is the case when the minimum period of tool life should be expected;

b) the use of uncoated cutting ceramics leads to an increase in all cutting force components, therefore, the use of a coating is rational;

c) in all the cases considered, the vertical component of the cutting force dominates, therefore, it will limit the period of tool life.

Table 3 presents the results obtained during the simulation modelling of the architecture of different coatings. The table shows how many times the service life of cutting ceramics is predicted to increase when applying one of the three studied coatings. The effect of the Ti+TiN+(NbZrTiAl)N coating is shown for the entire range of cutting speeds. The effect of the other coatings is shown selectively for those cases where the maximum increase in the service life was predicted. It follows from Table 3 that:

a) the use of the Ti+TiN+(NbZrTiAl)N coating is preferable at a cutting speed of less than 100 m/min for VOK-60 cutting ceramics, with an increase in the cutting speed, the use of VOK-71 ceramics is preferable;

b) at high cutting speeds, the Ti+Zr+(TiCN)+(TiZrAl)CN coating is preferable for VOK-60 cutting ceramics.

Table 4 gives an example of the effect of coatings on the cutting force components. The data in Table 4 show a significant contribution of the coating to the reduction of the cutting force components, which allows predicting a reduction in the tool wear intensity and an increase in its service life. The use of the coating led to a decrease in the vertical cutting force component (it is this that limits the tool service life) by 1.2 times for VOK-60 ceramics and by 1.4 times for VOK-71 ceramics, while the use of heat treatment and ion nitriding led to its reduction by only 1.2 times.

DISCUSSION

The study confirmed the hypothesis that cutting ceramics is capable of working when processing viscous hard-to-machine corrosion-resistant specialised stainless steels such as 09H17N7Yu steel. Previously, it was believed that cutting ceramics is intended for processing hard materials. Thus, the scope of application of black cutting ceramics has been expanded. The study also confirmed the hypothesis about the possibility of processing 09H17N7Yu (EU 1.4568, X7CrNiAl17-7) steel, which has a high content of chromium (16–17.5 %) and nickel (7–8 %).

When confirming the hypothesis, unique technological methods for increasing the performance of cutting ceramics through special heat treatment and coating deposition have been proposed. In particular, the authors proposed heat treatment in a vacuum at a temperature of 1100–1400 °C for 20–40 min, which increased the bulk strength of the ceramics, and additional thermochemical treatment by ion nitriding performed at the final stage of heat treatment made it possible to alloy the bond. This set of proposed technological measures ensured an increase in the cutting speed by up to three times, which increased the processing productivity to 17 %.

The results of simulation modelling of the cutting process with cutting ceramics and experimental studies, presented in the paper, allowed discovering a number of features that were previously unknown. The effect of a significant increase in processing productivity was revealed, which makes cutting ceramics an effective competitor to hard-alloy cutting tools in turning hard-to-machine specialised stainless steels such as 09H17N7Yu. The authors associate this effect with several factors, including the use of coatings, as well as the use of heat treatment and ion nitriding.

It was found that the processing productivity in comparison with the VK8 hard alloy increased by 1.4–1.6 times for the VOK-60 cutting ceramics, and by 2.6 times for the VOK-71 cutting ceramics. The possibility of high-speed processing of hard-to-machine viscous steels with the specified cutting ceramics was substantiated and experimentally confirmed. This was achieved, among other things, by applying hardening coatings by condensation with ion bombardment, which ensured an increase in the cutting speed to 100 m/min and more with an increase in the service life of the cutting ceramics from 3 to 3.8 times.

This allows considering that the above objective of the work (to study the possibility of high-performance turning

Table 1. Service life of plates made of VOK-71 cutting ceramics during external turning of 09H17N7Yu steel (cutting speed is 120–140 m/min; feed is 0.21 mm/rev of a blank; cutting depth is 1 mm; without the use of lubricating and cooling process media)

Таблица 1. Период стойкости пластин из режущей керамики ВОК-71 при наружном точении стали 09Х17Н7Ю (скорость резания 120–140 м/мин, подача 0,21 мм/об. заготовки, глубина резания 1 мм, без применения смазывающе-охлаждающих технологических сред)

Cutting plate state		
VOK-71 in the initial state	VOK-71 + heat treatment	VOK-71 + heat treatment + ion nitriding
5 min	9 min	14 min

Note. Values are given as the average of five measurements with a coefficient of variation of 0.27.
Примечание. Значения даны как среднее по 5 измерениям при коэффициенте вариации 0,27.

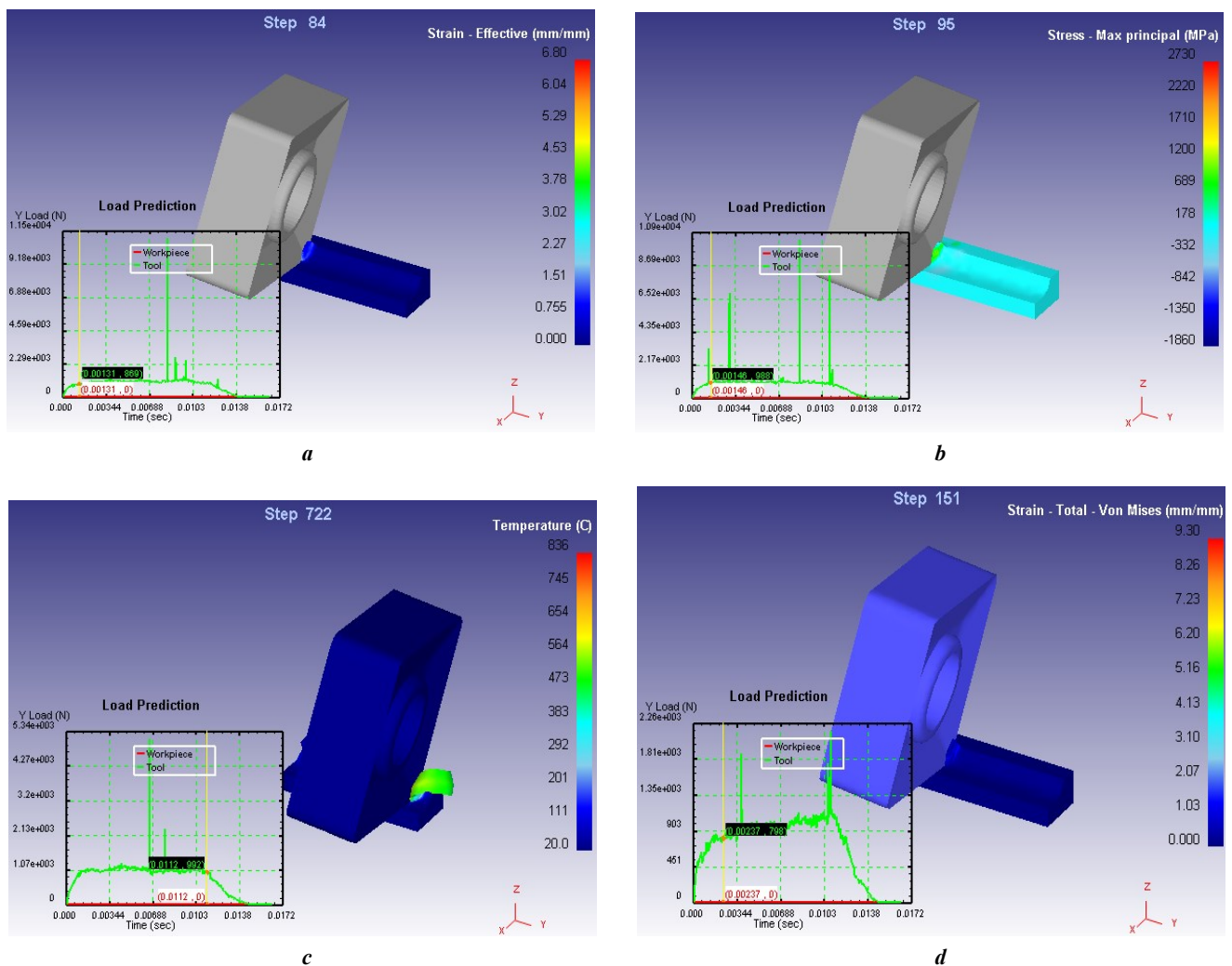


Fig. 3. Results of simulation modelling of the stress state of the cutting tool when turning 09H17N7Yu steel with VOK-71 cutting ceramics (a, b) and VOK-71 cutting ceramics with a Ti+TiN+(NbZrTiAl)N coating (c, d): a, b – maximum primary stresses (MPa); c, d – resulting strain rates (mm/s).

The colour scheme demonstrates the range of the illustrated parameter, a graph reflecting the dynamics of this process is shown at the bottom left

Рис. 3. Результаты имитационного моделирования напряженного состояния режущего инструмента при точении стали марки 09Х17Н7Ю режущей керамикой марки ВОК-71 (a, b) и режущей керамикой ВОК-71 с покрытием Ti+TiN+(NbZrTiAl)N (c, d): a, b – максимальные основные напряжения (МПа); c, d – результирующие скорости деформации (мм/с).

Цветовая гамма демонстрирует диапазон иллюстрируемого параметра, слева внизу приведен график, отражающий динамику данного процесса

Table 2. Numerical values of the quantities composing the cutting forces when turning with VOK-71 cutting ceramics with a Ti+TiN+(NbZrTiAl)N coating at a cutting speed of 120 m/min with a cutting depth of 0.1 mm
Таблица 2. Числовые значения величин, составляющих силы резания, при точении режущей керамикой VOK-71 с покрытием Ti+TiN+(NbZrTiAl)N при скорости резания 120 м/мин с глубиной резания 0,1 мм

Resulting cutting force components	Steel grade		
	09H17N7Yu	12H18N10T	13H15N AM-3
Cutting force longitudinal component F_x , N	85.5/106	64.7/98	35.2/54
Cutting force radial component F_y , N	305.2/382	308.0/396	310.1/404
Cutting force vertical component F_z , N	362.5/465	284.6/320	191.4/241

Note. The denominator shows the values for the case of using VOK-71 without coating.
 Примечание. В знаменателе указаны значения для случая применения VOK-71 без покрытия.

Table 3. Results of simulation modelling of the coating architecture
Таблица 3. Результаты имитационного моделирования архитектуры покрытия

Grade of cutting ceramics	Cutting speed	Coating		
		Ti+TiN+(NbZrTiAl)N	Ti+Zr+ZrN+(ZrAlNb)N	Ti+Zr+(TiCN)+(TiZrAl)CN
Increase in the service life, times				
VOK-60	up to 100 m/min	3.2*		
VOK-71		3**	3.8***	
VOK-60	from 100 m/min to 130 m/min	3		3.5
VOK-71		3.6		3.3

Note. * when increasing the cutting speed by 25 %;
 ** when increasing the cutting speed by 20 %;
 *** when increasing the cutting speed by 32 %.
 Примечание. * при повышении скорости резания на 25 %;
 ** при повышении скорости резания на 20 %;
 *** при повышении скорости резания на 32 %.

Table 4. Values of predicted cutting force components when turning 09H17N7Yu steel with cutting ceramics in different states
Таблица 4. Значения прогнозируемых составляющих силы резания при точении стали 09Х17Н7Ю режущей керамикой, находящейся в разном состоянии

Tool material	Cutting force longitudinal component F_x , N	Cutting force radial component F_y , N	Cutting force vertical component F_z , N
VOK-60	120	340	440
VOK-60 with a Ti+TiN+(NbZrTiAl)N coating	95	300	370
VOK-71	96	310	370
VOK-71 + heat treatment + ion nitriding	82	270	310
VOK-71 with a Ti+TiN+(NbZrTiAl)N coating	64	220	260

of blanks made of hard-to-machine 09H17N7Yu steel, with a cutting speed of more than 50 m/min by applying nanostructured coatings to the VOK-60 and VOK-71 cutting ceramics, and due to previous heat treatment) has been achieved. Thermochemical treatment in the form of ion nitriding was performed on a Bulat-type installation (Russia), which operates using the condensation with ion bombardment (CIB) method. This made it possible to alloy the bond, which increased the strength of the grain boundaries of the cutting ceramics.

Comparison with other existing studies [12; 13] showed a high result of using cutting ceramics. This study established the fact of an increase in the service life of cutting ceramics in comparison with the VK8 hard alloy by 7–10 times, depending on the applied technological process of hardening the cutting tool. It was identified that in comparison with cutting ceramics in the initial state, the service life for VOK-71 increased by 1.8 times due to the use of heat treatment, and by 2.8 times due to the use of heat treatment followed by ion nitriding. The obtained results supplement (update) the recommendations of the world’s leading tool companies – Walter (Germany), Sandvik Coromant (Sweden), Mitsubishi (Japan), ISCAR (Israel). The results do not contradict the existing concepts formulated in the works [14–18]. It is shown that the obtained results are applicable to related hard-to-machine 12H18N10T and 13H15N AM-3 stainless steels.

The authors plan to conduct further research in the area of identifying the contribution of a particular coating to increasing the tool life, identifying the share of the contribution of heat treatment and heat treatment followed by ion nitriding.

According to the authors, the scientific novelty of the work is that the possibility of using VOK-60 and VOK-71 cutting ceramics for turning blanks of parts made of hard-to-machine 09H17N7Yu specialized stainless steel has been substantiated by using hardening coatings, as well as by heat treatment and heat treatment followed by ion nitriding. In fact, the use of the DEFORM software environment as a tool for designing coatings is also a scientific novelty of the work. The practical significance of such application of the DEFORM software environment allowed selecting the most rational coatings from all possible options at the stage of coating design. This is a significant saving of research funds and time.

As a result of the conducted research, one can conclude the following: an arsenal of technological processes for manufacturing a tool made of cutting ceramics has been developed. For specific operating conditions of the tool, it is necessary just to select from this arsenal the most rational technological process in terms of the tool performance indicator, taking into account productivity and cost.

The practical significance of the work is that the cutting mode parameters have been identified, at which the effects of increasing productivity and the tool life period are most fully realised.

CONCLUSIONS

During the simulation modelling of the cutting tool stress state, as well as the study of the process of turning hard-to-machine corrosion-resistant 09H17N7Yu stainless

steel, the possibility of using VOK-60 and VOK-71 cutting ceramics was proven.

The use of coatings in comparison with cutting ceramics without a coating allowed increasing the service life of cutting ceramics from 25 to 32 % with an increase in the cutting speed to 100 m/min.

The processing productivity in comparison with the VK8 hard alloy increased by 1.4–2.6 times.

The increase in the service life in comparison with the VK8 alloy was 7–10 times.

In comparison with cutting ceramics in the initial state, the service life increased by 1.8 times due to the use of heat treatment and by 2.8 times due to the use of heat treatment followed by ion nitriding.

REFERENCES

1. Mokritskiy B.Ya., Mokritskaya E.B. Blade processing of hardened materials (in parts). Part 3. Processing of workpieces of parts hardened by high-hardness surfacing. *Uprochnyayushchie tekhnologii i pokrytiya*, 2021, vol. 17, no. 11, pp. 495–497. DOI: [10.36652/1813-1336-2021-17-11-495-497](https://doi.org/10.36652/1813-1336-2021-17-11-495-497).
2. Mokritskiy B.Ya., Shelkovnikov V.Yu., Sitamov E.S., Morozova A.V., Mokritskaya E.B. Carbide inserts and coatings to them for turning hard-to-machine stainless steels. *Transportnoe mashinostroenie*, 2022, no. 1-2, pp. 60–68. DOI: [10.30987/2782-5957-2022-01-02-60-68](https://doi.org/10.30987/2782-5957-2022-01-02-60-68).
3. Özel T., Altan N. Determination of workpiece flow stress and friction at the chip-tool contact for high-speed cutting. *International Journal of Machine Tools and Manufacture*, 2000, vol. 40, no. 1, pp. 133–152. DOI: [10.1016/S0890-6955\(99\)00051-6](https://doi.org/10.1016/S0890-6955(99)00051-6).
4. Deederich N. Metallischer Zwischeuschichten im Bereich der Aufbanschneidesbildung. *Ind.-Anz.*, 1968, vol. 90, no. 24, pp. 457–460.
5. Fuch M., Scheffer M. Ab initio pseudopotentials for electronic structure calculations of poly-atomic systems using density-functional theory. *Computer Physics Communications*, 1999, vol. 119, no. 1, pp. 67–98. DOI: [10.1016/S0010-4655\(98\)00201-X](https://doi.org/10.1016/S0010-4655(98)00201-X).
6. Petrushin S.I., Proskokov A.V. Chip formation with the developed area of plastic deformations at material cutting. *Izvestiya Tomskogo politekhnicheskogo universiteta*, 2009, vol. 314, no. 2, pp. 57–62. EDN: [KWMASR](https://www.edn.ru/KWMASR).
7. Petrushin S.I. *Osnovy formoobrazovaniya rezaniem lezviynymi instrumentami* [Basics of shaping by cutting with blade tools]. Tomsk, TPU Publ., 2004. 204 p.
8. Music D., Schneider J.M. Effect of transition metal additives on electronic structure and elastic properties of TiAl and Ti₃Al. *Physical Review B*, 2006, vol. 74, no. 17, article number 174110. DOI: [10.1103/PhysRevB.74.174110](https://doi.org/10.1103/PhysRevB.74.174110).
9. Krivoruchko D.V., Zaloga V.A. *Modelirovanie protsessov rezaniya metodom konechnykh elementov: metodologicheskie osnovy* [Modeling of cutting processes by the finite element method: methodological foundations]. Sumy, Universitetskaya kniga Publ., 2012. 496 p.
10. Metel A.S., Volosova M.A., Mustafaev E.S., Melnik Y.A., Okunkova A.A., Grigoriev S.N. Improving the Quality

- of Ceramic Products by Removing the Defective Surface Layer. *Ceramics*, 2024, vol. 7, no. 1, pp. 55–67. DOI: [10.3390/ceramics7010005](https://doi.org/10.3390/ceramics7010005).
11. Grigoriev S.N., Vereschaka A.A., Fyodorov S.V., Sitnikov N.N., Batako A.D. Comparative analysis of cutting properties and nature of wear of carbide cutting tools with multi-layered nano-structured and gradient coatings produced by using of various deposition methods. *The International Journal of Advanced Manufacturing Technology*, 2017, vol. 90, pp. 3421–3435. DOI: [10.1007/s00170-016-9676-z](https://doi.org/10.1007/s00170-016-9676-z).
 12. Vereschaka A.A., Mokritskii B.Ya., Sitnikov N.N., Oganyan G.V., Aksenenko A.Y. Study of mechanism of failure and wear of multi-layered composite nano-structured coating based on system Ti-TiN-(ZrNbTi)N deposited on carbide substrates. *Journal of Nano Research*, 2017, vol. 45, pp. 110–123. DOI: [10.4028/www.scientific.net/JNanoR.45.110](https://doi.org/10.4028/www.scientific.net/JNanoR.45.110).
 13. Lin Zhijun, Wang Lin, Zhan Jianzhong, Mao Hongkwang, Zhao Yusheng. Nanocrystalline tungsten carbide: As incompressible as diamond. *Applied Physics Letters*, 2009, vol. 95, no. 21, article number 211906. DOI: [10.1063/1.3268457](https://doi.org/10.1063/1.3268457).
 14. Pyatykh A.S., Savilov A.V., Timofeev S.A., Svinin V.M., Maizel I.G. Influence of Protective Coatings of Inserts on Cutting Forces during Milling of Hadfield Steel. *Journal of Friction and Wear*, 2023, vol. 44, no. 3, pp. 156–163. DOI: [10.3103/s1068366623030078](https://doi.org/10.3103/s1068366623030078).
 15. Horlin N. TiC coated cemented carbides – their introduction and impact on metal cutting. *Product Engineering*, 1971, vol. 50, no. 4, pp. 153–159.
 16. Yadollahi A., Shamsaei N., Thompson S.M., Elwany A., Bian L. Effects of building orientation and heat treatment on fatigue behavior of selective laser melted 17-4 PH stainless steel. *International Journal of Fatigue*, 2017, vol. 94, part 2, pp. 218–235. DOI: [10.1016/j.ijfatigue.2016.03.014](https://doi.org/10.1016/j.ijfatigue.2016.03.014).
 17. Ahmadkhaniha D., Möller H., Zanella C. Studying the Microstructural Effect of Selective Laser Melting and Electropolishing on the Performance of Maraging Steel. *Journal of Materials Engineering and Performance*, 2021, vol. 30, pp. 6588–6605. DOI: [10.1007/s11665-021-05927-6](https://doi.org/10.1007/s11665-021-05927-6).
 18. Jovičević-Klug P., Lipovšek N., Jovičević-Klug M., Podgornik B. Optimized Preparation of Deep Cryogenic Treated Steel and Al-alloy Samples for Optimal Microstructure Imaging Results. *Materials Today Communications*, 2021, vol. 27, article number 102211. DOI: [10.1016/j.mtcomm.2021.102211](https://doi.org/10.1016/j.mtcomm.2021.102211).
 - ностроение. 2022. № 1-2. С. 60–68. DOI: [10.30987/2782-5957-2022-01-02-60-68](https://doi.org/10.30987/2782-5957-2022-01-02-60-68).
 3. Özel T., Altan N. Determination of workpiece flow stress and friction at the chip-tool contact for high-speed cutting // *International Journal of Machine Tools and Manufacture*. 2000. Vol. 40. № 1. P. 133–152. DOI: [10.1016/S0890-6955\(99\)00051-6](https://doi.org/10.1016/S0890-6955(99)00051-6).
 4. Deederich N. Metallischer Zwischenschichten im Bereich der Aufbanschneidesbildung // *Ind.-Anz.* 1968. Vol. 90. № 24. P. 457–460.
 5. Fuch M., Scheffer M. Ab initio pseudopotentials for electronic structure calculations of poly-atomic systems using density-functional theory // *Computer Physics Communications*. 1999. Vol. 119. № 1. P. 67–98. DOI: [10.1016/S0010-4655\(98\)00201-X](https://doi.org/10.1016/S0010-4655(98)00201-X).
 6. Петрушин С.И., Просококов А.В. Стружкообразование с развитой зоной пластических деформации при резании металлов // *Известия Томского политехнического университета*. 2009. Т. 314. № 2. С. 57–62. EDN: [KWMASR](https://www.edn.ru/kwmasr).
 7. Петрушин С.И. Основы формообразования резанием лезвийными инструментами. Томск: ТПУ, 2004. 204 с.
 8. Music D., Schneider J.M. Effect of transition metal additives on electronic structure and elastic properties of TiAl and Ti₃Al. *Physical Review B*, 2006, vol. 74, no. 17, article number 174110. DOI: [10.1103/PhysRevB.74.174110](https://doi.org/10.1103/PhysRevB.74.174110).
 9. Криворучко Д.В., Залогова В.А. Моделирование процессов резания методом конечных элементов: методологические основы. Сумы: Университетская книга, 2012. 496 с.
 10. Metel A.S., Volosova M.A., Mustafaev E.S., Melnik Y.A., Okunkova A.A., Grigoriev S.N. Improving the Quality of Ceramic Products by Removing the Defective Surface Layer // *Ceramics*. 2024. Vol. 7. № 1. P. 55–67. DOI: [10.3390/ceramics7010005](https://doi.org/10.3390/ceramics7010005).
 11. Grigoriev S.N., Vereschaka A.A., Fyodorov S.V., Sitnikov N.N., Batako A.D. Comparative analysis of cutting properties and nature of wear of carbide cutting tools with multi-layered nano-structured and gradient coatings produced by using of various deposition methods // *The International Journal of Advanced Manufacturing Technology*. 2017. Vol. 90. P. 3421–3435. DOI: [10.1007/s00170-016-9676-z](https://doi.org/10.1007/s00170-016-9676-z).
 12. Vereschaka A.A., Mokritskii B.Ya., Sitnikov N.N., Oganyan G.V., Aksenenko A.Y. Study of mechanism of failure and wear of multi-layered composite nano-structured coating based on system Ti-TiN-(ZrNbTi)N deposited on carbide substrates // *Journal of Nano Research*. 2017. Vol. 45. P. 110–123. DOI: [10.4028/www.scientific.net/JNanoR.45.110](https://doi.org/10.4028/www.scientific.net/JNanoR.45.110).
 13. Lin Zhijun, Wang Lin, Zhan Jianzhong, Mao Hongkwang, Zhao Yusheng. Nanocrystalline tungsten carbide: As incompressible as diamond // *Applied Physics Letters*. 2009. Vol. 95. № 21. Article number 211906. DOI: [10.1063/1.3268457](https://doi.org/10.1063/1.3268457).
 14. Pyatykh A.S., Savilov A.V., Timofeev S.A., Svinin V.M., Maizel I.G. Influence of Protective Coatings of Inserts on Cutting Forces during Milling of Hadfield Steel // *Journal of Friction and Wear*. 2023. Vol. 44. № 3. P. 156–163. DOI: [10.3103/s1068366623030078](https://doi.org/10.3103/s1068366623030078).

СПИСОК ЛИТЕРАТУРЫ

1. Мокрицкий Б.Я., Мокрицкая Е.Б. Лезвийная обработка упрочненных материалов. Часть 3. Обработка заготовок деталей, упрочненных наплавками высокой твердости // *Упрочняющие технологии и покрытия*. 2021. Т. 17. № 11. С. 495–497. DOI: [10.36652/1813-1336-2021-17-11-495-497](https://doi.org/10.36652/1813-1336-2021-17-11-495-497).
2. Мокрицкий Б.Я., Шелковников В.Ю., Ситамов Э.С., Морозова А.В., Мокрицкая Е.Б. Твёрдосплавные пластины и покрытия к ним для точения труднообрабатываемых нержавеющей сталей // *Транспортное маши-*

15. Horlin N. TiC coated cemented carbides – their introduction and impact on metal cutting // Product Engineering. 1971. Vol. 50. № 4. P. 153–159.
16. Yadollahi A., Shamsaei N., Thompson S.M., Elwany A., Bian L. Effects of building orientation and heat treatment on fatigue behavior of selective laser melted 17-4 PH stainless steel // International Journal of Fatigue. 2017. Vol. 94. Part 2. P. 218–235. DOI: [10.1016/j.ijfatigue.2016.03.014](https://doi.org/10.1016/j.ijfatigue.2016.03.014).
17. Ahmadkhaniha D., Möller H., Zanella C. Studying the Microstructural Effect of Selective Laser Melting and Electropolishing on the Performance of Maraging Steel // Journal of Materials Engineering and Performance. 2021. Vol. 30. P. 6588–6605. DOI: [10.1007/s11665-021-05927-6](https://doi.org/10.1007/s11665-021-05927-6).
18. Jovičević-Klug P., Lipovšek N., Jovičević-Klug M., Podgornik B. Optimized Preparation of Deep Cryogenic Treated Steel and Al-alloy Samples for Optimal Microstructure Imaging Results // Materials Today Communications. 2021. Vol. 27. Article number 102211. DOI: [10.1016/j.mtcomm.2021.102211](https://doi.org/10.1016/j.mtcomm.2021.102211).

Режущая керамика для точения специализированной нержавеющей труднообрабатываемой стали

*Мокрицкий Борис Яковлевич*¹, доктор технических наук, профессор,
профессор кафедры «Машиностроение»

Саблин Павел Алексеевич^{*2}, кандидат технических наук, доцент,
доцент кафедры «Машиностроение»

*Космынин Александр Витальевич*³, доктор технических наук, профессор,
профессор кафедры «Кораблестроение и компьютерный инжиниринг»

Комсомольский-на-Амуре государственный университет, Комсомольск-на-Амуре (Россия)

*E-mail: ikpmto@knastu.ru

¹ORCID: <https://orcid.org/0000-0003-4727-9873>

²ORCID: <https://orcid.org/0000-0001-5950-9010>

³ORCID: <https://orcid.org/0000-0002-3200-0190>

Поступила в редакцию 08.09.2023

Пересмотрена 23.01.2024

Принята к публикации 20.02.2025

Аннотация: Показана возможность применения в качестве токарного инструмента режущей керамики. Используются сменные типовые режущие пластины, выполненные из режущей керамики марок ВОК-60 и ВОК-71. В работе на основе имитационного моделирования в программной среде *deform* обоснована и затем экспериментально подтверждена возможность высокоскоростной обработки указанной режущей керамикой. Дополнительно предложено нанесение упрочняющих покрытий методом конденсации с ионной бомбардировкой, что обеспечило повышение скорости резания до 100 м/мин и более с повышением периода стойкости режущей керамики с 3 до 3,8 раз. Проведены исследования максимальных напряжений в инструментальном материале и скорости деформации обрабатываемого материала. Для выбора рациональных решений при имитационном моделировании использовали параметры «температура в зоне резания», «напряжения в инструментальном материале», «износ инструмента», что характеризует сложно-напряженное состояние материала инструмента. Переход от этих параметров к прогнозному проектированию режущей керамики выполняли путем измерения силы резания при натуральном резании. Измеренные значения составляющих силы резания использовали для расчета напряжений в инструментальном материале. В результате выполненного исследования подтверждена гипотеза о том, что режущая керамика способна работать в условиях обработки вязких труднообрабатываемых коррозионностойких специализированных нержавеющей сталей типа марки 09X17H7Ю (EU 1.4568, X7CrNiAl17-7), имеющих высокое содержание хрома (16–17,5 %) и никеля (7–8 %). Предложены оригинальные технологические приемы повышения работоспособности режущей керамики за счет специальной термообработки и нанесения покрытий. В частности, термообработка в вакууме при температуре 1100–1400 °С в течение 20–40 мин повысила объемную прочность керамики, а дополнительная химико-термическая обработка путем ионного азотирования, выполненная на заключительном этапе термообработки, позволила легировать связку.

Ключевые слова: режущая керамика; точение нержавеющей стали; моделирование процесса точения; скорость резания.

Благодарности: Исследование выполнено за счет гранта Российского научного фонда № 23-29-00393, <https://rscf.ru/project/23-29-00393/>.

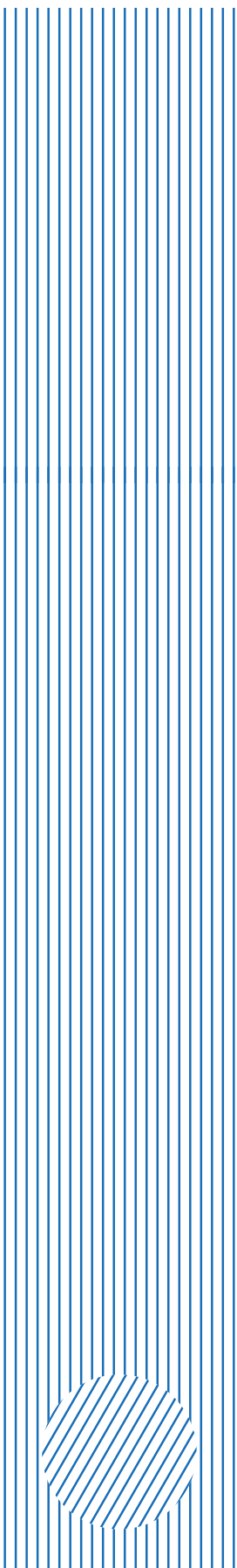
Для цитирования: Мокрицкий Б.Я., Саблин П.А., Космынин А.В. Режущая керамика для точения специализированной нержавеющей труднообрабатываемой стали // Frontier Materials & Technologies. 2025. № 1. С. 35–45. DOI: 10.18323/2782-4039-2025-1-71-3.

The Research and Development Institute of Advanced Technologies is a structural division of Togliatti State University.

The Research and Development Institute of Advanced Technologies today

- More than 60 employees, including seven Doctors of Sciences and fourteen PhDs.
- Three centers, four departments, nineteen laboratories equipped with the up-to-date testing and research facilities for amount over 500 million roubles.
- Accreditation in three systems for testing and research, including in the ILAC international system (laboratory accreditation authority – Association of Analytical Centers “Analitika”, a full member and participant of the ILAC and APLAC mutual recognition agreements).
- Basic areas: fundamental research in the field of physical materials science (the development of the promising materials design, the issues of strength, plasticity, corrosion resistance, fatigue strength, stress corrosion cracking, improving the surface functional properties) and chemistry (methods for synthesis of molecules with the properties of selective fluorescent probes); applied research and inventions in the field of non-destructive control, micro-arc oxidation, manufacturing of cast products, etc.; services for testing and research of various materials, metallographic evaluations, environmental analyses, chemical monitoring of the environment.

Main achievements of the Research and Development Institute of Advanced Technologies

- Three mega-grants were implemented according to the Resolution of the Government of the Russian Federation dated April 9, 2010 No. 220; five projects within the Federal Targeted Programme for Research and Development in Priority Areas of Development of the Russian Scientific and Technological Complex for 2014–2020, including three international ones; in 2023, nine projects of the Russian Science Foundation and two state assignments are being implemented; under the auspices of the extraterritorial scientific and educational center “Engineering of the Future”, a youth Laboratory for the design of magnesium alloys was created.
 - Annually:
 - the number of papers is more than 35, half of them are in specialized journals of the Q1 and Q2 levels;
 - more than 1,500 test reports and conclusions at the request of enterprises, arbitration courts, and the prosecutor’s office
 - An initiator and organizer of 11 Physical Materials Science international schools with the participation of leading scientists-material engineers and metal physicists, the lectures of which became the basis for publishing nine volumes of the Advanced Materials textbook
 - International cooperation with the universities of Kumamoto (Japan), Seoul (South Korea), Prague (Czech Republic), and Freiberg (Germany), academic cooperation with IMP UB RAS (Yekaterinburg), IMSP RAS (Ufa), ISPMS SB RAS (Tomsk) and others; technical cooperation with more than 150 organizations in the real sector of the economy.
- 

The influence of silicon content on the structure of Cu55Ni6Mn4Zn brazing alloy and on the structure and properties of brazed joints

Igor N. Pashkov^{1,3}, Doctor of Sciences (Engineering), professor of Chair No.1101

Magomed R. Gadzhiev^{*1,4}, postgraduate student

Stanislav A. Tavalzhanskiy^{2,5}, PhD (Engineering), assistant professor of Chair “Foundry Technologies and Material Art Working”

Tatiana A. Bazlova^{2,6}, PhD (Engineering), assistant professor of Chair “Foundry Technologies and Material Art Working”

Vyacheslav E. Bazhenov^{2,7}, PhD (Engineering), assistant professor of Chair “Foundry Technologies and Material Art Working”

Diana A. Katanaeva², graduate student

¹Moscow Aviation Institute, Moscow (Russia)

²University of Science and Technology MISIS, Moscow (Russia)

*E-mail: maga.2630@gmail.com

³ORCID: <https://orcid.org/0000-0003-2511-2845>

⁴ORCID: <https://orcid.org/0000-0003-1922-6635>

⁵ORCID: <https://orcid.org/0000-0001-6062-397X>

⁶ORCID: <https://orcid.org/0000-0001-9517-5871>

⁷ORCID: <https://orcid.org/0000-0003-3214-1935>

Received 24.06.2024

Revised 12.12.2024

Accepted 06.03.2025

Abstract: Cu55Ni6Mn4Zn (MNMts55-6-4) copper-zinc alloy is widely used for brazing hard-alloy tools and steels. However, the presence of silicon in the alloy (0.1–0.4 wt. %) can lead to the formation of brittle silicides of iron, nickel, and manganese, which negatively influences the strength of brazed joints. The purpose of the study was to determine the influence of the quantitative content of silicon in copper-zinc brazing alloy doped jointly with nickel and manganese on the structure of brazing alloy blanks before brazing and the structure and properties of brazed joints. In the work, to study the distribution of silicides in ingots, tapes, and brazed seams, the authors used microstructural analysis methods, including electron microscopy and X-ray spectral microanalysis. The results showed that with a silicon content of up to 0.2 wt. %, silicides form finely dispersed inclusions uniformly distributed throughout the seam. However, with an increase in the silicon content to 0.4 wt. %, the formation of continuous layers of iron silicides along the brazing alloy – steel boundary is observed, which leads to brittle failure of the joints under mechanical loads. The influence of small gaps turned out to be especially critical during brazing, where the formation of large crystals of iron silicides significantly reduces the strength of the joints. The scientific novelty of the work lies in identifying the optimal silicon content in the alloy (no more than 0.2 wt. %) to minimize the negative effect of silicides on the properties of brazed joints. The results obtained can be used to develop process recommendations for the production of brazing alloys and brazing of steels, which will allow improving the reliability and durability of brazed joints under production-line conditions.

Keywords: brazing of hard-alloy tools; Cu55Ni6Mn4Zn (MNMts55-6-4); influence of silicon on brazed joints; iron silicides in brazed seams; brazed seam microstructure; embrittlement of brazed joints; optimization of brazing alloy composition.

For citation: Pashkov I.N., Gadzhiev M.R., Tavalzhanskiy S.A., Bazlova T.A., Bazhenov V.E., Katanaeva D.A. The influence of silicon content on the structure of Cu55Ni6Mn4Zn brazing alloy and on the structure and properties of brazed joints. *Frontier Materials & Technologies*, 2025, no. 1, pp. 47–57. DOI: 10.18323/2782-4039-2025-1-71-4.

INTRODUCTION

One of the most common methods of joining hard alloys to steel is brazing [1]. The Cu55Ni6Mn4Zn alloy (MNMts55-6-4) is nickel silver with a high manganese content and is successfully used in Russia and abroad for brazing hard-alloy tools [2; 3] along with the Cu49Ni9Zn (LNMts49-9-0.2) brazing alloy [4; 5]. The composition and melting point of these alloys are presented in Table 1. The high melting and brazing temperature allows, after

the brazing alloy has solidified, to carry out heat treatment of the steel tool bodies using quenching from 860–900 °C in oil or emulsion, followed by tempering [6].

The influence of alloying elements on the properties of copper-zinc alloys has been studied in sufficient detail. Additions of aluminum, manganese, iron, and nickel improve the mechanical properties of brasses and their heat resistance [7; 8]. Alloying with manganese improves the wetting of steel and hard alloy with molten brazing alloy [9].

© Pashkov I.N., Gadzhiev M.R., Tavalzhanskiy S.A., Bazlova T.A., Bazhenov V.E., Katanaeva D.A., 2025

Table 1. Compositions of Cu55Ni6Mn4Zn35 and Cu49Ni9Zn42 alloys and their melting and brazing temperatures
Таблица 1. Состав сплавов Cu55Ni6Mn4Zn35 и Cu49Ni9Zn42, а также их температуры плавления и пайки

Alloy	Chemical composition, % wt.					T _{solidus} , °C	T _{liquidus} , °C	T _{brazing} , °C
	Cu	Zn	Ni	Mn	Si			
Cu55Ni6Mn4Zn35	54–56	the rest	5.5–6.5	3.5–4.5	0.1–0.4	890	920	920–1040
Cu49Ni9Zn42	48–50	the rest	9–11	0.1–0.2	0.1–0.25	915	930	930–980

Alloying with nickel significantly improves the mechanical properties of brass [10]. Alloying with tin can slightly increase the shear strength of steel-hard alloy joints [11]. The Cu49Ni9Zn42 alloy, due to alloying with nickel, allows producing significantly stronger joints than those brazed with two-component brass [12–14]. Comparative studies of joints made using brass brazing alloy and Cu49Ni9Zn42 nickel silver confirm the thesis that the addition of nickel significantly increases the strength of the joints [15; 16]. Brazing alloys based on copper-zinc alloys for brazing hard alloy are usually doped together with nickel and manganese. The reference literature and standards for brazing alloys also indicate the presence of silicon in an amount of 0.1–0.4 wt. %. However, there is practically no mentioning of the influence of the quantitative silicon content on the formation of the brazed seam and the properties of brazed joints made using brazing alloys doped with nickel and manganese.

It is considered that silicon neutralizes the negative effect of iron impurities on the corrosion resistance of brass due to the formation of iron silicides [17]. It improves the technological efficiency of brazing and welding processes due to the fact that the silicon oxide film reduces zinc oxidation at high temperatures. Brasses containing silicon additives have better technological properties and provide higher density and tightness of the seam.

The addition of silicon to brass brazing alloys can reduce the ductility and strength of the brazed joint made of steel through the formation of a brittle Fe-Si intermetallic layer at the brazing alloy – steel interface. Therefore, when brazing steels with brass, it is recommended to limit the alloying of the latter with silicon – no more than 0.3 wt. %. Nickel has a greater chemical affinity for silicon than for iron. When Cu–Zn is introduced into a brazing alloy containing 0.5 % of Si and 2 % of Ni, silicon binds with nickel into a chemical compound and does not form an intermetallic compound with iron along the seam boundary¹. The same effect is observed during laser brazing of steels using a copper-based brazing alloy with 3 wt. % of silicon [18]. Despite the short time of heating to high temperatures, a layer of iron silicides is formed at the brazing alloy – steel boundary [19], which are also present as small inclusions in the weld volume. Mechanical tests of such joints show that destruction mainly occurs precisely along the brazing alloy – steel boundary due to the presence of such compounds [20].

¹ Lashko S.V., Lashko N.F. Payka metallov [Brazing of metals]. Moscow, Mashinostroenie Publ., 1988. 376 p.

Iron, nickel and manganese silicides have a high melting point: NiSi – 992 °C, FeSi – 1410 °C, and MnSi – 1280 °C^{2,3}. The enthalpies of formation of various silicides have similar values, so that the complex formation of manganese and nickel silicides is also possible, and in the presence of iron in the brazing alloy – of iron silicides. It is known that some iron silicides have a lower standard enthalpy of formation than nickel silicides. This may lead to the fact that even in brazed seams produced using nickel-alloyed brazing alloys, iron silicides may form [21].

Therefore, the effect of the silicon quantitative content in copper-zinc brazing alloys with joint alloying with nickel and manganese on the structure and properties of brazed joints has not been sufficiently studied.

The purpose of the study is to determine the influence of the quantitative content of silicon in copper-zinc brazing alloy doped jointly with nickel and manganese on the structure of brazing alloy blanks before brazing and the structure and properties of brazed joints.

METHODS

To study the structure of ingots and pressed bands made of Cu55Ni6Mn4Zn35 (MNMt55-6-4) alloy, industrial samples produced by AO ALARM (Russia) were selected, cast in a metal chill mold. The samples were melted in an induction furnace in an AH 200 clay-graphite crucible, where 200 is the crucible capacity (for copper) of 200 kg. After melting copper and nickel, copper was deoxidized with phosphorus and lump silicon was introduced. Silicon was introduced at the rate of 0.35 wt. %. Mn985 electrolytic manganese was used (manganese content of at least 98.5 %). During melting, 30–40 % of own production waste was used. The resulting 50 mm diameter ingots were hot pressed in a hydraulic press with a force of 300 t through a 10×1 mm matrix. The ingot temperature during pressing was 700 °C. The pressed band had dimensions of 10×1 mm.

To study the influence of silicon content in the brazed seams, small-volume alloy samples with different silicon content were separately melted. The melting differed by the fact that, unlike industrial melting, the copper melt

² Lyakishev N.P., ed. Diagrammy sostoyaniya dvoynnykh metallicheskih sistem [State diagrams of two-component metal systems]. Moscow, Mashinostroenie Publ., 2001. Vol. 3, kn. 1, 972 p.

³ Lyakishev N.P., ed. Diagrammy sostoyaniya dvoynnykh metallicheskih sistem [State diagrams of two-component metal systems]. Moscow, Metallurgiya Publ., 1997. Vol. 2, 1024 p.

was not deoxidized with phosphorus and silicon was introduced in the form of a Cu – 10 wt. % Si alloy. The samples were melted in an induction furnace in an AH 5 clay-graphite crucible of the OAO Luga Abrasives Plant (Russia). The blending was carried on the basis of producing 2.5 kg of alloy from pure components, M0 oxygen-free copper (copper content of at least 99.95 %), NP-1 nickel (high-purity nickel, nickel content of at least 99.9 %), Mn985 manganese, Ts0 zinc (high-purity zinc, zinc content of at least 99.9 %). In molten copper under a Probat Fluss layer, nickel and manganese were dissolved one after another, after which the Cu–Si alloy and zinc were added. The calculated silicon content in the alloy was 0.1, 0.2, and 0.4 wt. %. The resulting melt was poured into a water-cooled casting form with a diameter of 50 mm. The resulting ingots were pressed on a hydraulic press at a temperature of 700 °C to form a brazing alloy tape measuring 10×1 mm.

The produced samples of ingots and bands were used to make sections for examination using a TESCAN VEGA SBH 3 scanning electron microscope (Czech Republic) with an Oxford Instruments attachment (UK) for X-ray spectral microanalysis (XSMA). The probe diameter was 1 µm.

To study the influence of silicon on the structure of brazed seams, experimental models of joints were made in size and shape close to brazed mining cutters. The only difference was that instead of hard alloy, an insert made of 30HGSA steel (GOST 4543-71) (chemical composition: 0.28–0.34 % C, 0.9–1.2 % Cr, 0.8–1.1 % Mn, 0.8–1.1 % Si, the rest is Fe) with a diameter of 18 mm was used, and the outer casing was made of low-carbon steel 1010 (Fig. 1). Heating of the models for brazing was carried out on the SELT-001-15/66-T induction unit (Russia) with the frequency of 40–70 kHz in the cylindrical inductor. The brazing temperature was 940–950 °C. The brazing time was 90 s. The model of the 30HGSA steel insert was dipped in the FP2 flux paste based on potassium borax, borates and fluorides of alkali metals (TU 48-17228138/OPP-004-2001) and placed in the housing bore, on the bottom of which the brazing alloy plates with the total weight of 3.6 g were placed to ensure filling of the entire gap. During the heating process, the brazing alloy melted, and the insert was lowered to the bottom of the housing. The time and power on the brazing unit were

selected so that a solid fillet was formed at the end of the process. This ensured the same holding time for all samples during brazing.

After brazing, the samples were cut along the axis and metallographic sections were prepared for examination using a TESCAN VEGA SBH 3 electron microscope (Czech Republic). The elemental composition was determined using an Oxford Instruments energy dispersive microanalyzer (UK).

RESULTS

Structure of Cu55Ni6Mn4Zn35 (MNMts55-6-4) brazing alloy ingots and bands depending on silicon content

Fig. 2 shows images of microstructure of cast samples produced during industrial melting using deoxidation with phosphorus and the introduction of 0.35 wt. % lump silicon in comparison with a sample manufactured without copper deoxidation with phosphorus and with the introduction of 0.2 wt. % silicon in the form of Cu10Si alloy. The structure contains dark areas located along the boundaries of dendritic cells; the results of their X-ray spectral microanalysis are presented in Table 2.

The structure of industrial brazing alloy bands after hot pressing is shown in Fig. 3. One can see that the dark areas look like dispersed inclusions 2–10 µm in size and are uniformly distributed over the area of the section. All samples contain iron in an amount of 0.2 wt. %. One should note that with decreasing silicon content, the dark phase becomes more dispersed. The composition of the dark areas is similar to the phases in the cast structure and contains silicon in an amount of about 10 wt. % and phosphorus in an amount of 1.7–3 wt. %.

Structure of brazed joints produced with brazing alloy with different silicon content

When brazing steel models of mining cutters, different structures were obtained in the bottom and side parts of the joint. In the structure of the brazed joints, finely dispersed inclusions are observed, mainly iron, as well as nickel and manganese in the central part of the joint and along the interface of the brazing alloy and base material, which is confirmed by the results of X-ray microanalysis (Fig. 4). Due to the small size of the phase, it was not possible to identify its exact composition;

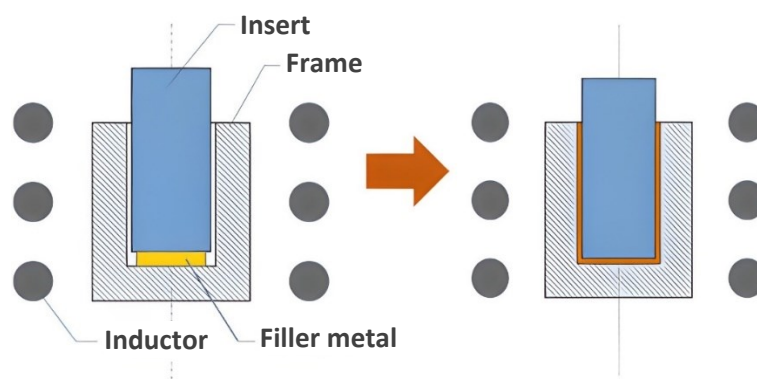


Fig. 1. Scheme of induction brazing of a mining cutter model with the Cu55Ni6Mn4Zn35 brazing alloy
Рис. 1. Схема индукционной пайки макета горного резца припоем Cu55Ni6Mn4Zn35

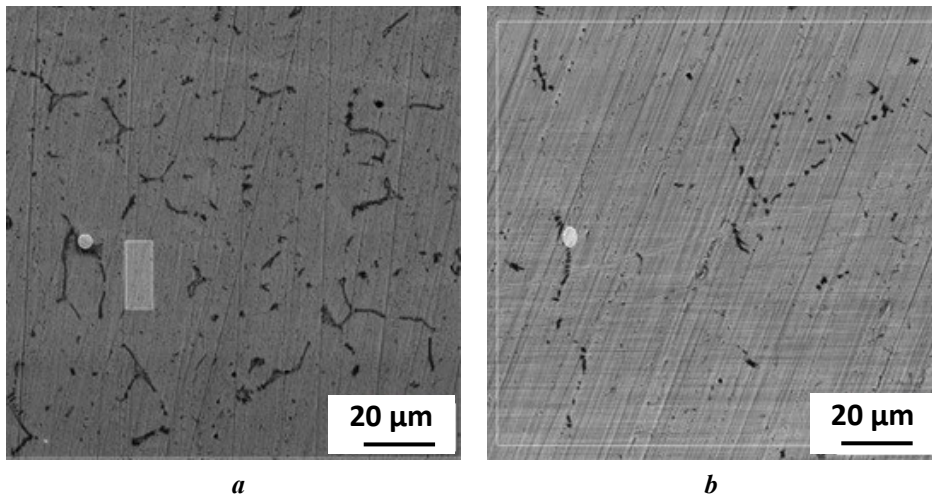


Fig. 2. Microstructure of Cu55Ni6Mn4Zn35 (MNMts55-6-4) brazing alloy ingots: **a** – industrial melting; **b** – experimental melting without deoxidation with phosphorous and with the introduction of silicon by doping material
Рис. 2. Микроструктура слитков припоя Cu55Ni6Mn4Zn35 (МНМц55-6-4): **a** – промышленная плавка; **b** – экспериментальная плавка без раскисления фосфором и с введением кремния лигатурой

Table 2. Results of X-ray spectral microanalysis of ingots in as-cast condition, % wt.
Таблица 2. Результаты микрорентгеноспектрального анализа слитков в литом состоянии, % мас.

Area of analysis	Si	P	Cr	Mn	Fe	Ni	Cu	Zn
Industrial sample								
Bright area	0.01	–	0.87	3.37	–	5.75	54.2	33.42
Dark area	9.1	2.43	–	16.96	1.12	44.13	17.0	9.26
Analysis of alloy	0.4	–	–	3.92	0.18	5.6	52.01	37.89
Experimental sample								
Dark area	10.56	–	–	18.23	0.05	52.35	13.48	5.33
Analysis of alloy	0.26	–	–	4.26	0.02	5.98	54.78	34.7

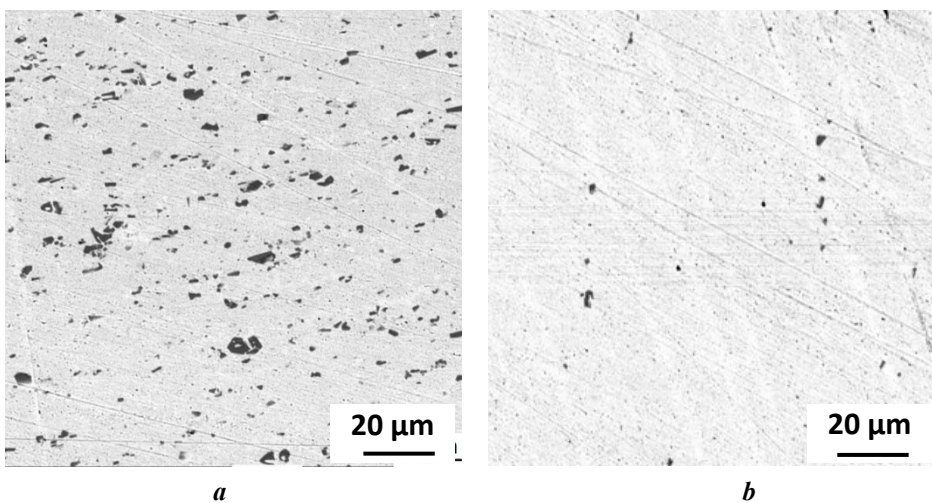


Fig. 3. Microstructure of brazing alloy bands with different silicon content (not etched): **a** – 0.57 % of Si; **b** – 0.31 % of Si
Рис. 3. Микроструктура лент припоя при различном содержании кремния (не травлено): **a** – 0,57 % Si; **b** – 0,31 % Si

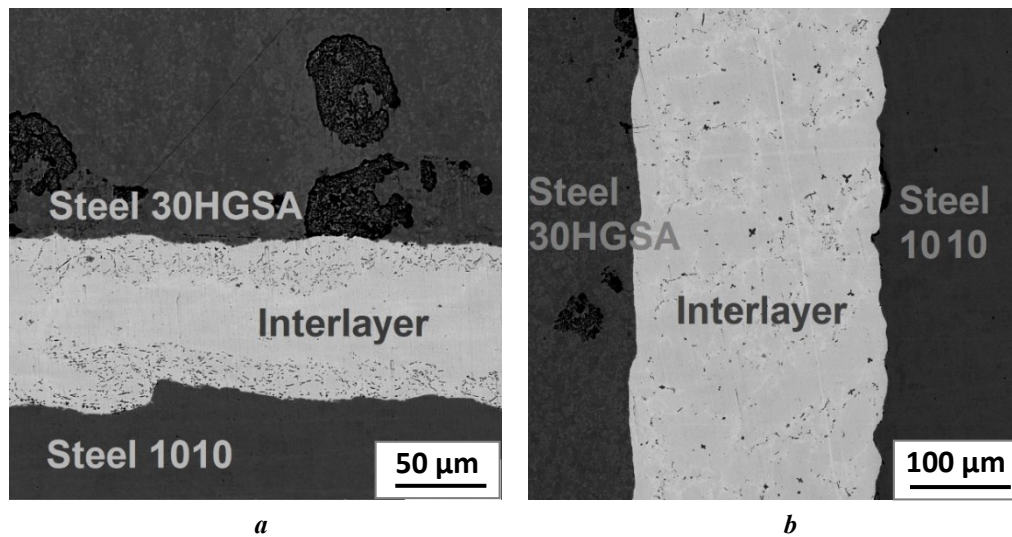


Fig. 4. Microstructure of the model of the joints of mining cutters made with Cu55Ni6Mn4Zn35 (MNMts55-6-4) brazing alloy with a silicon content of 0.2 wt. %: **a** – bottom part; **b** – side part

Рис. 4. Микроструктура макета соединений горных резцов, выполненных припоем Cu55Ni6Mn4Zn35 (МНМц55-6-4) с содержанием кремния 0,2 % мас.: **a** – донная часть; **b** – боковая часть

presumably, these are iron silicides. At low silicon contents of 0.1 and 0.2 wt. %, dispersed inclusions are located in the volume of the joint and do not form large formations that could become stress concentrators for crack formation when the joints are loaded. The structure of the seams with a silicon content of 0.1 and 0.2 wt. % is identical, therefore Fig. 4 shows the structure of the joint with 0.2 wt. % of silicon. The structure of the seams with a silicon content of 0.4 wt. % is shown in Fig. 5.

With a silicon content of 0.4 wt. %, the picture changes radically. At the boundary of the steel with the

brazing alloy, especially on the side of 30HGSA steel containing silicon (0.8 wt. % according to X-ray microanalysis), the formation of large regular-shape crystals is observed, forming a continuous layer at the steel – brazing alloy boundary. Such a pattern is observed with a normal brazing gap size (50–100 µm). The structure in small gaps (less than 50 µm) is formed completely differently. During brazing, a tortuous seam boundary is formed (Fig. 6). Large crystals based on iron and nickel compounds with silicon are formed at the brazing alloy – steel interface, which in some places practically cover

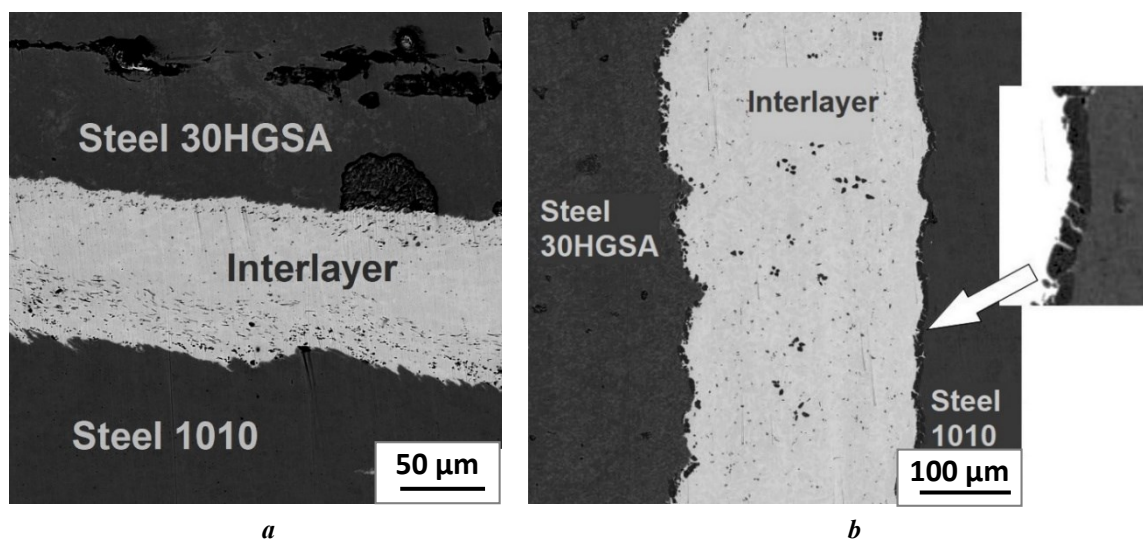


Fig. 5. Microstructure of the model of the joints of mining cutters made with Cu55Ni6Mn4Zn35 (MNMts55-6-4) brazing alloy with a silicon content of 0.4 wt. %: **a** – bottom part; **b** – side part

Рис. 5. Микроструктура макета соединений горных резцов, выполненных припоем Cu55Ni6Mn4Zn35 (МНМц55-6-4) с содержанием кремния 0,4 % мас.: **a** – донная часть; **b** – боковая часть

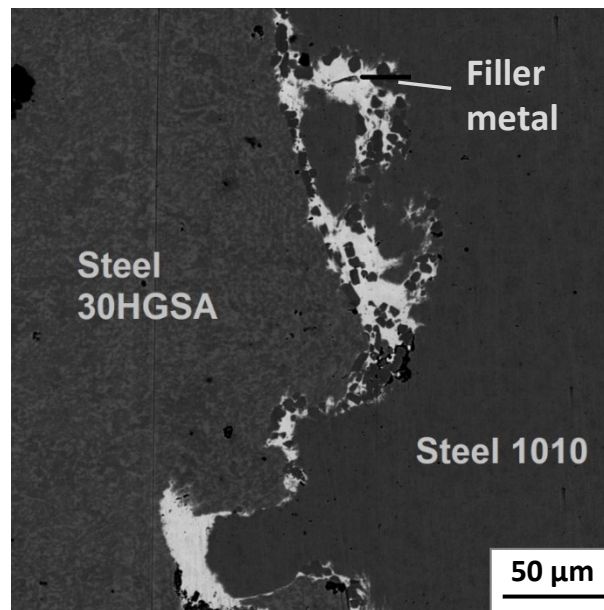


Fig. 6. The structure of the brazed seam at its thickness less than 50 μm
Рис. 6. Структура паяного шва при его толщине менее 50 $\mu\text{м}$

the entire seam. Analysis of the element distribution profiles indicates that these are iron and nickel silicides (Fig. 7). The size of the inclusions reaches 10 μm .

The formation of a continuous layer of iron and nickel silicides led to a four-fold decrease in shear strength compared to the sample where the silicon content was 0.2 wt. %. The fracture surface runs along the brazing alloy – steel interface along this layer (Fig. 8).

DISCUSSION

Influence of silicon on the structure of ingots and pressed bands

The cast structure of the Cu55Ni6Mn4Zn35 (MNMts55-6-4) alloy of industrial production is characterized by the presence of inclusions at the grain boundaries. These inclusions contain both silicon and phosphorus. It is obvious that the alloy deoxidation with phosphorus is excessive and even a small content of it provokes the formation of phases at the grain boundaries. The cast structure of the experimental alloy, which does not contain phosphorus, differs from the structure of the industrial sample. The presence of dark areas rich in silicon, manganese and nickel is observed, but they have a less extended shape and are more dispersed, which generally corresponds to the literature data [21].

The use of hot pressing of ingots to produce bands leads to a noticeable crushing of inclusions. The crushing of inclusions occurs when pressing a band measuring 10×1 mm from an ingot with a diameter of 50 mm. The result of pressing the alloy into such a form is a high degree of compression (about 200). With a silicon content of over 0.3 wt. %, inclusions become larger – up to 10 μm or more, compared to 2–4 μm with a low silicon content.

The amount of silicon-containing phase increases with increasing silicon content in the alloy. The influence of iron content of approximately 0.2 wt. % on the alloy structure was not revealed.

Influence of silicon on the structure of brazed seams

In brazed seams, except for silicon contained in the brazing alloy, silicon from 30HGSA steel can participate in diffusion processes. In the structure of the seams, the formation of small inclusions of iron and nickel compounds with silicon is observed that are mainly located along the brazing alloy – base metal boundary, which corresponds to the data on laser brazing of steels with Cu–Si brazing alloy [18]. Their concentration increases in the areas of small gaps, however, no continuous layers capable of acting as stress concentrators were detected with a silicon content of 0.1–0.2 wt. %, in contrast to 0.4 wt. % of silicon in capillary brazing and 3 wt. % of silicon in laser brazing. It is obvious that these inclusions are formed due to the dissolution of iron in the brazing alloy and its interaction with silicon, which leads to the formation of silicides in the melt volume located along the steel boundaries. Thus, silicon in the brazing alloy is bound with iron into stable compounds, which can be located both in the volume of the copper-zinc alloy [17] and along the brazing alloy – steel interface without forming a continuous layer [19].

With an increase in the silicon content in the brazing alloy up to 0.4 wt. %, the formation of large clearly defined crystals in the form of a continuous layer along the steel – brazing alloy boundary is observed. In this case, their sizes and concentration are higher on the side of steel alloyed with silicon (30HGSA), which is more consistent with brazed seams with Cu–3 % Si brazing alloy [20]. This confirms the statements about the danger of

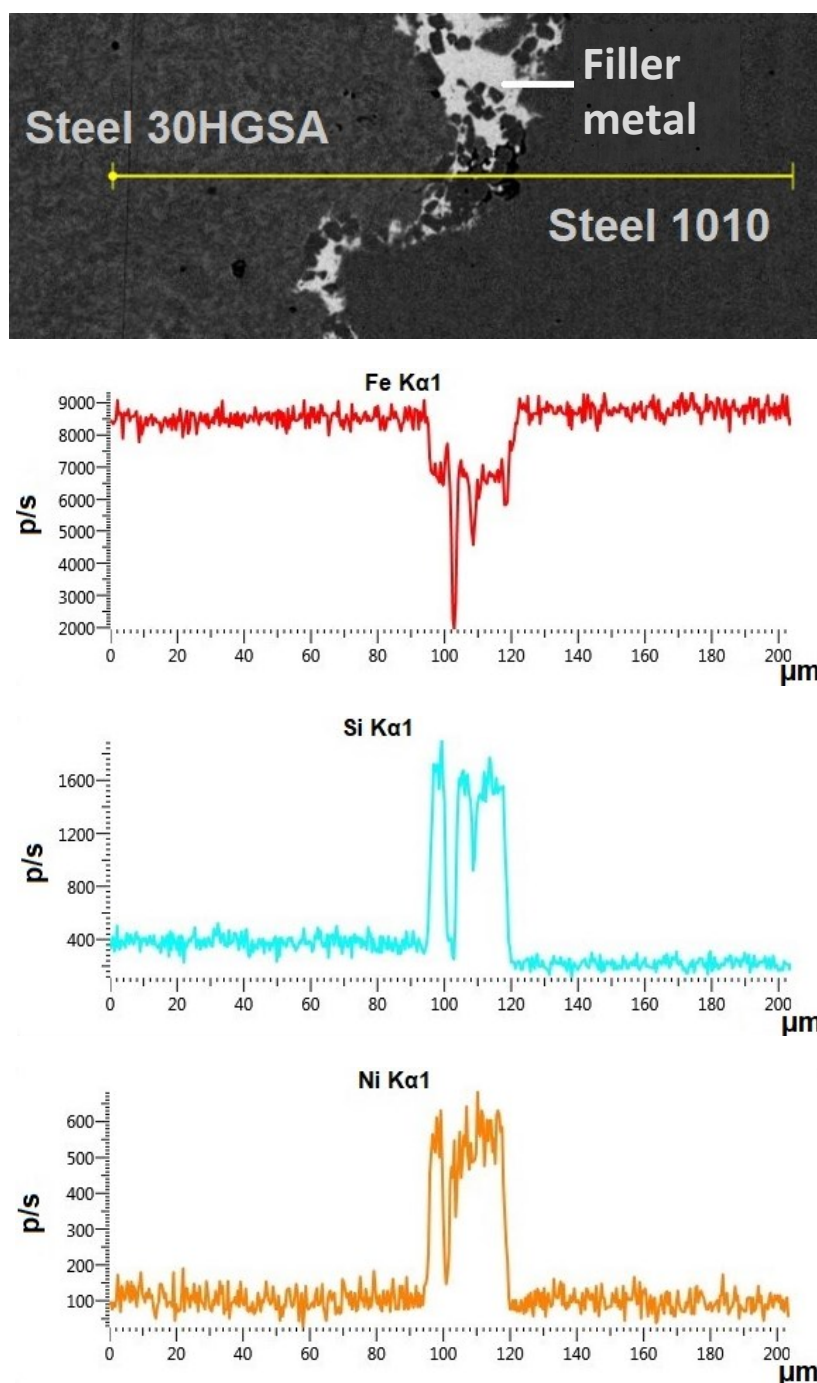


Fig. 7. Change in the content of iron, silicon and nickel across the brazed seam at a silicon content in the brazing alloy of 0.4 wt. %
Рис. 7. Изменение содержания железа, кремния и никеля поперек паяного шва при содержании кремния в припое 0,4 % мас.

exceeding the silicon content in copper-zinc brazing alloys over 0.3 wt. %. However, for copper-zinc brazing alloys jointly doped with nickel and manganese, we did not find a noticeable influence of nickel on reducing the formation of iron silicides, although it was previously believed that nickel blocks the formation of silicides at the base metal – brazing alloy⁴ boundary. Probably, this is because the Cu55Ni6Mn4Zn35 (MNMts55-6-4)

brazing alloy is not brass, but a nickel silver alloy. Due to the high nickel and manganese content, the solubility of iron in the alloy also changes. It is possible that under given conditions, iron silicides having a lower standard enthalpy of formation than nickel silicides are formed, which is described in [21].

A critical influence of the gap was found when brazing with a brazing alloy with a high silicon content (0.4 wt. %). On the one hand, with a small melt layer of brazing alloy, a change in the curvature of the brazing alloy – steel interface is observed, on the other hand, the crystals of silicon,

⁴ Lashko S.V., Lashko N.F. *Payka metallov [Brazing of metals]*. Moscow, Mashinostroenie Publ., 1988. 376 p.

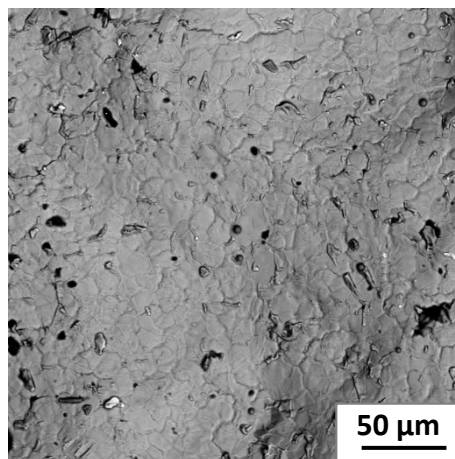


Fig. 8. Brazed joint destruction along the brazing alloy – steel interface at a silicon content in the brazing alloy of 0.4 wt. %
Рис. 8. Разрушение паяного соединения вдоль границы «припой – сталь» при содержании кремния в припое 0,4 % мас.

iron and nickel compounds become larger and can occupy a significant volume of the seam. These crystals can act as stress concentrators when loading the joints and lead to brittle fracture of the seams similar to the fracture of seams along the steel – brazing alloy boundary in [20]. Previously, this phenomenon of enhanced mass transfer at small gaps has not been described.

CONCLUSIONS

1. The silicon content in the Cu55Ni6Mn4Zn35 (MNMts55-6-4) brazing alloy plays a significant role in the formation of the structure of the brazed seams due to the formation of dispersed inclusions of silicides of complex composition. The presence of residual phosphorus in the alloy leads to the formation of inclusions along the grain boundaries, which can negatively affect the strength properties of the brazing alloy. Deoxidation of this alloy by phosphorus is excessive and has a negative influence on the cast structure.

2. The application of hot pressing of ingots when producing brazing alloy band leads to the crushing of inclusions, but their size and quantity clearly correlate with the silicon content in the alloy. With an increase in the silicon content to 0.4 wt. %, the size of the inclusions and their share in the structure of the brazed seams increase.

3. It was found that the silicon content in the brazing alloy up to 0.2 wt. % leads to the formation of finely dispersed compounds of iron and nickel with silicon due to the dissolution of iron in the brazing alloy melt and the formation of complex silicides in the volume of the seam and along the brazing alloy – base material boundary. These inclusions are distributed unevenly in the seam.

4. When the silicon content reaches 0.4 wt. %, the silicides form a continuous layer along the steel – brazing alloy boundary in the form of larger regular-shape crystals; a high nickel content does not prevent this formation.

5. A critical factor that can affect the properties of the brazed joint is the size of the brazing gap. With a high silicon content, a change in the curvature of the boundaries

and the presence of crystals based on iron and nickel silicides in the seams are observed. In this case, a decrease in the strength of the joints and the destruction of the joints along these formations are observed.

REFERENCES

1. Amelzadeh M., Mirsalehi S.E. Dissimilar joining of WC-Co to steel by low-temperature brazing. *Materials Science and Engineering: B*, 2020, vol. 259, article number 114597. DOI: [10.1016/j.mseb.2020.114597](https://doi.org/10.1016/j.mseb.2020.114597).
2. Kolomeychenko A.V., Solovev R.R., Solovev R.Yu., Maksimov E.A., Karyakin S.B. Import substitution of working units for mulchers. *Vestnik Kazanskogo gosudarstvennogo agrarnogo universiteta*, 2023, vol. 18, no. 2, pp. 86–93. DOI: [10.12737/2073-0462-2023-86-93](https://doi.org/10.12737/2073-0462-2023-86-93).
3. Pashkov I.N., Misnikov V.E., Morozov V.A., Tavolzhanskiy S.A. Induction brazing of carbide cutters for a mining tool. The choice of composition and solder form. *Welding international*, 2019, vol. 33, no. 10-12, pp. 411–417. DOI: [10.1080/09507116.2021.1894032](https://doi.org/10.1080/09507116.2021.1894032).
4. Haghshenas M.S., Parvin N., Amirnasiri A. Effect of bonding temperature on microstructure and mechanical properties of WC-Co/steel diffusion brazed joint. *Transactions of the Indian Institute of Metals*, 2018, vol. 71, pp. 649–658. DOI: [10.1007/s12666-017-1197-4](https://doi.org/10.1007/s12666-017-1197-4).
5. Amirnasiri A., Parvin N. Dissimilar diffusion brazing of WC-Co to AISI 4145 steel using RBCuZn-D interlayer. *Journal of Manufacturing Processes*, 2017, vol. 28, part 1, pp. 82–93. DOI: [10.1016/j.jmapro.2017.06.001](https://doi.org/10.1016/j.jmapro.2017.06.001).
6. Pashkov I.N., Misnikov V.E., Morozov V.A., Gadzhiev M., Bazlova T.A. Influence of solder and flux composition on thermal stability of brazed PDC cutters. *Welding International*, 2021, vol. 35, no. 1-3, pp. 121–126. DOI: [10.1080/09507116.2021.1963535](https://doi.org/10.1080/09507116.2021.1963535).
7. Yakovtseva O.A., Mikhaylovskaya A.V., Kotov A.D., Medvedeva S.V., Irzhak A.V. Comparison of contributions of the mechanisms of the superplastic deformation of binary and multicomponent brasses. *Physics of Metals and Metallography*, 2020, vol. 121, no. 6, pp. 582–589. DOI: [10.1134/S0031918X20060186](https://doi.org/10.1134/S0031918X20060186).

8. Yakovtseva O.A., Mikhaylovskaya A.V., Pozdniakov A.V., Kotov A.D., Portnoy V.K. Superplastic deformation behaviour of aluminium containing brasses. *Materials Science and Engineering: A*, 2016, vol. 674, pp. 135–143. DOI: [10.1016/j.msea.2016.07.053](https://doi.org/10.1016/j.msea.2016.07.053).
9. Sui Yanwei, Luo Haibo, Lv Yang, Wei Fuxiang, Qi Jiqu, He Yezeng, Meng Qingkun, Sun Zhi. Influence of brazing technology on the microstructure and properties of YG20C cemented carbide and 16Mn steel joints. *Welding in the World*, 2016, vol. 60, pp. 1269–1275. DOI: [10.1007/s40194-016-0374-0](https://doi.org/10.1007/s40194-016-0374-0).
10. Habibi F., Mostafapour A., Heydarpour K. Microstructural evaluation and mechanical properties of WC-6%Co/AISI 1045 steel joints brazed by copper, brass, and Ag-based filler metals: Selection of the filler material. *Journal of Advanced Joining Processes*, 2024, vol. 9, article number 100212. DOI: [10.1016/j.jaip.2024.100212](https://doi.org/10.1016/j.jaip.2024.100212).
11. Chiu Liu Ho, Wang Hsin Fu, Huang Chia Pao, Hsu Ching Tsung, Chen Tsung Chi. Effect of brazing temperature on the microstructure and property of vacuum brazed WC-Co and carbon steel joint. *Advanced materials research*, 2008, vol. 47–50, pp. 682–685. DOI: [10.4028/www.scientific.net/AMR.47-50.682](https://doi.org/10.4028/www.scientific.net/AMR.47-50.682).
12. Li Yuanxing, Zhu Zongtao, He Yongpan, Chen Hui, Jiang Chao, Han Dengquan, Li Junfu. WC particulate reinforced joint by ultrasonic-associated brazing of WC-Co/35CrMo. *Journal of Materials Processing Technology*, 2016, vol. 238, pp. 15–21. DOI: [10.1016/j.jmatprotec.2016.06.037](https://doi.org/10.1016/j.jmatprotec.2016.06.037).
13. Geng Haibin, Li Jinglong, Xiong Jiangtao, Shao Changbin, Zhang Fusheng. Interface Evolution of YG11C/42CrMo Joint Brazed with BCu64MnNi Filler Metal. *Powder Metallurgy and Metal Ceramics*, 2017, vol. 56, pp. 473–480. DOI: [10.1007/s11106-017-9918-0](https://doi.org/10.1007/s11106-017-9918-0).
14. Yin Xiaohui, Ma Qunshuang, Cui Bing, Zhang Lei, Xue Xingyan, Zhong Sujuan, Xu Dong. Current review on the research status of cemented carbide brazing: filler materials and mechanical properties. *Metals and Materials International*, 2021, vol. 27, pp. 571–583. DOI: [10.1007/s12540-020-00608-w](https://doi.org/10.1007/s12540-020-00608-w).
15. Amelzadeh M., Mirsalehi S.E. Influence of braze type on microstructure and mechanical behavior of WC-Co/steel dissimilar joints. *Journal of Manufacturing Processes*, 2018, vol. 36, pp. 450–458. DOI: [10.1016/j.jmapro.2018.10.015](https://doi.org/10.1016/j.jmapro.2018.10.015).
16. Jiang Chao, Chen Hui, Zhao Xu, Qui Sifu, Han Dengquan, Gou Guoqing. Microstructure and mechanical properties of brazing bonded WC-15Co/35CrMo joint using AgNi/CuZn/AgNi composite interlayers. *International Journal of Refractory Metals and Hard Materials*, 2018, vol. 70, pp. 1–8. DOI: [10.1016/j.jirmhm.2017.08.021](https://doi.org/10.1016/j.jirmhm.2017.08.021).
17. Levin D.O., Sulitsin A.V., Usov D.A., Shevchenko K.A., Strugov S.S., Brusnitsyn S.V. Influence of iron and silicon on corrosion resistance brass. *Liteynoe proizvodstvo*, 2023, no. 12, pp. 22–27. EDN: [YTNIUR](https://www.edn.ru/ytniur).
18. Cheng Zhi, Huang Jihua, Ye Zheng, Yang Jian, Chen Shuhai. Butt brazing of titanium alloys/stainless steel plates by MIG-TIG double-sided arc welding process with copper filler metal. *Journal of Materials Research and Technology*, 2019, vol. 8, no. 1, pp. 1566–1570. DOI: [10.1016/j.jmrt.2018.06.009](https://doi.org/10.1016/j.jmrt.2018.06.009).
19. Koltsov A., Bailly N., Cretteur L. Wetting and laser brazing of Zn-coated steel products by Cu–Si filler metal. *Journal of materials science*, 2010, vol. 45, no. 8, pp. 2118–2125. DOI: [10.1007/s10853-009-3949-y](https://doi.org/10.1007/s10853-009-3949-y).
20. Suga T., Murai Ya., Kobashi T., Ueno K., Shindo M., Kanno K., Nakata K. Laser brazing of dissimilar joint of austenitic stainless steel and pure copper. *Welding International*, 2016, vol. 30, no. 3, pp. 166–174. DOI: [10.1080/09507116.2014.921090](https://doi.org/10.1080/09507116.2014.921090).
21. Ryabukhin A.G., Gruba O.N. Enthalpy of formation of silicides of 3D elements of the periodic system of D.I. Mendeleev. *Vestnik Yuzhno-Uralskogo gosudarstvennogo universiteta. Seriya: Matematika. Mekhanika. Fizika*, 2007, no. 3, pp. 74–82. EDN: [KYSTJEJ](https://www.edn.ru/kystej).

СПИСОК ЛИТЕРАТУРЫ

1. Amelzadeh M., Mirsalehi S.E. Dissimilar joining of WC-Co to steel by low-temperature brazing // *Materials Science and Engineering: B*. 2020. Vol. 259. Article number 114597. DOI: [10.1016/j.mseb.2020.114597](https://doi.org/10.1016/j.mseb.2020.114597).
2. Коломейченко А.В., Соловьев Р.Р., Соловьев Р.Ю., Максимов Е.А., Карякин С.Б. Импортзамещение рабочих органов для мульчеров // *Вестник Казанского государственного аграрного университета*. 2023. Т. 18. № 2. С. 86–93. DOI: [10.12737/2073-0462-2023-86-93](https://doi.org/10.12737/2073-0462-2023-86-93).
3. Пашков И.Н., Мисников В.Е., Морозов В.А., Таволжанский С.А. Индукционная пайка твердосплавных резцов горного инструмента. Выбор состава и формы припоя // *Сварочное производство*. 2020. № 8. С. 20–27. EDN: [NXKPBV](https://www.edn.ru/nxkpbv).
4. Haghshenas M.S., Parvin N., Amirasiri A. Effect of bonding temperature on microstructure and mechanical properties of WC–Co/steel diffusion brazed joint // *Transactions of the Indian Institute of Metals*. 2018. Vol. 71. P. 649–658. DOI: [10.1007/s12666-017-1197-4](https://doi.org/10.1007/s12666-017-1197-4).
5. Amirasiri A., Parvin N. Dissimilar diffusion brazing of WC-Co to AISI 4145 steel using RBCuZn-D interlayer // *Journal of Manufacturing Processes*. 2017. Vol. 28. Part 1. P. 82–93. DOI: [10.1016/j.jmapro.2017.06.001](https://doi.org/10.1016/j.jmapro.2017.06.001).
6. Пашков И.Н., Мисников В.Е., Морозов В.А., Гаджиев М., Базлова Т.А. Влияние состава припоя и флюса на термическую стабильность паяных PDC резцов // *Сварочное производство*. 2021. № 1. С. 44–50. EDN: [XTZQZM](https://www.edn.ru/xtzqzm).
7. Яковцева О.А., Михайловская А.В., Иржак А.В., Котов А.Д., Медведева С.В. Сравнение вкладов действующих механизмов сверхпластической деформации двойной и многокомпонентных латуней // *Физика металлов и металловедение*. 2020. Т. 121. № 6. С. 643–650. DOI: [10.31857/S0015323020060182](https://doi.org/10.31857/S0015323020060182).
8. Yakovtseva O.A., Mikhaylovskaya A.V., Pozdniakov A.V., Kotov A.D., Portnoy V.K. Superplastic deformation behaviour of aluminium containing brasses // *Materials Science and Engineering: A*. 2016. Vol. 674. P. 135–143. DOI: [10.1016/j.msea.2016.07.053](https://doi.org/10.1016/j.msea.2016.07.053).
9. Sui Yanwei, Luo Haibo, Lv Yang, Wei Fuxiang, Qi Jiqu, He Yezeng, Meng Qingkun, Sun Zhi. Influence of brazing technology on the microstructure and properties of YG20C cemented carbide and 16Mn steel joints // *Welding in the World*. 2016. Vol. 60. P. 1269–1275. DOI: [10.1007/s40194-016-0374-0](https://doi.org/10.1007/s40194-016-0374-0).
10. Habibi F., Mostafapour A., Heydarpour K. Microstructural evaluation and mechanical properties of WC-6%Co/

- AISI 1045 steel joints brazed by copper, brass, and Ag-based filler metals: Selection of the filler material // Journal of Advanced Joining Processes. 2024. Vol. 9. Article number 100212. DOI: [10.1016/j.jajp.2024.100212](https://doi.org/10.1016/j.jajp.2024.100212).
11. Chiu Liu Ho, Wang Hsin Fu, Huang Chia Pao, Hsu Ching Tsung, Chen Tsung Chi. Effect of brazing temperature on the microstructure and property of vacuum brazed WC-Co and carbon steel joint // Advanced materials research. 2008. Vol. 47-50. P. 682–685. DOI: [10.4028/www.scientific.net/AMR.47-50.682](https://doi.org/10.4028/www.scientific.net/AMR.47-50.682).
 12. Li Yuanxing, Zhu Zongtao, He Yongpan, Chen Hui, Jiang Chao, Han Dengquan, Li Junfu. WC particulate reinforced joint by ultrasonic-associated brazing of WC-Co/35CrMo // Journal of Materials Processing Technology. 2016. Vol. 238. P. 15–21. DOI: [10.1016/j.jmatprotec.2016.06.037](https://doi.org/10.1016/j.jmatprotec.2016.06.037).
 13. Geng Haibin, Li Jinglong, Xiong Jiangtao, Shao Changbin, Zhang Fusheng. Interface Evolution of YG11C/42CrMo Joint Brazed with BCu64MnNi Filler Metal // Powder Metallurgy and Metal Ceramics. 2017. Vol. 56. P. 473–480. DOI: [10.1007/s11106-017-9918-0](https://doi.org/10.1007/s11106-017-9918-0).
 14. Yin Xiaohui, Ma Qunshuang, Cui Bing, Zhang Lei, Xue Xingyan, Zhong Sujuan, Xu Dong. Current review on the research status of cemented carbide brazing: filler materials and mechanical properties // Metals and Materials International. 2021. Vol. 27. P. 571–583. DOI: [10.1007/s12540-020-00608-w](https://doi.org/10.1007/s12540-020-00608-w).
 15. Amelzadeh M., Mirsalehi S.E. Influence of braze type on microstructure and mechanical behavior of WC-Co/steel dissimilar joints // Journal of Manufacturing Processes. 2018. Vol. 36. P. 450–458. DOI: [10.1016/j.jmapro.2018.10.015](https://doi.org/10.1016/j.jmapro.2018.10.015).
 16. Jiang Chao, Chen Hui, Zhao Xu, Qui Sifu, Han Dengquan, Gou Guoqing. Microstructure and mechanical properties of brazing bonded WC-15Co/35CrMo joint using AgNi/CuZn/AgNi composite interlayers // International Journal of Refractory Metals and Hard Materials. 2018. Vol. 70. P. 1–8. DOI: [10.1016/j.ijrmhm.2017.08.021](https://doi.org/10.1016/j.ijrmhm.2017.08.021).
 17. Левин Д.О., Сулицин А.В., Усов Д.А., Шевченко К.А., Стругов С.С., Брусницын С.В. Влияние железа и кремния на коррозионную стойкость литейной // Литейное производство. 2023. № 12. С. 22–27. EDN: [YTNIUR](https://www.edn.ru/ytniu/).
 18. Cheng Zhi, Huang Jihua, Ye Zheng, Yang Jian, Chen Shuhai. Butt brazing of titanium alloys/stainless steel plates by MIG-TIG double-sided arc welding process with copper filler metal // Journal of Materials Research and Technology. 2019. Vol. 8. № 1. P. 1566–1570. DOI: [10.1016/j.jmrt.2018.06.009](https://doi.org/10.1016/j.jmrt.2018.06.009).
 19. Koltsov A., Bailly N., Cretteur L. Wetting and laser brazing of Zn-coated steel products by Cu–Si filler metal // Journal of materials science. 2010. Vol. 45. № 8. P. 2118–2125. DOI: [10.1007/s10853-009-3949-y](https://doi.org/10.1007/s10853-009-3949-y).
 20. Suga T., Murai Ya., Kobashi T., Ueno K., Shindo M., Kanno K., Nakata K. Laser brazing of dissimilar joint of austenitic stainless steel and pure copper // Welding International. 2016. Vol. 30. № 3. P. 166–174. DOI: [10.1080/09507116.2014.921090](https://doi.org/10.1080/09507116.2014.921090).
 21. Рябухин А.Г., Груба О.Н. Энтальпия образования силицидов 3D-элементов периодической системы Д.И. Менделеева // Вестник Южно-Уральского государственного университета. Серия: Математика. Механика. Физика. 2007. № 3. С. 74–82. EDN: [KYSTJEJ](https://www.edn.ru/kystej/).

Влияние количественного содержания кремния на структуру припоя Cu55Ni6Mn4Zn и на структуру и свойства паяных соединений

Пашков Игорь Николаевич^{1,3}, доктор технических наук, профессор кафедры 1101

Гаджиев Магомед Ражабович^{*1,4}, аспирант

Таволжанский Станислав Анатольевич^{2,5}, кандидат технических наук, доцент кафедры «Литейные технологии и художественная обработка материалов»

Базлова Татьяна Алексеевна^{2,6}, кандидат технических наук, доцент кафедры «Литейные технологии и художественная обработка материалов»

Баженов Вячеслав Евгеньевич^{2,7}, кандидат технических наук, доцент кафедры «Литейные технологии и художественная обработка материалов»

*Катанова Диана Андреевна*², магистрант

¹Московский авиационный институт, Москва (Россия)

²Университет науки и технологий МИСИС, Москва (Россия)

*E-mail: maga.2630@gmail.com

³ORCID: <https://orcid.org/0000-0003-2511-2845>

⁴ORCID: <https://orcid.org/0000-0003-1922-6635>

⁵ORCID: <https://orcid.org/0000-0001-6062-397X>

⁶ORCID: <https://orcid.org/0000-0001-9517-5871>

⁷ORCID: <https://orcid.org/0000-0003-3214-1935>

Поступила в редакцию 24.06.2024

Пересмотрена 12.12.2024

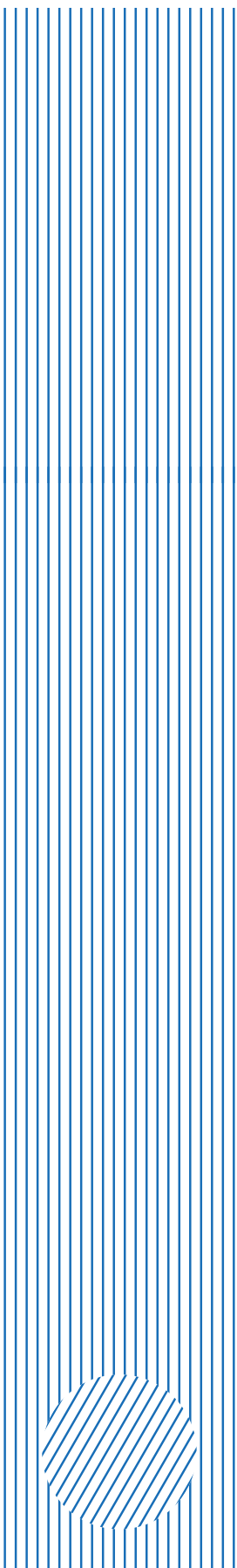
Принята к публикации 06.03.2025

Аннотация: Медно-цинковый сплав Cu55Ni6Mn4Zn (МНМц55-6-4) широко применяется для пайки твердо-сплавного инструмента и сталей. Однако наличие кремния в составе сплава (0,1–0,4 % мас.) может приводить к образованию хрупких силицидов железа, никеля и марганца, что негативно влияет на прочность паяных соединений. Цель исследования – определение влияния количественного содержания кремния в медно-цинковом припое, легированном совместно никелем и марганцем, на структуру заготовок припоя перед пайкой и структуру и свойства пая-

ных соединений. В работе использовались методы микроструктурного анализа, включая электронную микроскопию и микрорентгеноспектральный анализ, для изучения распределения силицидов в слитках, лентах и паяных швах. Результаты показали, что при содержании кремния до 0,2 % мас. силициды образуют мелкодисперсные включения, равномерно распределенные в объеме шва. Однако при увеличении содержания кремния до 0,4 % мас. наблюдается формирование сплошных слоев силицидов железа вдоль границы «припой – сталь», что приводит к хрупкому разрушению соединений при механических нагрузках. Особенно критичным оказалось влияние малых зазоров при пайке, где образование крупных кристаллов силицидов железа значительно снижает прочность соединений. Научная новизна работы заключается в установлении оптимального содержания кремния в сплаве (не более 0,2 % мас.) для минимизации негативного влияния силицидов на свойства паяных соединений. Полученные результаты могут быть использованы для разработки технологических рекомендаций при производстве припоев и пайке сталей, что позволит повысить надежность и долговечность паяных соединений в промышленных условиях.

Ключевые слова: пайка твердосплавного инструмента; Cu55Ni6Mn4Zn (МНМц55-6-4); влияние кремния на паяные соединения; силициды железа в паяных швах; микроструктура паяного шва; хрупкость паяных соединений; оптимизация состава припоя.

Для цитирования: Пашков И.Н., Гаджиев М.Р., Таволжанский С.А., Базлова Т.А., Баженов В.Е., Катанаева Д.А. Влияние количественного содержания кремния на структуру припоя Cu55Ni6Mn4Zn и на структуру и свойства паяных соединений // Frontier Materials & Technologies. 2025. № 1. С. 47–57. DOI: 10.18323/2782-4039-2025-1-71-4.



The Publishing Center (until November 1, 2011 – the Editorial and Publishing Center) is a structural subdivision of Togliatti State University, which takes an important place in providing the educational process with high-quality instructional, educational, methodological, and scientific literature.

TSU Publishing Center today

– Publishing center includes an editorial office and a printing shop. In recent years, the base of computer equipment, printing and post-printing equipment has been almost completely updated.

– It publishes books and electronic textbooks for students, graduate students, lecturers, and specialists in almost all branches of modern scientific knowledge, as well as popular science and reference literature, fiction, books of reports (papers) of conferences. Published literature corresponds to all areas of the educational cycles of the university disciplines.

– A considerable volume of printing job is the prompt execution of promotional and information products.

– The publishing center team is a collaboration of highly skilled professionals with wide work experience and young motivated employees.

– Publishing center employees participate in practical seminars to become acquainted with new opportunities in the field of printing technologies and equipment, as well as with advanced materials for digital printing.

Main areas of activity

– Publication of paper-based educational and scientific literature, production of electronic educational and scientific aids.

– Implementation of editorial and publishing cycle stages: editing, production of original layouts, replication, pre-printing and post-printing treatment.

– Methodological and advisory work with the university departments on the issue of educational and scientific publications.

– Interaction with the Russian Book Chamber on the assignment of ISBNs to publications issued by Togliatti State University.

– Preparation of publications issued by Togliatti State University for state registration and sending of statutory copies.

– Markup of papers published in the TSU journals in the Articulus program to place on the eLibrary platform.

Main achievements

– The results of the work were awarded with diplomas of the winners of the annual interregional and all-Russian University Book competitions.

– Publishing center regularly participates in the academic book exhibition of publishing activities “University – Science – City”.

Calculation of the effective solidification range and its relationship with hot brittleness of alloys based on Mg–Al and Mg–Zn systems

Andrey V. Pozdniakov, PhD (Engineering), Associate Professor
University of Science and Technology MISIS, Moscow (Russia)

E-mail: pozdniakov@misis.ru

ORCID: <https://orcid.org/0000-0002-5975-4849>

Received 05.02.2025

Revised 19.02.2025

Accepted 27.02.2025

Abstract: Magnesium alloys of the Mg–Al and Mg–Zn systems have a wide effective solidification range (ESR), and as a result, have the tendency to hot brittleness during casting. There are several methods for analyzing and calculating the hot brittleness of magnesium alloys, but they are very labor-intensive. In this regard, the objective of the study is to develop a model for calculating the hot brittleness index (HBI) based on the value of the calculated effective solidification range, identifying and analyzing their relationship in binary and multicomponent alloys based on the Mg–Al and Mg–Zn systems. The ESR was calculated using the Thermo-Calc program (TTMG3 database). The ESR was calculated as the difference between the temperature of formation of a given amount of solid phases and the nonequilibrium solidus temperature. The study showed a good correlation between the calculated values of ESR and HBI in both binary and multicomponent magnesium alloys. In the Mg–Al system alloys, the calculated dependences of the ESR at 90 % of solid phases (ESR_{90}) show the best correlation with the experimental values of HBI. In the binary alloys of the Mg–Zn system, a qualitatively similar dependence is observed. However, no clear correlation was noted between the ESR and HBI. The ESR_{65} and ESR_{80} dependences demonstrate the closest nature. According to the relationship between HBI and ESR, the considered multicomponent alloys are divided into two groups as a first approximation: the first one is the Mg–Al–Zn system alloys; the second one is the Mg–Zn–Zr and Mg–Nd–Zr alloys. Within these groups, the dependence of HBI and ESR has a nature close to a linear one. To describe the dependence of all alloys, a single equation can be applied if ESR_{65} is used in the calculations for Mg–Al–Zn alloys and ESR_{90} – for Mg–Zn–Zr and Mg–Nd–Zr alloys. The proposed model will allow for easy and quick calculation of the HBI, which is very important in the development of new high-tech magnesium alloys.

Keywords: magnesium alloys; hot brittleness; effective solidification range; thermodynamic calculation; nonequilibrium solidification.

For citation: Pozdniakov A.V. Calculation of the effective solidification range and its relationship with hot brittleness of alloys based on Mg–Al and Mg–Zn systems. *Frontier Materials & Technologies*, 2025, no. 1, pp. 59–68. DOI: 10.18323/2782-4039-2025-1-71-5.

INTRODUCTION

Magnesium alloys combine a good level of mechanical properties with low density. Almost all cast magnesium alloys belong to two basic alloying systems – Mg–Al and Mg–Zn [1; 2]. Alloys of the Mg–Al and Mg–Zn systems have a very wide solidification range [3]. In this regard, when selecting the composition of cast alloys, it is necessary to take into account the possibility of narrowing the solidification range, or more precisely, the effective solidification range (ESR) – the range between the temperature of the onset of linear shrinkage and the nonequilibrium solidus of the alloy [3]. It can be said that the ESR value directly determines the tendency of the alloy to form cracks of solidification origin or hot brittleness [3; 4]. The appearance of solidification cracks in castings is an irreparable defect. Experimental determination of the ESR value is a very labor-intensive process [3; 4]. The authors of the work [5] proposed a method for calculating the ESR value using thermodynamic calculations of nonequilibrium solidification for binary and ternary aluminum-based alloys. It was shown that it is the effective solidification range, and not the full solidification interval, that determines the manu-

facturability during casting [6], and the possibility of calculating the ESR and the hot brittleness index (HBI) in multicomponent aluminum-based alloys was identified [7].

The problem of the formation of cracks of solidification origin is no less acute during casting of castings from magnesium alloys [8–10]. There are several methods for analyzing and calculating the hot brittleness of magnesium alloys, but they are very labor-intensive [11–14]. For example, the authors of the work [11] estimated the tendency to form cracks of solidification origin based on the characteristics of mechanical properties in the solid-liquid state and the location of the layers of the last liquid. The results of [12] are based on the optimization of the Clyne – Davies model and use a very narrow parameter for determining the HBI on a 4-point scale. In the work [14], a complex and inaccessible method of neutron diffraction was used to analyze the initiation of hot cracks. The proposed approach is faster and sufficiently accurate.

When designing castings for casting from known magnesium alloys, when developing new casting magnesium alloys, it is necessary to take into account the level of casting properties, especially the HBI. Cracks of solidification

origin can also form in ingots of deformable magnesium alloys. As shown in the example of aluminum alloys, the HBI is directly related to the ESR value. Therefore, there is a need to analyze the relationship between the ESR and the HBI value for magnesium alloys. Identifying patterns similar to those obtained in aluminum alloying systems will allow using this technique for calculating the HBI, which is especially important when developing new magnesium alloys. This study is aimed at adapting the method for calculating the ESR for binary and multicomponent alloys based on the Mg–Al and Mg–Zn systems and analyzing the relationship between the calculated ESR and the experimentally determined HBI.

The aim of this study is to develop a model for calculating the hot brittleness index based on the value of the calculated effective solidification range, establishing and analyzing their relationship in binary and multicomponent alloys based on the Mg–Al and Mg–Zn systems.

METHODS

The calculation of the ESR was performed using the Thermo-Calc software product (TTMG3 magnesium alloy database). The ESR was calculated as the difference between the temperature of formation of a given amount of solid phases (from 65 to 90 %) and the nonequilibrium solidus temperature. Additionally, the values of the total equilibrium solidification range TSR_{eq} were calculated as the difference between the liquidus temperature and the equilibrium solidus temperature; the total nonequilibrium solidification range TSR_{noneq} – as the difference between the liquidus temperature and the nonequilibrium solidus temperature. The calculation of nonequilibrium solidification is based on the Sheil model, which assumes complete passage of diffusion processes in the liquid and complete suppression of diffusion in the solid phase. To compare the calculated values of ESR and TSR with hot brittleness, experimental data on the HBI of binary and multicomponent alloys from work [3] were used, which are in good agreement with more recent information on binary Mg–Zn alloys [14; 15], Mg–Zn alloys with the addition of Y [16] or Y and Zr [17–19], Mg–Al alloys [20–22]. The HBI of magnesium alloys in work [3] was determined by one of the most common tests for magnesium and aluminum alloys – the ring test. In this test, the melt is poured into a sand mold with a metal rod and a refrigerator on half of the ring, and the critical width of the ring in millimeters is determined.

RESULTS

For binary alloys of the Mg–Al and Mg–Zn systems in the concentration range from 0 to 6 % of Al and from 0 to 10 % of Zn, nonequilibrium solidification curves were constructed. Fig. 1 presents typical dependences of the change in the mass fraction of solid phases during nonequilibrium solidification of Mg–0.75%Al, Mg–1.5%Al, Mg–1%Zn, and Mg–2%Zn binary alloys. The solidification process of the Mg–0.75%Al alloy (Fig. 1 a) begins at a temperature of 646 °C with the formation of a magnesium solid solution (Mg). Under equilibrium condi-

tions, solidification ends at 637 °C, in accordance with the dotted curve. Under nonequilibrium conditions, solidification ends at 553 °C, in accordance with the solid curve. As a result, TRS_{eq} and TRS_{noneq} are 9 and 93 °C, respectively.

As mentioned above, the ESR is the interval between the temperature of the onset of linear shrinkage and the nonequilibrium solidus. The temperature of the linear shrinkage onset usually corresponds to the formation of 65–90 % of solid phases in the alloy. It is for this range of the amount of solid phases that the ESR values were calculated (Table 1). Using the Mg–0.75%Al alloy as an example, Fig. 1 a shows the intervals corresponding to the calculated ESR values for 65, 80 and 90 % of the solid phases. For comparison, the solidification process of the Mg–1.5%Al alloy (Fig. 1 b) begins at 642 °C and ends under equilibrium conditions at 624 °C, and under nonequilibrium conditions – at 437 °C. In this case, the solidification of the Mg–1.5%Al alloy (Fig. 1 b) ends with the formation of the $Mg_{17}Al_{12}$ phase in the eutectic with (Mg). A similar solidification pattern was observed in the Mg–1%Zn (Fig. 1 c) and Mg–2%Zn (Fig. 1 d) alloys. The obtained calculation data were used to construct a nonequilibrium solidus in the Mg–Al and Mg–Zn systems. All critical temperatures of formation of 65, 80 and 90 % solid phases, nonequilibrium and equilibrium solidus and liquidus ($T_{65\%}$, $T_{80\%}$, $T_{90\%}$, $T_{n.s.}$, $T_{eq.s.}$, $T_{liq.}$), calculated ESR values corresponding to formation of 65, 80 and 90 % solid phases (ESR_{65} , ESR_{80} , ESR_{90}), calculated values of equilibrium and nonequilibrium TSR (TSR_{eq} , TSR_{noneq}) for all binary alloy compositions (first column of the table) are collected in Table 1. The calculation results are used to analyze the relationship of ESR and TSR with the experimental HBI values in binary alloys of the Mg–Al and Mg–Zn systems.

Fig. 2 shows as an example the dependences of the mass fraction of solid phases in the process of nonequilibrium solidification of multicomponent ML5 (Mg–Al–Zn) and ML10 (Mg–Nd–Zr) alloys. Similar dependences were used to calculate the critical temperatures and intervals for all multicomponent alloys. The solidification process of the ML5 alloy begins at 629 °C with the formation of the Al_8Mn_5 phase (Fig. 2 a). Under equilibrium conditions, solidification ends at 489 °C, and under nonequilibrium conditions – at 412 °C, which corresponds to $TSR_{eq}=140$ °C and $TSR_{noneq}=217$ °C (Table 2). In the process of nonequilibrium solidification, the (Mg), $Al_{11}Mn_4$ and Al_4Mn phases are formed by eutectic and peritectic reactions, and the $Al_{11}Mn_4$ and Al_8Mn_5 phases dissolve (Fig. 2 a). Solidification of the ML10 alloy begins at 737 °C with the formation of the α -Zr phase, then the (Mg) and $Mg_{41}Nd_5$ phases appear (Fig. 2 b). In this case, in the ML10 alloy, $TSR_{noneq}=237$ °C (Table 2), i.e. wider than in the ML5 alloy. However, in this case, ESR_{65} in the ML10 alloy is significantly narrower – 55 °C versus 139 °C in the ML5 alloy (Table 2). Results of calculations of critical $T_{65\%}$, $T_{80\%}$, $T_{90\%}$, $T_{n.s.}$, $T_{eq.s.}$, and $T_{liq.}$ temperatures and ESR_{65} , ESR_{80} , ESR_{90} , TSR_{eq} , TSR_{noneq} intervals for different multicomponent alloys based on the Mg–Al–Zn (ML1, ML2, ML3, ML4, ML5, ML6, ML7-1), Mg–Zn–Zr (ML12, ML15), and Mg–Nd–Zr (ML10) systems are collected in Table 2. The obtained calculated data on the ESR values are analyzed in comparison with the experimentally determined HBI.

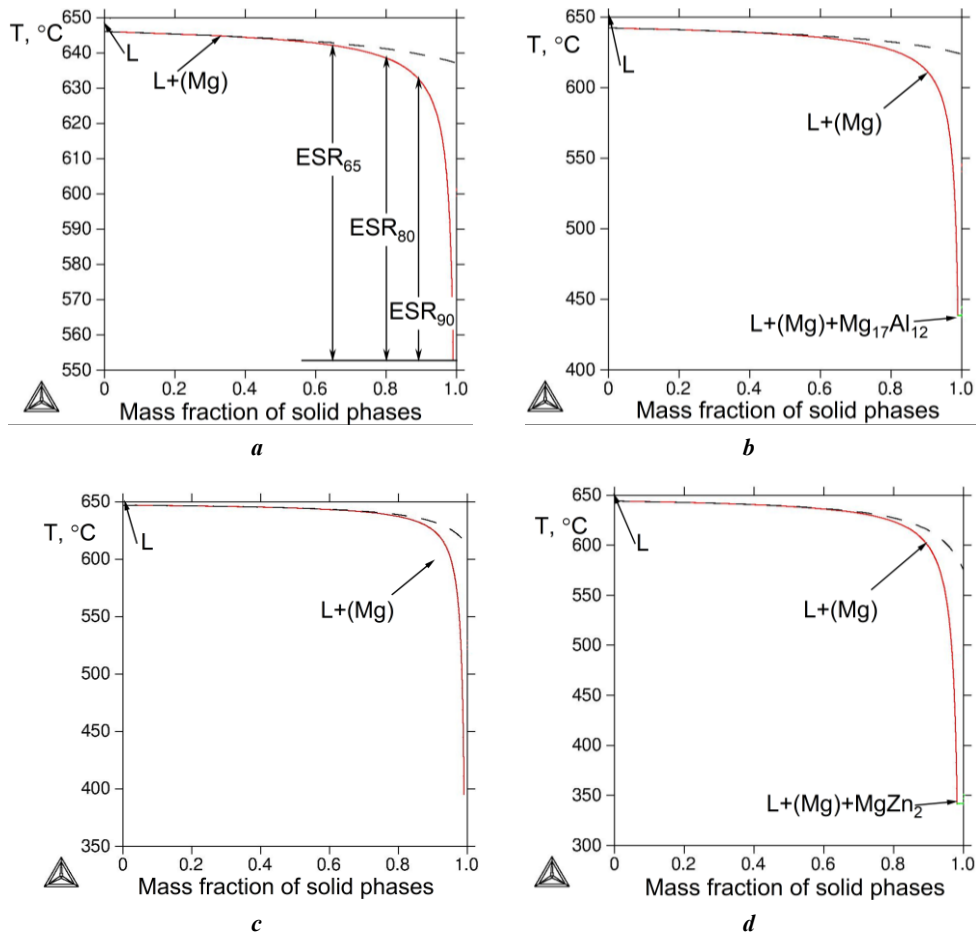


Fig. 1. Change in the mass fraction of solid phases during nonequilibrium solidification (dashed line – equilibrium solidification) of binary alloys: **a** – Mg–0.75%Al; **b** – Mg–1.5%Al; **c** – Mg–1%Zn; **d** – Mg–2%Zn (L – liquid phase)

Рис. 1. Изменение массовой доли твердых фаз в процессе неравновесной кристаллизации (пунктир – равновесная кристаллизация) двойных сплавов: **a** – Mg–0,75%Al; **b** – Mg–1,5%Al; **c** – Mg–1%Zn; **d** – Mg–2%Zn (L – жидкая фаза)

Table 1. Values of calculated temperatures and ranges for alloys of the Mg–Al and Mg–Zn systems
Таблица 1. Значения расчетных температур и интервалов для сплавов систем Mg–Al и Mg–Zn

Al, %	T ₆₅ %, °C	T ₈₀ %, °C	T ₉₀ %, °C	T _{n.s.} , °C	T _{eq.s.} , °C	T _{liq} , °C	ESR ₆₅ , °C	ESR ₈₀ , °C	ESR ₉₀ , °C	TSR _{eq} , °C	TSR _{noneq} , °C
Mg–Al											
0.1	649	648.5	648	642	648	649.3	7	6.5	6	1.3	7.3
0.5	645	643	638	590	641	647	55	53	48	6	57
0.75	642	638	631	553	637	646	89	85	78	9	93
1	639	635	623	511	632	645	128	124	112	13	134
1.25	636	631	617	464	629	643	172	167	153	14	179
1.5	634	624	611	437	624	642	197	187	174	18	205
2	628	618	598	437	615	640	191	181	161	25	203
4	607	584	535	437	582	630	170	147	98	48	193
6	583	545	465	437	542	618	146	108	28	76	181

Mg–Zn											
0.1	649.2	648.6	647.8	632	646	649.7	17.2	16.6	15.8	3.7	17.7
0.5	646	643	638	540	634	648	106	103	98	14	108
1	643	637	626	396	619	647	247	241	230	28	251
1.5	638	630	6112	341	600	645	297	289	5771	45	304
2	635	623	599	341	577	644	294	282	258	67	303
3	626	608	568	341	548	641	285	267	227	93	300
4	618	596	536	341	502	638	277	255	195	136	297
6	599	563	455	341	424	632	258	222	114	208	291
10	560	485	341	341	341	618	219	144	0	277	277

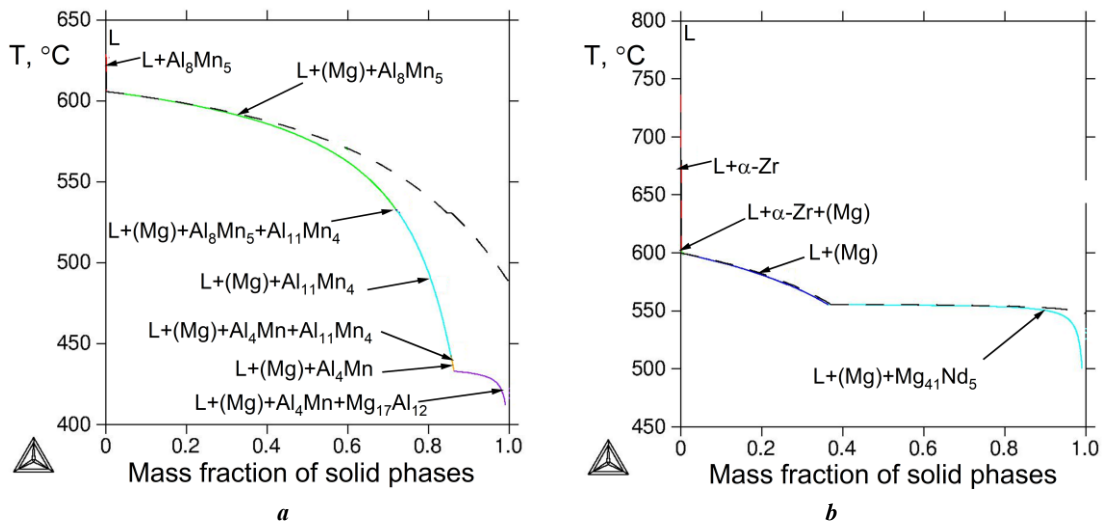


Fig. 2. Change in the mass fraction of solid phases in the process of nonequilibrium solidification (dashed line – equilibrium solidification) of multicomponent alloys: a – ML5; b – ML10

Рис. 2. Изменение массовой доли твердых фаз в процессе неравновесной кристаллизации (пунктир – равновесная кристаллизация) многокомпонентных сплавов: а – МЛ5; б – МЛ10

DISCUSSION

Based on the results of calculating the nonequilibrium solidification of binary alloys, the nonequilibrium solidus lines were plotted in the magnesium angle of the Mg–Al and Mg–Zn systems (Fig. 3 a, 3 c). During solidification of the Mg–1.5%Al and Mg–2%Zn alloys, a nonequilibrium excess of the Mg₁₇Al₁₂ phase appears at a temperature of 437 °C (Fig. 1 b) and MgZn₂ at a temperature of 341 °C (Fig. 1 d). Fig. 3 b, 3 d shows the dependences of the calculated values of ESR (for different amounts of solid phases), TSR_{eq}, TSR_{noneq} and the experimental values of HBI for binary alloys of the Mg–Al and Mg–Zn systems. The calculated values of TSR_{eq} do not correlate with the values of ESR and, accordingly, with HBI. In this case, as in aluminum alloys of eutectic systems [5; 6], the TSR_{noneq} values are in good agreement with the ESR value. In the Mg–Al

system alloys (Fig. 3 b), the calculated dependences of ESR₉₀ show the best correlation with the experimental values of HBI. The rate of decrease in HBI practically coincides with the rate of decrease in the calculated value of ESR₉₀. In binary alloys of the Mg–Zn system, a qualitatively similar dependence is observed (Fig. 3 d). However, no clear correlation was noted between ESR and HBI. The ESR₆₅ and ESR₈₀ dependences demonstrate the closest nature (Fig. 3 d).

The position of the HBI maximum somewhat diverges from the maximum calculated ESR value. Thus, in the Mg–Al system, an alloy with 1 % of Al has the maximum HBI, which is confirmed by the data of work [9; 10], and the Mg–1.5%Al alloy has the highest calculated ESR. It is worth noting that in works [9; 10], alloys containing more than 1 but less than 2 % of Al were not considered.

Table 2. Values of calculated temperatures and ranges for multicomponent alloys
Таблица 2. Значения расчетных температур и интервалов для многокомпонентных сплавов

Alloy	T _{65 %} , °C	T _{80 %} , °C	T _{90 %} , °C	T _{n.s.} , °C	T _{eq.s.} , °C	T _{liq} , °C	ESR ₆₅ , °C	ESR ₈₀ , °C	ESR ₉₀ , °C	TSR _{eq} , °C	TSR _{noneq} , °C
ML3	610	589	540	363	564	631	247	226	177	67	268
ML4	562	503	405	350	464	612	212	153	55	148	262
ML5	551	489	431	412	489	629	139	77	19	140	217
ML6	531	451	426	389	460	630	142	62	37	170	241
ML7-1	579	542	445	400	487	640	179	142	45	153	240
ML10	555	553	548	500	548	737	55	53	48	189	237
ML12	612	585	514	339	482	732	273	246	175	250	393
ML15	608	573	498	339	477	730	269	234	159	253	391

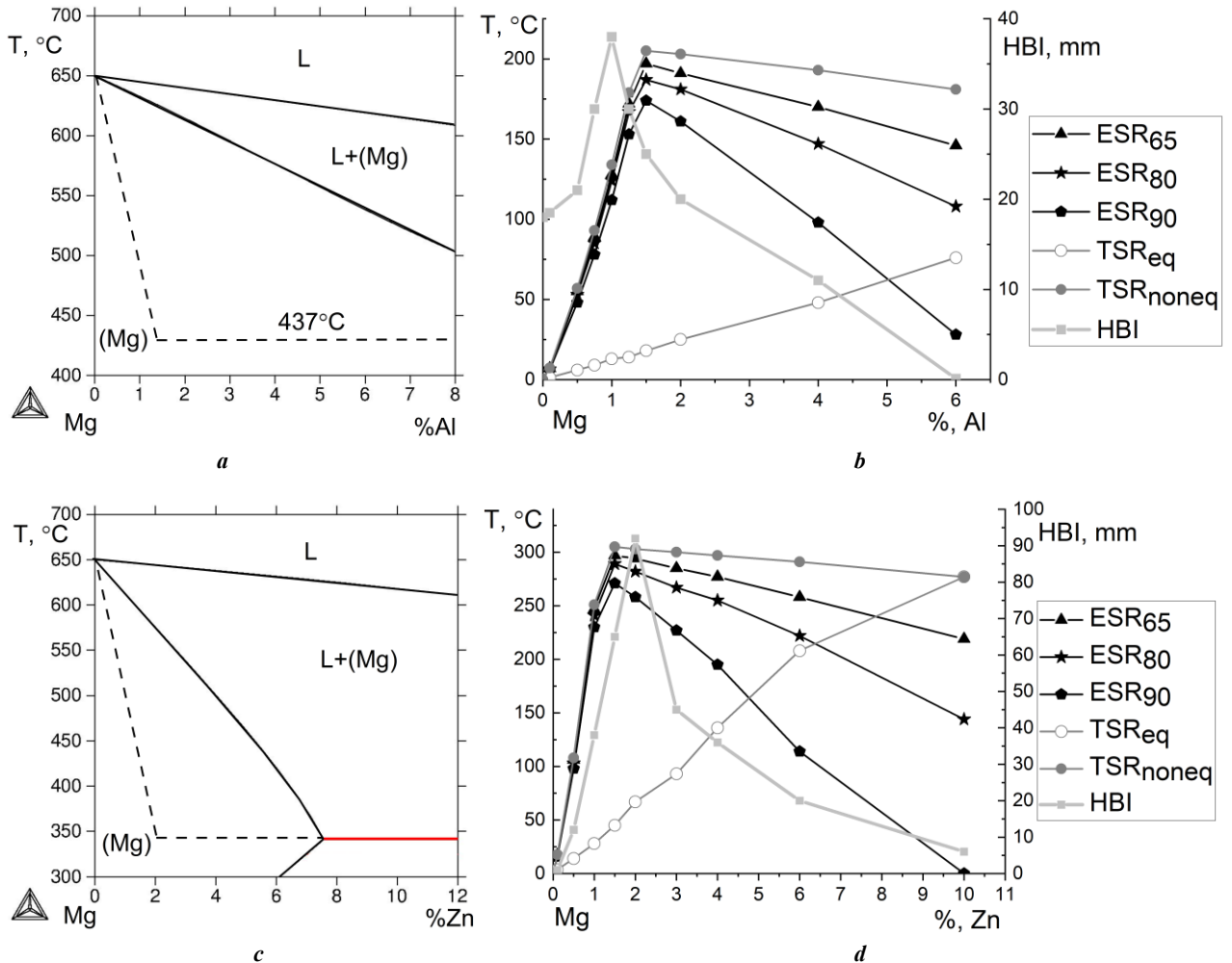


Fig. 3. Magnesium angle of the phase diagrams of the Mg–Al (a) and Mg–Zn (c) systems (dotted line – nonequilibrium solidus) and the dependences of the calculated values of effective solidification range ESR (for different amounts of solid phases), total equilibrium solidification range TSR_{eq}, total nonequilibrium solidification range TSR_{noneq}, and experimental values of the hot brittleness index HBI for binary alloys of the Mg–Al (b) and Mg–Zn (d) systems

Рис. 3. Магнийевый угол фазовых диаграмм систем Mg–Al (a) и Mg–Zn (c) (пунктир – неравновесный солидус) и зависимости расчетных значений эффективного интервала кристаллизации ESR (для разного количества твердых фаз), полного равновесного интервала кристаллизации TSR_{eq}, полного неравновесного интервала кристаллизации TSR_{noneq} и экспериментальных значений показателя горячеломкости HBI для двойных сплавов систем Mg–Al (b) и Mg–Zn (d)

In the Mg–Zn system, the maximum hot brittleness index is found at 2 % of Zn [3], however, according to the data of works [9; 11], the most hot-brittle alloy is Mg–1.5%Zn, which has the highest calculated ESR (Fig. 3).

The nature of solidification of multicomponent alloys is somewhat more complicated (Fig. 2). Mg–Zn–Zr system alloys (just as Mg–Zn) have a low nonequilibrium solidus, and accordingly, a very wide ESR, but at the same time approximately the same tendency to form solidification cracks as Mg–Al–Zn alloys, whose ESR is approximately 100 °C narrower (Table 3). The ML10 alloy (Mg–Nd–Zr system), having a high temperature of nonequilibrium soli-

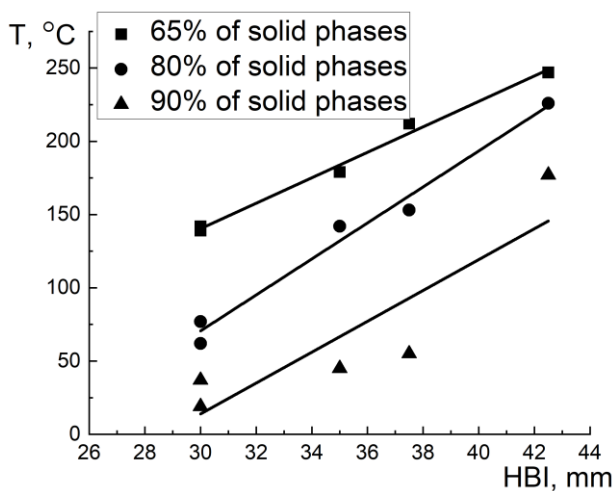
us, is distinguished by a very narrow ESR (48–55 °C) and low HBI (Table 3). The calculated values of solidification intervals in comparison with the experimental HBI for multicomponent magnesium alloys are collected in Table 3.

According to the relationship between HBI and ESR, the considered multicomponent alloys are divided into two groups: the first one is the Mg–Al–Zn system alloys; the second one is the alloys of the Mg–Zn–Zr and Mg–Nd–Zr systems. Within these groups, the dependence of HBI and ESR has a nature close to a linear one, hot brittleness index increases with an increase in the ESR (Fig. 4). At the same time, for the Mg–Al–Zn system alloys, all points lie as

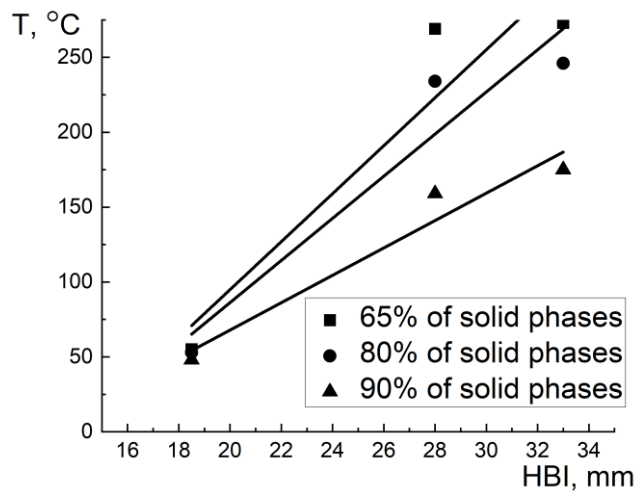
Table 3. Effective solidification range ESR and total equilibrium solidification range TSR values in comparison with the experimental hot brittleness index for multicomponent alloys

Таблица 3. Значения эффективного интервала кристаллизации ESR и полного равновесного интервала кристаллизации TSR в сравнении с экспериментальным показателем горячеломкости для многокомпонентных сплавов

Alloy	ESR ₆₅ , °C	ESR ₈₀ , °C	ESR ₉₀ , °C	TSR _{eq} , °C	TSR _{noneq} , °C	HBI, mm
ML3	247	226	177	67	268	42.5
ML4	212	153	55	148	262	37.5
ML5	139	77	19	140	217	30
ML6	142	62	37	170	241	30
ML7-1	179	142	45	153	240	35
ML10	55	53	48	189	237	18.5
ML12	273	246	175	250	393	33
ML15	269	234	159	253	391	28



a



b

Fig. 4. Comparison of calculated effective solidification range ESR values (for different amounts of solid phases) and experimental values of the hot brittleness index HBI for multicomponent alloys based on the systems: a – Mg–Al–Zn; b – Mg–Zn–Zr and Mg–Nd–Zr

Рис. 4. Сопоставление расчетных значений эффективного интервала кристаллизации ESR (для разного количества твердых фаз) и экспериментальных значений показателя горячеломкости HBI для многокомпонентных сплавов на основе систем: a – Mg–Al–Zn; b – Mg–Zn–Zr и Mg–Nd–Zr

closely as possible on the linear dependence for the calculated values of ESR₆₅ (Fig. 4 a). The obtained dependence can be described by a simple linear equation with a confidence probability of $R^2=0.99$:

$$\text{HBI}=0.11\times\text{ESR} + 14. \quad (1)$$

For the Mg–Zn–Zr and Mg–Nd–Zr systems, the calculated ESR₉₀ values demonstrate the dependence closest to linear (Fig. 4 b). For this group, the dependence can be described by a simple linear equation with a lower confidence probability of $R^2=0.94$:

$$\text{HBI}=0.1\times\text{ESR}+13.2. \quad (2)$$

Equations (1) and (2) for the two groups have close coefficients. Combining the data from the two groups obtained for ESR for different amounts of solid phases allows distinguishing a linear dependence with a confidence probability of $R^2=0.96$:

$$\text{HBI}=0.12\times\text{ESR}+12.5. \quad (3)$$

Equation (3) can be applied in the first approximation to both groups of alloys, if ESR₆₅ is used in the calculations for Mg–Al–Zn alloys and ESR₉₀ – for Mg–Zn–Zr and Mg–Nd–Zr alloys. However, it is not entirely correct to consider alloys of different systems with very different nonequilibrium solidus within the same group.

In general, the study showed the possibility of assessing the tendency of magnesium alloys of the Mg–Al and Mg–Zn systems to form cracks of solidification origin based on the calculation of the effective solidification range. All deviations of the calculated ESR values and experimental HBI values are due to other factors affecting hot brittleness, such as mechanical properties in the solid-liquid state and modification [3; 4]. For example, zirconium in wide-range Mg–Zn alloys can act as a modifier, which improves casting properties. The proposed equation for calculation requires experimental verification on alloys of other compositions not used in the calculations. However, such a possibility is not currently available. Based on the existing successful experience of applying a similar model using the example of creating new aluminum alloys [23; 24], the proposed method for calculating the hot brittleness index will also work in magnesium alloys.

CONCLUSIONS

The calculations of the temperatures of formation of a given amount of solid phases, effective and total solidification ranges in binary and multicomponent alloys based on the Mg–Al and Mg–Zn systems are carried out using thermodynamic calculations of nonequilibrium solidification. A good correlation of the calculated values of the effective solidification range with the hot brittleness index in both binary and multicomponent magnesium alloys is shown. According to the relationship between HBI and ESR, the considered multicomponent alloys are divided into 2 groups in the first approximation: the first group is the alloys of the Mg–Al–Zn

system; the second group is the Mg–Zn–Zr and Mg–Nd–Zr alloys. Within these groups, the dependence of HBI and ESR has a nature close to a linear one.

REFERENCES

1. Pan Fusheng, Yang Mingbo, Chen Xianhua. A Review on Casting Magnesium Alloys: Modification of Commercial Alloys and Development of New Alloys. *Journal of Materials Science & Technology*, 2016, vol. 32, no. 12, pp. 1211–1221. DOI: [10.1016/j.jmst.2016.07.001](https://doi.org/10.1016/j.jmst.2016.07.001).
2. Xie Hecong, Zhao Hua, Guo Xin, Li Yongfeng, Hu Hengrui, Song Jiangfeng, Jiang Bin, Pan Fusheng. Recent progress on cast magnesium alloy and components. *Journal of Materials Science*, 2024, vol. 59, pp. 9969–10002. DOI: [10.1007/s10853-024-09459-x](https://doi.org/10.1007/s10853-024-09459-x).
3. Novikov I.I. *Goryachelomkost tsvetnykh metallov i splavov* [Hot brittleness of non-ferrous metals and alloys]. Moscow, Nauka Publ., 1966. 299 p.
4. Eskin D.G., Suyitno, Katgerman L. Mechanical properties in the semi-solid state and hot tearing of aluminium alloys. *Progress in Materials Science*, 2004, vol. 49, no. 5, pp. 629–711. DOI: [10.1016/S0079-6425\(03\)00037-9](https://doi.org/10.1016/S0079-6425(03)00037-9).
5. Zolotarevskiy V.S., Pozdniakov A.V., Khvan A.V. Thermodynamic Calculations of the Effective Solidification Range and Its Relation to Hot Cracking of Aluminum-Based Ternary Alloys. *Russian Journal of Non-Ferrous Metals*, 2011, vol. 52, no. 1, pp. 50–55. DOI: [10.3103/S1067821211010275](https://doi.org/10.3103/S1067821211010275).
6. Zolotarevskiy V.S., Pozdniakov A.V., Kanakidi Ya.Yu. Relation between the Full and effective solidification ranges and the hot cracking of multicomponent aluminum-based alloys. *Russian Journal of Non-Ferrous Metals*, 2012, vol. 53, no. 5, pp. 392–398. DOI: [10.3103/S1067821212050148](https://doi.org/10.3103/S1067821212050148).
7. Zolotarevskiy V.S., Pozdniakov A.V., Churyumov A.Yu. Search for promising compositions for developing new multiphase casting alloys based on Al–Cu–Mg matrix using thermodynamic calculations and mathematic simulation. *Physics of Metals and Metallography*, 2012, vol. 113, no. 11, pp. 1052–1060. DOI: [10.1134/S0031918X12110154](https://doi.org/10.1134/S0031918X12110154).
8. Song Jiangfeng, Pan Fusheng, Jiang Bin, Atrens A., Zhang Ming-Xing, Lu Yung. A review on hot tearing of magnesium alloys. *Journal of Magnesium and Alloys*, 2016, vol. 4, no. 3, pp. 151–172. DOI: [10.1016/j.jma.2016.08.003](https://doi.org/10.1016/j.jma.2016.08.003).
9. Bai Shengwei, Wang Feng, Du Xudong, Wang Zhi, Zhou Le, Wei Ziqi, Mao Pingli, Li Jinwei. Reduced hot tearing susceptibility of Mg-4Zn-1.5Ca-xY-0.3Zr alloy by introducing intergranular bridging secondary phases. *Journal of Alloys and Compounds*, 2025, vol. 1014, article number 178663. DOI: [10.1016/j.jallcom.2025.178663](https://doi.org/10.1016/j.jallcom.2025.178663).
10. Zhong Honggang, Lin Zenghuang, Han Qingyou, Song Jiangfeng, Chen Meicheng, Chen Xiangru, Li Lijuan, Zhai Qijie. Hot tearing behavior of AZ91D magnesium alloy. *Journal of Magnesium and Alloys*, 2024, vol. 12, no. 8, pp. 3431–3440. DOI: [10.1016/j.jma.2023.02.010](https://doi.org/10.1016/j.jma.2023.02.010).
11. Zhen Zisheng, Hort N., Huang Yuan Ding, Petri N., Utke O., Kainer K.U. Quantitative Determination on

- Hot Tearing in Mg–Al Binary Alloys. *Materials Science Forum*, 2009, vol. 618-619, pp. 533–540. DOI: [10.4028/www.scientific.net/MSF.618-619.533](https://doi.org/10.4028/www.scientific.net/MSF.618-619.533).
12. Easton M.A., Gibson M.A., Zhu Suming, Abbott T.B. An A Priori Hot-Tearing Indicator Applied to Die-Cast Magnesium-Rare Earth Alloys. *Metallurgical and Materials Transactions A*, 2014, vol. 45, pp. 3586–3595. DOI: [10.1007/s11661-014-2272-7](https://doi.org/10.1007/s11661-014-2272-7).
 13. Li Tianyu, Lin Zenghuang, Su Chenxi, Gu Guangqi, Wang Hao, Li Lijuan, Zhong Honggang, Han Qingyou, Zhai Qijie. A method for predicting hot tearing during alloy solidification and its application in AZ91D magnesium alloy. *Engineering Failure Analysis*, 2025, vol. 169, article number 109194. DOI: [10.1016/j.engfailanal.2024.109194](https://doi.org/10.1016/j.engfailanal.2024.109194).
 14. Gan Wei Min, Huang Yuan Ding, Wang Zhi, Hort N., Hofmann M. Residual stresses near the hot sprues of as-cast Mg–Zn alloys investigated by stress-spec neutron diffractometer. *Materials Science Forum*, 2014, vol. 768-769, pp. 428–432. DOI: [10.4028/www.scientific.net/MSF.768-769.428](https://doi.org/10.4028/www.scientific.net/MSF.768-769.428).
 15. Gunde P., Schiffel A., Uggowitzer P.J. Influence of yttrium additions on the hot tearing susceptibility of magnesium–zinc alloys. *Materials Science and Engineering: A*, 2010, vol. 527, no. 26, pp. 7074–7079. DOI: [10.1016/j.msea.2010.07.086](https://doi.org/10.1016/j.msea.2010.07.086).
 16. Wang Zhi, Huang Yuan Ding, Srinivasan A., Liu Zheng, Kainer K.U., Hort N. Influences of Y additions on the hot tearing susceptibility of Mg-1.5wt.%Zn alloys. *Materials Science Forum*, 2013, vol. 765, pp. 306–310. DOI: [10.4028/www.scientific.net/MSF.765.306](https://doi.org/10.4028/www.scientific.net/MSF.765.306).
 17. Liu Zheng, Zhang Si-bo, Mao Ping-li, Wang Feng. Effects of Y on hot tearing susceptibility of Mg–Zn–Y–Zr alloys. *Transactions of Nonferrous Metals Society of China*, 2014, vol. 24, no. 4, pp. 907–914. DOI: [10.1016/S1003-6326\(14\)63142-3](https://doi.org/10.1016/S1003-6326(14)63142-3).
 18. Wang Zhi, Song Jiangfeng, Huang Yuanding, Srinivasan A., Liu Zheng, Kainer K.U., Hort N. An Investigation on Hot Tearing of Mg-4.5Zn-(0.5Zr) Alloys with Y Additions. *Metallurgical and Materials Transactions A*, 2015, vol. 46, pp. 2108–2118. DOI: [10.1007/s11661-015-2755-1](https://doi.org/10.1007/s11661-015-2755-1).
 19. Liu Shimeng, Wei Ziqi, Liu Zheng, Mao Pingli, Wang Feng, Wang Zhi, Zhou Le, Yin Xiunan. Effect of Zn content on hot tearing susceptibility of LPSO enhanced Mg–Zn_x–Y₂–Zr_{0.06} alloys with different initial mold temperatures. *Journal of Alloys and Compounds*, 2022, vol. 904, article number 163963. DOI: [10.1016/j.jallcom.2022.163963](https://doi.org/10.1016/j.jallcom.2022.163963).
 20. Wang Yeshuang, Wang Qudong, Wu Guohua, Zhu Yanping, Ding Wenjiang. Hot-tearing susceptibility of Mg–9Al–xZn alloy. *Materials Letters*, 2002, vol. 57, no. 4, pp. 929–934. DOI: [10.1016/S0167-577X\(02\)00898-4](https://doi.org/10.1016/S0167-577X(02)00898-4).
 21. Li Bingcheng, Zhang Jing, Ye Fawang, Tang R., Dong Quan, Chen Jianhao. An approach to studying the hot tearing mechanism of alloying elements in ternary Mg–Zn–Al alloys. *Journal of Materials Processing Technology*, 2023, vol. 317, article number 117980. DOI: [10.1016/j.jmatprotec.2023.117980](https://doi.org/10.1016/j.jmatprotec.2023.117980).
 22. Du Xudong, Wang Feng, Wang Zhi, Zhou Le, Wei Ziqi, Liu Zheng, Mao Pingli. Effect of Ca/Al ratio on hot tearing susceptibility of Mg–Al–Ca alloy. *Journal of Alloys and Compounds*, 2022, vol. 911, article number 165113. DOI: [10.1016/j.jallcom.2022.165113](https://doi.org/10.1016/j.jallcom.2022.165113).
 23. Glavatskikh M.V., Barkov R.Yu., Gorlov L.E., Khomutov M.G., Pozdniakov A.V. Microstructure and Phase Composition of Novel Crossover Al–Zn–Mg–Cu–Zr–Y(Er) Alloys with Equal Zn/Mg/Cu Ratio and Cr Addition. *Metals*, 2024, vol. 14, no. 5, article number 547. DOI: [10.3390/met14050547](https://doi.org/10.3390/met14050547).
 24. Glavatskikh M.V., Barkov R.Yu., Gorlov L.E., Khomutov M.G., Pozdniakov A.V. Novel Cast and Wrought Al-3Zn-3Mg-3Cu-Zr-Y(Er) Alloys with Improved Heat Resistance. *Metals*, 2023, vol. 13, no. 5, article number 909. DOI: [10.3390/met13050909](https://doi.org/10.3390/met13050909).

СПИСОК ЛИТЕРАТУРЫ

1. Pan Fusheng, Yang Mingbo, Chen Xianhua. A Review on Casting Magnesium Alloys: Modification of Commercial Alloys and Development of New Alloys // *Journal of Materials Science & Technology*. 2016. Vol. 32. № 12. P. 1211–1221. DOI: [10.1016/j.jmst.2016.07.001](https://doi.org/10.1016/j.jmst.2016.07.001).
2. Xie Hecong, Zhao Hua, Guo Xin, Li Yongfeng, Hu Hengrui, Song Jiangfeng, Jiang Bin, Pan Fusheng. Recent progress on cast magnesium alloy and components // *Journal of Materials Science*. 2024. Vol. 59. P. 9969–10002. DOI: [10.1007/s10853-024-09459-x](https://doi.org/10.1007/s10853-024-09459-x).
3. Новиков И.И. Горячеломкость цветных металлов и сплавов. М.: Наука, 1966. 299 с.
4. Eskin D.G., Suyitno, Katgerman L. Mechanical properties in the semi-solid state and hot tearing of aluminium alloys // *Progress in Materials Science*. 2004. Vol. 49. № 5. P. 629–711. DOI: [10.1016/S0079-6425\(03\)00037-9](https://doi.org/10.1016/S0079-6425(03)00037-9).
5. Zolotarevskiy V.S., Pozdniakov A.V., Khvan A.V. Thermodynamic Calculations of the Effective Solidification Range and Its Relation to Hot Cracking of Aluminum-Based Ternary Alloys // *Russian Journal of Non-Ferrous Metals*. 2011. Vol. 52. № 1. P. 50–55. DOI: [10.3103/S1067821211010275](https://doi.org/10.3103/S1067821211010275).
6. Zolotarevskiy V.S., Pozdniakov A.V., Kanakidi Ya.Yu. Relation between the Full and effective solidification ranges and the hot cracking of multicomponent aluminum-based alloys // *Russian Journal of Non-Ferrous Metals*. 2012. Vol. 53. № 5. P. 392–398. DOI: [10.3103/S1067821212050148](https://doi.org/10.3103/S1067821212050148).
7. Zolotarevskiy V.S., Pozdniakov A.V., Churyumov A.Yu. Search for promising compositions for developing new multiphase casting alloys based on Al–Cu–Mg matrix using thermodynamic calculations and mathematic simulation // *Physics of Metals and Metallography*. 2012. Vol. 113. № 11. P. 1052–1060. DOI: [10.1134/S0031918X12110154](https://doi.org/10.1134/S0031918X12110154).
8. Song Jiangfeng, Pan Fusheng, Jiang Bin, Atrens A., Zhang Ming-Xing, Lu Yung. A review on hot tearing of magnesium alloys // *Journal of Magnesium and Alloys*. 2016. Vol. 4. № 3. P. 151–172. DOI: [10.1016/j.jma.2016.08.003](https://doi.org/10.1016/j.jma.2016.08.003).
9. Bai Shengwei, Wang Feng, Du Xudong, Wang Zhi, Zhou Le, Wei Ziqi, Mao Pingli, Li Jinwei. Reduced hot

- tearing susceptibility of Mg-4Zn-1.5Ca-xY-0.3Zr alloy by introducing intergranular bridging secondary phases // Journal of Alloys and Compounds. 2025. Vol. 1014. Article number 178663. DOI: [10.1016/j.jallcom.2025.178663](https://doi.org/10.1016/j.jallcom.2025.178663).
10. Zhong Honggang, Lin Zenghuang, Han Qingyou, Song Jiangfeng, Chen Meicheng, Chen Xiangru, Li Lijuan, Zhai Qijie. Hot tearing behavior of AZ91D magnesium alloy // Journal of Magnesium and Alloys. 2024. Vol. 12. № 8. P. 3431–3440. DOI: [10.1016/j.jma.2023.02.010](https://doi.org/10.1016/j.jma.2023.02.010).
 11. Zhen Zisheng, Hort N., Huang Yuan Ding, Petri N., Utke O., Kainer K.U. Quantitative Determination on Hot Tearing in Mg–Al Binary Alloys // Materials Science Forum. 2009. Vol. 618-619. P. 533–540. DOI: [10.4028/www.scientific.net/MSF.618-619.533](https://doi.org/10.4028/www.scientific.net/MSF.618-619.533).
 12. Easton M.A., Gibson M.A., Zhu Suming, Abbott T.B. An A Priori Hot-Tearing Indicator Applied to Die-Cast Magnesium-Rare Earth Alloys // Metallurgical and Materials Transactions A. 2014. Vol. 45. P. 3586–3595. DOI: [10.1007/s11661-014-2272-7](https://doi.org/10.1007/s11661-014-2272-7).
 13. Li Tianyu, Lin Zenghuang, Su Chenxi, Gu Guangqi, Wang Hao, Li Lijuan, Zhong Honggang, Han Qingyou, Zhai Qijie. A method for predicting hot tearing during alloy solidification and its application in AZ91D magnesium alloy // Engineering Failure Analysis. 2025. Vol. 169. Article number 109194. DOI: [10.1016/j.engfailanal.2024.109194](https://doi.org/10.1016/j.engfailanal.2024.109194).
 14. Gan Wei Min, Huang Yuan Ding, Wang Zhi, Hort N., Hofmann M. Residual stresses near the hot sprues of as-cast Mg–Zn alloys investigated by stress-spec neutron diffractometer // Materials Science Forum. 2014. Vol. 768-769. P. 428–432. DOI: [10.4028/www.scientific.net/MSF.768-769.428](https://doi.org/10.4028/www.scientific.net/MSF.768-769.428).
 15. Gunde P., Schiffl A., Uggowitz P.J. Influence of yttrium additions on the hot tearing susceptibility of magnesium–zinc alloys // Materials Science and Engineering: A. 2010. Vol. 527. № 26. P. 7074–7079. DOI: [10.1016/j.msea.2010.07.086](https://doi.org/10.1016/j.msea.2010.07.086).
 16. Wang Zhi, Huang Yuan Ding, Srinivasan A., Liu Zheng, Kainer K.U., Hort N. Influences of Y additions on the hot tearing susceptibility of Mg-1.5wt.%Zn alloys // Materials Science Forum. 2013. Vol. 765. P. 306–310. DOI: [10.4028/www.scientific.net/MSF.765.306](https://doi.org/10.4028/www.scientific.net/MSF.765.306).
 17. Liu Zheng, Zhang Si-bo, Mao Ping-li, Wang Feng. Effects of Y on hot tearing susceptibility of Mg–Zn–Y–Zr alloys // Transactions of Nonferrous Metals Society of China. 2014. Vol. 24. № 4. P. 907–914. DOI: [10.1016/S1003-6326\(14\)63142-3](https://doi.org/10.1016/S1003-6326(14)63142-3).
 18. Wang Zhi, Song Jiangfeng, Huang Yuanding, Srinivasan A., Liu Zheng, Kainer K.U., Hort N. An Investigation on Hot Tearing of Mg-4.5Zn-(0.5Zr) Alloys with Y Additions // Metallurgical and Materials Transactions A. 2015. Vol. 46. P. 2108–2118. DOI: [10.1007/s11661-015-2755-1](https://doi.org/10.1007/s11661-015-2755-1).
 19. Liu Shimeng, Wei Ziqi, Liu Zheng, Mao Pingli, Wang Feng, Wang Zhi, Zhou Le, Yin Xiunan. Effect of Zn content on hot tearing susceptibility of LPSO enhanced Mg–Znx–Y₂–Zr_{0.06} alloys with different initial mold temperatures // Journal of Alloys and Compounds. 2022. Vol. 904. Article number 163963. DOI: [10.1016/j.jallcom.2022.163963](https://doi.org/10.1016/j.jallcom.2022.163963).
 20. Wang Yeshuang, Wang Qudong, Wu Guohua, Zhu Yanping, Ding Wenjiang. Hot-tearing susceptibility of Mg–9Al–xZn alloy // Materials Letters. 2002. Vol. 57. № 4. P. 929–934. DOI: [10.1016/S0167-577X\(02\)00898-4](https://doi.org/10.1016/S0167-577X(02)00898-4).
 21. Li Bingcheng, Zhang Jing, Ye Fawang, Tang R., Dong Quan, Chen Jianhao. An approach to studying the hot tearing mechanism of alloying elements in ternary Mg–Zn–Al alloys // Journal of Materials Processing Technology. 2023. Vol. 317. Article number 117980. DOI: [10.1016/j.jmatprotec.2023.117980](https://doi.org/10.1016/j.jmatprotec.2023.117980).
 22. Du Xudong, Wang Feng, Wang Zhi, Zhou Le, Wei Ziqi, Liu Zheng, Mao Pingli. Effect of Ca/Al ratio on hot tearing susceptibility of Mg–Al–Ca alloy // Journal of Alloys and Compounds. 2022. Vol. 911. Article number 165113. DOI: [10.1016/j.jallcom.2022.165113](https://doi.org/10.1016/j.jallcom.2022.165113).
 23. Glavatskikh M.V., Barkov R.Yu., Gorlov L.E., Khomutov M.G., Pozdniakov A.V. Microstructure and Phase Composition of Novel Crossover Al–Zn–Mg–Cu–Zr–Y(Er) Alloys with Equal Zn/Mg/Cu Ratio and Cr Addition // Metals. 2024. Vol. 14. № 5. Article number 547. DOI: [10.3390/met14050547](https://doi.org/10.3390/met14050547).
 24. Glavatskikh M.V., Barkov R.Yu., Gorlov L.E., Khomutov M.G., Pozdniakov A.V. Novel Cast and Wrought Al-3Zn-3Mg-3Cu-Zr-Y(Er) Alloys with Improved Heat Resistance // Metals. 2023. Vol. 13. № 5. Article number 909. DOI: [10.3390/met13050909](https://doi.org/10.3390/met13050909).

Расчет эффективного интервала кристаллизации и его связь с горячеломкостью сплавов на основе систем Mg–Al и Mg–Zn

Поздняков Андрей Владимирович, кандидат технических наук, доцент

Университет науки и технологий МИСИС, Москва (Россия)

E-mail: pozdniakov@misis.ru

ORCID: <https://orcid.org/0000-0002-5975-4849>

Поступила в редакцию 05.02.2025

Пересмотрена 19.02.2025

Принята к публикации 27.02.2025

Аннотация: Магниево-цинковые сплавы систем Mg–Al и Mg–Zn имеют широкий эффективный интервал кристаллизации (ЭИК) и, как следствие, склонны к горячеломкости при литье. Существует несколько методик анализа и расчета горячеломкости магниевых сплавов, но они являются очень трудоемкими. В связи с этим целью исследования – разработать модель расчета показателя горячеломкости (ПГ) по величине расчетного эффективного интервала

кристаллизации, установив и проанализировав их связь в двойных и многокомпонентных сплавах на основе систем Mg–Al и Mg–Zn. Расчет ЭИК проведен с использованием программы Thermo-Calc (база данных TTMG3). ЭИК рассчитывался как разница между температурой образования заданного количества твердых фаз и температурой неравновесного солидуса. Показана хорошая корреляция рассчитанных значений ЭИК с ПГ как в двойных, так и в многокомпонентных магниевых сплавах. В сплавах системы Mg–Al расчетные зависимости ЭИК при 90 % твердых фаз (ЭИК₉₀) показывают наилучшую корреляцию с экспериментальными значениями ПГ. В двойных сплавах системы Mg–Zn наблюдается качественно такая же зависимость. Однако четкой корреляции между ЭИК и ПГ не отмечено. Наиболее близкий характер демонстрируют зависимости ЭИК₆₅ и ЭИК₈₀. По связи ПГ и ЭИК рассмотренные многокомпонентные сплавы в первом приближении разделены на 2 группы: первая – сплавы системы Mg–Al–Zn, вторая – Mg–Zn–Zr и Mg–Nd–Zr. В пределах этих групп зависимость ПГ и ЭИК имеет близкий к линейному характер. Для описания зависимости всех сплавов можно применить одно уравнение при условии использования в расчетах ЭИК₆₅ для сплавов системы Mg–Al–Zn и ЭИК₉₀ для сплавов систем Mg–Zn–Zr и Mg–Nd–Zr. Предложенная модель позволит легко и быстро произвести расчет ПГ, что весьма актуально при разработке новых высокотехнологичных магниевых сплавов.

Ключевые слова: магниевые сплавы; горячеломкость; эффективный интервал кристаллизации; термодинамические расчеты; неравновесная кристаллизация.

Для цитирования: Поздняков А.В. Расчет эффективного интервала кристаллизации и его связь с горячеломкостью сплавов на основе систем Mg–Al и Mg–Zn // Frontier Materials & Technologies. 2025. № 1. С. 59–68. DOI: 10.18323/2782-4039-2025-1-71-5.

Effect of erbium and hafnium microalloying on the formation of Al₃Sc particles in aluminium alloy with a high magnesium content

Aleksandr A. Ragazin^{1,4}, engineer

of Aviation Materials Study Industrial Research Laboratory (ONIL-4)

Evgeny V. Aryshenskiy^{*2,5}, Doctor of Sciences (Engineering), PhD, Associate Professor, chief researcher of Scientific Research Department

Vladimir Yu. Aryshenskiy^{1,6}, Doctor of Sciences (Engineering), Professor, chief researcher of Aviation Materials Study Industrial Research Laboratory (ONIL-4)

Dmitry Yu. Rasposienko^{3,7}, PhD (Engineering), senior researcher of the Laboratory of Non-ferrous Alloys

Sergey V. Konovalov^{1,2,8}, Doctor of Sciences (Engineering), Professor, chief researcher of Aviation Materials Study Industrial Research Laboratory (ONIL-4), Pro-rector for Research and Innovative Activities

Inzil D. Bakhtegareev^{1,9}, master

¹Academician S.P. Korolev Samara National Research University, Samara (Russia)

²Siberian State Industrial University, Novokuznetsk (Russia)

³M.N. Mikheev Institute of Metal Physics of the Ural Branch of RAS, Yekaterinburg (Russia)

*E-mail: arishenskiy_ev@sibsiu.ru

⁴ORCID: <https://orcid.org/0000-0002-6762-7436>

⁵ORCID: <https://orcid.org/0000-0003-3875-7749>

⁶ORCID: <https://orcid.org/0000-0001-6869-4764>

⁷ORCID: <https://orcid.org/0000-0002-7670-9054>

⁸ORCID: <https://orcid.org/0000-0003-4809-8660>

⁹ORCID: <https://orcid.org/0009-0004-3081-9049>

Received 07.10.2024

Revised 27.11.2024

Accepted 04.02.2025

Abstract: The paper studies the effect of hafnium and erbium additives on the microstructure formation during heat treatment of aluminium alloys with a high magnesium content additionally alloyed with scandium and zirconium. For the study, ingots of aluminium alloys with a high content of magnesium alloyed with scandium, erbium and hafnium with a content in the ranges of 0.03–0.16 % and 0.05–0.16 %, respectively, were produced by casting in a steel chill mould. After casting, the samples were treated with heat at a temperature of 370 and 440 °C with a holding time of 2 to 96 h. Changes in microhardness depending on the heat treatment were studied. For 1590-3 and 1590-4 alloys in the as-cast condition and after heat treatment at a temperature of 440 °C for 2 and 48 h, the fine microstructure and coarse intermetallic compounds were studied using transmission microscopy. The study found that additions of hafnium and erbium lead to an increase in microhardness due to a decrease in the size and an increase in the number of Al₃Sc nanoparticles. After heat treatment at a temperature of 440 °C for 4 h, Al₃Sc particles of the same size (8 nm) and density precipitate in all the alloys under study. However, with an increase in the holding time in the alloy with a lower hafnium content and a higher erbium content, the particle size increases by 2 times compared to the particles of the alloy where the hafnium content is higher and the erbium content is low.

Keywords: aluminium alloys; microalloying; scandium; hafnium; erbium; formation of Al₃Sc particles; microhardness; microstructure; nanoparticles.

Acknowledgments: The study was supported by the grant of the Russian Science Foundation No. 22-19-00810, <https://rscf.ru/project/22-19-00810/>.

For citation: Ragazin A.A., Aryshenskiy E.V., Aryshenskiy V.Yu., Rasposienko D.Yu., Konovalov S.V., Bakhtegareev I.D. Effect of erbium and hafnium microalloying on the formation of Al₃Sc particles in aluminium alloy with a high magnesium content. *Frontier Materials & Technologies*, 2025, no. 1, pp. 69–80. DOI: 10.18323/2782-4039-2025-1-71-6.

INTRODUCTION

Aluminium alloys are in high demand in many advanced industries. Among them, the Al–Mg alloys stand out characterised by lower weight, increased strength and good corrosion resistance [1–3].

To improve the properties, various alloying components are added to the alloys. One of the most effective is scandium,

which increases strength due to the formation of reinforcing Al₃Sc nanoparticles with the L₁₂ structure, improves weldability, corrosion properties and helps modify the grain structure [4–6]. The efficiency of scandium alloying can be further increased by adding zirconium. Its introduction reduces the scandium concentration required for effective grain refinement during casting, and creates a shell promoting

© Ragazin A.A., Aryshenskiy E.V., Aryshenskiy V.Yu., Rasposienko D.Yu., Konovalov S.V., Bakhtegareev I.D., 2025

thermal stabilisation of Al₃Sc nanoparticles [6; 7]. Most often, combined scandium-zirconium microalloying is used in Al–Mg system alloys. This is explained by the fact that due to solid solution strengthening caused by magnesium, these alloys themselves have high strength characteristics [3]. One of such alloys is 1570 alloy with a scandium content of 0.25 %.

However, due to the high cost, reducing the scandium content from 0.25 to 0.15±0.1 % seems promising [8]. At the same time, reducing the scandium concentration will lead to a decrease in mechanical properties [9]. One way to solve this problem is the additional use of additives such as erbium and hafnium. Erbium helps to increase the number and rate of formation of Al₃Sc particles. This occurs because erbium, having a higher diffusion coefficient than scandium, forms Al₃Er nanoparticles with aluminium with an L₁₂ structure, which are also coherent in the aluminium matrix [10; 11]. Due to the solubility of scandium in erbium, these particles serve as a nucleus for Al₃Sc, actually being their core [9].

Hafnium partially dissolves in Al₃Sc particles, creating a shell around them and thermally stabilising them due to a lower diffusion coefficient. Moreover, hafnium additives, like zirconium, increase modifications of the cast structure [12], thereby increasing mechanical properties.

However, the combined effect of erbium and hafnium on Al₃Sc particles has not been studied previously. There are only studies of the effect of erbium and hafnium on Al₃Sc separately. As a rule, studies were carried out for pure aluminium and only in some cases for high-magnesium alloys, which have become widespread in industry [13–15]. Moreover, in the case of the effect of hafnium, studies were carried out with a scandium content of 0.2 % [13; 15], while the effect of hafnium may be different with a further decrease in the scandium concentration.

The aim of this work is to study the influence of erbium and hafnium content on the formation of the microstructure, and mechanical properties of high-magnesium aluminium alloys sparingly alloyed with scandium during their thermomechanical processing.

METHODS

A new aluminium high-magnesium 1590 alloy sparingly doped with scandium, microalloyed both with scandium and zirconium and with erbium and hafnium [16] was selected for the study. The Er and Hf content in this alloy varies in the ranges of 0.03–0.16 wt. % and 0.05–0.16 wt. %, respectively. By changing the content of elements in these ranges, it is possible to study the effect of their concentration on the formation of Al₃Sc particles. Four modifications of the 1590 alloy were selected to study the effect of the content of these elements on the formation of the microstructure. Table 1 presents the chemical composition of these modifications, which differ from each other in the content of erbium and hafnium.

To produce ingots of 1590, 1590-3, 1590-4 and 1599A alloys, UI-25P medium-frequency (1–20 kHz) induction furnace was used. The ingot dimensions were 20×40×400 mm. The ingots were cast in a steel chill mould and then cooled in water. The cast ingot weight was 5 kg. The following materials were used as a charge for the alloy: A85 grade aluminium, MG90 grade magnesium, alloying elements of Al–Sc₂, Al–Zr₅, Al–Hf₂, Al–Er₅ grades and Mn90Al10 grade alloying tablets. First, aluminium was loaded and melted. After the aluminium melted and the temperature reached 730 °C, slag was removed from the melt surface. Then the melt was heated to 770–790 °C and the AlSc₂, AlZr₅, Al–Hf₂, Al–Er₅ alloying elements were added in portions weighing no more than 300 g, followed by stirring and holding the melt for 5 min. After adding the entire calculated alloying elements, the melt was cooled to 750 °C and alloying components (Mg, Mn) were added according to the calculation results. The melt was stirred for 3 min, followed by heating to 740 °C, and a sample was taken for express analysis of the chemical composition of the melt. The chemical composition of the alloys (Table 1) was determined by the spectral method on an ARL 3460 atomic emission spectrometer (GOST 25086, GOST 7727, GOST 3221, ASTM E 716, ASTM E 1251) using the Al–Er₅ alloying element. The Er and Hf content in the ingot was determined by calculation due to the lack of standard samples.

Table 1. Chemical composition of the 1590, 1590-3, 1590-4, and 1599 alloys
Таблица 1. Химический состав сплавов 1590, 1590-3, 1590-4, 1599

Alloy	Weight content of elements, %								
	Si	Fe	Mn	Mg	Zn	Zr	Sc	Er*	Hf*
1590	0.04	0.07	0.41	5.57	0.21	0.1	0.14	0.1	0.05
1590-3	0.05	0.08	0.41	5.58	0.2	0.1	0.14	0.03	0.16
1590-4	0.05	0.08	0.41	5.53	0.21	0.1	0.14	0.1	0.1
1599	0.04	0.08	0.41	5.53	0.2	0.09	0.07	0.06	0.1

Note. * is content of Er, Hf according to calculation.

Примечание. * – содержание Er, Hf согласно расчету.

To study how heat treatment influences the formation of the microstructure and mechanical properties, the ingots were annealed in a muffle electric furnace at 370 and 440 °C with holding for 2, 4, 8, 24, 48, 72, 96 h and subsequent cooling in water to fix the supersaturated solid solution.

Microhardness measurements were carried out on an HV-1000 microhardness tester using the restored indentation method. The calculation was carried out in the Nexsys Image Expert Micro Hardness 2 software package in accordance with GOST 9450-76 "Measuring Microhardness by Indentation of Diamond Tips", a tetrahedral pyramid with a square base was used as a tip. A pre-prepared sample (with a polished surface) was installed using a special device that ensured that the working surface of the sample was parallel to the surface of the table. Then, under a load of 0.025 kgf, the tip dug into the sample surface, and was kept at the specified load for 10 s. To obtain correct microhardness values, ten measurements were taken for each sample, the distance between measurements was more than three diagonals of the indentation, the measurement locations were evenly distributed over the sample surface. Then, for each measurement, the actual microhardness values were calculated. The average was calculated for the obtained values and indicated on the graph with a confidence interval.

To study fine particles, transmission microscopy (hereinafter referred to as TEM) was used for the as-cast state and after annealing at 440 °C for 4 and 48 h. The studies were carried out on a Tecnai G2 30 (FEI Company, Holland, USA) high-resolution scanning transmission electron microscope (SEM), equipped with a GATAN scanning system, a system for mapping images in characteristic X-ray radiation, an EELS electron energy loss spectroscopy system and an EDAX energy-dispersive spectrometer for elemental analysis.

For electron microscopic studies, the samples were mechanically thinned by double-sided grinding on fine-grained grinding paper to a thickness of 40–60 μm. The resulting plates were electrolytically thinned to a thickness suitable for transmission in an electron microscope. After that, disks with a diameter of 3 mm were cut from the samples using the Ultrasonic Disk Cutter module. Electropolishing was carried out in a Struers Tenupol electrolytic thinning unit using the standard A2 electrolyte for aluminium alloys recommended by Struers. To clean the foil surface from carbon traces, and if necessary, for final thinning and increasing the viewing fields, a PIPS II ion-polishing device was used.

Identification of the phases precipitated during the decomposition of the supersaturated solid solution, was carried out by calculating their interplanar distances from additional reflections in the electron diffraction patterns and analysing their chemical composition. The calculated interplanar distances were compared with the data given in the international X-ray tables (JCPDS-ICDD). To identify the morphology and distribution pattern of each of the precipitated phases, dark-field images in additional reflections of these phases were analysed.

Considering the fact that TEM is a rather resource- and labor-intensive operation, only two alloys were studied by this method – 1590-3 and 1590-4. The 1590-4 alloy was chosen because it contains the minimum amount of erbium

and the maximum amount of hafnium, and the 1590-3 alloy – because it contains the median value of the concentrations of these elements.

RESULTS

In the as-cast state, the 1590-4 alloy demonstrates the maximum microhardness value (Fig. 1). The lowest microhardness values in the as-cast state were found in the 1590 alloy with a minimum hafnium content.

However, after 2 h of holding at a temperature of 370 °C, a sharp increase in microhardness is observed in 1590, 1590-3 and 1590-4 alloys. In the 1599 alloy, no changes in microhardness are observed; throughout the entire holding time, it varies within the range of 75–80 HV 0.25. In the 1590-3 alloy, after 8 h of holding, a sharp increase in microhardness begins to 109.2 HV 0.25, which after 24 h is replaced by a decrease down to 89 HV 0.25 at 96 h of holding. The 1590-4 alloy shows high microhardness values from 100.2 to 101.1 HV 0.25 during the first 48 h of holding, after which a smooth decrease in its values to 94.7 HV 0.25 occurs. The maximum microhardness value in the case of annealing of alloys at 370 °C is observed in the 1590-3 alloy after 24 h of holding and amounts to 109.2 HV 0.25.

It can be seen (Fig. 2) that in 1590, 1590-3, 1590-4 alloys after 2 h of heat treatment at a temperature of 440 °C there is a sharp increase in microhardness, in contrast to 1599 alloy. After 8 h of holding, the microhardness of the 1590-4 alloy drops. This is not observed in the 1590-3 alloy with a higher hafnium content, which, after 48 h of holding at a temperature of 440 °C, only increases the microhardness values to 97.1 HV 0.25, after which a gentle decline in microhardness occurs. However, in the 1590 alloy with an erbium content of 0.1 % and a hafnium content of 0.05 %, an increase in microhardness is observed compared to the 1590-4 alloy, where the erbium and hafnium content is equal and amounts to 0.1 %. The 1599 alloy shows the lowest microhardness values compared to other alloys. After holding for 24 h, it begins to grow. After 48 h of holding, it reaches its maximum values, after which it decreases.

In the structure of 1590-3 and 1590-4 alloys, the precipitation of Al₃Sc dispersoids was detected already in the as-cast state (Fig. 3). Apparently, they were formed during the decomposition of the supersaturated solid solution during cooling of the materials from the crystallisation temperature to room temperature. In the 1590-3 alloy, the Al₃Sc phase precipitates in the form of equiaxed particles with a diameter of 10–25 nm with a sufficiently high volume fraction and density of spatial distribution (Fig. 3). A comparative analysis of the TEM results for the 1590-3 and 1590-4 alloys in the as-cast state identified an increase in the volume fraction and density of spatial distribution of dispersoids (Fig. 4). It is worth noting that the 1590-4 alloy contains 0.07 % more erbium and 0.06 % less hafnium than the 1590-3 alloy. Thus, this change in the chemical composition affects the amount of nanoparticles.

Annealing for 4 h at a temperature of 440 °C led to an increase in the particle size. After treatment, the diameter of the smallest particles is 15 nm, which is 5 nm more

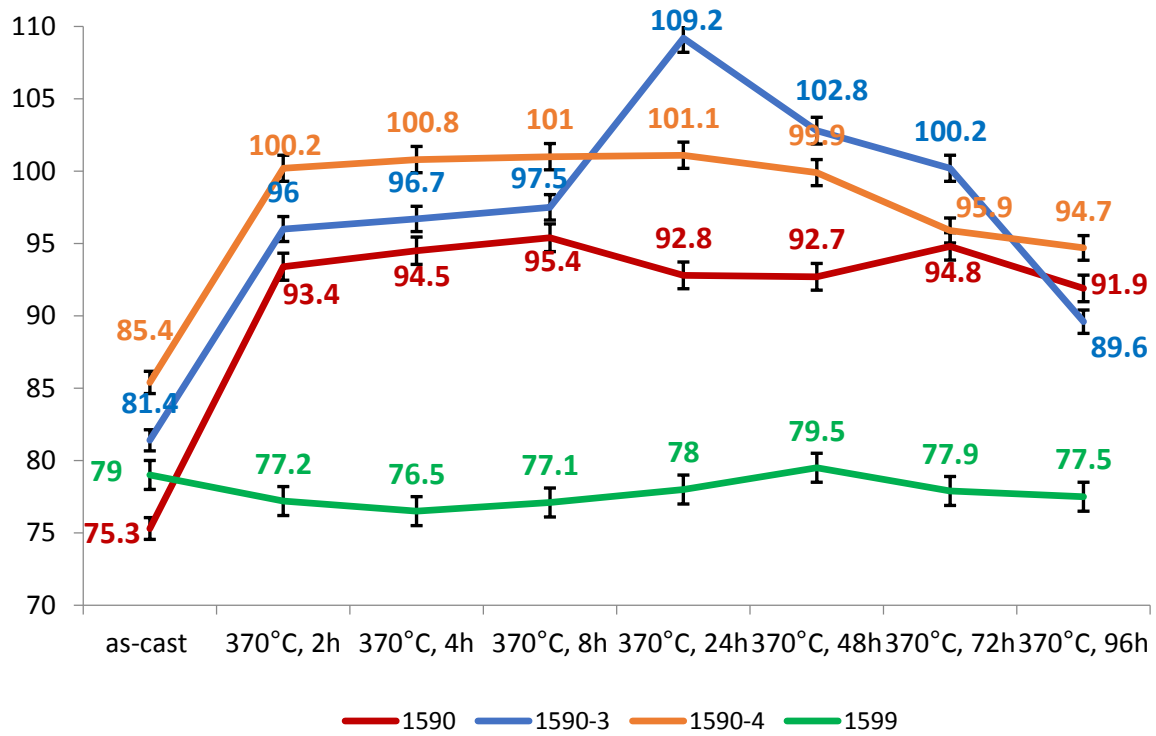


Fig. 1. Dynamics of changes in microhardness for alloys of 1590, 1590-3, 1590-4, 1599 grades in the as-cast state and after heat treatment at a temperature of 370 °C in the range from 2 to 96 h

Рис. 1. Динамика изменения микротвердости сплавов марок 1590, 1590-3, 1590-4, 1599 в литом состоянии и после термической обработки при температуре 370 °C и выдержке от 2 до 96 ч

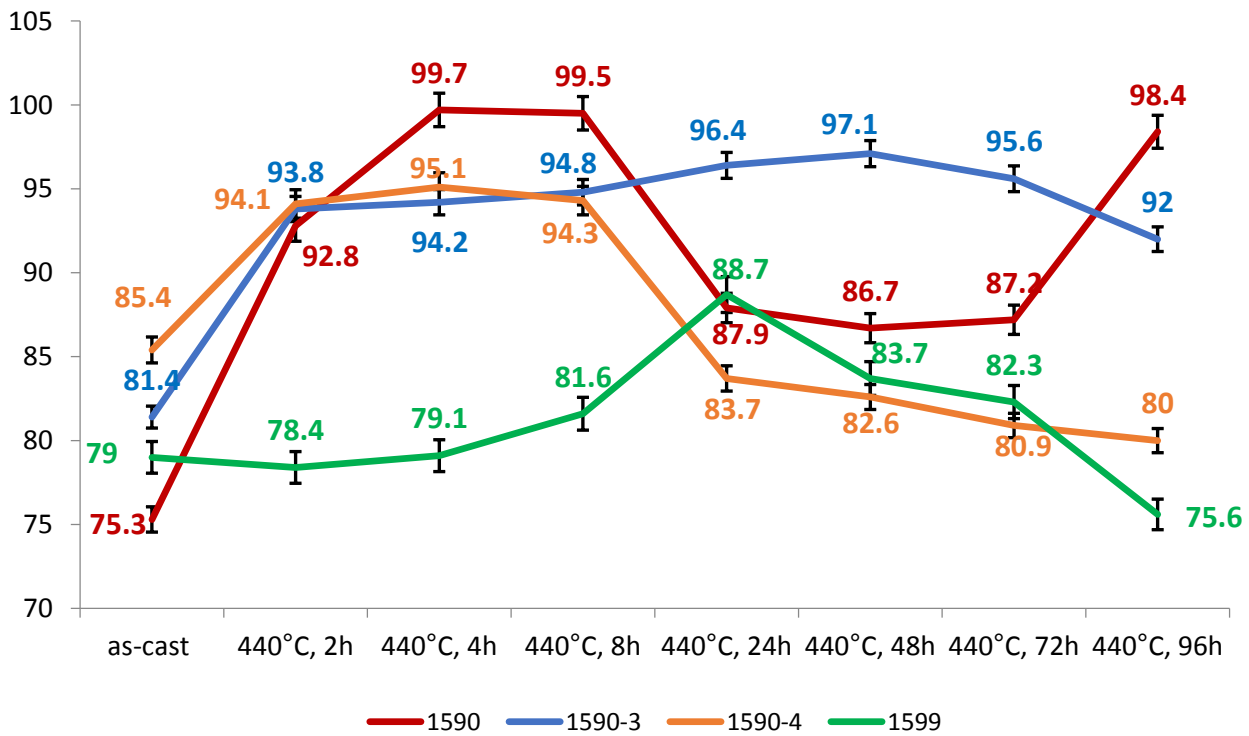


Fig. 2. Dynamics of changes in microhardness for alloys of 1590, 1590-3, 1590-4, 1599 grades in the as-cast state and after heat treatment at a temperature of 440 °C in the range from 2 to 96 h

Рис. 2. Динамика изменения микротвердости сплавов марок 1590, 1590-3, 1590-4, 1599 в литом состоянии и после термической обработки при температуре 440 °C и выдержке от 2 до 96 ч

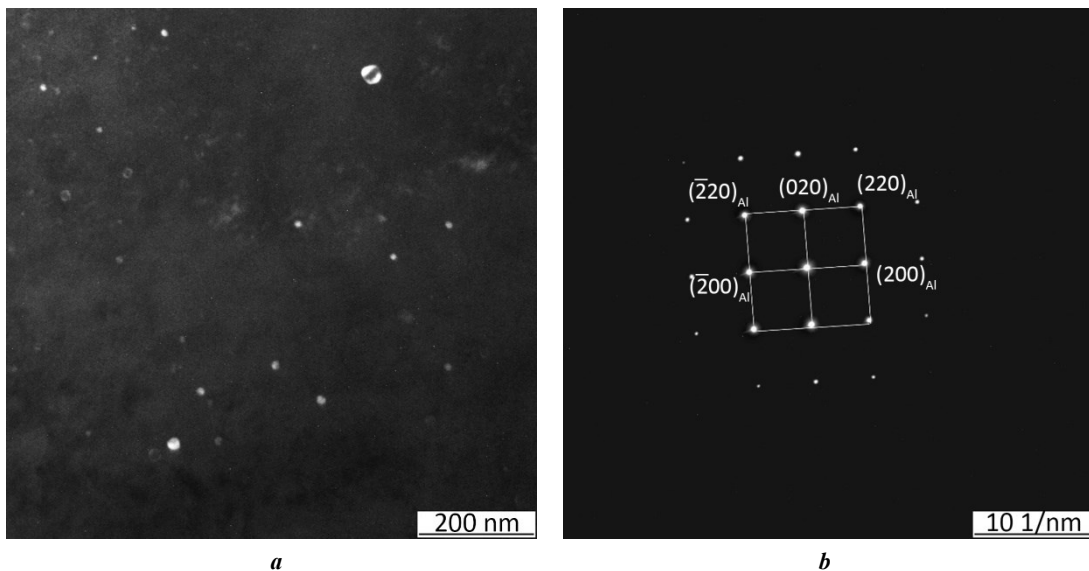


Fig. 3. Electron microscopic images of the microstructure of the 1590-3 alloy in the as-cast state:

a – dark-field image in the $(110)_{Al_3Sc}$ reflex;

b – micro-electron-diffraction pattern, $[100]_{Al}$ zone axis

Рис. 3. Электронно-микроскопические изображения микроструктуры сплава 1590-3 в литом состоянии:

a – темнопольное изображение в рефлексе $(110)_{Al_3Sc}$;

b – микроэлектронограмма, ось зоны $[100]_{Al}$

than in the as-cast state. At the same time, the diameter of the largest particles did not change and remained equal to 25 nm (Fig. 5).

The Al₃Sc particles formed during the heat treatment were characterised by a diameter of 6–8 nm, smaller than that of the dispersoids found in the as-cast state. The reason for the precipitation of more dispersed particles during

the heat treatment may be their lower formation temperature and lower saturation of the solid solution with Sc atoms.

Just as in the 1590-3 alloy, in the structure of the 1590-4 alloy sample annealed for 4 h at a temperature of 440 °C, two types of Al₃Sc particles are observed: more dispersed ones with a diameter of about 8 nm (apparently precipitated during annealing) constituting the majority, and rarer large

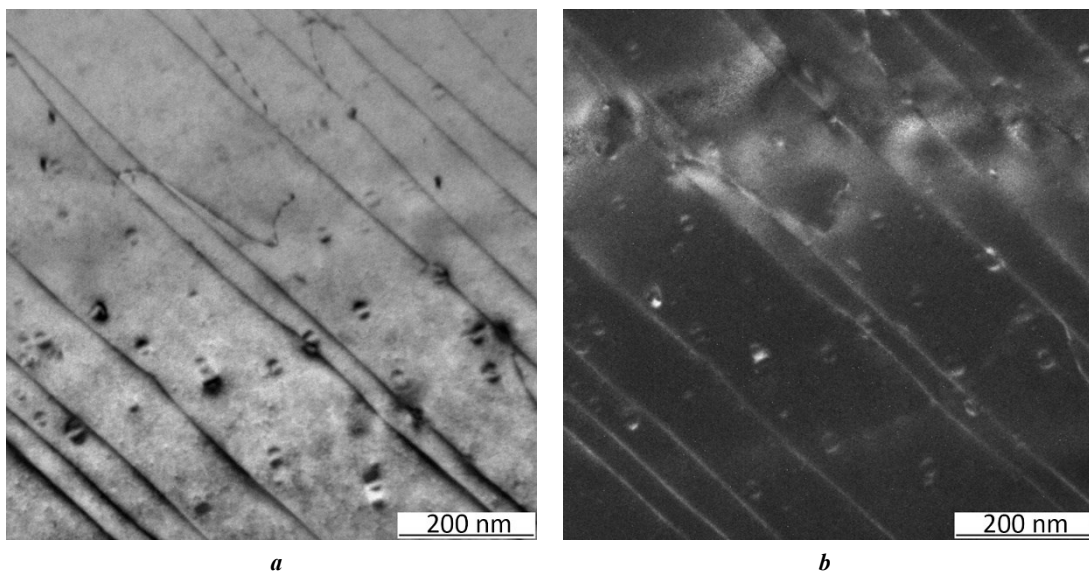


Fig. 4. Electron microscopic images of the microstructure of the 1590-4 alloy in the as-cast state:

a – light-field image; **b** – dark-field image in $(111)_{Al}$ reflex

Рис. 4. Электронно-микроскопические изображения микроструктуры сплава 1590-4 в литом состоянии:

a – светлопольное изображение; **b** – темнопольное изображение в рефлексе $(111)_{Al}$

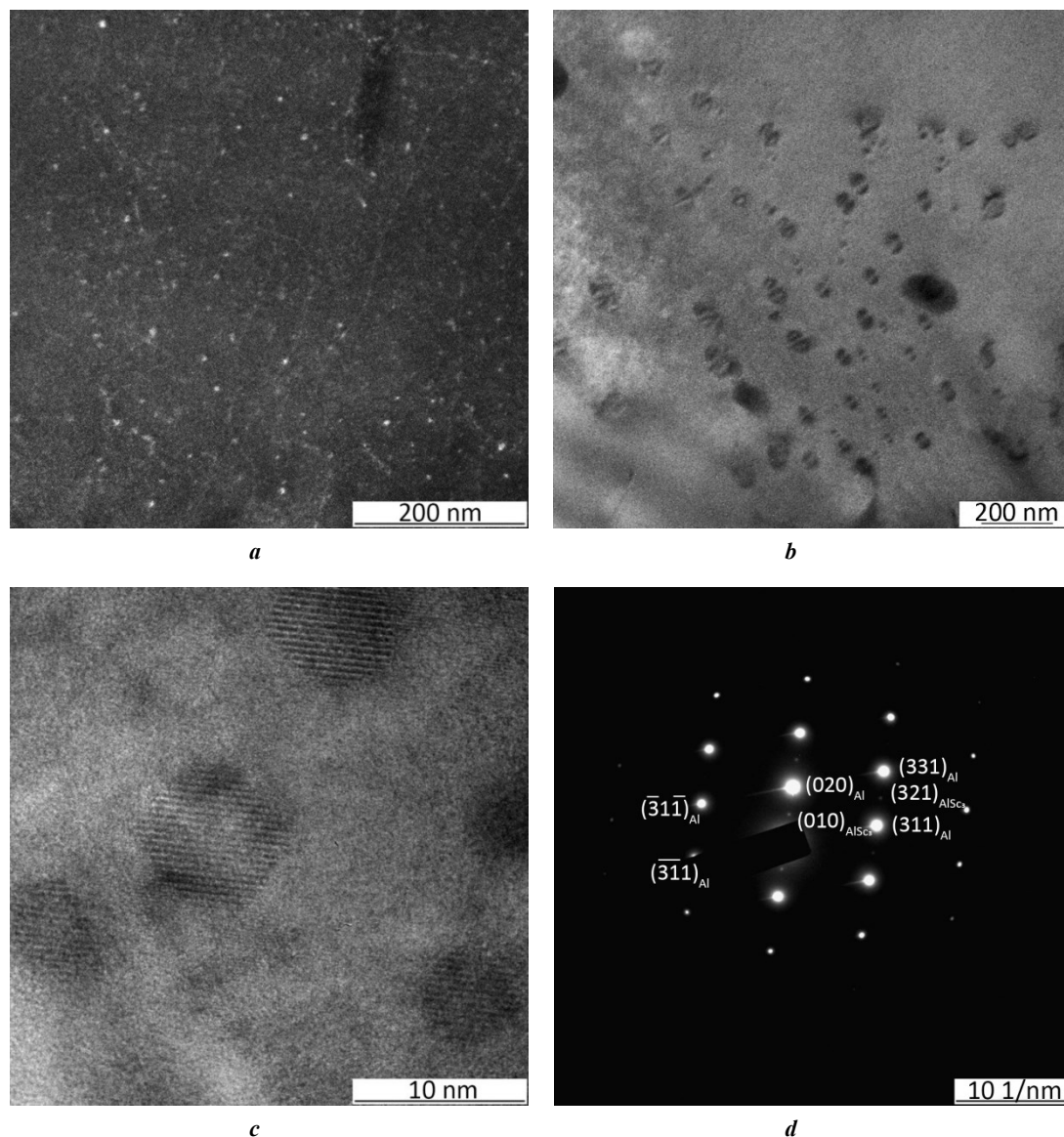


Fig. 5. Electron microscopic images of the microstructure of the 1590-3 alloy after annealing at 440 °C, 4 h:

a – dark-field image in the $(110)_{\text{Al}_3\text{Sc}}$ reflex; *b*, *c* – light-field images;

d – micro-electron-diffraction pattern, $[103]_{\text{Al}}$ zone axis

Рис. 5. Электронно-микроскопические изображения микроструктуры сплава 1590-3 после отжига при 440 °C в течение 4 ч:

a – темнопольное изображение в рефлексе $(110)_{\text{Al}_3\text{Sc}}$; *b*, *c* – светлопольные изображения;

d – микроэлектроннограмма, ось зоны $[103]_{\text{Al}}$

ones, mainly 15–25 nm in size (formed earlier during cooling of the ingot) (Fig. 6).

In the bright-field images, Al₆Mn plates up to 250 nm long and 100 nm wide were also identified with their distribution throughout the grain volume being non-uniform: in some areas, their clusters and alignment of particles along certain directions were observed (Fig. 6).

Increasing the duration of annealing at 440 °C to 48 h leads to an increase in the diameter of the most dispersed precipitates. The average size of dispersoids is about 15 nm, with the sizes of the largest particles remaining at the level of 25 nm (Fig. 7).

Particle coagulation contributes to their more uniform size distribution: the range of most of the observed dispersoids is 13–15 nm, and only single particles are charac-

terised by larger or smaller sizes. At the same time, the volume fraction and spatial distribution density of dispersoids remain high.

With an increase in the duration of annealing at 440 °C to 48 h, similar changes in the structure also occur in the 1590-4 alloy. After heat treatment in this mode, electron microscopic images show equiaxed dispersoids with sizes from 15 to 30 nm (Fig. 8).

A comparative analysis showed that changes in the chemical composition of the 1590-4 alloy lead to the precipitation of larger particles and a less uniform distribution of their sizes. Most dispersoids are characterised by a diameter in the range of 20–25 nm, however, more dispersed precipitates with sizes of 15 nm and more are also preserved, and particles with a diameter of 30 nm and more are also formed.

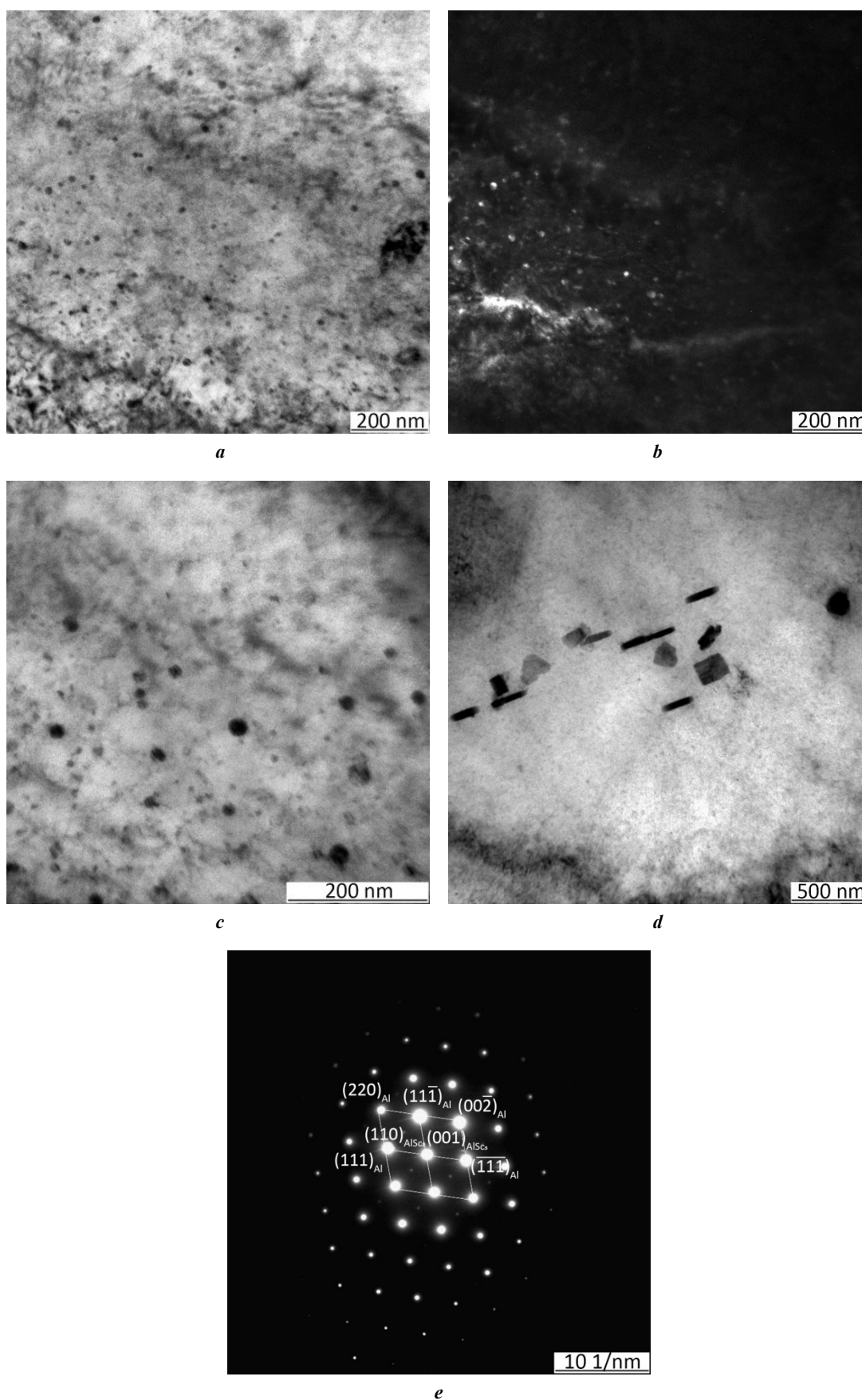


Fig. 6. Electron microscopic images of the microstructure of the 1590-4 alloy after annealing at 440 °C, 4 h:
a, c, d – light-field images; *b* – dark-field images in the $(110)_{Al_3Sc}$ reflex; *e* – micro-electron-diffraction pattern, $[110]_{Al}$ zone axis

Рис. 6. Электронно-микроскопические изображения микроструктуры сплава 1590-4 после отжига при 440 °C в течение 4 ч:

a, c, d – светлопольные изображения; *b* – темнопольное изображение в рефлексе $(110)_{Al_3Sc}$;
e – микроэлектронограмма, ось зоны $[110]_{Al}$

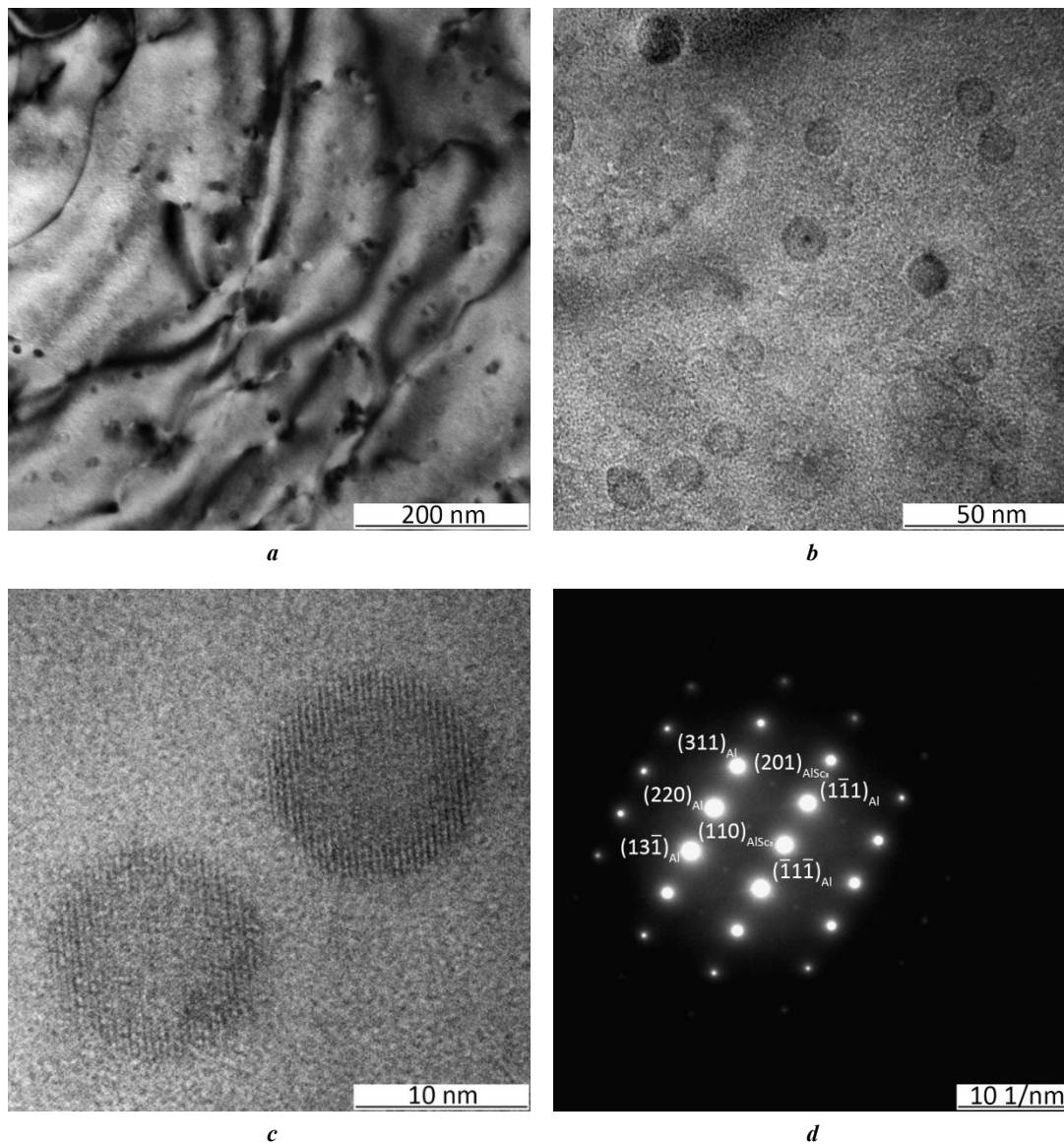


Fig. 7. Electron microscopic images of the microstructure of the 1590-3 alloy after annealing at 440 °C, 48 h: *a, b, c* – light-field images; *d* – micro-electron-diffraction pattern, $[112]_{Al}$ zone axis

Рис. 7. Электронно-микроскопические изображения микроструктуры сплава 1590-3 после отжига при 440 °C в течение 48 ч: *a, b, c* – светлопольные изображения; *d* – микроэлектрондиограмма, ось зоны $[112]_{Al}$

DISCUSSION

First, it should be noted that in both alloys studied using TEM, discontinuous precipitation of the supersaturated solid solution is observed. Discontinuous precipitation has a negative effect on the mechanical properties, since it leads to a decrease in the amount of scandium in the solid solution, which causes the decrease in the number of finer particles.

The particles formed during discontinuous precipitation can be either equiaxed or elongated. As a rule, they are either completely or partially coherent with the aluminium matrix [17–19]. However, their strengthening effect is not as high as that of particles formed during continuous precipitation [20]. In this case, the cause of discontinuous precipitation could be erbium, which accelerates the formation of Al₃Sc particles. This is also evidenced by the fact that with an increase in the erbium content from 0.03 to 0.10 %, the number and size of Al₃Sc particles increases.

The highest value of microhardness in the as-cast state for the 1590-4 alloy in Fig. 1 is explained by the fact that this alloy is maximally doped with hafnium and erbium with their total content of 0.2 %. Dissolving in the solid solution, hafnium and erbium cause maximum strengthening. The subsequent increase in microhardness observed in 1590, 1590-3 and 1590-4 alloys (Fig. 1) is explained by the fact that in these alloys, a precipitation of Al₃Sc type dispersoids occurs, which significantly increase their strength properties. The main reason that this increase does not occur in the 1599 alloy is the insufficient amount of Sc for the formation of finely dispersed strengthening Al₃(ScZr) particles. The main reason for the sharp increase in microhardness after 8 h of annealing of the 1590-3 alloy (Fig. 1) is the maximum precipitation of finely dispersed Al₃(ScZrHf) particles from the solid supersaturated solution, and the drop in microhardness after 24 h of annealing

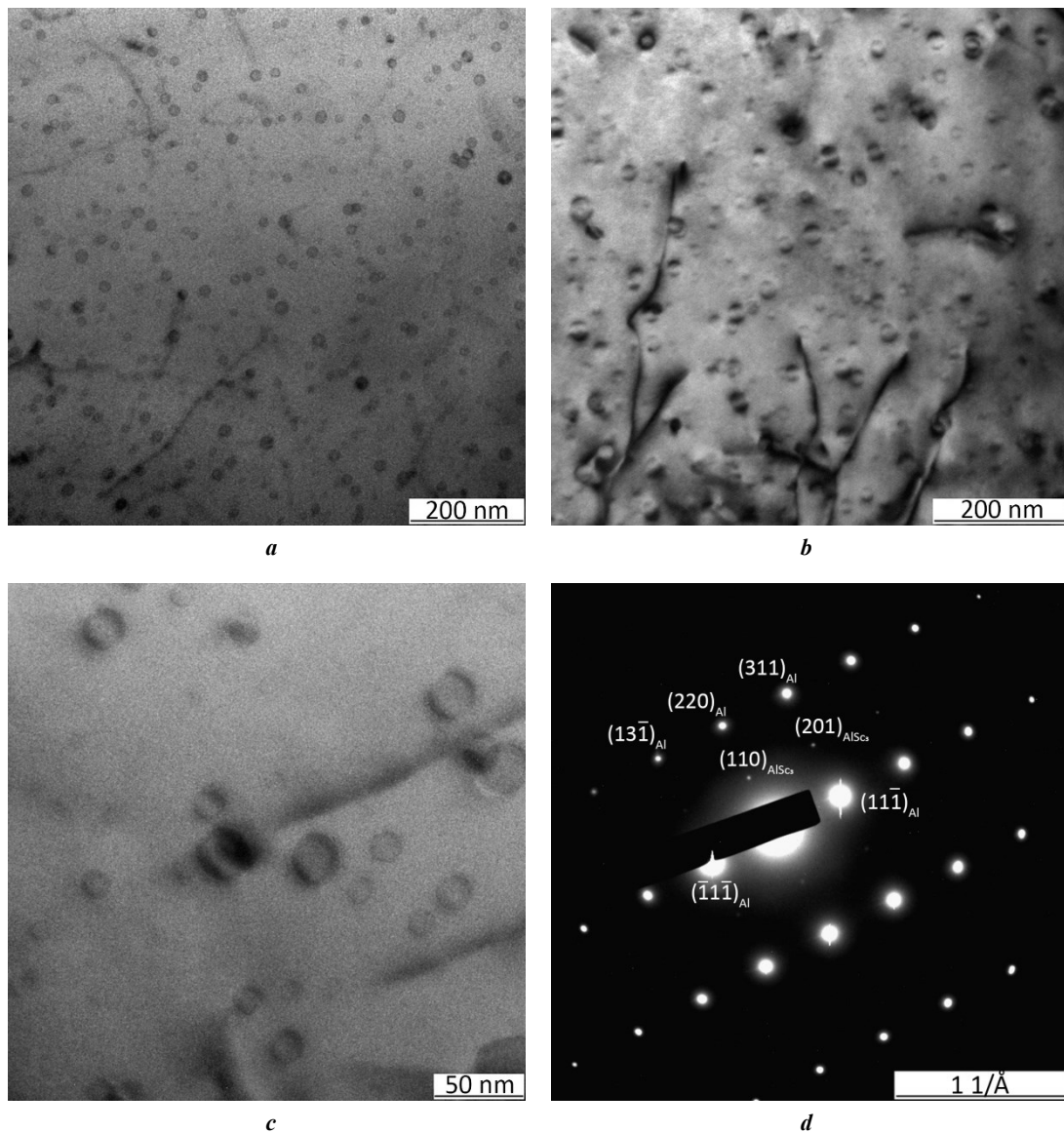


Fig. 8. Electron microscopic images of the microstructure of the 1590-4 alloy after annealing at 440 °C, 48 h: *a, b, c* – light-field images; *d* – micro-electron-diffraction pattern, $[112]_{Al}$ zone axis

Рис. 8. Электронно-микроскопические изображения микроструктуры сплава 1590-4 после отжига при 440 °C в течение 48 ч: *a, b, c* – светлопольные изображения; *d* – микроэлектронограмма, ось зоны $[112]_{Al}$

indicates the beginning of their coagulation process. The constancy of microhardness values during the first 48 h after holding of the 1590-4 alloy (Fig. 1) indicates the stability of finely dispersed particles in this range. A further decrease in the microhardness of the alloy indicates the beginning of the coagulation processes of these particles.

The differences in the change in microhardness in 1590, 1590-3, 1590-4 and 1599 alloys during the first 2 h of annealing at a temperature of 440 °C are explained by the fact that the first three alloys have a higher Sc content than the last one. Therefore, in 1590, 1590-3, 1590-4 alloys, the formation of Al₃Sc dispersoids occurs faster. The decrease in microhardness observed in the 1599 alloy after 48 h of holding occurs due to the low scandium content.

One should note that according to the microhardness measurement data and the results of the study using transmission microscopy, hafnium has a positive effect on

the mechanical properties, especially at a temperature of 440 °C. This is explained by the fact that Al₃Sc particles containing a larger amount of hafnium are more thermally stable. It is worth noting that active diffusion of hafnium begins to occur when heated above 400 °C [20]. This is why the effect of hafnium is more clearly visible at high temperatures. Based on the data on the change in microhardness, it is evident that a hafnium concentration of 0.07 % is insufficient to form Al₃Sc particles. A noticeable change in microhardness occurs only with a longer holding time. Therefore, with the addition of hafnium, the microhardness remains stable for at least the first 8 h at 440 °C. In alloys containing only scandium and zirconium, the microhardness at a temperature of 450 °C begins to decrease after several tens of minutes of holding [5]. One should note that in the present paper, unlike [5], both the thermal stability of nanoparticles and its effect on mechanical prop-

erties were studied. Based on the results of microhardness changes obtained in this study, one can conclude that the hafnium concentration of 0.44 % used in [13] is excessive, since 0.16 % of hafnium is sufficient to stabilise the microhardness for 96 h of holding.

It is worth noting that if the effect of hafnium on the formation of nanoparticles and microhardness is obvious, then the effect of erbium is not so clear. The growth of microhardness in the first 2 h of heating in all the studied alloys occurs with the same intensity, which indicates the absence of differences in the formation of nanoparticles. In this case, erbium affects the formation of nuclei. Such pattern is associated with the fact that the precipitation of Al₃Er nanoparticles occurs at lower temperatures [11]. Perhaps, a two-stage annealing scheme will be effective: with the first stage at 250–300 °C for the formation of Al₃Er particles and the second stage at 400–450 °C for the formation of a shell of Sc, Zr and Hf. Therefore, an obvious direction for further research is to study the effect of erbium on the formation of the microstructure and mechanical properties in this group of alloys during their two-stage annealing.

CONCLUSIONS

The results of the conducted studies revealed a positive effect of hafnium and erbium on the formation of the microstructure and mechanical properties of alloys sparingly alloyed with scandium. An increase in the erbium content in the alloys leads to an increase in microhardness during heat treatment in the modes of 370 °C, up to 24 h of holding, and 440 °C, up to 8 h of holding. With an increase in the temperature and annealing duration, coagulation of Al₃Sc particles occurs, while the particle sizes in the 1590-4 alloy with an increased erbium content increase by 2 times compared to the particle size in the 1590-3 alloy, where the hafnium content is maximum. It is worth noting that in alloys with a high hafnium content, a significant increase in microhardness occurs at a temperature of 440 °C after 8 h of holding, which is confirmed by the TEM results after heat treatment at 440 °C for 48 h. The main explanation for the smaller size of nanoparticles in the 1590-3 alloy is that hafnium forms a shell around the Al₃Sc particles, which slows down their growth at high heat treatment temperatures and long holding times and has a positive effect on microhardness.

REFERENCES

- Ibrokhimov S.Zh., Ganiev I.N., Eshov B.B. Hardness and strength of AMg4 alloy hardened with rare-earth metals (Sc, Y, La, Pr, Nd). *Vestnik Saratovskogo gosudarstvennogo tekhnicheskogo universiteta*, 2023, no. 1, pp. 74–82. EDN: [BATVYU](#).
- Kokovin P.L., Maltseva T.V. About the possibility of changing the technology for production of large-sized flat ingots from AMg3 aluminum alloy. *Tekhnologiya legkikh splavov*, 2024, no. 1, pp. 29–35. DOI: [10.24412/0321-4664-2024-1-29-35](#).
- Mondolfo L.F. *Struktura i svoystva alyuminievykh splavov* [Aluminium Alloys: Structure and Properties]. Moscow, Metallurgiya Publ., 1979. 639 p.
- Lei Zhiguo, Wen Shengping, Huang Hui, Wei Wu, Nie Zuoren. Grain refinement of aluminum and aluminum alloys by Sc and Zr. *Metals*, 2023, vol. 13, no. 4, article number 751. DOI: [10.3390/met13040751](#).
- Davydov V.G., Elagin V.I., Zakharov V.V., Rostoval D. Alloying aluminum alloys with scandium and zirconium additives. *Metal Science and Heat Treatment*, 1996, vol. 38, no. 7-8, pp. 347–352. DOI: [10.1007/bf01395323](#).
- Zakharov V.V. Alloying of industrial aluminum alloys with scandium. *Metal Science and Heat Treatment*, 2024, vol. 66, pp. 338–342. DOI: [10.1007/s11041-024-01056-8](#).
- Forbord B., Lefebvre W., Danoix F., Hallem H., Marthinsen K. Three dimensional atom probe investigation on the formation of Al₃(Sc, Zr)-dispersoids in aluminium alloys. *Scripta materialia*, 2004, vol. 51, no. 4, pp. 333–337. DOI: [10.1016/j.scriptamat.2004.03.033](#).
- Zakharov V.V., Filatov Yu.A. Aluminum alloys sparingly alloyed with scandium. *Tekhnologiya legkikh splavov*, 2021, no. 4, pp. 31–37. DOI: [10.24412/0321-4664-2021-4-31-37](#).
- Zakharov V.V., Fisenko I.A., Kunyavskaya T.M. Principles for creating aluminum-based alloys sparingly alloyed with scandium. *Metal Science and Heat Treatment*, 2024, vol. 66, pp. 294–298. DOI: [10.1007/s11041-024-01049-7](#).
- Karnesky R.A., Dunand D.C., Seidman D.N. Evolution of nanoscale precipitates in Al microalloyed with Sc and Er. *Acta Materialia*, 2009, vol. 57, no. 14, pp. 4022–4031. DOI: [10.1016/j.actamat.2009.04.034](#).
- Liu Xiaomin, Wang Qian, Zhao Chuan, Li Hongping, Wang Mingliang, Chen Dong, Wang Haowei. Formation of ordered precipitates in Al-Sc-Er-(Si/Zr) alloy from first-principles study. *Journal of Rare Earths*, 2021, vol. 39, no. 5, pp. 609–620. DOI: [10.1016/j.jre.2020.08.005](#).
- Zorin I.A., Aryshenskiy E.V., Drits A.M., Konovalov S.V., Komarov V.S. Metallurgy Effect of hafnium on cast microstructure in alloy 1570. *Izvestiya vysshikh uchebnykh zavedeniy. Tsvetnaya metallurgiya*, 2023, vol. 29, no. 1, pp. 56–65. DOI: [10.17073/0021-3438-2023-1-56-65](#).
- Hallem H., Lefebvre W., Forbord B., Danoix F., Marthinsen K. The formation of Al₃(Sc_xZr_yHf_{1-x-y})-dispersoids in aluminium alloys. *Materials Science and Engineering: A*, 2006, vol. 421, no. 1-2, pp. 154–160. DOI: [10.1016/j.msea.2005.11.063](#).
- Hallem H., Forbord B., Marthinsen K. Investigation of Al-Fe-Si alloys with additions of Hf, Sc and Zr. *Materials Forum*, 2004, vol. 28, pp. 825–831.
- Zorin I.A., Aryshenskiy E.V., Kudryavtsev E.A., Drits A.M., Konovalov S.V. The influence of hafnium on high-magnesium alloys doped with transition metals during heat treatment. *Frontier Materials & Technologies*, 2024, no. 1, pp. 29–36. DOI: [10.18323/2782-4039-2024-1-67-3](#).
- Drits A.M., Aryshenskiy V.Yu., Aryshenskiy E.V., Zakharov V.V. *Svarivaemyy termicheski ne uprochnyaemyy splav na osnove sistemy Al-Mg* [A thermally non-hardenable welded alloy based on the Al-Mg system], patent na izobretenie RF no. 2726520, 2020. 5 p.
- Norman A.F., Prangnell P.B., McEwen R.S. The solidification behaviour of dilute aluminium-scandium alloys.

- Acta materialia*, 1998, vol. 46, no. 16, pp. 5715–5732. DOI: [10.1016/S1359-6454\(98\)00257-2](https://doi.org/10.1016/S1359-6454(98)00257-2).
18. Blake N., Hopkins M.A. Constitution and age hardening of Al-Sc alloys. *Journal of Materials Science*, 1985, vol. 20, pp. 2861–2867. DOI: [10.1007/BF00553049](https://doi.org/10.1007/BF00553049).
 19. Aryshenskii E., Lapshov M., Hirsch J., Kononov S., Bazhenov V., Drits A., Zaitsev D. Influence of the small Sc and Zr additions on the as-cast microstructure of Al–Mg–Si alloys with excess silicon. *Metals*, 2021, vol. 11, no. 11, article number 1797. DOI: [10.3390/met11111797](https://doi.org/10.3390/met11111797).
 20. Røyset J., Ryum N. Scandium in aluminium alloys. *International Materials Reviews*, 2005, vol. 50, no. 1, pp. 19–44. DOI: [10.1179/174328005X14311](https://doi.org/10.1179/174328005X14311).
- ### СПИСОК ЛИТЕРАТУРЫ
1. Иброхимов С.Ж., Ганиев И.Н., Эшов Б.Б. Твердость и прочность сплава АМг4, легированного редкоземельными металлами (Sc, Y, La, Pr, Nd) // Вестник Саратовского государственного технического университета. 2023. № 1. С. 74–82. EDN: [BATVYU](https://doi.org/10.24412/0321-4664-2024-1-29-35).
 2. Коковин П.Л., Мальцева Т.В. О возможности изменения технологии получения крупногабаритных плоских слитков из алюминиевого сплава АМг3 // Технология легких сплавов. 2024. № 1. С. 29–35. DOI: [10.24412/0321-4664-2024-1-29-35](https://doi.org/10.24412/0321-4664-2024-1-29-35).
 3. Мондольфо Л.Ф. Структура и свойства алюминиевых сплавов. М.: Металлургия, 1979. 639 с.
 4. Lei Zhiguo, Wen Shengping, Huang Hui, Wei Wu, Nie Zuoren. Grain refinement of aluminum and aluminum alloys by Sc and Zr // *Metals*. 2023. Vol. 13. № 4. Article number 751. DOI: [10.3390/met13040751](https://doi.org/10.3390/met13040751).
 5. Давыдов В.Г., Елагин В.И., Захаров В.В., Ростова Т.Д. О легировании алюминиевых сплавов добавками скандия и циркония // *Металловедение и термическая обработка металлов*. 1996. № 8. С. 25–30. EDN: [MOVQJR](https://doi.org/10.1016/j.scriptamat.2004.03.033).
 6. Захаров В.В. Легирование промышленных алюминиевых сплавов скандием // *Металловедение и термическая обработка металлов*. 2024. № 6. С. 18–23. EDN: [EPOIUO](https://doi.org/10.24412/0321-4664-2021-4-31-37).
 7. Forbord B., Lefebvre W., Danoix F., Hallem H., Marthinsen K. Three dimensional atom probe investigation on the formation of Al₃(Sc, Zr)-dispersoids in aluminium alloys // *Scripta materialia*. 2004. Vol. 51. № 4. P. 333–337. DOI: [10.1016/j.scriptamat.2004.03.033](https://doi.org/10.1016/j.scriptamat.2004.03.033).
 8. Захаров В.В., Филатов Ю.А. Экономнолегированные скандием алюминиевые сплавы // *Технология легких сплавов*. 2021. № 4. С. 31–37. DOI: [10.24412/0321-4664-2021-4-31-37](https://doi.org/10.24412/0321-4664-2021-4-31-37).
 9. Захаров В.В., Фисенко И.А., Кунявская Т.М. Принципы создания сплавов на основе алюминия, экономнолегированных скандием // *Металловедение и термическая обработка металлов*. 2024. № 5. С. 39–43. EDN: [KPMAYK](https://doi.org/10.17073/0021-3438-2023-1-56-65).
 10. Karnesky R.A., Dunand D.C., Seidman D.N. Evolution of nanoscale precipitates in Al microalloyed with Sc and Er // *Acta Materialia*. 2009. Vol. 57. № 14. P. 4022–4031. DOI: [10.1016/j.actamat.2009.04.034](https://doi.org/10.1016/j.actamat.2009.04.034).
 11. Liu Xiaomin, Wang Qian, Zhao Chuan, Li Hongping, Wang Mingliang, Chen Dong, Wang Haowei. Formation of ordered precipitates in Al-Sc-Er-(Si/Zr) alloy from first-principles study // *Journal of Rare Earths*. 2021. Vol. 39. № 5. P. 609–620. DOI: [10.1016/j.jre.2020.08.005](https://doi.org/10.1016/j.jre.2020.08.005).
 12. Зорин И.А., Арышенский Е.В., Дриц А.М., Коновалов С.В., Комаров В.С. Влияние гафния на литую микроструктуру в сплаве 1570 // *Известия высших учебных заведений. Цветная металлургия*. 2023. Т. 29. № 1. С. 56–65. DOI: [10.17073/0021-3438-2023-1-56-65](https://doi.org/10.17073/0021-3438-2023-1-56-65).
 13. Hallem H., Lefebvre W., Forbord B., Danoix F., Marthinsen K. The formation of Al₃(Sc_xZr_yHf_{1-x-y})-dispersoids in aluminium alloys // *Materials Science and Engineering: A*. 2006. Vol. 421. № 1-2. P. 154–160. DOI: [10.1016/j.msea.2005.11.063](https://doi.org/10.1016/j.msea.2005.11.063).
 14. Hallem H., Forbord B., Marthinsen K. Investigation of Al-Fe-Si alloys with additions of Hf, Sc and Zr // *Materials Forum*. 2004. Vol. 28. P. 825–831.
 15. Зорин И.А., Арышенский Е.В., Кудрявцев Е.А., Дриц А.М., Коновалов С.В. Влияние гафния на высокомагниевого сплавы, легированные переходными металлами, при термической обработке // *Frontier Materials & Technologies*. 2024. № 1. С. 29–36. DOI: [10.18323/2782-4039-2024-1-67-3](https://doi.org/10.18323/2782-4039-2024-1-67-3).
 16. Дриц А.М., Арышенский В.Ю., Арышенский Е.В., Захаров В.В. Свариваемый термически не упрочняемый сплав на основе системы Al-Mg: патент на изобретение RU № 2726520, 2020. 5 с.
 17. Norman A.F., Prangnell P.B., McEwen R.S. The solidification behaviour of dilute aluminium-scandium alloys // *Acta materialia*. 1998. Vol. 46. № 16. P. 5715–5732. DOI: [10.1016/S1359-6454\(98\)00257-2](https://doi.org/10.1016/S1359-6454(98)00257-2).
 18. Blake N., Hopkins M.A. Constitution and age hardening of Al-Sc alloys // *Journal of Materials Science*. 1985. Vol. 20. P. 2861–2867. DOI: [10.1007/BF00553049](https://doi.org/10.1007/BF00553049).
 19. Aryshenskii E., Lapshov M., Hirsch J., Kononov S., Bazhenov V., Drits A., Zaitsev D. Influence of the small Sc and Zr additions on the as-cast microstructure of Al–Mg–Si alloys with excess silicon // *Metals*. 2021. Vol. 11. № 11. Article number 1797. DOI: [10.3390/met11111797](https://doi.org/10.3390/met11111797).
 20. Røyset J., Ryum N. Scandium in aluminium alloys // *International Materials Reviews*. 2005. Vol. 50. № 1. P. 19–44. DOI: [10.1179/174328005X14311](https://doi.org/10.1179/174328005X14311).

Влияние микролегирования эрбием и гафнием на формирование частиц Al₃Sc в алюминиевом сплаве с высоким содержанием магния

Рагазин Александр Алексеевич^{1,4}, инженер

отраслевой научно-исследовательской лаборатории авиационного материаловедения № 4 (ОНИЛ-4)

Арышенский Евгений Владимирович^{*2,5}, доктор технических наук, PhD, доцент,
главный научный сотрудник управления научных исследований

Арышенский Владимир Юрьевич^{1,6}, доктор технических наук, профессор,
главный научный сотрудник отраслевой научно-исследовательской лаборатории
авиационного материаловедения № 4 (ОНИЛ-4)

Распоиенко Дмитрий Юрьевич^{3,7}, кандидат технических наук,
старший научный сотрудник лаборатории цветных сплавов

Коновалов Сергей Валерьевич^{1,2,8}, доктор технических наук, профессор,
главный научный сотрудник отраслевой научно-исследовательской лаборатории
авиационного материаловедения № 4 (ОНИЛ-4), проректор по научной и инновационной деятельности

Бахтегареев Инзиль Дамирович^{1,9}, магистр

¹Самарский национальный исследовательский университет имени академика С.П. Королева, Самара (Россия)

²Сибирский государственный индустриальный университет, Новокузнецк (Россия)

³Институт физики металлов имени М.Н. Михеева Уральского отделения РАН, Екатеринбург (Россия)

*E-mail: arishenskiy_ev@sibsru.ru

⁴ORCID: <https://orcid.org/0000-0002-6762-7436>

⁵ORCID: <https://orcid.org/0000-0003-3875-7749>

⁶ORCID: <https://orcid.org/0000-0001-6869-4764>

⁷ORCID: <https://orcid.org/0000-0002-7670-9054>

⁸ORCID: <https://orcid.org/0000-0003-4809-8660>

⁹ORCID: <https://orcid.org/0009-0004-3081-9049>

Поступила в редакцию 07.10.2024

Пересмотрена 27.11.2024

Принята к публикации 04.02.2025

Аннотация: Исследовано влияние добавок гафния и эрбия на формирование микроструктуры при термической обработке алюминиевых сплавов с высоким содержанием магния, дополнительно легированных скандием и цирконием. Для исследования методом литья в стальной кокиль были получены слитки из алюминиевых сплавов с высоким содержанием магния, легированного скандием, эрбием и гафнием с содержанием в диапазонах 0,03–0,16 % и 0,05–0,16 % соответственно. После отливки образцы подвергали термической обработке при температуре 370 и 440 °С с выдержкой от 2 до 96 ч. Были исследованы изменения микротвердости в зависимости от термической обработки. Для сплавов 1590-3 и 1590-4 в литом состоянии и после термической обработки при температуре 440 °С в течение 2 и 48 ч с помощью просвечивающей микроскопии исследовали тонкую микроструктуру и крупные интерметаллиды. Установлено, что добавки гафния и эрбия приводят к повышению микротвердости за счет уменьшения размера и увеличения количества наночастиц Al₃Sc. После проведения термической обработки при температуре 440 °С в течение 4 ч во всех исследуемых сплавах происходит выпадение частиц Al₃Sc, имеющих одинаковый размер (8 нм) и плотность, однако с увеличением времени выдержки в сплаве с меньшим содержанием гафния и большим содержанием эрбия размер частиц увеличивается в 2 раза по сравнению с частицами сплава, где содержание гафния больше, а содержание эрбия низкое.

Ключевые слова: алюминиевые сплавы; микролегирование; скандий; гафний; эрбий; формирование частиц Al₃Sc; микротвердость; микроструктура; наночастицы.

Благодарности: Исследование выполнено за счет гранта Российского научного фонда № 22-19-00810, <https://rscf.ru/project/22-19-00810/>.

Для цитирования: Рагазин А.А., Арышенский Е.В., Арышенский В.Ю., Распоиенко Д.Ю., Коновалов С.В., Бахтегареев И.Д. Влияние микролегирования эрбием и гафнием на формирование частиц Al₃Sc в алюминиевом сплаве с высоким содержанием магния // Frontier Materials & Technologies. 2025. № 1. С. 69–80. DOI: 10.18323/2782-4039-2025-1-71-6.

Influence of crystallographic texture on the strength and electrical conductivity of ultrafine-grained copper

Danila V. Tarov*, student of Chair of Materials Science and Physics of Metals
Konstantin M. Nesterov, PhD (Physics and Mathematics),
assistant professor of Chair of Materials Science and Physics of Metals
Rinat K. Islamgaliev, Doctor of Sciences (Physics and Mathematics),
professor of Chair of Materials Science and Physics of Metals
Elena A. Korznikova¹, Doctor of Sciences (Physics and Mathematics),
professor of Chair of Materials Science and Physics of Metals

Ufa University of Science and Technology, Ufa (Russia)

*E-mail: tarovdv@gmail.com

¹ORCID: <https://orcid.org/0000-0002-5975-4849>

Received 05.07.2023

Revised 09.11.2023

Accepted 04.02.2025

Abstract: The paper covers the study of the influence of equal-channel angular pressing (ECAP) on the structure, crystallographic texture, mechanical properties and electrical conductivity of Cu-ETP copper (Russian analogue – M1), as well as the dependence of these characteristics on the orientation of the measurement direction relative to the cross-section (from -45° to 90°). The specific electrical conductivity and strength characteristics of the material in the as-delivered condition (hot-rolled) and the effect of annealing at a temperature of 450°C of the original sample are investigated. Mechanical tests for uniaxial tension, a study of microhardness using the Vickers method and a study of specific electrical conductivity based on measuring the parameters of the vortex field excited in the surface layers of the body are carried out. It is found that ECAP processing leads to a significant increase in the ultimate tensile strength to 425 MPa compared to the initial state of 300 MPa. The maximum tensile strength of 425 MPa is achieved at orientation angles relative to the ECAP cross-section of -45° . A significant increase in microhardness to 1364–1405 MPa, tensile strength to 350–425 MPa and electrical conductivity to 101.4–102.4 % IACS is a consequence of the selected directions of cutting the samples relative to the ECAP axis. This indicates the dependence of both mechanical and electrical properties of ultrafine-grained samples on the crystallographic texture orientation. A Cu-ETP copper sample subjected to ECAP with a cutting angle deviating from the ECAP cross-section of the sample by 7.5° has the most optimal crystallographic orientation. In this case, the values of microhardness and electrical conductivity reached 1405 MPa and 102.4 % IACS, respectively.

Keywords: crystallographic texture; strength; electrical conductivity; ultrafine-grained copper; equal-channel angular pressing; structure.

Acknowledgements: The study was supported by the Ministry of Science and Higher Education of the Russian Federation as part of the State Assignment “Research of physical, chemical and mechanical processes in the formation and hardening of parts for aerospace and transport equipment” No. FEUE-2023-0006.

The paper was written on the reports of the participants of the XI International School of Physical Materials Science (SPM-2023), Togliatti, September 11–15, 2023.

For citation: Tarov D.V., Nesterov K.M., Islamgaliev R.K., Korznikova E.A. Influence of crystallographic texture on the strength and electrical conductivity of ultrafine-grained copper. *Frontier Materials & Technologies*, 2025, no. 1, pp. 81–91. DOI: 10.18323/2782-4039-2025-1-71-7.

INTRODUCTION

Copper and low-alloyed copper alloys, due to their high electrical conductivity, are widely used in mechanical engineering for the manufacture of contacts and wires. Copper parts must have a unique combination of properties: high electrical conductivity, strength, ductility, and corrosion resistance. Good technological properties and relatively low cost determine the wide application of copper in industry both in the form of alloys and in pure form. In the work [1], it is shown that the mechanical strength and electrical conductivity of these materials are primarily controlled by their microstructure, the most important parameters of which are the grain size and dislocation structure. Dislocations and

grain boundaries make a large contribution to increasing the yield strength, but a smaller contribution to increasing the specific electrical resistance [2].

In recent years, a promising research area has been the formation of an ultrafine-grained (UFG) structure with an average grain size of less than $1\ \mu\text{m}$, which contributes to the manifestation of unique mechanical properties (high strength, increased fatigue limit) [3; 4]. At the same time, it is known that treatment by severe plastic deformation (SPD) is accompanied by active movement of dislocations and twinning, which leads to reorientation of grains and formation of developed crystallographic textures [5; 6]. Crystallographic texture usually occurs as a result of

directed external mechanical action, in this case – the SPD process. The presence of a preferred orientation enhances the anisotropy of the material properties and can significantly change the performance characteristics of the product. Therefore, the possibility of texture formation should be taken into account when carrying out various deformation and heat treatments [7]. In particular, in samples of pure copper subjected to SPD, it was found that at the initial stages of deformation, a strong preferred orientation of crystallites occurs, which is characteristic of the simple shear texture [5]. At the same time, an increase in the degree of accumulated deformation contributes to the blurring of texture maxima, which is of interest for studying the influence of crystallographic texture on the strength and electrical properties of UFG copper.

The works are known that consider the influence of crystallographic texture on the strength and electrical conductivity of UFG copper produced by rotational forging [8] and electrodeposition [9], but the studies in them were carried out using the example of samples in the form of a wire or films with a different crystallographic texture.

The purpose of the study is to analyze the structure and crystallographic texture in ultrafine-grained samples of Cu-ETP copper produced by equal-channel angular pressing (ECAP) in order to identify structural factors leading to achieving higher strength while maintaining high electrical conductivity of the material.

METHODS

Materials and methods of research

A Cu-ETP (Russian analogue M1) copper commercial rod with a diameter of 20 mm, GOST 859-2001 (Table 1), was selected as the material for research.

To analyze the initial microstructure, two samples were studied, one of which was in the as-delivered condition – hot-rolled. The sample in the initial condition was annealed at 450 °C for 2 h. Before annealing, the initial sample was immersed in a melt of a mixture of KOH and NaOH salts to prevent oxidation of the material surface.

The formation of the UFG structure in a billet with a diameter of 20 mm and a length of 150 mm was carried out by the ECAP method in eight passes along the B_C route, which involves rotating the sample between two subsequent cycles counterclockwise for an angle of 90° around the longitudinal axis [6]. The passes of the billets were carried out on equipment with an angle of intersection of the channels of 120° at a temperature of 20 °C.

Preparation of samples for metallographic analysis included cutting out samples (Fig. 1) on an ARTA-120 electrical discharge cutting-off machine taking into account the angles relative to the cross-section of ECAP of the billet (0°, 7.5°, ±15°, ±22.5°, ±45°, 90°), grinding, polishing, and etching.

Grinding of samples was carried out on a NERIS grinding and polishing machine with a stepwise decrease in the grain size of the sanding paper from P100 to P4000 at a machine speed of 500–600 rpm.

Polishing was carried out on diamond paste with a gradual decrease in its grain size from 7/5 to 3/2. When moving to the next paste number, the paste residues were carefully removed from the metallographic section using alcohol, and the polishing direction was changed by 90° to ensure complete disappearance of the scratches from the previous paste.

To identify the microstructure, the sample was etched. The etchant composition: perchloric acid (HCl) – 50 %, nitric acid (HNO₃) – 25 %, acetic acid (CH₃COOH) – 25 %. The etching mode was selected experimentally. The sample was etched for 2–3 s by dipping into the etchant, then washed with distilled water and dried with filter paper.

Structural studies

Microstructure images were obtained using a JEM-6390 scanning electron microscope and a JEM-2100 transmission electron microscope. Thin foils were prepared using a Tenupol-5 device by jet electrolytic polishing at 22–24 V using an electrolyte of the following composition: 920 ml of water (H₂O), 70 ml of orthophosphoric acid (H₃PO₄), 15 ml of glycerol (C₃H₅(OH)₃). The ECAP structure of the samples was studied in cross-section. The grain size was calculated using the GrainSize program based on the obtained structure images.

After ECAP processing, the Cu-ETP copper sample was cut with the following orientations (angles) relative to the ECAP cross-section of the billet: 0°, 7.5°, ±15°, ±22.5°, ±45°, 90°; thickness 1.5–2.5 mm, diameter 20 mm. The analysis of texture formation processes in copper was performed using a DRON-3m diffractometer equipped with an automatic texture attachment. Filtered Cu-K_{α1} X-ray radiation (0.15406 nm) was used to shoot pole figures. Reflection imaging was carried out within the range of radial γ angle from 0 to 75° and azimuthal δ angle from 0 to 360°. The diameter of the irradiated area was 0.6 mm. In the case of ECAP, the study was carried out in the geometric centre of the longitudinal section of the billet.

Table 1. Chemical composition of Cu-ETP grade copper
Таблица 1. Химический состав меди марки М1

Content, %											
Cu	Fe	O	Pb	S	Zn	Ag	Sb	As	Ni	Sn	Bi
99.9	≤0.005	≤0.05	≤0.005	≤0.004	≤0.004	≤0.003	≤0.002	≤0.002	≤0.002	≤0.002	≤0.001

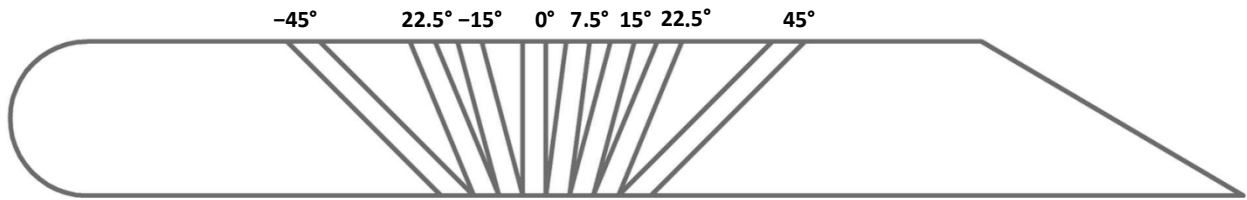


Fig. 1. Scheme of orientations of cutting ECAP samples
Рис. 1. Схема ориентаций вырезки РКВП образцов

The result was a set of intensities of reflected X-rays. The experimental results calculated using the LaboTEX software package (www.labosoft.com.pl) are presented as complete pole figures in the shear plane.

Microhardness study

The measurements were carried out on a MicroMet 5101 device using the Vickers method in the cross-section of the ECAP samples under a load of 100 g, the indenter holding time was 10 s. The results were recorded along the sample diameter.

Electrical conductivity study

The specific electrical conductivity was determined at room temperature by the eddy current method using a VE-27NTs device with a relative measurement error of 2%. Annealed pure copper with an electrical conductivity of 58 MS/m (electrical resistance of 0.017241 $\mu\Omega\cdot\text{m}$) corresponds to the 100% IACS designation according to the IACS (International Annealed Copper Standard) international standard. The results of electrical conductivity measurements in this paper are presented in % IACS, i. e. as a percentage of the electrical conductivity of pure copper.

Uniaxial tensile tests

The tests were carried out on a small sample deformation device at room temperature at a rate of $3 \times 10^{-3} \text{ s}^{-1}$.

In each state, two samples with working base dimensions of $6.0 \times 1.0 \times 0.7 \text{ mm}$ (Fig. 2) cut from the initial, annealed and ECAP billets were tested.

RESULTS

The obtained microstructure images are shown in Fig. 3. The initial structure of Cu-ETP copper consists of large irregular-shaped grains with an average size of $7 \pm 4 \mu\text{m}$ (Fig. 3 a). The grain distribution histogram shows that most grains are located in the range of 2.5–10 μm (Fig. 3 b). The microhardness value in the initial state is $1211 \pm 65 \text{ MPa}$, the electrical conductivity value was $101.3 \pm 1.36 \%$ IACS. Such electrical conductivity values were obtained due to the presence of a relative error of the measuring device, therefore, for the correct experiment and possible comparison of the results, the value obtained using the VE-27NTs device was taken.

After heat treatment at $450 \text{ }^\circ\text{C}$, the grain size increased to $10.2 \pm 2.3 \mu\text{m}$ (Fig. 3 c). The grain distribution histogram shows that the majority of grains are located in the range of 5.5–15.5 μm (Fig. 3 d). The microhardness value is $773 \pm 37 \text{ MPa}$, and the electrical conductivity is $102.2 \pm 1.79 \%$ IACS.

After ECAP processing, the grain size decreased to 300 nm on average (Fig. 3 e). The grain distribution histogram shows that the great number of grains are located in the range of 250–324 nm (Fig. 3 f).

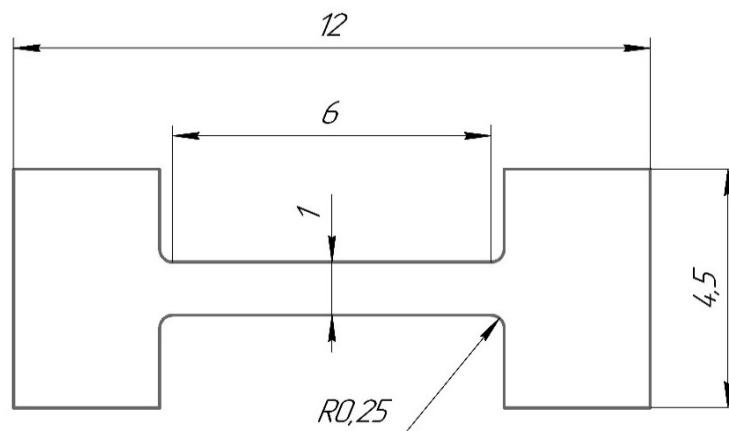


Fig. 2. The geometry of a specimen for mechanical tensile testing
Рис. 2. Геометрия образца для механических испытаний на растяжение

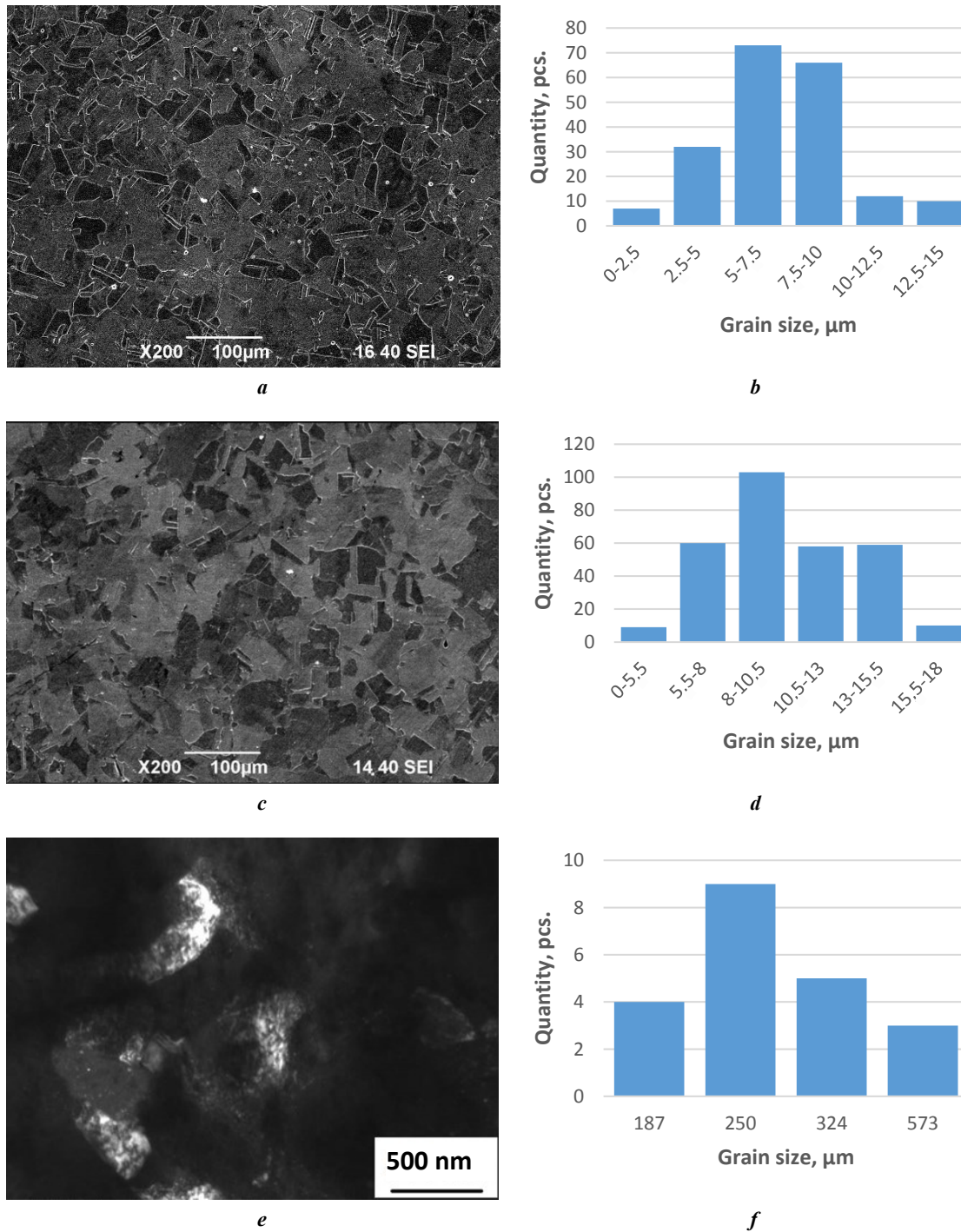


Fig. 3. Results of microscopy and grain size calculation:
a – structure of the initial sample; *b* – grain size (initial sample);
c – microstructure of the annealed sample; *d* – grain size (annealed sample);
e – dark-field TEM image of copper (ECAP); *f* – grain size (ECAP)

Рис. 3. Результаты микроскопии и расчета размеров зерна:
a – структура исходного образца; *b* – размер зерна (исходный образец);
c – микроструктура отожженного образца; *d* – размер зерна (отожженный образец);
e – темнопольное изображение ПЭМ меди (ПКУП); *f* – размер зерна (ПКУП)

As a result of texture analysis, direct pole figures were obtained (Fig. 4), which were rearranged for further analysis with a 90° rotation along the equatorial plane (Fig. 5). After eight ECAP passes at $T=20$ °C, on the (111) pole figure, clearly defined maxima are visible, the arrangement nature of which is quite ordered (Fig. 5). The crystallographic texture after eight ECAP passes can be described by ideal orientations (Fig. 6) corresponding to the state after simple shear taking into account the rotation by an angle of 60° counterclockwise. The (111) pole figure is characterized by a set of seven maxima (Fig. 5 d): six maxima are symmetrically located on the pole figure periphery and one in its centre. These maxima correspond to the A $\{111\}\langle uvw\rangle$, B $\{hkl\}\langle 110\rangle$, and C $\{001\}\langle 110\rangle$ components of the simple shear texture. Their intensity increases with increasing shear angle (from 0 to 22°).

The crystallographic textures of all sections of the copper sample subjected to eight ECAP passes are identical and are characterized by dominant $\{110\}\langle 111\rangle$ components (Fig. 5). At the same time, the pole figures obtained for different sections are characterized by the fact that the A_{10}^* , A_{20}^* and C_0 maxima located on the periphery of the pole figure shift toward its centre with an increase in the cutting angle. In general, the finally formed texture can be described by the main textural $(111)[\bar{1}\bar{1}\bar{2}]$, $(111)[1\bar{1}\bar{2}]$, $(\bar{1}\bar{1}\bar{1})[110]$, $(\bar{1}\bar{1}\bar{1})[\bar{1}\bar{1}0]$, $(\bar{1}\bar{1}\bar{2})[110]$, $(\bar{1}\bar{1}\bar{2})[\bar{1}\bar{1}0]$, and $(001)[110]$ maxima characteristic of simple shear textures.

The indicated A_0 , A_{10}^* , A_{20}^* , \bar{A}_0 , B_0 , \bar{B}_0 , and C_0 ideal orientations lie on the $\{111\}\theta$ and $\langle 110\rangle\theta$ fibres (Fig. 6). For the (111) pole figure obtained for a 7.5° cut, a superposition of the recrystallization texture on the simple shear texture is observed (Figs. 5 b and 6 b). The recrystallization process is associated with the absorption of old grains by new equiaxed grains with high-angle boundaries. It is activated when a certain deformation degree is reached. In the case under consideration, in addition to the simple shear texture component on the (111) pole figure, the formation of dominant $R1(\bar{1}\bar{1}\bar{1})[113]$, $R2(120)[\bar{2}11]$, $R3(023)[\bar{3}\bar{3}\bar{2}]$, and $R4(\bar{1}\bar{1}\bar{2})[\bar{2}\bar{2}\bar{1}]$ components characteristic of the recrystallization texture is observed (Fig. 6 b).

In sections of 15 and 22.5°, a broken symmetry of the crystalline structure is observed. 0° section corresponds to the crystalline texture of simple shear of the metal fcc lattice. In section of 7.5°, the location of texture maxima corresponds to an absolutely symmetrical pattern of the crystal structure, which indicates its greatest ordering and explains the highest electrical conductivity (Fig. 4).

The mechanical test curves were obtained for the initial, annealed initial (Fig. 7 a) and ECAP-treated samples (Fig. 7 b). After annealing the initial samples, a decrease in the ultimate tensile strength from 300 to 210 MPa occurred due to an increase in the average grain size, as well as an increase in plasticity due to an increase in the stage of strain hardening (Fig. 7 a). In the ECAP samples, different values of the ultimate tensile strength were observed in the range from 330 to 425 MPa depending on the angle of cutting relative to the ECAP axis (Fig. 7 b). At the same time, all the studied samples showed close values of relative

elongation before failure of about 5 %. Figs. 8, 9 show the changes in microhardness, ultimate tensile strength, and electrical conductivity depending on the direction of sample cutting relative to the ECAP axis, which indicates a strong influence of the crystallographic texture on these characteristics of the samples. The maximum (425 MPa) and minimum (330 MPa) ultimate tensile strengths were observed at orientation angles relative to the ECAP cross section of -45° and 15°, respectively. The highest values of microhardness and electrical conductivity were observed at 7.5° - 1405 MPa and 102.4 % IACS, respectively.

DISCUSSION

An increase in the strength properties of Cu-ETP copper after grain structure refinement has already been observed in the literature using the example of UFG samples produced by SPD [10; 11]. It can be explained by the well-known Hall-Petch relationship [12; 13], which describes the dependence of the yield strength on the average grain size. In [14], it was noted that in order to achieve a combination of high strength and good electrical conductivity in copper materials, grain refinement to an average size of 200 nm is sufficient. In the present work, a close average grain size of 300 nm was observed in the ECAP samples, as well as a high ultimate strength of 425 MPa close to the values of 450 MPa previously observed in the pure copper ECAP samples [15].

A combination of increased strength and electrical conductivity values was also noted using the example of UFG copper samples produced by electrodeposition [17], multiple rolling [18] and drawing [19], which were characterized by the presence of a crystallographic texture. The features of crystallographic texture in ECAP copper samples were investigated in [20; 21]. In the work [20], it was noted that there is a texture gradient in different directions of equal-channel angular pressing of samples, which can create anisotropy of mechanical properties in them. The work [21] demonstrated that the electrical conductivity of ECAP copper is affected by various structural factors, including grain orientation and crystallographic texture. In this paper, it is shown that the difference in strength and electrical conductivity of ECAP copper samples relative to different crystallographic directions can reach 20–30 and 2–3 %, respectively.

CONCLUSIONS

1. The structure of Cu-ETP copper in the initial state is represented by grains of irregular shape with an average size of 7 µm, subsequent annealing at 450 °C leads to an increase in the grain size to 10.2 µm. After ECAP processing, the grain size decreased to 300 nm. ECAP processing led to a significant increase in the tensile strength compared to the initial state (300 MPa). The maximum (425 MPa) and minimum (350 MPa) tensile strengths were observed at orientation angles relative to the ECAP cross-section of -45° and 15°, respectively.

2. A significant dependence of the change in microhardness (1364–1405 MPa), tensile strength (350–425 MPa) and electrical conductivity (101.4–102.4 % IACS) on the directions of cutting of the samples relative to the ECAP

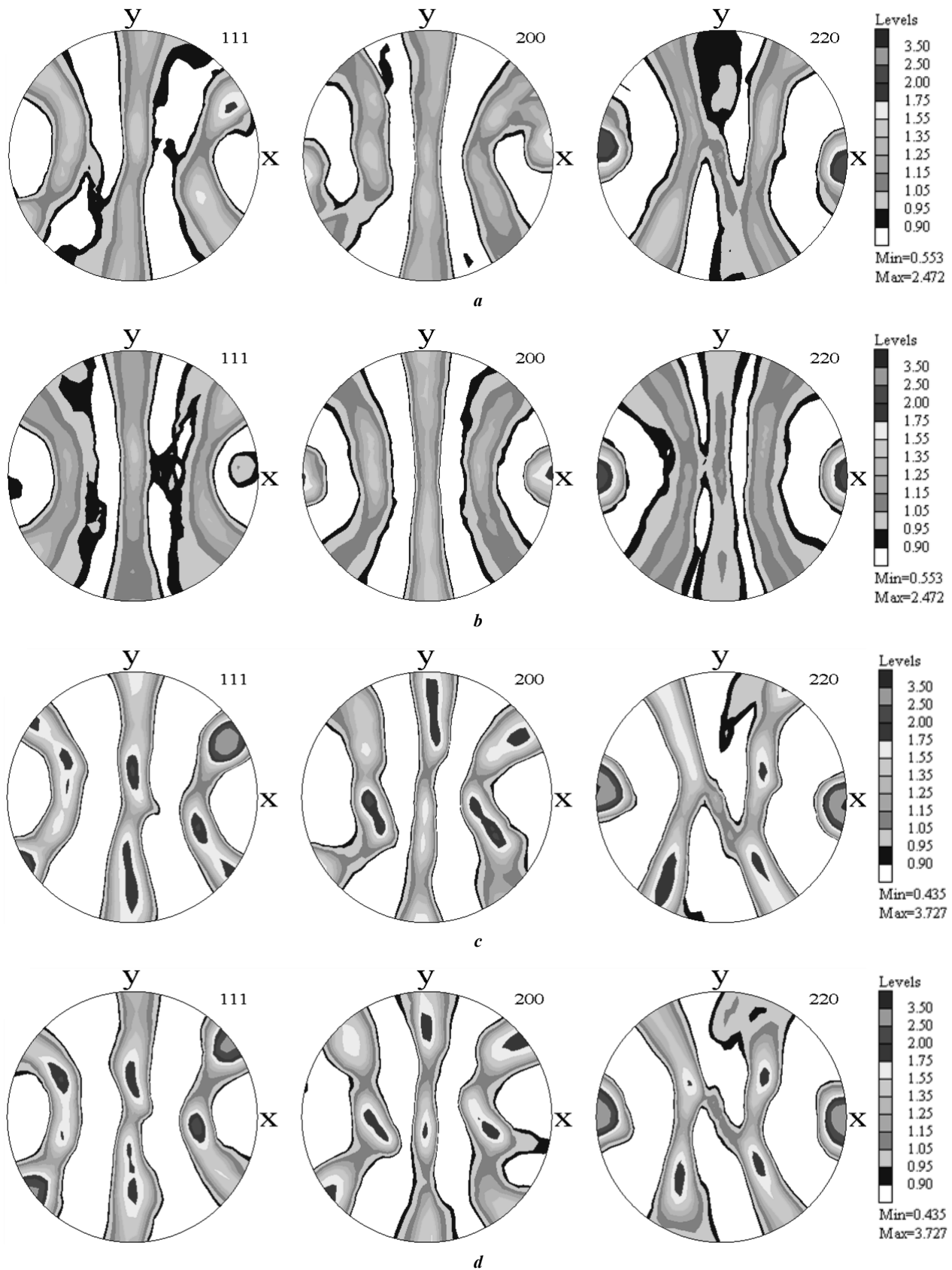


Fig. 4. Direct pole figures of copper after eight ECAP passes in different sections:
a – 0°; *b* – 7.5°; *c* – 15°; *d* – 22.5°

Рис. 4. Прямые полюсные фигуры меди после 8 проходов РКВП в различных сечениях:
a – 0°; *b* – 7,5°; *c* – 15°; *d* – 22,5°

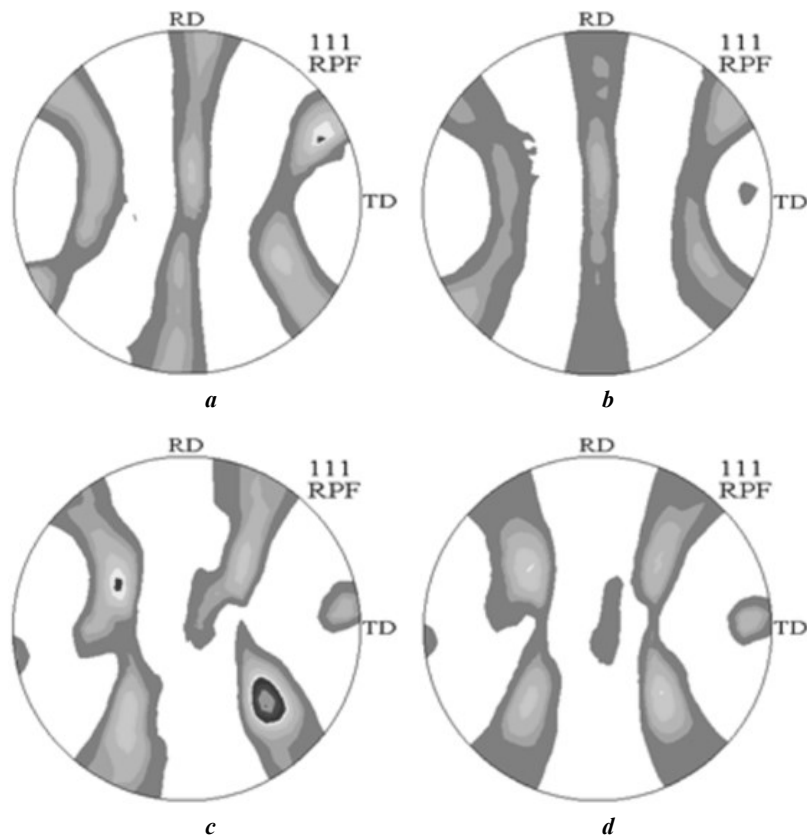


Fig. 5. Rearranged direct pole figures in different studied states:

a – 0°; b – 7.5°; c – 15°; d – 22.5°

Рис. 5. Перестроенные прямые полюсные фигуры в различных исследованных состояниях:

a – 0°; b – 7,5°; c – 15°; d – 22,5°

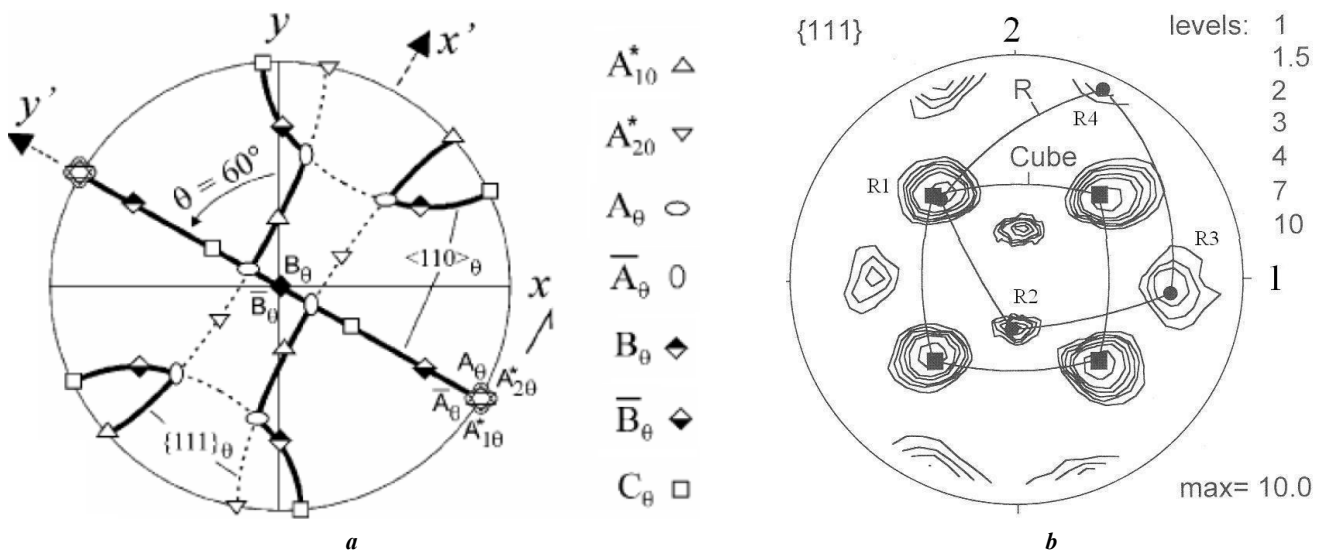
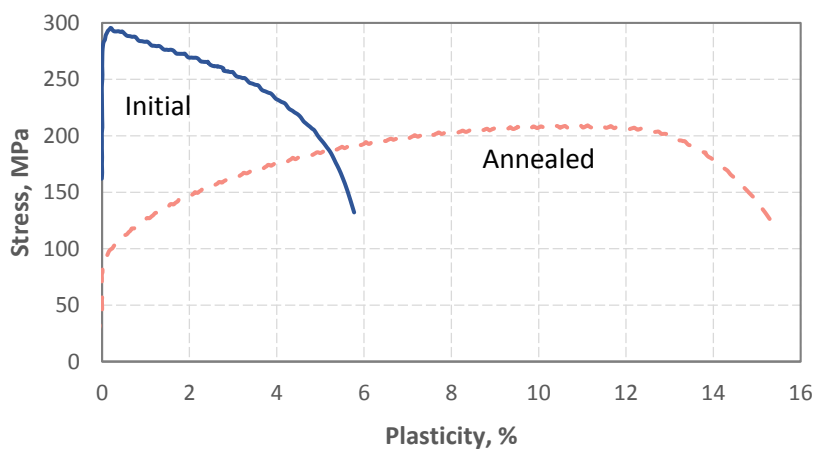


Fig. 6. Positions of ideal orientations corresponding to the state after a simple shear taking into account a rotation by an angle of 60° counterclockwise:

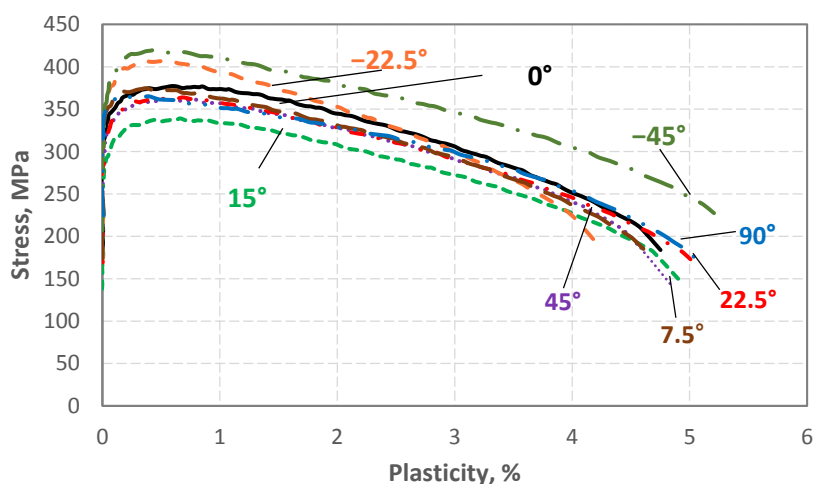
a – cubic orientation; b – R-orientation

Рис. 6. Положения идеальных ориентировок, соответствующих состоянию после простого сдвига с учетом поворота на угол 60° против часовой стрелки:

a – кубическая ориентировка; b – R-ориентировка



a



b

Fig. 7. Curves of mechanical tests of samples:
a – initial and annealed; **b** – cut at different cross-sections from ECAP billet
Рис. 7. Кривые механических испытаний образцов:
a – исходного и отожженного;
b – вырезанных при различных сечениях из РКВП заготовки

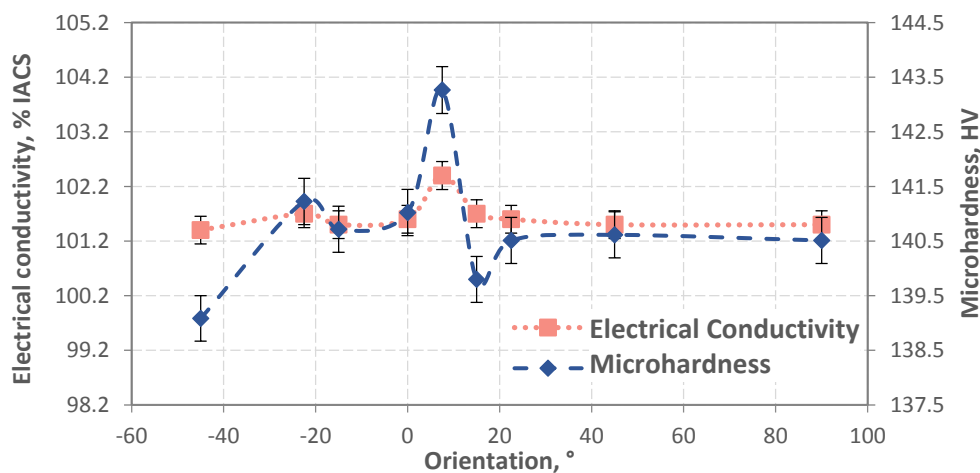


Fig. 8. Orientation angle dependence curves microhardness and electrical conductivity
Рис. 8. Кривые зависимости от угла ориентации микротвердости и электропроводности

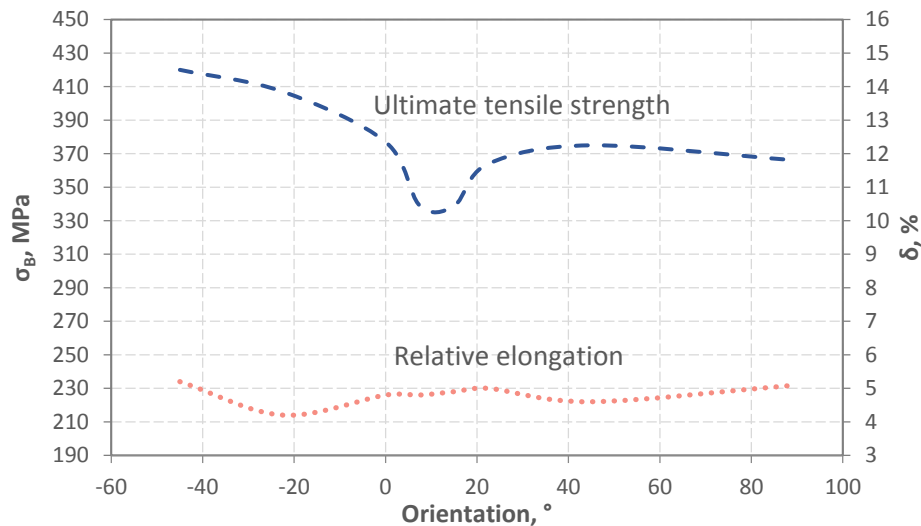


Fig. 9. Orientation angle dependence curves strength and elongation
Рис. 9. Кривые зависимости от угла ориентации прочности и удлинения

axis indicates a strong influence of the crystallographic texture both on the mechanical and on the electrical properties of the UFG samples. The most favourable crystallographic orientation is exhibited by the Cu-ETP copper sample with a cutting angle deviating from the cross-section of the ECAP sample by 7.5°. In this case, the values of microhardness and electrical conductivity reached 1405 MPa and 102.4 % IACS, respectively.

REFERENCES

- Murashkin M.Y., Sabirov I., Sauvage X., Valiev R.Z. Nanostructured Al and Cu alloys with superior strength and electrical conductivity. *Journal of Materials Science*, 2016, vol. 51, pp. 33–49. DOI: [10.1007/s10853-015-9354-9](https://doi.org/10.1007/s10853-015-9354-9).
- Fu Qianqian, Li Bing, Gao Minqiang, Fu Ying, Yu Rongzhou, Wang Changfeng, Guan Renguo. Quantitative mechanisms behind the high strength and electrical conductivity of Cu-Te alloy manufactured by continuous extrusion. *Journal of Materials Science & Technology*, 2022, vol. 121, pp. 9–18. DOI: [10.1016/j.jmst.2021.12.046](https://doi.org/10.1016/j.jmst.2021.12.046).
- Fan G.J., Choo H., Liaw P.K., Lavernia E.J. Plastic deformation and fracture of ultrafine-grained Al–Mg alloys with a bimodal grain size distribution. *Acta Materialia*, 2006, vol. 54, no. 7, pp. 1759–1766. DOI: [10.1016/j.actamat.2005.11.044](https://doi.org/10.1016/j.actamat.2005.11.044).
- Cui Lang, Shao Shengmin, Wang Haitao, Zhang Guoqing, Zhao Zejia, Zhao Chunyang. Recent Advances in the Equal Channel Angular Pressing of Metallic Materials. *Processes*, 2022, vol. 10, no. 11, article number 2181. DOI: [10.3390/pr10112181](https://doi.org/10.3390/pr10112181).
- Mao Qingzhong, Zhang Yusheng, Guo Yazhou, Zhao Yonghao. Enhanced electrical conductivity and mechanical properties in thermally stable fine-grained copper wire. *Communications Materials*, 2021, no. 2, article number 46. DOI: [10.1038/s43246-021-00150-1](https://doi.org/10.1038/s43246-021-00150-1).
- Damavandi E., Nourouzi S., Rabiee S.M., Jamaati R., Szpunar J.A. Effect of route BC-ECAP on microstructural evolution and mechanical properties of Al–Si–Cu alloy. *Journal of Materials Science*, 2021, vol. 56, pp. 3535–3550. DOI: [10.1007/s10853-020-05479-5](https://doi.org/10.1007/s10853-020-05479-5).
- Beyerlein I.J., Toth L.S. Texture evolution in equal-channel angular extrusion. *Progress in Materials Science*, 2009, vol. 54, no. 4, pp. 427–510. DOI: [10.1016/j.pmatsci.2009.01.001](https://doi.org/10.1016/j.pmatsci.2009.01.001).
- Alateyah A.I., Ahmed M.M.Z., Zedan Y., El-Hafez H.A., Alawad M.O., El-Garaihy W.H. Experimental and Numerical Investigation of the ECAP Processed Copper: Microstructural Evolution, Crystallographic Texture and Hardness Homogeneity. *Metals*, 2021, vol. 11, no. 4, article number 607. DOI: [10.3390/met11040607](https://doi.org/10.3390/met11040607).
- Chen Jianqing, Su Yehan, Zhang Qiyu, Sun Jiapeng, Yang Donghui, Jiang Jinghua, Song Dan, Ma Aibin. Enhancement of strength-ductility synergy in ultrafine-grained Cu-Zn alloy prepared by ECAP and subsequent annealing. *Journal of Materials Research and Technology*, 2022, vol. 17, no. 2, pp. 433–440. DOI: [10.1016/j.jmrt.2022.01.026](https://doi.org/10.1016/j.jmrt.2022.01.026).
- Wang Y.M., Ma E. Three strategies to achieve uniform tensile deformation in a nanostructured metal. *Acta Materialia*, 2004, vol. 52, no. 6, pp. 1699–1709. DOI: [10.1016/j.actamat.2003.12.022](https://doi.org/10.1016/j.actamat.2003.12.022).
- Zhao Yong-Hao, Bingert J.F., Liao Xiao-Zhou et al. Simultaneously increasing the ductility and strength of ultrafine-grained pure copper. *Advanced Materials*, 2006, vol. 18, no. 22, pp. 2949–2953. DOI: [10.1002/adma.200601472](https://doi.org/10.1002/adma.200601472).
- Sanders P.G., Eastman J.A., Weertman J.R. Elastic and tensile behavior of nanocrystalline copper and palladium. *Acta Materialia*, 1997, vol. 45, no. 10, pp. 4019–4025. DOI: [10.1016/S1359-6454\(97\)00092-X](https://doi.org/10.1016/S1359-6454(97)00092-X).
- Fu H.H., Benson D.J., Meyers M.A. Analytical and computational description of effect of grain size on yield stress of metals. *Acta Materialia*, 2001, vol. 49,

- no. 13, pp. 2567–2582. DOI: [10.1016/S1359-6454\(01\)00062-3](https://doi.org/10.1016/S1359-6454(01)00062-3).
14. Lu Lei, Shen Yongfeng, Chen Xianhua, Qian Lihua, Lu K. Ultrahigh strength and high electrical conductivity in copper. *Science*, 2004, vol. 304, no. 5669, pp. 422–426. DOI: [10.1126/science.1092905](https://doi.org/10.1126/science.1092905).
 15. Islamgaliev R.K., Nesterov K.M., Bourgon J., Champion Y., Valiev R.Z. Nanostructured Cu-Cr alloy with high strength and electrical conductivity. *Journal of Applied Physics*, 2014, vol. 115, no. 19, article number 194301. DOI: [10.1063/1.4874655](https://doi.org/10.1063/1.4874655).
 16. Dalla Torre F., Lapovok R., Sandlin J., Thomson P.F., Davies C.H.J., Pereloma E.V. Microstructures and properties of copper processed by equal channel extrusion for 1-16 passes. *Acta Materialia*, 2004, vol. 52, no. 16, pp. 4819–4832. DOI: [10.1016/j.actamat.2004.06.040](https://doi.org/10.1016/j.actamat.2004.06.040).
 17. Sarada B.V., Pavithra Ch.L.P., Ramakrishna M., Rao T.N., Sundararajan G. Highly (111) textured copper foils with high hardness and high electrical conductivity by pulse reverse electrodeposition. *Electrochemical and Solid-State Letters*, 2010, vol. 13, no. 6, pp. D40–D42. DOI: [10.1149/1.3358145](https://doi.org/10.1149/1.3358145).
 18. Takata N., Lee Seong-Hee, Tsuji N. Ultrafine grained copper alloy sheets having both high strength and high electric conductivity. *Materials Letters*, 2009, vol. 63, no. 21, pp. 1757–1760. DOI: [10.1016/j.matlet.2009.05.021](https://doi.org/10.1016/j.matlet.2009.05.021).
 19. Hanazaki K., Shigeiri N., Tsuji N. Change in microstructures and mechanical properties during deep wire drawing of copper. *Materials Science and Engineering: A*, 2010, vol. 527, no. 21–22, pp. 5699–5707. DOI: [10.1016/j.msea.2010.05.057](https://doi.org/10.1016/j.msea.2010.05.057).
 20. Skrotzki W., Tränkner C., Chulist R., Beausir B., Suwas S., Tóth L.S. Texture heterogeneity in ECAP deformed copper. *Solid State Phenomena*, 2010, vol. 160, pp. 47–54. DOI: [10.4028/www.scientific.net/SSP.160.47](https://doi.org/10.4028/www.scientific.net/SSP.160.47).
 21. Guo Tingbiao, Wei Shiru, Wang Chen, Li Qi, Jia Zhi. Texture evolution and strengthening mechanism of single crystal copper during ECAP. *Materials Science and Engineering: A*, 2019, vol. 759, pp. 97–104. DOI: [10.1016/j.msea.2019.05.042](https://doi.org/10.1016/j.msea.2019.05.042).
 22. Mao Qingzhong, Zhang Yusheng, Guo Yazhou, Zhao Yonghao. Enhanced electrical conductivity and mechanical properties in thermally stable fine-grained copper wire // *Communications Materials*. 2021. № 2. Article number 46. DOI: [10.1038/s43246-021-00150-1](https://doi.org/10.1038/s43246-021-00150-1).
 23. Damavandi E., Nourouzi S., Rabiee S.M., Jamaati R., Szpunar J.A. Effect of route BC-ECAP on microstructural evolution and mechanical properties of Al–Si–Cu alloy // *Journal of Materials Science*. 2021. Vol. 56. P. 3535–3550. DOI: [10.1007/s10853-020-05479-5](https://doi.org/10.1007/s10853-020-05479-5).
 24. Beyerlein I.J., Toth L.S. Texture evolution in equal-channel angular extrusion // *Progress in Materials Science*. 2009. Vol. 54. № 4. P. 427–510. DOI: [10.1016/j.pmatsci.2009.01.001](https://doi.org/10.1016/j.pmatsci.2009.01.001).
 25. Alateyah A.I., Ahmed M.M.Z., Zedan Y., El-Hafez H.A., Alawad M.O., El-Garaihy W.H. Experimental and Numerical Investigation of the ECAP Processed Copper: Microstructural Evolution, Crystallographic Texture and Hardness Homogeneity // *Metals*. 2021. Vol. 11. № 4. Article number 607. DOI: [10.3390/met11040607](https://doi.org/10.3390/met11040607).
 26. Chen Jianqing, Su Yehan, Zhang Qiyu, Sun Jiapeng, Yang Donghui, Jiang Jinghua, Song Dan, Ma Aibin. Enhancement of strength-ductility synergy in ultrafine-grained Cu-Zn alloy prepared by ECAP and subsequent annealing // *Journal of Materials Research and Technology*. 2022. Vol. 17. № 2. P. 433–440. DOI: [10.1016/j.jmrt.2022.01.026](https://doi.org/10.1016/j.jmrt.2022.01.026).
 27. Wang Y.M., Ma E. Three strategies to achieve uniform tensile deformation in a nanostructured metal // *Acta Materialia*. 2004. Vol. 52. № 6. P. 1699–1709. DOI: [10.1016/j.actamat.2003.12.022](https://doi.org/10.1016/j.actamat.2003.12.022).
 28. Zhao Yong-Hao, Bingert J.F., Liao Xiao-Zhou et al. Simultaneously increasing the ductility and strength of ultrafine-grained pure copper // *Advanced Materials*. 2006. Vol. 18. № 22. P. 2949–2953. DOI: [10.1002/adma.200601472](https://doi.org/10.1002/adma.200601472).
 29. Sanders P.G., Eastman J.A., Weertman J.R. Elastic and tensile behavior of nanocrystalline copper and palladium // *Acta Materialia*. 1997. Vol. 45. № 10. P. 4019–4025. DOI: [10.1016/S1359-6454\(97\)00092-X](https://doi.org/10.1016/S1359-6454(97)00092-X).
 30. Fu H.H., Benson D.J., Meyers M.A. Analytical and computational description of effect of grain size on yield stress of metals // *Acta Materialia*. 2001. Vol. 49. № 13. P. 2567–2582. DOI: [10.1016/S1359-6454\(01\)00062-3](https://doi.org/10.1016/S1359-6454(01)00062-3).
 31. Lu Lei, Shen Yongfeng, Chen Xianhua, Qian Lihua, Lu K. Ultrahigh strength and high electrical conductivity in copper // *Science*. 2004. Vol. 304. № 5669. P. 422–426. DOI: [10.1126/science.1092905](https://doi.org/10.1126/science.1092905).
 32. Islamgaliev R.K., Nesterov K.M., Bourgon J., Champion Y., Valiev R.Z. Nanostructured Cu-Cr alloy with high strength and electrical conductivity // *Journal of Applied Physics*. 2014. Vol. 115. № 19. Article number 194301. DOI: [10.1063/1.4874655](https://doi.org/10.1063/1.4874655).
 33. Dalla Torre F., Lapovok R., Sandlin J., Thomson P.F., Davies C.H.J., Pereloma E.V. Microstructures and properties of copper processed by equal channel extrusion for 1-16 passes // *Acta Materialia*. 2004. Vol. 52. № 16. P. 4819–4832. DOI: [10.1016/j.actamat.2004.06.040](https://doi.org/10.1016/j.actamat.2004.06.040).
 34. Sarada B.V., Pavithra Ch.L.P., Ramakrishna M., Rao T.N., Sundararajan G. Highly (111) textured copper foils with

СПИСОК ЛИТЕРАТУРЫ

1. Murashkin M.Y., Sabirov I., Sauvage X., Valiev R.Z. Nanostructured Al and Cu alloys with superior strength and electrical conductivity // *Journal of Materials Science*. 2016. Vol. 51. P. 33–49. DOI: [10.1007/s10853-015-9354-9](https://doi.org/10.1007/s10853-015-9354-9).
2. Fu Qianqian, Li Bing, Gao Minqiang, Fu Ying, Yu Rongzhou, Wang Changfeng, Guan Renguo. Quantitative mechanisms behind the high strength and electrical conductivity of Cu-Te alloy manufactured by continuous extrusion // *Journal of Materials Science & Technology*. 2022. Vol. 121. P. 9–18. DOI: [10.1016/j.jmst.2021.12.046](https://doi.org/10.1016/j.jmst.2021.12.046).
3. Fan G.J., Choo H., Liaw P.K., Lavernia E.J. Plastic deformation and fracture of ultrafine-grained Al–Mg alloys with a bimodal grain size distribution // *Acta Materialia*. 2006. Vol. 54. № 7. P. 1759–1766. DOI: [10.1016/j.actamat.2005.11.044](https://doi.org/10.1016/j.actamat.2005.11.044).
4. Cui Lang, Shao Shengmin, Wang Haitao, Zhang Guoqing, Zhao Zejia, Zhao Chunyang. Recent Advances in the Equal Channel Angular Pressing of Metallic Materi-

- high hardness and high electrical conductivity by pulse reverse electrodeposition // *Electrochemical and Solid-State Letters*. 2010. Vol. 13. № 6. P. D40–D42. DOI: [10.1149/1.3358145](https://doi.org/10.1149/1.3358145).
18. Takata N., Lee Seong-Hee, Tsuji N. Ultrafine grained copper alloy sheets having both high strength and high electric conductivity // *Materials Letters*. 2009. Vol. 63. № 21. P. 1757–1760. DOI: [10.1016/j.matlet.2009.05.021](https://doi.org/10.1016/j.matlet.2009.05.021).
19. Hanazaki K., Shigeiri N., Tsuji N. Change in microstructures and mechanical properties during deep wire drawing of copper // *Materials Science and Engineering: A*. 2010. Vol. 527. № 21–22. P. 5699–5707. DOI: [10.1016/j.msea.2010.05.057](https://doi.org/10.1016/j.msea.2010.05.057).
20. Skrotzki W., Tränkner C., Chulist R., Beausir B., Suwas S., Tóth L.S. Texture heterogeneity in ECAP deformed copper // *Solid State Phenomena*. 2010. Vol. 160. P. 47–54. DOI: [10.4028/www.scientific.net/SSP.160.47](https://doi.org/10.4028/www.scientific.net/SSP.160.47).
21. Guo Tingbiao, Wei Shiru, Wang Chen, Li Qi, Jia Zhi. Texture evolution and strengthening mechanism of single crystal copper during ECAP // *Materials Science and Engineering: A*. 2019. Vol. 759. P. 97–104. DOI: [10.1016/j.msea.2019.05.042](https://doi.org/10.1016/j.msea.2019.05.042).

Влияние кристаллографической текстуры на прочность и электропроводность ультрамелкозернистой меди

*Таров Данила Владимирович**, студент кафедры материаловедения и физики металлов

Нестеров Константин Михайлович, кандидат физико-математических наук, доцент кафедры материаловедения и физики металлов

Исламгалиев Ринат Кадыханович, доктор физико-математических наук, профессор кафедры материаловедения и физики металлов

Корзникова Елена Александровна¹, доктор физико-математических наук, профессор кафедры материаловедения и физики металлов

Уфимский университет науки и технологий, Уфа (Россия)

*E-mail: tarovdv@gmail.com

¹ORCID: <https://orcid.org/0000-0002-5975-4849>

Поступила в редакцию 05.07.2023

Пересмотрена 09.11.2023

Принята к публикации 04.02.2025

Аннотация: Работа посвящена исследованию влияния равноканального углового прессования (РКУП) на структуру, кристаллографическую текстуру, механические свойства и электропроводность меди марки М1, а также зависимости этих характеристик от ориентации направления измерения относительно поперечного сечения (от -45° до 90°). Исследованы удельная электропроводность и прочностные характеристики материала в состоянии поставки (горячекатаного) и влияние отжига при температуре 450°C исходного образца. Проведены механические испытания на одноосное растяжение, исследование микротвердости по методу Виккерса и исследование удельной электропроводности, основанное на измерении параметров вихревого поля, возбуждаемого в поверхностных слоях тела. Установлено, что обработка РКУП приводит к значительному увеличению предела прочности до 425 МПа по сравнению с исходным состоянием 300 МПа. Максимальный предел прочности 425 МПа достигается при углах ориентаций относительно поперечного сечения РКУП -45° . Существенный разброс в повышении микротвердости до значений 1364–1405 МПа, предела прочности до 350–425 МПа и электропроводности до 101,4–102,4 % IACS является следствием выбранных направлений вырезки образцов относительно оси РКУП. Это свидетельствует о зависимости не только механических, но и электрических свойств ультрамелкозернистых образцов от ориентации кристаллографической текстуры. Наиболее оптимальной кристаллографической ориентровкой обладает образец меди марки М1, подвергнутый РКУП с углом реза, отступающим от поперечного сечения РКУП образца на $7,5^\circ$. В данном случае значения микротвердости и электропроводности достигали 1405 МПа и 102,4 % IACS соответственно.

Ключевые слова: кристаллографическая текстура; прочность; электропроводность; ультрамелкозернистая медь; равноканальное угловое прессование; структура.

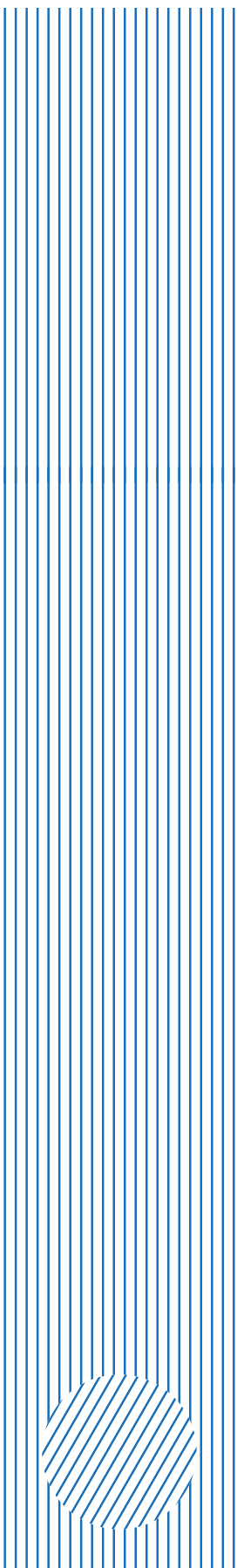
Благодарности: Исследование выполнено при поддержке Министерства науки и высшего образования Российской Федерации в рамках государственного задания «Исследование физико-химических и механических процессов при формообразовании и упрочнении деталей для авиакосмической и транспортной техники» № FEUE-2023-0006.

Статья подготовлена по материалам докладов участников XI Международной школы «Физическое материаловедение» (ШФМ-2023), Тольятти, 11–15 сентября 2023 года.

Для цитирования: Таров Д.В., Нестеров К.М., Исламгалиев Р.К., Корзникова Е.А. Влияние кристаллографической текстуры на прочность и электропроводность ультрамелкозернистой меди // *Frontier Materials & Technologies*. 2025. № 1. С. 81–91. DOI: [10.18323/2782-4039-2025-1-71-7](https://doi.org/10.18323/2782-4039-2025-1-71-7).



GENERAL PUBLICATION REQUIREMENTS FOR AUTHORS



The journal publishes two versions of papers: in Russian and in English. The data of manuscript has to be original and never submitted or published before in other journals. All submitted papers are checked in the Anti-Plagiarism system (“Antiplagiat” system).

For publication, authors need to submit an application to the editorial office by sending the materials to the e-mail of the journal vektornaukitgu@yandex.ru or by uploading them to their personal account on the website <https://www.vektornaukitech.ru>.

Required structural elements of the manuscript

- *UDC identifier*;
- *the title* of the scientific manuscript;
- *copyright sign and year*;
- *information about the authors*: surname and initials of the author, academic degree, academic status, occupation; company, city, country; ORCID. The author corresponding to the editorial staff should provide his/her E-mail;
 - *abstract* (200–250 words) should contain a brief summary of the paper’s concept in order to interest a potential reader;
 - *keywords* (the main criterion of choosing keywords is their potential value to summarize the content of the document or to help the readers to find the document);
 - *acknowledgements* to individuals, granting organizations;
 - *the text of the manuscript* structured in accordance with the rules;
 - *references* (at least 20 sources).

Article structure

The structure of the article should conform to the IMRAD (Introduction, Methods, Results, and Discussion) standard, applied by Science World Community:

- INTRODUCTION
- METHODS
- RESULTS
- DISCUSSION
- CONCLUSIONS

Tables and figures formatting

Tables and figures should not fall outside the page layout. The use of landscape pages is not allowed. The titles of the tables and figures captures are required. If the text contains figures, diagrams, and tables from other literary sources, it is necessary to indicate where they were taken from..

Formulas typing

Formulas are edited in Microsoft Equation 3 formula editor. Formulas should not be longer than 80 mm. The size of the formula is 100 %. Converting formulas to figures is not allowed.

References and citations formatting

References are listed in the order of citation in the article. Reference list should not include the sources not cited in the article. In the journal it is not common to cite textbooks and study guides, except the flagship in their respective field, thesis papers and synopsis of a thesis. Not less than a quarter of the sources listed in the reference list should be published in the last 3–5 years. References to print publications only are acceptable (excluding e-journals). References to internet sites are not accepted. Not more than 20 % of the sources can be references on the own author’s publications. If a cited source has a DOI, the DOI should be indicated at the end of bibliographic description of this source. All DOIs should be valid links

Mathematical modelling to predict the tensile strength of additively manufactured AlSi10Mg alloy using artificial neural networks

Sunita K. Srivastava*¹, researcher
of Department of Mechanical Engineering
N. Rajesh Mathivanan², PhD,
professor of Department of Mechanical Engineering

PES University, Bangalore (India)

*E-mail: sunita.shri45@gmail.com

¹ORCID: <https://orcid.org/0009-0005-2174-2067>

²ORCID: <https://orcid.org/0000-0003-1903-2005>

Received 10.09.2024

Revised 29.10.2024

Accepted 25.11.2024

Abstract: Integrating machine learning in additive manufacturing to simulate real manufacturing outcomes can significantly reduce the cost of manufacturing through selective manufacturing. However, limited research exists on developing a prediction model for the mechanical properties of the material. The input variables include key selective laser melting process parameters such as laser power, layer thickness, scan speed, and hatch spacing, with tensile strength as the output. The artificial neural network (ANN) based mathematical model is compared with a second-degree polynomial regression model. The robustness of both models was further assessed with the new data points beyond those used in the development of ANN-based mathematical model and regression model. The results demonstrate that the proposed ANN-based mathematical model offers superior accuracy, with a mean absolute percentage error (MAPE) value of 4.74 % and the R^2 (goodness of fit) value of 0.898 in predicting the strength of AlSi10Mg. The ANN-based mathematical method also demonstrates the strong performance on the new data, achieving a regression value of 0.68. This concludes that the model shows sufficient proof to consider a viable option for predicting the tensile strength.

Keywords: AlSi10Mg alloy; additive manufacturing; artificial neural network (ANN); machine learning; selective laser melting; mathematical model.

For citation: Srivastava S.K., Mathivanan N.R. Mathematical modelling to predict the tensile strength of additively manufactured AlSi10Mg alloy using artificial neural networks. *Frontier Materials & Technologies*, 2025, no. 1, pp. 93–110. DOI: 10.18323/2782-4039-2025-1-71-8.

INTRODUCTION

Additive manufacturing has been the cornerstone of industrial innovation for several decades and has seemingly adapted to handle diverse materials including metal, alloy, polymer, composite, etc. It offers various processes such as binder jetting, fused deposition, powder bed fusion, sheet lamination, material jetting, etc. to meet diverse manufacturing requirements. The fabrication of the metals or composite is majorly done by selective laser melting and laser metal deposition. Additive manufacturing is a preferred manufacturing process for the aluminium alloy and aluminium metal matrix composite for its ability to deliver great accuracy, lesser lead time, cost effectiveness, and superior part qualities compared to conventional manufacturing methods [1]. Pure aluminium however poses challenges during laser melting because of its high reflectivity absorbing only 7 % of the incident laser energy. In contrast, silicon has a high laser absorptivity of around 70 %, which makes aluminium-silicon alloys an ideal candidate for selective laser melting (SLM) due to their enhanced laser absorption [2]. Among the aluminium-silicon alloys, AlSi10Mg stands out as extremely promising because of its excellent mechanical properties and lightweight characteris-

tics. The alloy is very popular in the automobile and aerospace sectors for its exceptional mechanical attributes and remarkable thermal conductivity.

However, the printing parameters of the SLM process such as laser power, layer thickness, scan speed, hatch spacing etc. have a significant impact on the properties of the material, which can be modulated to get the optimum product. For instance, the densification property of the metal can be controlled by varying the laser energy density, which is the combined form of all four process parameters (laser power, layer thickness, scan speed and the hatch spacing). The adjustment helps to achieve the desired mechanical properties of the metal such as tensile strength, compressive strength, hardness, and microhardness, etc. [3].

Machine learning, which is the subset of artificial intelligence plays a vital role in generating a model/system by enabling automatic learning from the provided data and improving the accuracy without any extensive programming [4].

Within this realm, an artificial neural network (ANN), a part of deep learning, mimics the working principle of a human brain. It has interconnected nodes within its

architecture that simulate the biological neurons. The ANN architecture comprises of input layers (comprising independent variables), hidden layers (comprising one or more) and output layers (comprising dependent variables). Each node of a layer is connected to the next set of nodes through weights, biases and a transfer function to send the signal. ANN uses the training data to establish the connection between input and output. It learns and fine-tunes the accuracy of the model through iterative learning which makes it a very powerful tool in the domain of artificial intelligence [5]. The basic ANN architecture used in this study is depicted in the Fig. 1.

This model can be used for the prediction of unknowns and for finding optimal solutions by analysing the influence of input parameters. However, there are very few studies have been performed in this area.

Shubham et al. [6] assessed six different machine learning models such as deep learning, bagging, decision tree, linear regression, random forest and ridge regression to evaluate the influence of manufacturing parameters such as laser power, scan speed, scan space, and island size on the tensile strength of AlSi10Mg alloy. It was concluded that deep learning and decision trees can have prediction accuracy of up to 99 and 89 % respectively. It was also highlighted that laser power is the most influencing parameter among all the four parameters considered. Ghetiya et al. [7] explored the machine learning approach to optimise the process parameters of friction stir welding of aluminium plates. The input welding parameters considered are tool rotational speed, welding speed, tool shoulder diameter and axial force. An ANN model was developed utilising a backpropagation algorithm to predict the tensile strength for the given process parameters. The results show a good alignment of the model with the experimental values and can be used as an alternate way to calculate the tensile strength.

M. Khalefa [8] developed the ANN model from the experimental data of stir-casting manufactured Al–Si

alloy. The application of the model is to predict the effect of silicon content on tensile strength, hardness, and wear loss. The obtained results exhibit that the predicted values satisfactorily align with the experimental values with mean square error (MSE) of 0.0335, 0.0023, and 0.014 for the tensile test, the hardness test, and the wear loss respectively. Alamri et al. [9] explored the prediction of the part quality that includes assessing relative density, surface roughness, and hardness in relation to laser power, hatch spacing, scan velocity and layer thickness of selective laser melting manufactured AlSi10Mg alloy. This study has used five different supervised learning algorithms such as artificial neural network (ANN), support vector regression (SVR), kernel ridge regression (KRR), random forest (RF), and Lasso regression to compare the results. The ANN was found to be outperformed among other models based on computation results. Additionally, laser power and scan speed emerged as the predominant parameters influencing relative density and hardness, while layer thickness and scan speed impact the surface roughness the most.

Given limited research, this study develops a novel approach to integrate an ANN-based mathematical model and regression model to predict the tensile strength of additively manufactured (SLM) AlSi10Mg alloys based on available data.

The emphasis of the study is on the development of a correlation between tensile strength and selective laser melting parameters such as laser power, layer thickness, scan speed, and hatch spacing. Furthermore, this research contributes valuable insight into using a machine learning model to predict material properties without the need of actual experimentation.

The objective of this work is to enhance the ability to predict and optimise the material properties from the experimental data and to provide better control over the production process, through a reliable predictive model.

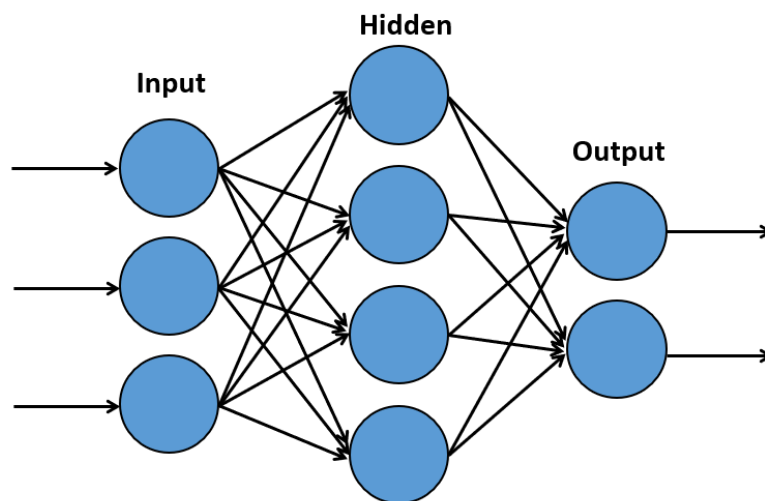


Fig. 1. Architecture of an artificial neural network
 Рис. 1. Архитектура искусственной нейронной сети

The work aims to support a more cost and time effective approach for the material assessment. In doing so, this study lays a foundation for future research by integrating machine learning and neural network models into additive manufacturing.

METHODS

Data collection for the artificial neural network and regression model

The input dataset for the ANN and regression models are gathered from the existing literature for the as-built AlSi10Mg sample fabricated via a selective laser melting process. Additionally, a new experiment was conducted in this study as part of data collection for the ANN model. The ANN model and regression model were developed using 108 data points (Appendix 1) and a further 27 data points (Appendix 2) were used to assess the precision of the model selected randomly. The model's predicted output was compared with the experimental value reported in the literature. Both the artificial neural network and regression models were implemented using MATLAB R2023b. The model utilises the laser power denoted by (P), layer thickness denoted (T), scan speed denoted by (V), and hatch spacing denoted by (H) as the input variables. The input data range for the ANN model was taken as 150–1000 W for laser power, 20–80 μm for layer thickness, 195–2400 mm/s for the scan speed, and 42–240 μm for hatch spacing.

Experiment

The gas-atomised AlSi10Mg powder of average particle size range 20–63 μm was used in the manufacturing which primarily consists of up to 10 % silicon, a trace amount of magnesium and iron. The detailed composition of the powder is shown in Table 1.

The samples were fabricated using the SLM process in RenAM 500E machine (UK). The key manufacturing parameters of the manufacturing include laser power is 275 W, layer thickness is 30 μm , scanning speed is 2000 mm/s and hatch distance is 80 μm . The build chamber was filled with 99.999 % pure argon gas to protect from the oxidation of the powder. The building direction has been kept horizontal and the layers were oriented to an angle of 67° from the preceding layer. The temperature of the build plate was maintained at 80 °C initially to avoid failure due to the change in temperature between the bottom layer and the building plate.

The flat-type sub-size tensile test specimens of gauge length 25 mm were manufactured following the ASTM E8 standard as shown in Fig. 2. The as-built components were kept at stress relieved at 300±10 °C for 2 h and air cooled.

Tensile tests were conducted on the universal testing machine, model ETM (Wance, China) of 50 kN capacity at a strain rate of 1 mm/min. The axial displacement was monitored by a computer integrated video extensometer connected to a tensile testing machine which captures real-time elongation data to construct the stress–strain diagram.

The yield strength was determined using the 0.2 % offset method using the stress–strain Excel graph. First, the linear (elastic) region of the stress–strain graph was identified to determine the slope (elastic modulus). A line was then drawn parallel to this linear part of the graph, passing through 0.2 % of the strain (Y-axis). The yield strength is defined as the point where the offset line intersects the stress–strain curve.

Development of an artificial neural network

MATLAB R2023b version was used to implement the ANN model using the neural network fitting tool within the deep learning toolbox. A supervised machine learning approach was employed to predict the strength of the material. The training was run for the target epoch value of 1000 with four input variables (laser power, layer thickness, scan speed/velocity, and hatch spacing/distance) and two outputs (yield and tensile strength).

It is worth noting that the neural network uses two two-layer feedforward designs. The input layer and output layer use hyperbolic tangent (tansig) and liner (purelin) transfer function respectively as shown in Fig. 3.

The neural network structure consists of 10 neurons in the hidden layers and 2 neurons corresponding to the output variables. This configuration is selected based on the complexity and performance requirements of the ANN model. The hidden layer is designed to effectively extract features from the input layers. A common approach to determine the number of neurons in the hidden layer is to double the number of neurons in the input layer and add the number of neurons in the output layer¹.

The adopted data is categorised into three different categories randomly training, validation, and testing in 80:10:10 ratio. The Levenberg–Marquardt algorithm (trainlm) is used for the training of the ANN model, which is often considered the fastest back-propagation algorithm. The input and output data are normalised between –1 and +1 to achieve dimensional consistency and to achieve compatibility with tansig transfer function using equation (1) [10]:

$$M_{norm} = \frac{2 \times (N_i - N_{min})}{N_{max} - N_{min}} - 1, \quad (1)$$

where M_{norm} is normalised parameters;

N_i is actual data;

N_{min} and N_{max} are the minimum and maximum values of the actual data respectively.

Polynomial regression analysis

A multivariate polynomial regression model was created using MATLAB to create the correlation between the dependent variable (ultimate tensile strength) and independent variables (laser power, layer thickness, scan speed/velocity, and hatch spacing/distance). The same experimental results that were used to develop the ANN model are utilised for

¹ Livshin I. *Artificial Neural Networks with Java: Tools for Building Neural Network Applications*. Chicago, 2019. 575 p. DOI: [10.1007/978-1-4842-4421-0](https://doi.org/10.1007/978-1-4842-4421-0).

Table 1. Composition of AlSi10Mg powder
Таблица 1. Состав порошка AlSi10Mg

Element	Al	Si	Mg	Fe	N	O	Ti	Zn	Mn	Ni	Cu	Pb	Sn
Mass. %	Balance	9-11	0.25-0.45	<0.25	<0.20	<0.20	<0.15	<0.10	<0.10	<0.05	<0.05	<0.02	<0.02

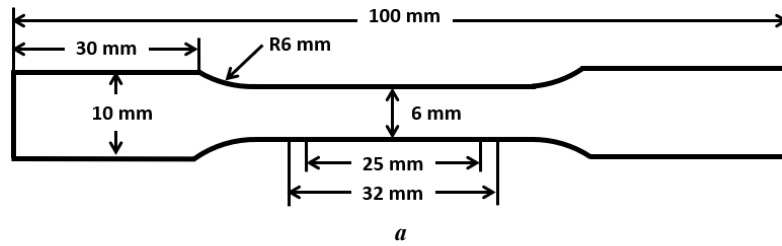


Fig. 2. Sample details: a – sample dimension; b – fabricated sample
Рис. 2. Параметры образца: a – размеры; b – образец

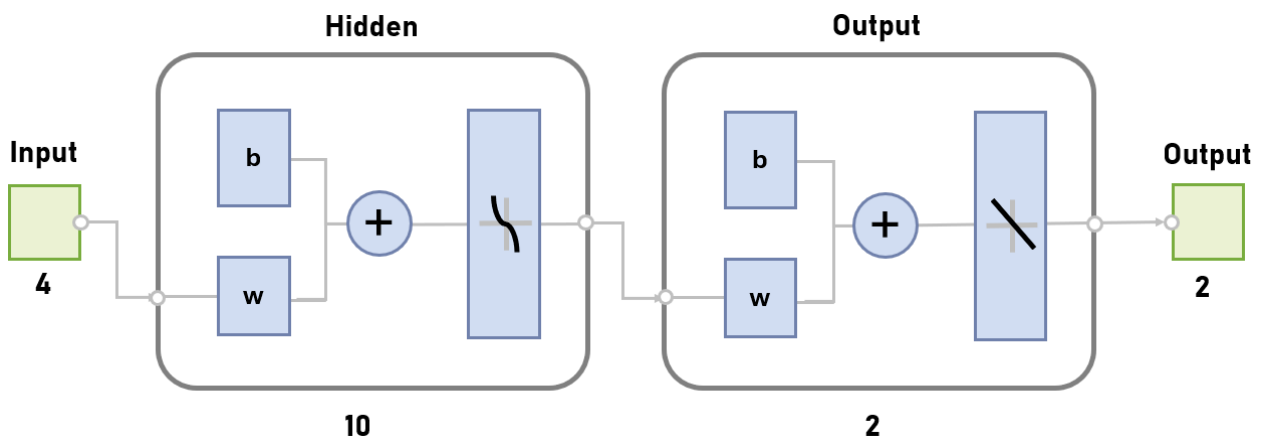


Fig. 3. Network architecture
Рис. 3. Архитектура сети

the multivariate regression model. The multi-variant polynomial regression, *fitlm* facilitates the modelling of the relation between multiple input predictors and a single response. The model computes coefficients for each set of variables and the intercept terms. It determines the impact of each predictor on the response variable. The second-degree polynomial function is calculated using statistics and machine learning toolbox:

$$Y(X) = a_0 + \sum_{i=0}^N a_i X_i + \sum_{i < j}^N a_{ij} X_i X_j + \sum_{i=0}^N a_{ij} X_i^2, \tag{2}$$

where Y is the predicted response;
 a_0 is the intercept coefficient;
 $a_i X_i$ are the linear terms;
 $a_{ij} X_i X_j$ are the interaction terms;
 $a_{ij} X_i^2$ are the square terms.

RESULTS

Experimental values

The tensile test of the SLM fabricated specimen is performed as per ASTM E8 standard and results are presented in the Table 2. In the tensile test, the specimen is broken in the direction perpendicular to the applied force as shown in Fig. 4. The tensile strength of the specimen is reported as 436.95 MPa at the maximum force of 15.7 KN and the specimen exhibits an elongation of 9.59 %. The failure of the specimen is identified as brittle and sudden occurring before the material entered the plastic

zone as shown in stress–strain diagram (Fig. 5). The yield strength was found to be 58 MPa, calculated using the 0.2 % proof/offset method.

Artificial neural network results

The performance of the developed ANN is assessed using various evaluations and analytical metrics. The comprehensive output of the ANN is shown in Table 3.

ANN regression plot for overall training, validation, and test data for yield and tensile strength is shown in Fig. 6. The X -axis represents the value of the target (experimental data) and the Y -axis shows the output data predicted using the ANN model. The dotted line illustrates the ideal correlation where actual and predicted values are equal, while the solid line represents the actual/true correlation between the X and Y axis.

It is observed that the correlation coefficient (R -value) for the overall output of the training, validation, and test data is 0.96, 0.94, and 0.91 respectively. The overall R -value is 0.96 which shows a strong correlation between actual (target) and predicted output.

The value at which MSE between actual and predicted values converges is shown by the best validation of the performance curve. The back-propagation algorithm calibrates the values of weights and biases with each iteration and generates the lowest MSE value. The number of epochs represents the number of iterations performed by the network to converge it to a minimum [11]. The performance curve of this study is shown in Fig. 7, which shows the best performance of the model of value 0.024 at epoch 44. From the performance curve, it was evident that there is no over-fitting observed. Additionally, similar trends have been observed for training, testing, and validation data.

Table 2. Tensile test results
Таблица 2. Результаты испытаний на растяжение

Mechanical properties	Values
Yield stress, MPa	58
Tensile strength, MPa	436.95
Elongation, %	9.59
Maximum force, KN	15.73



Fig. 4. Fractured sample
Рис. 4. Разрушенный образец

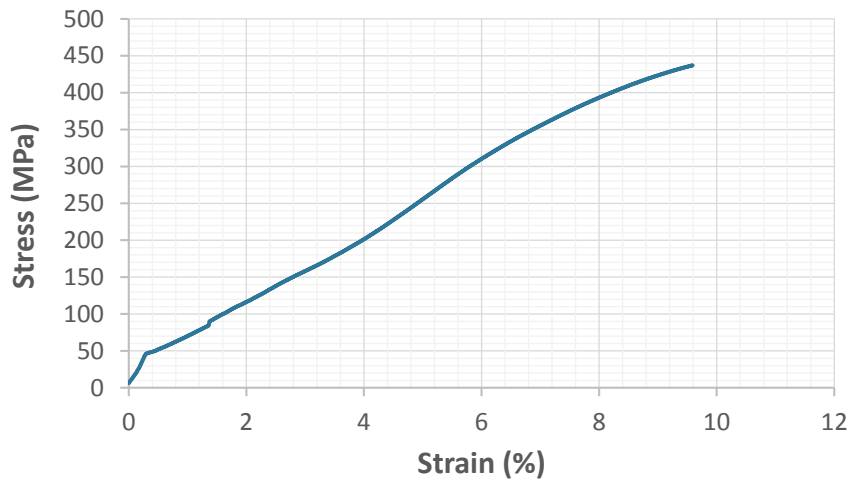


Fig. 5. Stress–strain diagram
 Рис. 5. Диаграмма «напряжение – деформация»

Table 3. Artificial neural network output
 Таблица 3. Выходные данные искусственной нейронной сети

ANN output	Value
Epoch value	50
R-value – training	0.96
R-value – validation	0.94
R-value – test	0.91
R-value – all	0.96
MSE	0.0155

Development of mathematical formula based on ANN

Once the ANN model is trained it can be translated into a mathematical equation or model by integrating transfer function using weights and biases as depicted in equation [10]:

$$Y = b_0 + \sum_{k=1}^h \left(w_k \times f_{sig} \left(b_{hk} + \sum_{i=1}^m w_{ik} X_i \right) \right), \quad (3)$$

where Y is the normalised output variables;
 b_0 is the bias at the output layer;
 w_k is the weight that connects between the k th hidden layer and the single output neuron;
 b_{hk} is the bias at the k th neuron of the hidden layer;
 h and m are the number of neurons in the hidden layer and input layers, respectively;
 w_{ik} is the connection weight between the i th input variable and the hidden layer;
 X_i is the normalised input variable;
 f_{sig} is the transfer function used to train the ANN.

The number of neurons connected to the input and hidden layer is $h=10$. The adopted transfer function between the input and output layers is *tansig* ($f_{sig} = \text{tansig}$) and *purelin* respectively.

Therefore, the equation (3) can be converted into equation [12]:

$$TS_n = -0.0825 + [W] \times [q]^T, \quad (4)$$

where TS_n is the normalised tensile strength;
 $[W] = [1.279 \ 0.6628 \ -2.9155 \ 2.6693 \ -2.8315 \ -0.3615 \ 3.2800 \ 0.7236 \ -1.8831]$;
 $[q] = [\tanh A_1 \ \tanh A_2 \ \tanh A_3 \ \tanh A_4 \ \tanh A_5 \ \tanh A_6 \ \tanh A_7 \ \tanh A_8 \ \tanh A_9 \ \tanh A_{10}]$;

$$\tanh = f(x) = \frac{e^x - e^{-x}}{e^x + e^{-x}}.$$

The normalised variables A_1 to A_{10} can be calculated using matrix equations:

$$\begin{bmatrix} A_1 \\ A_2 \\ A_3 \\ A_4 \\ A_5 \\ A_6 \\ A_7 \\ A_8 \\ A_9 \\ A_{10} \end{bmatrix} = \begin{bmatrix} 0.4549 & -0.2335 & 1.5844 & -1.7360 \\ 0.6977 & 0.1801 & 4.0404 & 3.2143 \\ 0.5458 & 5.7727 & 4.3710 & -6.2395 \\ -1.9850 & -0.4610 & 1.2824 & -0.8306 \\ -4.5821 & 0.2266 & 1.3249 & -1.1109 \\ -2.520 & 5.4207 & 1.8587 & 0.2827 \\ -0.4423 & 0.1586 & -0.5219 & 3.0538 \\ -0.9543 & 2.7184 & 0.4837 & 0.6755 \\ 1.6739 & -2.8579 & 0.3978 & 2.3733 \\ 1.2295 & 3.2789 & -2.5835 & 1.1224 \end{bmatrix} \begin{bmatrix} P \\ T \\ V \\ H \end{bmatrix} + \begin{bmatrix} -2.5042 \\ 1.6432 \\ 4.3932 \\ -0.6902 \\ -1.3171 \\ -0.7925 \\ 0.3307 \\ -0.6097 \\ -0.9304 \\ -2.5837 \end{bmatrix}$$

The normalised tensile strength in equation (4) needs to be de-normalised to derive the required predictive mathematical equation. The de-normalised equation to predict the tensile strength is shown in equation (5):

$$TS_d = \frac{(TS_n + 1) \times 318.8}{2} + 160, \quad (5)$$

where TS_d is the de-normalised tensile strength, the minimum and maximum values of input tensile strength are 160 and 478.8 MPa respectively.

Hence equation (5) represents the ANN-based mathematical model to predict the tensile strength for the provided value of laser power, layer thickness, scan speed, and hatch spacing.

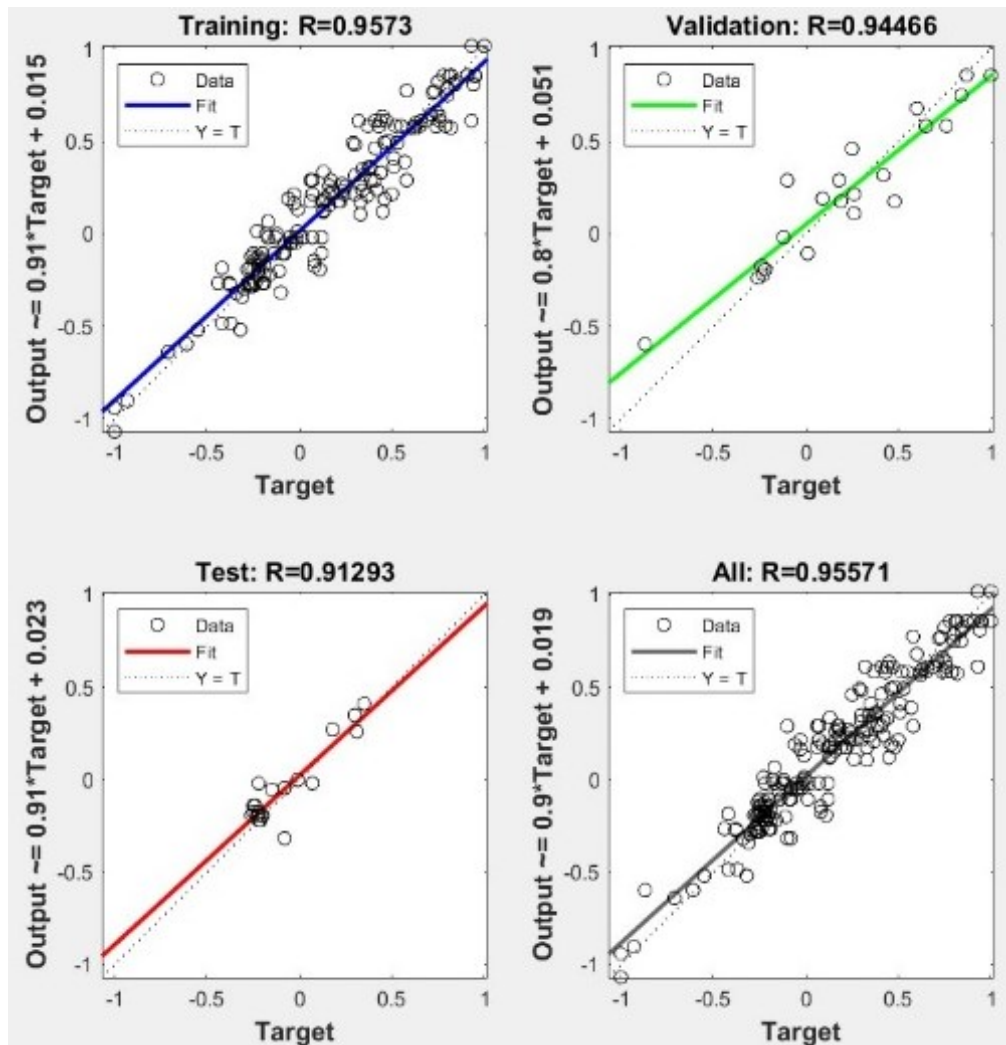


Fig. 6. Regression plot
Рис. 6. Графік регресії

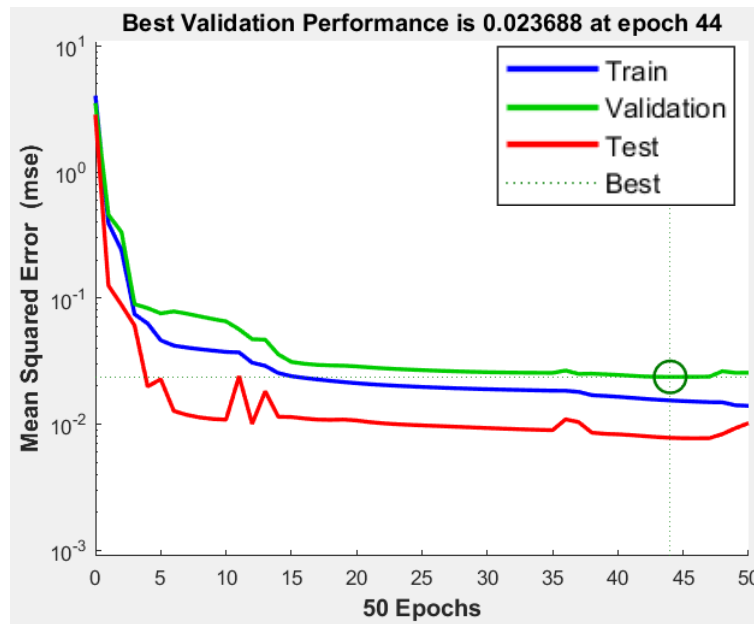


Fig. 7. Performance plot
Рис. 7. График эффективности

Polynomial regression analysis using MATLAB

The experimental results are fitted in the quadratic equation (2) resulting in the proposed regression model as shown in equation:

$$\begin{aligned}
 T.S = & -33.83 + 3.1866 \times P - 0.0435 \times T + 0.2681 \times V - \\
 & - 2.9162 \times H - 0.0313 \times P \times T - 0.0004 \times P \times V - \\
 & - 0.0182 \times P \times H - 0.0068 \times T \times V + \\
 & + 0.1159 \times T \times H + 0.0025 \times V \times H + 0.0005 \times P^2 + \\
 & + 0.0186 \times T^2 - 0.0001 \times V^2 + 0.0045 \times H^2
 \end{aligned}
 \tag{6}$$

where *T.S* is the tensile strength;
P is the laser power;
T is the layer thickness;
V is the scan speed;
H is the hatch spacing.

DISCUSSION

Validation of mathematical formula based on ANN

The comparison between ANN predicted output and mathematical model predicted output is plotted in Fig. 8. Evidently, the proposed mathematical model replicates the ANN output perfectly with a goodness of fit of (*R*²)=1 and can be used to predict the tensile strength without running the ANN model. Fig. 9 shows the trend comparison between actual experimental values and predicted output. The mean absolute percentage error (MAPE) between the experimental and predicted value stands at 4.74 % which demonstrates quite a good accuracy. The goodness of fit (*R*²) between the ANN predict-

ed data and actual experimental value is 0.898 (Fig. 10 a). This indicates that the predicted value matches the actual value by 89.8 %.

Validation of regression model

The calculated goodness of fit between the experimental value and predicted value using the polynomial regression model is 0.68, which means the predicted value aligns with the experimental value with an accuracy of 68 %, as shown in Fig. 10 b.

Additionally, the mean absolute percentage error (MAPE) calculated between experimental and predicted values are 8.83 %, which shows a moderate level of deviation with respect to experimental values. Fig. 11 shows the trend comparison between actual and predicted values.

F-test and standard error of the regression coefficients

The *F*-test of the regression model is performed to assess the predictive power and the significance of the relationship between dependent and independent variables using equations from:

$$SST = \sum (Y_i - \bar{Y})^2;$$

$$SSR = \sum (\hat{Y}_i - \bar{Y})^2;$$

$$SSE = \sum (Y_i - \hat{Y}_i)^2;$$

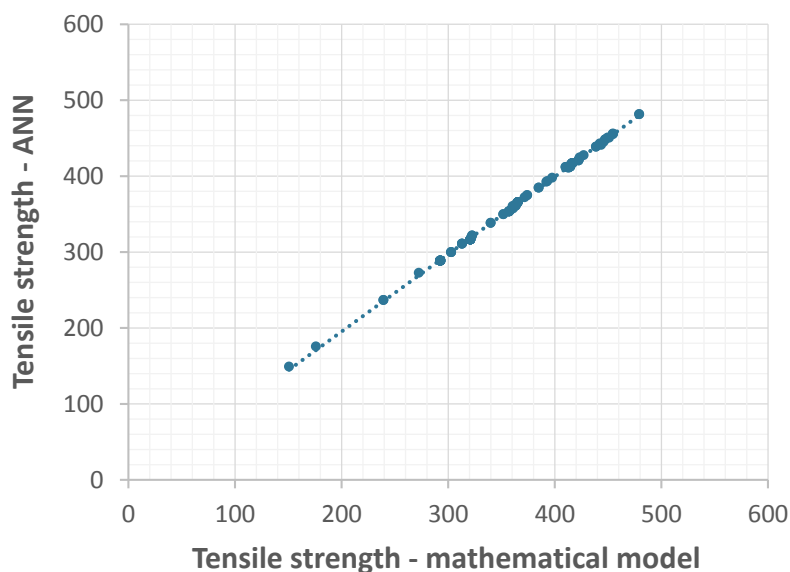


Fig. 8. Tensile strength predicted using ANN vs mathematical model
Рис. 8. Предел прочности, рассчитанный с помощью ИНС и математической модели

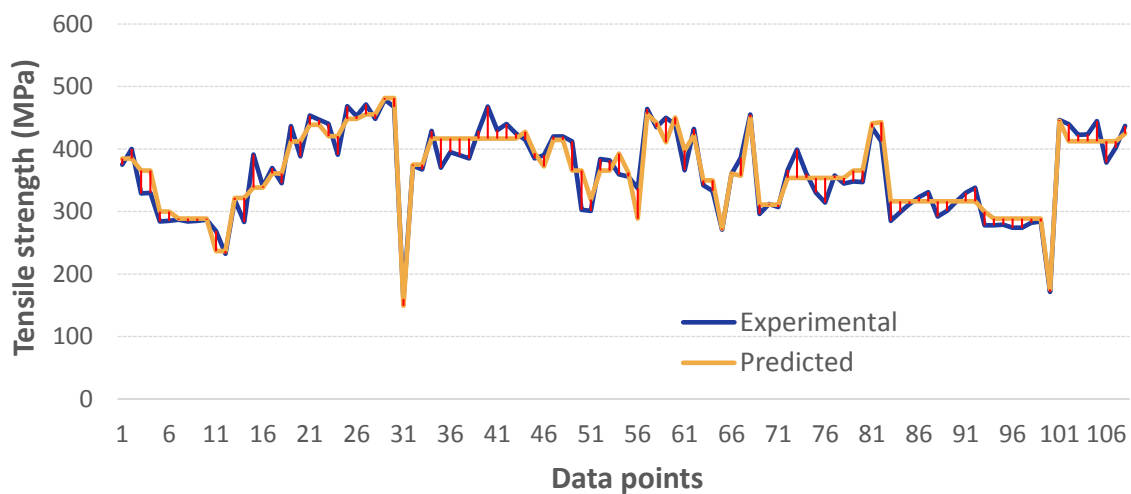


Fig. 9. Experimental vs predicted values of tensile strength (ANN)
Рис. 9. Экспериментальные и спрогнозированные значения предела прочности (ИНС)

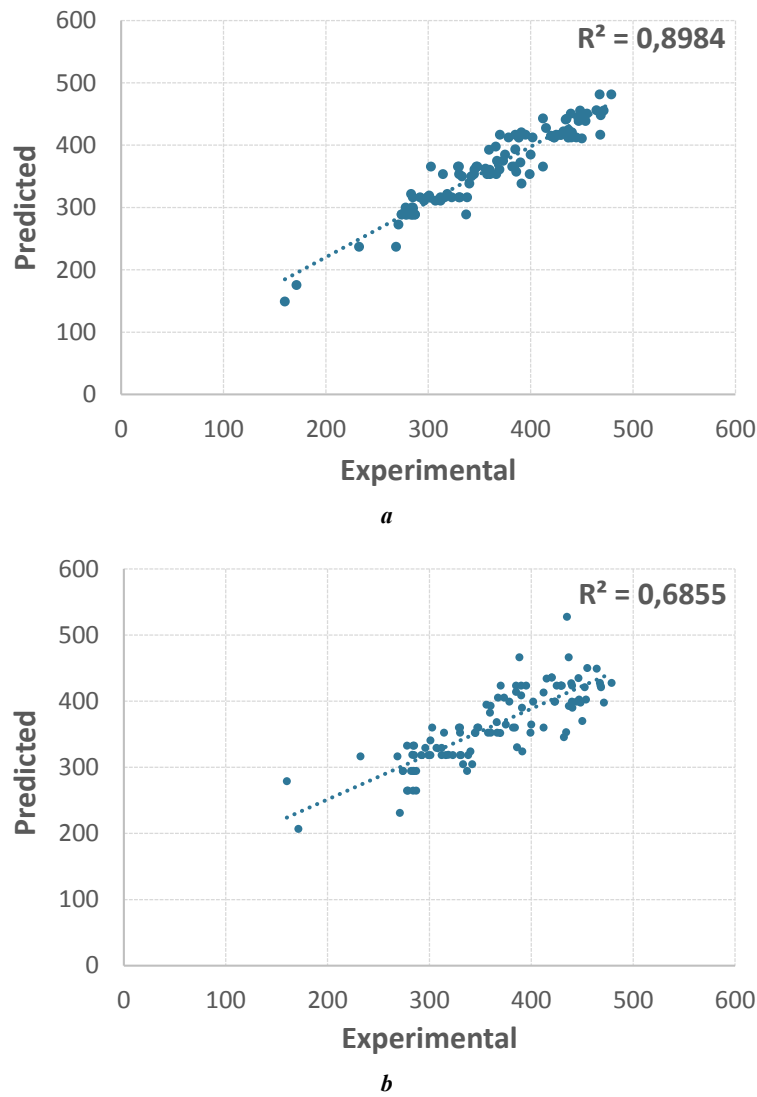


Fig. 10. Comparison of the measured vs predicted tensile strength:
a – ANN-based model; **b** – polynomial regression model
Рис. 10. Сравнение экспериментального и спрогнозированного предела прочности:
a – модель на основе ИНС; **b** – модель полиномиальной регрессии

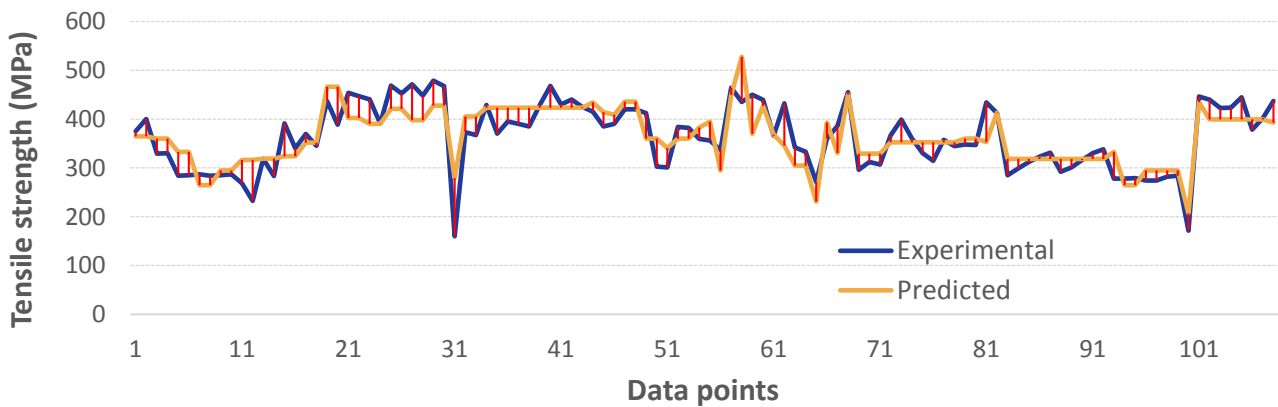


Fig. 11. Experimental vs predicted values of tensile strength (polynomial regression)
Рис. 11. Экспериментальные и спрогнозированные значения предела прочности (полиномиальная регрессия)

$$MSR = \frac{SSR}{k};$$

$$MSE = \frac{SSE}{n-k-1};$$

$$F - statistic = \frac{MSR}{MSE},$$

where *SST* is total sum of squares;

SSR is regression sum of squares;

SSE is residual sum of squares;

MSR is mean square for regression;

MSE is mean square for error;

Y_i is experimental values;

\bar{Y} is mean of experimental values;

\hat{Y}_i is predicted values;

k is No of independent variable;

n-k-1 is degrees of freedom.

Since *F* calculated 13.36 > *F_{critical}* at the 0.05 significance level, there is statistically significant relationship between the predictor and response variable.

The standard error of the regression coefficient measures the variability of the estimated coefficients if the study were repeated. It measures the uncertainty associated with the regression model and how much it is expected to vary due to sampling variability. The analysis is performed using MATLAB using equations:

$$X = \begin{bmatrix} 1 & P_1 & T_1 & V_1 & H_1 & P_1T_1 & P_1V_1 \\ 1 & P_2 & T_2 & V_2 & H_2 & P_2T_2 & P_2V_2 \\ \cdot & \cdot & \cdot & \cdot & \cdot & \cdot & \cdot \\ \cdot & \cdot & \cdot & \cdot & \cdot & \cdot & \cdot \\ 1 & P_n & T_n & V_n & H_n & P_nT_n & P_nV_n \end{bmatrix};$$

$$\begin{bmatrix} P_1H_1 & T_1V_1 & T_1H_1 & V_1H_1 & P_1^2 & T_1^2 & V_1^2 & H_1^2 \\ P_1H_2 & T_2V_2 & T_2H_2 & V_2H_2 & P_2^2 & T_2^2 & V_2^2 & H_2^2 \\ \cdot & \cdot \\ \cdot & \cdot \\ P_nH_n & T_nV_n & T_nH_n & V_nH_n & P_n^2 & T_n^2 & V_n^2 & H_n^2 \end{bmatrix};$$

$$\text{Residual Variance, } \sigma^2 = \frac{SSR}{n-p};$$

Variance – Covariance Matrix of Coefficients,

$$\text{Var}(\hat{\beta}) = \sigma^2 (X'X)^{-1}.$$

The standard errors are the square roots of the diagonal elements of variance-covariance matrix:

Standard error of Coefficients

$$SE(\hat{\beta}) = \sqrt{\text{diag}(\text{Var}(\hat{\beta}))}.$$

The result of the study is summarised in Table 4. As stated, the standard error of the coefficient provides the measure of uncertainty of the coefficients. The relatively small error indicates the precise estimate and significance of the impact of the coefficient as seen for the variables *V*, *V²*, *P²*, *T²*, *H²*, *P·T*, *P·V*, *P·H*, *T·V*, and *V·H*. In contrast, the relatively large standard error for the variable *T* and the intercept suggest that the estimations are not very precise and likely to vary more across the samples.

Validation of proposed models with the new data sets

ANN-based mathematical and polynomial regression models are validated on the new set of 27 data points, the datasets beyond those that are used in the model development. The experimental values of the data points are collected from the previous literature. ANN-based mathematical equation (5) and polynomial regression equation (6) were used for the prediction of the tensile strength of the new input datasets and the same was compared with the experimental values to assess the robustness of the model. The validation was done using statistical parameters such as goodness of fit (*R*-square) to measure how well the model fits the data, mean absolute percentage error (MAPE) to provide the relative accuracy of the prediction, mean absolute error (MAE) to measure overall prediction error and root mean squared error (RMSE) to find out the impact of the larger error as outlined in equations:

$$R^2 = 1 - \frac{\text{Sum of squares of residuals}}{\text{Total sum of squares}};$$

$$\text{Mean absolute percentage error (MAPE)} = \frac{1}{n} \sum \frac{\text{Prediction} - \text{Actual}}{\text{Actual}} \times 100;$$

$$\text{Mean absolute error (MAE)} = \frac{1}{n} \sum |\text{Prediction} - \text{Actual}|;$$

$$\text{Root Mean Square Error (RMSE)} = \sqrt{\frac{\sum (\text{Prediction} - \text{Actual})^2}{n}}.$$

Fig. 12 illustrates the comparison of experimental values with an ANN-based mathematical model and polynomial regression model. The mean error percentage was found to be 11.1 and 16.8 % for ANN-based equation and polynomial regression model respectively. The summary of the validation of the two models is shown in Table 5.

Comparison and validation with prior research

The experimental results of tensile properties assessment of SLM fabricated AlSi10Mg sample demonstrate strong consistency with the previous studies [13–17].

Table 4. Standard error of a regression coefficient
Таблица 4. Среднее квадратическое отклонение коэффициента регрессии

Variable	Coefficient	Standard errors of the regression
Intercept	-33.83	156.8213
P	3.1866	0.5771
T	-0.0435	4.3601
V	0.2681	0.0783
H	-2.9162	0.741
$P \cdot T$	-0.0313	0.006
$P \cdot V$	-0.0004	0.0002
$P \cdot H$	-0.0182	0.0024
$T \cdot V$	-0.0068	0.0015
$T \cdot H$	0.1159	0.0134
$V \cdot H$	0.0025	0.0007
P^2	0.0005	0.0003
T^2	0.0186	0.0397
V^2	-0.0001	0
H^2	0.0045	0.0022

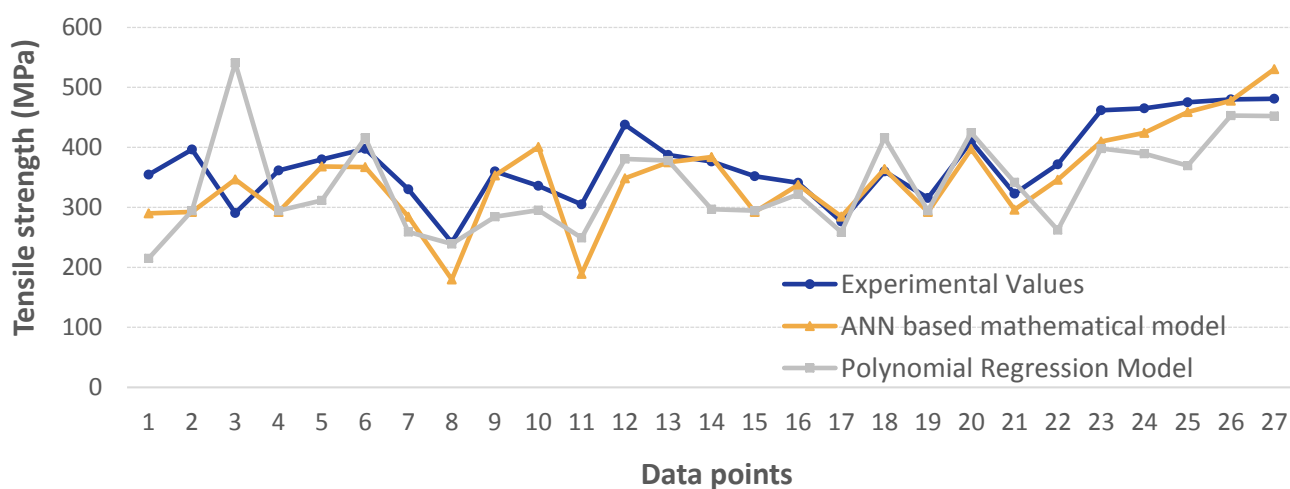


Fig. 12. Experimental vs predicted values of tensile strength for new data points
Рис. 12. Экспериментальные и спрогнозированные значения предела прочности для новых точек данных

Table 5. Summary of the validation of ANN-based and regression models
Таблица 5. Результат оценки модели на основе ИНС и регрессионной модели

Evaluation metric	ANN based mathematical model	Polynomial regression model
R -square (R^2)	0.68	0.25
Mean absolute error (MAE)	39.44	61.17
Mean absolute percentage error (MAPE)	11.10	16.89
Root mean square error (RMSE)	50.37	79.28

The tested specimen exhibited significantly higher tensile strength approximately 25 % higher than that of conventionally cast specimens [18].

The developed ANN model and regression model clearly show the dependency of the output on the key process parameters i. e. laser power, layer thickness, hatch spacing, and scan speed. The observation aligns with the previous studies, which identified the laser power and scan speed as the common predominant influencing factors on the material properties [6; 9].

The results clearly show that the ANN model outperformed the regression model, showing superior predictability for the material properties. This aligns with previous studies, that highlight the ability of the ANN model to handle complex, multi-functional, non-linear relationships [6; 9; 19]. For example, M. Khalefa [8] achieved an MSE of 0.0335 for tensile strength prediction using ANN, while other researchers [9] reported MSE values of 0.232, 0.395, 0.122 for relative density, surface roughness, and hardness respectively. Similarly, Ghetya et al. [7] achieved the MSE value less than 3 % using an ANN model for tensile strength prediction. In this study, the accuracy of the ANN surpasses some earlier findings by predicting material properties with an MSE value of 0.0155 and an overall R value of 0.96. This improvement is attributed to the use of a wider range of datasets for model training, which enhances its reliability and provides a comprehensive representation of the problem [20].

Contributions and implications of the study

The current study contributes to the additive manufacturing field by providing a precise machine learning based approach for the prediction of material properties using input process parameters. The work narrows down on the prediction of tensile strength of SLM manufactured AlSi10Mg alloy, offering a useful tool for manufacturing and design engineers.

This finding also offers a practical and efficient solution by minimising manufacturing time and resource usage. By enabling the real time optimisation of manufacturing costs, the research supports the production of high-quality parts.

Furthermore, as the machine learning model is trained to predict the properties under various conditions, the study also provides further advancements in this area by encouraging input parameters optimisation

to reduce material defects through the correlation between the inputs and outputs.

The study presents a boarder implication as it empowers the adoption and integration of machine learning applications in additive manufacturing. The work further promotes the artificial intelligence, data driven approach in advanced material properties optimisation.

Limitation of proposed ANN model

The proposed ANN model comes with certain limitations as follows:

1. The input variables should fall within the range of minimum and maximum range of the variables used in the development of the ANN model.
2. The input and output should be normalised using equation (1) before feeding it into the ANN model.
3. ANN is a complex system compared to the regression model, which requires more computational resources. ANN typically requires more datasets to train the model effectively. The availability of a limited experimental dataset can limit the capability of the ANN and cause overfitting.

CONCLUSIONS

In this study an artificial neural network model is adapted as a mathematical equation model and a regression model is developed to predict the tensile strength of additively manufactured (SLM) AlSi10Mg alloy based on existing experimental data. The effectiveness of the ANN-based mathematical model is then evaluated and compared to the regression model on the datasets distinct from those used in the model development. The following conclusion can be drawn from the study:

1. The proposed ANN-based mathematical model exhibits superior performance compared to the regression model with the R^2 (goodness of fit) value of 0.898 against 0.685 of the regression value for the input data sets used for the model development. The ANN-based mathematical model also performed comparatively well for the new datasets yielding a regression value of R^2 as 0.68.
2. Notably, the ANN-based mathematical model demonstrates low mean absolute percentage error of 4.74, and 11.1 % for the datasets used for model development and the new input data-sets respectively.
3. This concludes that the accuracy of the ANN-based mathematical model is good enough to consider it as

the viable option for the prediction. However, the efficacy of the ANN model is limited for the new input datasets, because of the limited data availability. The inclusion of more datasets into the development and validation of the ANN model is expected to bring more accuracy. Exploring various neural network techniques and fine tuning the hyperparameters can improve the model performance further.

REFERENCES

- Rouf S., Malik A., Singh N., Raina A., Naveed N., Siddiqui M.I.H., Haq M.I.U.I. Additive manufacturing technologies: Industrial and medical applications. *Sustainable Operations and Computers*, 2022, vol. 3, pp. 258–274. DOI: [10.1016/j.susoc.2022.05.001](https://doi.org/10.1016/j.susoc.2022.05.001).
- Sercombe T.B., Li X. Selective laser melting of aluminium and aluminium metal matrix composites: review. *Materials Technology*, 2016, vol. 31, no. 2, pp. 77–85. DOI: [10.1179/1753555715Y.0000000078](https://doi.org/10.1179/1753555715Y.0000000078).
- Chowdhury S., Yadaiah N., Prakash Ch., Ramakrishna S., Dixit S., Gulta L.R., Buddhi D. Laser Powder Bed Fusion: A State-of-the-Art Review of the Technology, Materials, Properties & Defects, and Numerical Modelling. *Journal of Materials Research and Technology*, 2022, vol. 20, pp. 2109–2172. DOI: [10.1016/j.jmrt.2022.07.121](https://doi.org/10.1016/j.jmrt.2022.07.121).
- Xu Yongjun, Liu Xin, Cao Xin et al. Artificial intelligence: A powerful paradigm for scientific research. *The Innovation*, 2021, vol. 2, no. 4, article number 100179. DOI: [10.1016/j.xinn.2021.100179](https://doi.org/10.1016/j.xinn.2021.100179).
- Osman E.-S., Aggour M.A. Artificial neural network model for accurate prediction of pressure drop in horizontal and near-horizontal-multiphase flow. *Petroleum Science and Technology*, 2002, vol. 20, no. 1-2, pp. 1–15. DOI: [10.1081/LFT-120002082](https://doi.org/10.1081/LFT-120002082).
- Shubham P., Sharma A., Vishwakarma P.N., Phanden R.K. Predicting Strength of Selective Laser Melting 3D Printed AlSi10Mg Alloy Parts by Machine Learning Models. *8th International Conference on Signal Processing and Integrated Networks (SPIN)*. India, 2021, pp. 745–749. DOI: [10.1109/SPIN52536.2021.9566142](https://doi.org/10.1109/SPIN52536.2021.9566142).
- Ghetiya N.D., Patel K.M. Prediction of Tensile Strength in Friction Stir Welded Aluminium Alloy Using Artificial Neural Network. *Procedia Technology*, 2014, vol. 14, pp. 274–281. DOI: [10.1016/j.protcy.2014.08.036](https://doi.org/10.1016/j.protcy.2014.08.036).
- Khalefa M. Use of artificial neural network for prediction of mechanical properties of Al–Si alloys synthesized by stir casting. *Journal of Petroleum and Mining Engineering*, 2019, vol. 21, pp. 97–103. DOI: [10.21608/jpme.2019.13857.1004](https://doi.org/10.21608/jpme.2019.13857.1004).
- Alamri F., Maalouf M., Barsoum I. *Prediction of Porosity, Hardness and Surface Roughness in Additive Manufactured AlSi10Mg Samples: preprint*. 2023. DOI: [10.21203/rs.3.rs-3186551/v1](https://doi.org/10.21203/rs.3.rs-3186551/v1).
- Lawal A.I., Aladejari A.E., Onifade M., Bada S., Idris M.A. Predictions of elemental composition of coal and biomass from their proximate analyses using ANFIS, ANN and MLR. *International Journal of Coal Science and Technology*, 2024, vol. 8, pp. 124–140. DOI: [10.1007/s40789-020-00346-9](https://doi.org/10.1007/s40789-020-00346-9).
- Owunna I., Ikpe A.E. Modelling and prediction of the mechanical properties of TIG welded joint for AISI 4130 low carbon steel plates using artificial neural network (ANN) approach. *Nigerian Journal of Technology (NIJOTECH)*, 2019, vol. 38, no. 1, pp. 117–126. DOI: [10.4314/njt.v38i1.16](https://doi.org/10.4314/njt.v38i1.16).
- Mahmoodi-Babolan N., Heydari A., Nematollahzadeh A. Removal of methylene blue via bioinspired catecholamine/starch superadsorbent and the efficiency prediction by response surface methodology and artificial neural network-particle swarm optimization. *Bioresource Technology*, 2019, vol. 294, article number 122084. DOI: [10.1016/j.biortech.2019.122084](https://doi.org/10.1016/j.biortech.2019.122084).
- Prasad M., Kempaiah U.N., Mohan R.M., Nagara M. Microstructure, Tensile and Compression Behavior of AlSi10Mg Alloy Developed by Direct Metal Laser Sintering. *Indian Journal of Science and Technology*, 2021, vol. 14, no. 45, pp. 3346–3353. DOI: [10.17485/IJST/v14i45.1705](https://doi.org/10.17485/IJST/v14i45.1705).
- Zhuo Longchao, Wang Zeyu, Zhang Hongjia, Yin Enhuai, Wang Yanlin, Xu Tao, Li Chao. Effect of post-process heat treatment on microstructure and properties of selective laser melted AlSi10Mg alloy. *Materials Letters*, 2019, vol. 234, pp. 196–200. DOI: [10.1016/j.matlet.2018.09.109](https://doi.org/10.1016/j.matlet.2018.09.109).
- Mei Jiahe, Han Ying, Zu Guoqing, Zhu Weiwei, Zhao Yu, Chen Hua, Ran Xu. Achieving Superior Strength and Ductility of AlSi10Mg Alloy Fabricated by Selective Laser Melting with Large Laser Power and High Scanning Speed. *Acta Metallurgica Sinica (English Letters)*, 2022, vol. 35, pp. 1665–1672. DOI: [10.1007/s40195-022-01410-w](https://doi.org/10.1007/s40195-022-01410-w).
- Zhou Suyuan, Su Yang, Gu Rui, Wang Zhenyu, Zhou Yinghao, Ma Qian, Yan Ming. Impacts of Defocusing Amount and Molten Pool Boundaries on Mechanical Properties and Microstructure of Selective Laser Melted AlSi10Mg. *Materials*, 2019, vol. 12, no. 1, article number 73. DOI: [10.3390/ma12010073](https://doi.org/10.3390/ma12010073).
- Zhang Shuzhe, Wei Pei, Chen Zhen, Li Bobo, Huang Ke, Zou Yatong, Lu Bingheng. Graphene/ZrO₂/aluminum alloy composite with enhanced strength and ductility fabricated by laser powder bed fusion. *Journal of Alloys and Compounds*, 2022, vol. 910, article number 164941. DOI: [10.1016/j.jallcom.2022.164941](https://doi.org/10.1016/j.jallcom.2022.164941).
- Wei Pei, Chen Zhen, Zhang Shuzhe, Li Bobo, Han Jiang, Lu Bingheng. Microstructure and mechanical properties of graphene and nano-zirconia reinforced AlSi10Mg composite fabricated by laser powder bed fusion. *Materials Science and Engineering: A*, 2023, vol. 864, article number 144574. DOI: [10.1016/j.msea.2022.144574](https://doi.org/10.1016/j.msea.2022.144574).
- Amor N., Noman M.T., Ismail A., Petru M., Sebastian N. Use of an Artificial Neural Network for Tensile Strength Prediction of Nano Titanium Dioxide Coated Cotton. *Polymers*, 2022, vol. 14, no. 5, article number 937. DOI: [10.3390/polym14050937](https://doi.org/10.3390/polym14050937).
- Khan A.Q., Awan H.A., Rasul M., Siddiqi Z.A., Pimanmas A. Optimized artificial neural network model for accurate prediction of compressive strength of normal and high strength concrete. *Cleaner Materials*, 2023, vol. 10, article number 100211. DOI: [10.1016/j.clema.2023.100211](https://doi.org/10.1016/j.clema.2023.100211).

СПИСОК ЛИТЕРАТУРЫ

- Rouf S., Malik A., Singh N., Raina A., Naveed N., Siddiqui M.I.H., Haq M.I.U.I. Additive manufacturing technologies: Industrial and medical applications // *Sustainable Operations and Computers*. 2022. Vol. 3. P. 258–274. DOI: [10.1016/j.susoc.2022.05.001](https://doi.org/10.1016/j.susoc.2022.05.001).
- Sercombe T.B., Li X. Selective laser melting of aluminium and aluminium metal matrix composites: review // *Materials Technology*. 2016. Vol. 31. № 2. P. 77–85. DOI: [10.1179/1753555715Y.0000000078](https://doi.org/10.1179/1753555715Y.0000000078).
- Chowdhury S., Yadaiah N., Prakash Ch., Ramakrishna S., Dixit S., Gulta L.R., Buddhi D. Laser Powder Bed Fusion: A State-of-the-Art Review of the Technology, Materials, Properties & Defects, and Numerical Modelling // *Journal of Materials Research and Technology*. 2022. Vol. 20. P. 2109–2172. DOI: [10.1016/j.jmrt.2022.07.121](https://doi.org/10.1016/j.jmrt.2022.07.121).
- Xu Yongjun, Liu Xin, Cao Xin et al. Artificial intelligence: A powerful paradigm for scientific research // *The Innovation*. 2021. Vol. 2. № 4. Article number 100179. DOI: [10.1016/j.xinn.2021.100179](https://doi.org/10.1016/j.xinn.2021.100179).
- Osman E.-S., Aggour M.A. Artificial neural network model for accurate prediction of pressure drop in horizontal and near-horizontal-multiphase flow // *Petroleum Science and Technology*. 2002. Vol. 20. № 1-2. P. 1–15. DOI: [10.1081/LFT-120002082](https://doi.org/10.1081/LFT-120002082).
- Shubham P., Sharma A., Vishwakarma P.N., Phanden R.K. Predicting Strength of Selective Laser Melting 3D Printed AlSi10Mg Alloy Parts by Machine Learning Models // 8th International Conference on Signal Processing and Integrated Networks (SPIN). India, 2021. P. 745–749. DOI: [10.1109/SPIN52536.2021.9566142](https://doi.org/10.1109/SPIN52536.2021.9566142).
- Ghetiya N.D., Patel K.M. Prediction of Tensile Strength in Friction Stir Welded Aluminium Alloy Using Artificial Neural Network // *Procedia Technology*. 2014. Vol. 14. P. 274–281. DOI: [10.1016/j.protcy.2014.08.036](https://doi.org/10.1016/j.protcy.2014.08.036).
- Khalefa M. Use of artificial neural network for prediction of mechanical properties of Al–Si alloys synthesized by stir casting // *Journal of Petroleum and Mining Engineering*. 2019. Vol. 21. P. 97–103. DOI: [10.21608/jpme.2019.13857.1004](https://doi.org/10.21608/jpme.2019.13857.1004).
- Alamri F., Maalouf M., Barsoum I. Prediction of Porosity, Hardness and Surface Roughness in Additive Manufactured AlSi10Mg Samples: preprint. 2023. DOI: [10.21203/rs.3.rs-3186551/v1](https://doi.org/10.21203/rs.3.rs-3186551/v1).
- Lawal A.I., Aladejari A.E., Onifade M., Bada S., Idris M.A. Predictions of elemental composition of coal and biomass from their proximate analyses using ANFIS, ANN and MLR // *International Journal of Coal Science and Technology*. 2024. Vol. 8. P. 124–140. DOI: [10.1007/s40789-020-00346-9](https://doi.org/10.1007/s40789-020-00346-9).
- Owunna I., Ikpe A.E. Modelling and prediction of the mechanical properties of TIG welded joint for AISI 4130 low carbon steel plates using artificial neural network (ANN) approach // *Nigerian Journal of Technology* (NIJOTECH). 2019. Vol. 38. № 1. P. 117–126. DOI: [10.4314/njt.v38i1.16](https://doi.org/10.4314/njt.v38i1.16).
- Mahmoodi-Babolan N., Heydari A., Nematollahzadeh A. Removal of methylene blue via bioinspired catecholamine/starch superadsorbent and the efficiency prediction by response surface methodology and artificial neural network-particle swarm optimization // *Bioresource Technology*. 2019. Vol. 294. Article number 122084. DOI: [10.1016/j.biortech.2019.122084](https://doi.org/10.1016/j.biortech.2019.122084).
- Prasad M., Kempaiah U.N., Mohan R.M., Nagara M. Microstructure, Tensile and Compression Behavior of AlSi10Mg Alloy Developed by Direct Metal Laser Sintering // *Indian Journal of Science and Technology*. 2021. Vol. 14. № 45. P. 3346–3353. DOI: [10.17485/IJST/v14i45.1705](https://doi.org/10.17485/IJST/v14i45.1705).
- Zhuo Longchao, Wang Zeyu, Zhang Hongjia, Yin Enhuai, Wang Yanlin, Xu Tao, Li Chao. Effect of post-process heat treatment on microstructure and properties of selective laser melted AlSi10Mg alloy // *Materials Letters*. 2019. Vol. 234. P. 196–200. DOI: [10.1016/j.matlet.2018.09.109](https://doi.org/10.1016/j.matlet.2018.09.109).
- Mei Jiahe, Han Ying, Zu Guoqing, Zhu Weiwei, Zhao Yu, Chen Hua, Ran Xu. Achieving Superior Strength and Ductility of AlSi10Mg Alloy Fabricated by Selective Laser Melting with Large Laser Power and High Scanning Speed // *Acta Metallurgica Sinica (English Letters)*. 2022. Vol. 35. P. 1665–1672. DOI: [10.1007/s40195-022-01410-w](https://doi.org/10.1007/s40195-022-01410-w).
- Zhou Suyuan, Su Yang, Gu Rui, Wang Zhenyu, Zhou Yinghao, Ma Qian, Yan Ming. Impacts of Defocusing Amount and Molten Pool Boundaries on Mechanical Properties and Microstructure of Selective Laser Melted AlSi10Mg // *Materials*. 2019. Vol. 12. № 1. Article number 73. DOI: [10.3390/ma12010073](https://doi.org/10.3390/ma12010073).
- Zhang Shuzhe, Wei Pei, Chen Zhen, Li Bobo, Huang Ke, Zou Yatong, Lu Bingheng. Graphene/ZrO₂/aluminum alloy composite with enhanced strength and ductility fabricated by laser powder bed fusion // *Journal of Alloys and Compounds*. 2022. Vol. 910. Article number 164941. DOI: [10.1016/j.jallcom.2022.164941](https://doi.org/10.1016/j.jallcom.2022.164941).
- Wei Pei, Chen Zhen, Zhang Shuzhe, Li Bobo, Han Jiang, Lu Bingheng. Microstructure and mechanical properties of graphene and nano-zirconia reinforced AlSi10Mg composite fabricated by laser powder bed fusion // *Materials Science and Engineering: A*. 2023. Vol. 864. Article number 144574. DOI: [10.1016/j.msea.2022.144574](https://doi.org/10.1016/j.msea.2022.144574).
- Amor N., Noman M.T., Ismail A., Petru M., Sebastian N. Use of an Artificial Neural Network for Tensile Strength Prediction of Nano Titanium Dioxide Coated Cotton // *Polymers*. 2022. Vol. 14. № 5. Article number 937. DOI: [10.3390/polym14050937](https://doi.org/10.3390/polym14050937).
- Khan A.Q., Awan H.A., Rasul M., Siddiqi Z.A., Pimanmas A. Optimized artificial neural network model for accurate prediction of compressive strength of normal and high strength concrete // *Cleaner Materials*. 2023. Vol. 10. Article number 100211. DOI: [10.1016/j.clema.2023.100211](https://doi.org/10.1016/j.clema.2023.100211).

Математическая модель прогнозирования предела прочности сплава AlSi10Mg, изготовленного аддитивным способом, с использованием искусственных нейронных сетей

Шривастава Сунита К.*¹, научный сотрудник кафедры машиностроения

Мативанан Н. Раджеши², кандидат наук, профессор кафедры машиностроения

Общественный университет народного просвещения, Бангалор (Индия)

*E-mail: sunita.shri45@gmail.com

¹ORCID: <https://orcid.org/0009-0005-2174-2067>

²ORCID: <https://orcid.org/0000-0003-1903-2005>

Поступила в редакцию 10.09.2024

Пересмотрена 29.10.2024

Принята к публикации 25.11.2024

Аннотация: Внедрение машинного обучения в аддитивное производство для моделирования реальных результатов может значительно снизить его стоимость за счет селективного производства. В настоящее время существует недостаточно исследований, посвященных разработке модели прогнозирования механических свойств материала. Входные переменные предложенной модели включали ключевые параметры процесса селективной лазерной плавки, такие как мощность лазера, толщина слоя, скорость сканирования и шаг штриховки, на выходе получая предел прочности. Математическая модель на основе искусственной нейронной сети сравнивалась с моделью полиномиальной регрессии второй степени. Надежность обеих моделей дополнительно оценивалась с новыми наборами данных, отличных от тех, которые использовались при разработке математической модели на основе искусственной нейронной сети и модели регрессии. Результаты показали, что предложенная математическая модель на основе искусственной нейронной сети обеспечивает превосходную точность: при прогнозировании прочности сплава AlSi10Mg среднее абсолютное процентное отклонение (MAPE) составило 4,74 %, критерий соответствия $R^2=0,898$. Математический метод на основе искусственной нейронной сети также показал высокую производительность на новых данных – значение регрессии достигало 0,68. Таким образом, разработанную модель возможно рассматривать как перспективный вариант для прогнозирования предела прочности материала.

Ключевые слова: сплав AlSi10Mg; аддитивное производство; искусственная нейронная сеть (ИНС); машинное обучение; селективная лазерная плавка; математическая модель.

Для цитирования: Шривастава С.К., Мативанан Н.Р. Математическая модель прогнозирования предела прочности сплава AlSi10Mg, изготовленного аддитивным способом, с использованием искусственных нейронных сетей // Frontier Materials & Technologies. 2025. № 1. С. 93–110. DOI: 10.18323/2782-4039-2025-1-71-8.

Appendix 1

- Raus A.A., Wahab M.S., Shayfull Z., Kamarudin K., Ibrahim M. The Influence of Selective Laser Melting Parameters on Density and Mechanical Properties of AlSi10Mg. *MATEC Web of Conferences*, 2016, vol. 78, article number 01078. DOI: [10.1051/mateconf/20167801078](https://doi.org/10.1051/mateconf/20167801078).
- Prasad M., Kempaiah U.N., Mohan R.M., Nagaral M. Microstructure, Tensile and Compression Behaviour of AlSi10Mg Alloy Developed by Direct Metal Laser Sintering. *Indian Journal of Science and Technology*, 2021, vol. 14, no. 45, pp. 3346–3353. DOI: [10.17485/IJST/v14i45.1705](https://doi.org/10.17485/IJST/v14i45.1705).
- Nirish M., Rajendra R. Heat Treatment Effect on the Mechanical Properties of AlSi10Mg Produced by Selective Laser Melting. *Journal of Mechanical Engineering Research and Developments*, 2022, vol. 45, no. 2, pp. 19–28. URL: https://www.researchgate.net/publication/360783808_Heat_Treatment_Effect_on_the_Mechanical_Properties_of_AlSi10Mg_Produced_by_Selective_Laser_Melting.
- Ashwath P., Xavier M.A., Batako A., Jeyapandiarajan P., Joel J. Selective laser melting of Al–Si–10Mg alloy: microstructural studies and mechanical properties assessment. *Journal of Materials Research and Technology*, 2022, vol. 17, pp. 2249–2258. DOI: [10.1016/j.jmrt.2022.01.135](https://doi.org/10.1016/j.jmrt.2022.01.135).
- Casati R., Hamidi Nasab M., Coduri M., Tirelli V., Vedani M. Effects of Platform Pre-Heating and Thermal-Treatment Strategies on Properties of AlSi10Mg Alloy Processed by Selective Laser Melting. *Metals*, 2018, vol. 8, no. 11, article number 954. DOI: [10.3390/met8110954](https://doi.org/10.3390/met8110954).
- Chen B., Moon S.K., Yao X., Bi G., Shen J., Umeda J., Kondoh K. Strength and strain hardening of a selective laser melted AlSi10Mg alloy. *Scripta Materialia*, 2017, vol. 141, pp. 45–49. DOI: [10.1016/j.scriptamat.2017.07.025](https://doi.org/10.1016/j.scriptamat.2017.07.025).
- Delahaye J., Tchoufang Tchuidjang J., Lecomte-Beckers J., Rigo O., Habraken A.M., Mertens A. Influence of Si precipitates on fracture mechanisms of AlSi10Mg parts processed by Selective Laser Melting. *Acta Materialia*, 2019, vol. 175, pp. 160–170. DOI: [10.1016/j.actamat.2019.06.013](https://doi.org/10.1016/j.actamat.2019.06.013).
- Hitzler L., Janousch C., Schanz J., Merkel M., Heine B., Mack F., Hall W., Öchsner A. Direction and location dependency of selective laser melted AlSi10Mg specimens. *Journal of Materials Processing Technology*, 2017, vol. 243, pp. 48–61. DOI: [10.1016/j.jmatprotec.2016.11.029](https://doi.org/10.1016/j.jmatprotec.2016.11.029).
- John M.D., Flaviana C., Paolo A.E. et al. Direct Metal Laser Sintering: an additive manufacturing technology ready to produce lightweight structural parts for robotic applications. *Politecnico di Torino*. URL: <https://iris.polito.it/handle/11583/2518303>.

10. Li Wei, Li Shuai, Liu Jie, Zhang Ang, Zhou Yan, Wei Qingsong, Yan Chunze, Shi Yusheng. Effect of heat treatment on AlSi10Mg alloy fabricated by selective laser melting: Microstructure evolution, mechanical properties and fracture mechanism. *Materials Science and Engineering: A*, 2016, vol. 663, pp. 116–125. DOI: [10.1016/j.msea.2016.03.088](https://doi.org/10.1016/j.msea.2016.03.088).
11. Rosenthal I., Stern A., Frage N. Strain rate sensitivity and fracture mechanism of AlSi10Mg parts produced by Selective Laser Melting. *Materials Science and Engineering: A*, 2017, vol. 682, pp. 509–517. DOI: [10.1016/j.msea.2016.11.070](https://doi.org/10.1016/j.msea.2016.11.070).
12. Tang M., Pistorius P.C. Anisotropic Mechanical Behavior of AlSi10Mg Parts Produced by Selective Laser Melting. *JOM*, 2017, vol. 69, pp. 516–522. DOI: [10.1007/s11837-016-2230-5](https://doi.org/10.1007/s11837-016-2230-5).
13. Wang Lianfeng, Sun Jing, Zhu Xiaogang, Cheng Lingyu, Shi Yun, Guo Lijie, Yan Biao. Effects of T2 Heat Treatment on Microstructure and Properties of the Selective Laser Melted Aluminum Alloy Samples. *Materials*, 2018, vol. 11, no. 1, article number 66. DOI: [10.3390/ma11010066](https://doi.org/10.3390/ma11010066).
14. Zhuo Longchao, Wang Zeyu, Zhang Hongjia, Yin Enhuai, Wang Yanlin, Xu Tao, Li Chao. Effect of post-process heat treatment on microstructure and properties of selective laser melted AlSi10Mg alloy. *Materials Letters*, 2019, vol. 234, pp. 196–200. DOI: [10.1016/j.matlet.2018.09.109](https://doi.org/10.1016/j.matlet.2018.09.109).
15. Larrosa N.O., Wang W., Read N., Loretto M.H., Evans C., Carr J., Tradowsky U., Attallah M.M., Withers P.J. Linking microstructure and processing defects to mechanical properties of selectively laser melted AlSi10Mg alloy. *Theoretical and Applied Fracture Mechanics*, 2018, vol. 98, pp. 123–133. DOI: [10.1016/j.tafmec.2018.09.011](https://doi.org/10.1016/j.tafmec.2018.09.011).
16. Manfredi D., Calignano F., Krishnan M., Canali R., Ambrosio E.P., Atzeni E. From Powders to Dense Metal Parts: Characterization of a Commercial AlSiMg Alloy Processed through Direct Metal Laser Sintering. *Materials*, 2013, vol. 6, no. 3, pp. 856–869. DOI: [10.3390/ma6030856](https://doi.org/10.3390/ma6030856).
17. Ming Tang, Pistorius P.C. Oxides, porosity and fatigue performance of AlSi10Mg parts produced by selective laser melting. *International Journal of Fatigue*, 2017, vol. 94, part 2, pp. 192–201. DOI: [10.1016/j.ijfatigue.2016.06.002](https://doi.org/10.1016/j.ijfatigue.2016.06.002).
18. Mei Jiahe, Han Ying, Zu Guoqing, Zhu Weiwei, Zhao Yu, Chen Hua, Ran Xu. Achieving Superior Strength and Ductility of AlSi10Mg Alloy Fabricated by Selective Laser Melting with Large Laser Power and High Scanning Speed. *Acta Metallurgica Sinica*, 2022, vol. 35, pp. 1665–1672. DOI: [10.1007/s40195-022-01410-w](https://doi.org/10.1007/s40195-022-01410-w).
19. Zyguła K., Nosek B., Pasowicz H., Szysiak N. Mechanical properties and microstructure of AlSi10Mg alloy obtained by casting and SLM technique. *World Scientific News*, 2018, vol. 104, pp. 462–472. URL: https://www.researchgate.net/publication/330215508_Mechanical_properties_and_microstructure_of_AlSi10Mg_alloy_obtained_by_casting_and_SLM_technique.
20. Hovig E.W., Azar A.S., Mhamdi M., Sørby K. Mechanical Properties of AlSi10Mg Processed by Laser Powder Bed Fusion at Elevated Temperature. *TMS 2020 149th Annual Meeting & Exhibition Supplemental Proceedings*. London, Springer Cham Publ., 2020, pp. 395–404. DOI: [10.1007/978-3-030-36296-6_37](https://doi.org/10.1007/978-3-030-36296-6_37).
21. Zhou Suyuan, Su Yang, Gu Rui, Wang Zhenyu, Zhou Yinghao, Ma Qian, Yan Ming. Impacts of Defocusing Amount and Molten Pool Boundaries on Mechanical Properties and Microstructure of Selective Laser Melted AlSi10Mg. *Materials*, 2019, vol. 12, no. 1, article number 73. DOI: [10.3390/ma12010073](https://doi.org/10.3390/ma12010073).
22. Tan Qiyang, Yin Yu, Fan Zhiqi, Zhang Jingqi, Liu Yingang, Zhang Ming-Xing. Uncovering the roles of LaB6-nanoparticle inoculant in the AlSi10Mg alloy fabricated via selective laser melting. *Materials Science and Engineering: A*, 2021, vol. 800, article number 140365. DOI: [10.1016/j.msea.2020.140365](https://doi.org/10.1016/j.msea.2020.140365).
23. Famodimu O.H., Stanford M., Oduzoa C.F., Lijuan Zhang. Effect of process parameters on the density and porosity of laser melted AlSi10Mg/SiC metal matrix composite. *Frontiers of Mechanical Engineering*, 2018, vol. 13, pp. 520–527. DOI: [10.1007/s11465-018-0521-y](https://doi.org/10.1007/s11465-018-0521-y).
24. Marchese G., Aversa A., Lorusso M., Manfredi D., Calignano F., Lombardi M., Biamino S., Pavese M. Development and Characterisation of Aluminium Matrix Nanocomposites AlSi10Mg/MgAl₂O₄ by Laser Powder Bed Fusion. *Metals*, 2018, vol. 8, no. 3, article number 175. DOI: [10.3390/met8030175](https://doi.org/10.3390/met8030175).
25. Gao C., Wu W., Shi J., Xiao Z., Akbarzadeh A.H. Simultaneous enhancement of strength, ductility, and hardness of TiN/AlSi10Mg nanocomposites via selective laser melting. *Additive Manufacturing*, 2020, vol. 34, article number 101378. DOI: [10.1016/j.addma.2020.101378](https://doi.org/10.1016/j.addma.2020.101378).
26. He Peidong, Kong Hui, Liu Qian, Ferry M., Kruzic J.J., Li Xiaopeng. Elevated temperature mechanical properties of TiCN reinforced AlSi10Mg fabricated by laser powder bed fusion additive manufacturing. *Materials Science and Engineering: A*, 2021, vol. 811, article number 141025. DOI: [10.1016/j.msea.2021.141025](https://doi.org/10.1016/j.msea.2021.141025).
27. Wang Yachao, Shi Jing, Lu Shiqiang, Xiao Weihai. Investigation of Porosity and Mechanical Properties of Graphene Nanoplatelets-Reinforced AlSi10Mg by Selective Laser Melting. *Journal of Micro and Nano Science and Engineering*, 2018, vol. 6, no. 1, article number 010902. DOI: [10.1115/1.4038454](https://doi.org/10.1115/1.4038454).
28. Wang Yachao, Shi Jing. Effect of hot isostatic pressing on nanoparticles reinforced AlSi10Mg produced by selective laser melting. *Materials Science and Engineering: A*, 2020, vol. 788, article number 139570. DOI: [10.1016/j.msea.2020.139570](https://doi.org/10.1016/j.msea.2020.139570).
29. Wei Pei, Chen Zhen, Zhang Shuzhe, Li Bobo, Han Jiang, Lu Bingheng. Microstructure and mechanical properties of graphene and nano-zirconia reinforced AlSi10Mg composite fabricated by laser powder bed fusion. *Materials Science and Engineering: A*, 2023, vol. 864, article number 144574. DOI: [10.1016/j.msea.2022.144574](https://doi.org/10.1016/j.msea.2022.144574).
30. Zhang Shuzhe, Chen Zhen, Wei Pei et al. Wear properties of graphene/zirconia biphasic nano-reinforced aluminium matrix composites prepared by SLM. *Materials Today Communications*, 2022, vol. 30, article number 103009. DOI: [10.1016/j.mtcomm.2021.103009](https://doi.org/10.1016/j.mtcomm.2021.103009).
31. Zhang Shuzhe, Wei Pei, Chen Zhen, Li Bobo, Huang Ke, Zou Yatong, Lu Bingheng. Graphene/ZrO₂/aluminum alloy composite with enhanced strength and ductility fabricated by laser powder bed fusion. *Journal of Alloys and Compounds*, 2022, vol. 910, article number 164941. DOI: [10.1016/j.jallcom.2022.164941](https://doi.org/10.1016/j.jallcom.2022.164941).
32. Yi Junchao, Zhang Xiaowei, Rao Jeremy Heng, Xiao Jingyu, Jiang Yehua. In-situ chemical reaction mechanism and non-equilibrium microstructural evolution of (TiB₂ + TiC)/AlSi10Mg composites prepared by SLM-CS processing. *Journal of Alloys and Compounds*, 2021, vol. 857, article number 157553. DOI: [10.1016/j.jallcom.2020.157553](https://doi.org/10.1016/j.jallcom.2020.157553).
33. Miao Kai, Zhou Hang, Gao Yunpeng, Deng Xin, Lu Zhongliang, Li Dichen. Laser powder-bed-fusion of Si₃N₄ reinforced AlSi10Mg composites: Processing, mechanical properties and strengthening mechanisms. *Materials Science and Engineering: A*, 2021, vol. 825, article number 141874. DOI: [10.1016/j.msea.2021.141874](https://doi.org/10.1016/j.msea.2021.141874).

34. Limbasiya N., Jain A., Soni H., Wankhede V., Krolczyk G., Sahlot R. A comprehensive review on the effect of process parameters and post-process treatments on microstructure and mechanical properties of selective laser melting of AlSi10Mg. *Journal of Materials Research and Technology*, 2022, vol. 21, pp. 1141–1176. DOI: [10.1016/j.jmrt.2022.09.092](https://doi.org/10.1016/j.jmrt.2022.09.092).

Appendix 2

1. Maamoun A.H., Xue Y.F., Elbestawi M.A., Veldhuis S.C. The Effect of Selective Laser Melting Process Parameters on the Microstructure and Mechanical Properties of Al6061 and AlSi10Mg Alloys. *Materials*, 2019, vol. 12, no. 1, article number 12. DOI: [10.3390/ma12010012](https://doi.org/10.3390/ma12010012).
2. Srinivasa Rakesh Ch., Raja A., Nadig P., Jayaganthan R., Vasa N.J. Influence of working environment and built orientation on the tensile properties of selective laser melted AlSi10Mg alloy. *Materials Science and Engineering: A*, 2019, vol. 750, pp. 141–151. DOI: [10.1016/j.msea.2019.01.103](https://doi.org/10.1016/j.msea.2019.01.103).
3. Dong Zhichao, Zhang Xiaoyu, Shi Wenhua, Zhou Hao, Lei Hongshuai, Liang Jun. Study of Size Effect on Microstructure and Mechanical Properties of AlSi10Mg Samples Made by Selective Laser Melting. *Materials*, 2018, vol. 11, no. 12, article number 2463. DOI: [10.3390/ma11122463](https://doi.org/10.3390/ma11122463).
4. Li Xinwei, Shi Shi, Han Shuang, Hu Xiaogang, Zhu Qiang, Lu Hongxing, Li Wenwu, Shi Yusheng, Ding Hui. Microstructure, solidification behavior and mechanical properties of Al-Si-Mg-Ti/TiC fabricated by selective laser melting. *Additive Manufacturing*, 2020, vol. 34, article number 10132. DOI: [10.1016/j.addma.2020.101326](https://doi.org/10.1016/j.addma.2020.101326).
5. Kempen K., Thijs L., Van Humbeeck J., Kruth J.-P. Processing AlSi10Mg by selective laser melting: parameter optimisation and material characterisation. *Materials Science and Technology*, 2014, vol. 31, no. 8, pp. 917–923. DOI: [10.1179/1743284714Y.0000000702](https://doi.org/10.1179/1743284714Y.0000000702).
6. Kim Dong-Kyu, Woo Wanchuck, Hwang Ji-Hyun, An Ke, Choi Shi-Hoon. Stress partitioning behavior of an AlSi10Mg alloy produced by selective laser melting during tensile deformation using in situ neutron diffraction. *Journal of Alloys and Compounds*, 2016, vol. 686, pp. 281–286. DOI: [10.1016/j.jallcom.2016.06.011](https://doi.org/10.1016/j.jallcom.2016.06.011).
7. Maskery I., Aboulkhair N.T., Tuck C.J., Wildman R., Ashcroft I., Everitt N.M., Hague R.J.M.. Fatigue Performance Enhancement of Selectively Laser Melted Aluminium Alloy by Heat Treatment. *26th Annual International Solid Freeform Fabrication Symposium*. Texas, 2015, pp. 1–10. URL: https://www.researchgate.net/publication/282816647_Fatigue_Performance_Enhancement_of_Selectively_Laser_Melted_Aluminium_Alloy_by_Heat_Treatment.
8. Sun Jing, Qiu Lianfang, Wang Fei, Yang Yang, Guo Lijie. A new modification effect of eutectic Si in selective laser melted AlSi10Mg. *Materials Science and Technology*, 2019, vol. 35, no. 6, pp. 1–7. DOI: [10.1080/02670836.2019.1589740](https://doi.org/10.1080/02670836.2019.1589740).
9. Wei Pei, Wei Zhengying, Chen Zhen, Du Jun, He Yuyang, Li Junfeng, Zhou Yatong. The AlSi10Mg samples produced by selective laser melting: single track, densification, microstructure and mechanical behaviour. *Applied Surface*, 2017, vol. 408, pp. 38–50. DOI: [10.1016/j.apsusc.2017.02.215](https://doi.org/10.1016/j.apsusc.2017.02.215).
10. Zhang Changchun, Zhu Haihong, Liao Hailong, Cheng Yong, Hu Zhiheng, Zeng Xiaoyan. Effect of heat treatments on fatigue property of selective laser melting AlSi10Mg. *International Journal of Fatigue*, 2018, vol. 116, pp. 513–522. DOI: [10.1016/j.ijfatigue.2018.07.016](https://doi.org/10.1016/j.ijfatigue.2018.07.016).
11. Yang Tao, Liu Tingting, Liao Wenhe, MacDonald E., Wei Huiliang, Zhang Changdong, Chen Xiangyuan, Zhang Kai. Laser powder bed fusion of AlSi10Mg: Influence of energy intensities on spatter and porosity evolution, microstructure and mechanical properties. *Journal of Alloys and Compounds*, 2020, vol. 849, article number 156300. DOI: [10.1016/j.jallcom.2020.156300](https://doi.org/10.1016/j.jallcom.2020.156300).
12. Yan Qian, Song Bo, Shi Yusheng. Comparative study of performance comparison of AlSi10Mg alloy prepared by selective laser melting and casting. *Journal of Materials Science & Technology*, 2020, vol. 41, pp. 199–208. DOI: [10.1016/j.jmst.2019.08.049](https://doi.org/10.1016/j.jmst.2019.08.049).
13. Suttey L.J. Evaluation of metallurgical and mechanical properties of AlSi10Mg produced by selective laser melting: Graduate Theses & Non-Theses. 2018. 174. *Digital Commons and Montana Tech*. URL: https://digitalcommons.mtech.edu/grad_rschn/174.
14. Liu Bin, Kuai Zezhou, Li Zhonghua, Tong Jianbin, Bai Peikang, Li Baoqiang, Nie Yunfei. Performance Consistency of AlSi10Mg Alloy Manufactured by Simulating Multi Laser Beam Selective Laser Melting (SLM): Microstructures and Mechanical Properties. *Materials*, 2018, vol. 11, no. 12, article number 2354. DOI: [10.3390/ma11122354](https://doi.org/10.3390/ma11122354).
15. Murphy D.M. Performance evaluation of AlSi10Mg fabricated by a selective laser melting process. *Missouri University of Science and Technology*. URL: https://scholarsmine.mst.edu/masters_theses/8006.
16. Kumar M.S., Mohan E., Robinson S., Prasad T.D. Comparative Study on Morphological, Physical and Mechanical Characteristics of L-PBF Based AlSi10Mg Parts with Conventional Stir Casted Al-10%SiC Composites. *Silicon*, 2022, vol. 14, pp. 2695–2706. DOI: [10.1007/s12633-021-01065-9](https://doi.org/10.1007/s12633-021-01065-9).
17. Zhou S.Y., Wang Z.Y., Su Y., Wang H., Liu G., Song T.T., Yan M. Effects of Micron/Submicron TiC on Additively Manufactured AlSi10Mg: A Comprehensive Study from Computer Simulation to Mechanical and Microstructural Analysis. *JOM*, 2020, vol. 72, pp. 3693–3704. DOI: [10.1007/s11837-019-03984-w](https://doi.org/10.1007/s11837-019-03984-w).

OUR AUTHORS

Aryshenskiy Evgeny Vladimirovich, Doctor of Sciences (Engineering), PhD, Associate Professor, chief researcher of Scientific Research Department.
Address: Siberian State Industrial University,
654007, Russia, Novokuznetsk, Kirov Street, 42.
E-mail: arishenskiy_ev@sibsiu.ru

Aryshenskiy Vladimir Yurievich, Doctor of Sciences (Engineering), Professor, chief researcher of Aviation Materials Study Industrial Research Laboratory (ONIL-4).
Address: Academician S.P. Korolev Samara National Research University,
443086, Russia, Samara, Moskovskoye Shosse, 34.
E-mail: arysh54@mail.ru

Bakhtegareev Inzil Damirovich, master.
Address: Academician S.P. Korolev Samara National Research University,
443086, Russia, Samara, Moskovskoye Shosse, 34.
E-mail: inzilbah@ya.ru

Bazhenov Vyacheslav Evgenievich, PhD (Engineering), assistant professor of Chair “Foundry Technologies and Material Art Working”.
Address: University of Science and Technology MISIS,
119049, Russia, Moscow, Leninsky Prospekt, 4, block 1.
E-mail: v.e.bagenov@gmail.com

Bazlova Tatiana Alekseevna, PhD (Engineering), assistant professor of Chair “Foundry Technologies and Material Art Working”.
Address: University of Science and Technology MISIS,
119049, Russia, Moscow, Leninsky Prospekt, 4, block 1.
E-mail: tbazlova@mail.ru

Drobyshev Vladislav Konstantinovich, postgraduate student of Chair of Metal Forming and Materials Science of EVRAZ ZSMK, researcher of the Laboratory of Electron Microscopy and Image Processing.
Address: Siberian State Industrial University,
654007, Russia, Novokuznetsk, Kirov Street, 42.
E-mail: drobyshev_v.k@mail.ru

Gadzhiev Magomed Razhabovich, postgraduate student.
Address: Moscow Aviation Institute,
125993, Russia, Moscow, Volokolamskoye Shosse, 4.
E-mail: maga.2630@gmail.com

Ibatullin Ildar Duglasovich, Doctor of Sciences (Engineering), Professor, Head “Chair of Machinery and Equipment of Petroleum and Chemical Production”.
Address: Samara State Technical University,
443100, Russia, Samara, Molodogvardeyskaya Street, 244.
E-mail: idi71@yandex.ru

Islamgaliev Rinat Kadykhanovich, Doctor of Sciences (Physics and Mathematics), professor of Chair of Materials Science and Physics of Metals.
Address: Ufa University of Science and Technology,
450076, Russia, Ufa, Zaki Validi Street, 32.
E-mail: rinatis@mail.ru

Katanaeva Diana Andreevna, graduate student.
Address: University of Science and Technology MISIS,
119049, Russia, Moscow, Leninsky Prospekt, 4, block 1.
E-mail: dianakat2001@mail.ru

Kolibasov Vladimir Aleksandrovich, postgraduate student, assistant of Chair “Machinery and Equipment of Petroleum and Chemical Production”.
Address: Samara State Technical University,
443100, Russia, Samara, Molodogvardeyskaya Street, 244.
E-mail: mahp@samgtu.ru, csstea@yandex.ru

Konovalov Sergey Valerievich, Doctor of Sciences (Engineering), Professor, Vice-Rector for Research and Innovation Activities, chief researcher of Aviation Materials Study Industrial Research Laboratory (ONIL-4).
Address 1: Siberian State Industrial University, 654007, Russia, Novokuznetsk, Kirov Street, 42.
Address 2: Harbin Engineering University, 264006, China, Yantai, Qingdao Street, No. 1.
Address 3: Academician S.P. Korolev Samara National Research University, 443086, Russia, Samara, Moskovskoye Shosse, 34.
E-mail: konovalov@sibsiu.ru

Korzniikova Elena Aleksandrovna, Doctor of Sciences (Physics and Mathematics), professor of Chair of Materials Science and Physics of Metals.
Address: Ufa University of Science and Technology, 450076, Russia, Ufa, Zaki Validi Street, 32.
E-mail: elena.a.korzniikova@gmail.com

Kosmyinin Aleksandr Vitalyevich, Doctor of Sciences (Engineering), Professor, professor of Chair “Shipbuilding and Computing Engineering”.
Address: Komsomolsk-na-Amure State University, 681013, Russia, Komsomolsk-on-Amur, Lenin Prospekt, 27.
E-mail: avkosm@knastu.ru

Li Haixin, PhD, associate professor of Yantai Research Institute.
Address: Harbin Engineering University, 264006, China, Yantai, Qingdao Street, No. 1.
E-mail: lihaixin@hrbeu.edu.cn

Mathivanan N. Rajesh, PhD, professor of Department of Mechanical Engineering.
Address: PES University, 560085, India, Bangalore, 100 Feet Ring Road.
E-mail: rajesh.mathivanan@pes.edu

Mokritskiy Boris Yakovlevich, Doctor of Sciences (Engineering), Professor, professor of Chair “Machine Engineering”.
Address: Komsomolsk-na-Amure State University, 681013, Russia, Komsomolsk-on-Amur, Lenin Prospekt, 27.
E-mail: boris@knastu.ru

Nesterov Konstantin Mikhaylovich, PhD (Physics and Mathematics), assistant professor of Chair of Materials Science and Physics of Metals.
Address: Ufa University of Science and Technology, 450076, Russia, Ufa, Zaki Validi Street, 32.
E-mail: kmnesterov@mail.ru

Novikov Vladislav Aleksandrovich, PhD (Engineering), assistant professor of Chair “Metal Science, Powder Metallurgy, Nanomaterials”, senior researcher of the Laboratory of X-ray Diffractometry, Electron and Probe Microscopy.
Address: Samara State Technical University, 443100, Russia, Samara, Molodogvardeyskaya Street, 244.
E-mail: vladislav_novyi@mail.ru

Panchenko Irina Alekseevna, PhD (Engineering), assistant professor of Chair of Quality Management and Innovation, Head of the Laboratory of Electron Microscopy and Image Processing.
Address: Siberian State Industrial University, 654007, Russia, Novokuznetsk, Kirov Street, 42.
E-mail: panchenko.sibsiu@yandex.ru

Pashkov Igor Nikolaevich, Doctor of Sciences (Engineering), professor of Chair No.1101.
Address: Moscow Aviation Institute, 125993, Russia, Moscow, Volokolamskoye Shosse, 4.
E-mail: pashkov_prof@mail.ru

Pozdniakov Andrey Vladimirovich, PhD (Engineering),
Associate Professor.
Address: University of Science and Technology MISIS,
119049, Russia, Moscow, Leninsky Prospekt, 4, block 1.
E-mail: pozdniakov@misis.ru

Ragazin Aleksandr Alekseevich, engineer
of Aviation Materials Study Industrial Research Laboratory (ONIL-4).
Address: Academician S.P. Korolev Samara National Research University,
443086, Russia, Samara, Moskovskoye Shosse, 34.
E-mail: sanekragazin63@mail.ru

Rasposienko Dmitry Yurievich, PhD (Engineering),
senior researcher of the Laboratory of Non-ferrous Alloys.
Address: M.N. Mikheev Institute of Metal Physics of the Ural Branch of RAS,
620108, Russia, Yekaterinburg, Sofya Kovalevskaya Street, 18.
E-mail: dmitrijrasp@gmail.com

Sablin Pavel Alekseevich, PhD (Engineering), Associate Professor,
assistant professor of Chair “Machine Engineering”.
Address: Komsomolsk-na-Amure State University,
681013, Russia, Komsomolsk-on-Amur, Lenin Prospekt, 27.
E-mail: ikpmto@knastu.ru

Srivastava Sunita K., researcher of Department of Mechanical Engineering.
Address: PES University,
560085, India, Bangalore, 100 Feet Ring Road.
E-mail: sunita.shri45@gmail.com

Tarov Danila Vladimirovich, student
of Chair of Materials Science and Physics of Metals.
Address: Ufa University of Science and Technology,
450076, Russia, Ufa, Zaki Validi Street, 32.
E-mail: tarovdv@gmail.com

Tavolzhanskiy Stanislav Anatolievich, PhD (Engineering),
assistant professor of Chair “Foundry Technologies and Material Art Working”.
Address: University of Science and Technology MISIS,
119049, Russia, Moscow, Leninsky Prospekt, 4, block 1.
E-mail: stavolj@gmail.com

НАШИ АВТОРЫ

Арышенский Владимир Юрьевич, доктор технических наук, профессор, главный научный сотрудник отраслевой научно-исследовательской лаборатории авиационного материаловедения № 4 (ОНИЛ-4).
Адрес: Самарский национальный исследовательский университет имени академика С.П. Королева, 443086, Россия, г. Самара, Московское шоссе, 34.
E-mail: arysh54@mail.ru

Арышенский Евгений Владимирович, доктор технических наук, PhD, доцент, главный научный сотрудник управления научных исследований.
Адрес: Сибирский государственный индустриальный университет, 654007, Россия, г. Новокузнецк, ул. Кирова, 42.
E-mail: arishenskiy_ev@sibsiu.ru

Баженов Вячеслав Евгеньевич, кандидат технических наук, доцент кафедры «Литейные технологии и художественная обработка материалов».
Адрес: Университет науки и технологий МИСИС, 119049, Россия, г. Москва, Ленинский пр-т, 4, стр. 1.
E-mail: v.e.bagenov@gmail.com

Базлова Татьяна Алексеевна, кандидат технических наук, доцент кафедры «Литейные технологии и художественная обработка материалов».
Адрес: Университет науки и технологий МИСИС, 119049, Россия, г. Москва, Ленинский пр-т, 4, стр. 1.
E-mail: tbazlova@mail.ru

Бахтегареев Инзиль Дамирович, магистр.
Адрес: Самарский национальный исследовательский университет имени академика С.П. Королева, 443086, Россия, г. Самара, Московское шоссе, 34.
E-mail: inzilbah@ya.ru

Гаджиев Магомед Ражабович, аспирант.
Адрес: Московский авиационный институт, 125993, Россия, г. Москва, Волоколамское шоссе, 4.
E-mail: maga.2630@gmail.com

Дробышев Владислав Константинович, аспирант кафедры обработки металлов давлением и материаловедения ЕВРАЗ ЗСМК, научный сотрудник лаборатории электронной микроскопии и обработки изображений.
Адрес: Сибирский государственный индустриальный университет, 654007, Россия, г. Новокузнецк, ул. Кирова, 42.
E-mail: drobyshev_v.k@mail.ru

Ибатуллин Ильдар Дугласович, доктор технических наук, профессор, заведующий кафедрой «Машины и оборудование нефтегазовых и химических производств».
Адрес: Самарский государственный технический университет, 443100, Россия, г. Самара, ул. Молодогвардейская, 244.
E-mail: idi71@yandex.ru

Исламгалиев Ринат Кадыханович, доктор физико-математических наук, профессор кафедры материаловедения и физики металлов.
Адрес: Уфимский университет науки и технологий, 450076, Россия, г. Уфа, ул. Заки Валиди, 32.
E-mail: rinatis@mail.ru

Катанаева Диана Андреевна, магистрант.
Адрес: Университет науки и технологий МИСИС, 119049, Россия, г. Москва, Ленинский пр-т, 4, стр. 1.
E-mail: dianakat2001@mail.ru

Колибасов Владимир Александрович, аспирант,
ассистент кафедры «Машины и оборудование нефтегазовых и химических производств».
Адрес: Самарский государственный технический университет,
443100, Россия, г. Самара, ул. Молодогвардейская, 244.
E-mail: mahp@samgtu.ru, csstea@yandex.ru

Коновалов Сергей Валерьевич, доктор технических наук, профессор,
проректор по научной и инновационной деятельности,
главный научный сотрудник отраслевой научно-исследовательской лаборатории
авиационного материаловедения № 4 (ОНИЛ-4).
Адрес 1: Сибирский государственный индустриальный университет,
654007, Россия, г. Новокузнецк, ул. Кирова, 42.
Адрес 2: Харбинский инженерный университет,
264006, Китай, г. Яньтай, ул. Циндао, 1.
Адрес 3: Самарский национальный исследовательский университет
имени академика С.П. Королева,
443086, Россия, г. Самара, Московское шоссе, 34.
E-mail: konovalov@sibsiu.ru

Корзникова Елена Александровна, доктор физико-математических наук,
профессор кафедры материаловедения и физики металлов.
Адрес: Уфимский университет науки и технологий,
450076, Россия, г. Уфа, ул. Заки Валиди, 32.
E-mail: elena.a.korznikova@gmail.com

Космынин Александр Витальевич, доктор технических наук, профессор,
профессор кафедры «Кораблестроение и компьютерный инжиниринг».
Адрес: Комсомольский-на-Амуре государственный университет,
681013, Россия, г. Комсомольск-на-Амуре, пр-т Ленина, 27.
E-mail: avkosm@knastu.ru

Ли Хайсинь, кандидат наук,
доцент Научно-исследовательского института в Яньтае.
Адрес: Харбинский инженерный университет,
264006, Китай, г. Яньтай, ул. Циндао, 1.
E-mail: lihaixin@hrbeu.edu.cn

Мативанан Н. Раджеш, кандидат наук,
профессор кафедры машиностроения.
Адрес: Общественный университет народного просвещения,
560085, Индия, г. Бангалор, 100 Фит Ринг Роад.
E-mail: rajesh.mathivanan@pes.edu

Мокрицкий Борис Яковлевич, доктор технических наук, профессор,
профессор кафедры «Машиностроение».
Адрес: Комсомольский-на-Амуре государственный университет,
681013, Россия, г. Комсомольск-на-Амуре, пр-т Ленина, 27.
E-mail: boris@knastu.ru

Нестеров Константин Михайлович, кандидат физико-математических наук,
доцент кафедры материаловедения и физики металлов.
Адрес: Уфимский университет науки и технологий,
450076, Россия, г. Уфа, ул. Заки Валиди, 32.
E-mail: kmnesterov@mail.ru

Новиков Владислав Александрович, кандидат технических наук,
доцент кафедры «Металловедение, порошковая металлургия, наноматериалы»,
старший научный сотрудник лаборатории рентгеновской дифрактометрии,
электронной и зондовой микроскопии.
Адрес: Самарский государственный технический университет,
443100, Россия, г. Самара, ул. Молодогвардейская, 244.
E-mail: vladislav_novyi@mail.ru

Панченко Ирина Алексеевна, кандидат технических наук,
доцент кафедры менеджмента качества и инноваций,
заведующий лабораторией электронной микроскопии и обработки изображений.
Адрес: Сибирский государственный индустриальный университет,
654007, Россия, г. Новокузнецк, ул. Кирова, 42.
E-mail: panchenko.sibsiu@yandex.ru

Пашков Игорь Николаевич, доктор технических наук,
профессор кафедры 1101.
Адрес: Московский авиационный институт,
125993, Россия, г. Москва, Волоколамское шоссе, 4.
E-mail: pashkov_prof@mail.ru

Поздняков Андрей Владимирович, кандидат технических наук, доцент.
Адрес: Университет науки и технологий МИСИС,
119049, Россия, г. Москва, Ленинский пр-т, 4, стр. 1.
E-mail: pozdniakov@misis.ru

Рагазин Александр Алексеевич, инженер
отраслевой научно-исследовательской лаборатории
авиационного материаловедения № 4 (ОНИЛ-4).
Адрес: Самарский национальный исследовательский университет
имени академика С.П. Королева,
443086, Россия, г. Самара, Московское шоссе, 34.
E-mail: sanekragazin63@mail.ru

Распосиенко Дмитрий Юрьевич, кандидат технических наук,
старший научный сотрудник лаборатории цветных сплавов.
Адрес: Институт физики металлов имени М.Н. Михеева Уральского отделения РАН,
620108, Россия, г. Екатеринбург, ул. Софьи Ковалевской, 18.
E-mail: dmitrijrasp@gmail.com

Саблин Павел Алексеевич, кандидат технических наук, доцент,
доцент кафедры «Машиностроение».
Адрес: Комсомольский-на-Амуре государственный университет,
681013, Россия, г. Комсомольск-на-Амуре, пр-т Ленина, 27.
E-mail: ikpmt@knastu.ru

Таволжанский Станислав Анатольевич, кандидат технических наук,
доцент кафедры «Литейные технологии и художественная обработка материалов».
Адрес: Университет науки и технологий МИСИС,
119049, Россия, г. Москва, Ленинский пр-т, 4, стр. 1.
E-mail: stavolj@gmail.com

Таров Данила Владимирович, студент
кафедры материаловедения и физики металлов.
Адрес: Уфимский университет науки и технологий,
450076, Россия, г. Уфа, ул. Заки Валиди, 32.
E-mail: tarovdv@gmail.com

Шривастава Сунита К., научный сотрудник кафедры машиностроения.
Адрес: Общественный университет народного просвещения,
560085, Индия, г. Бангалор, 100 Фит Ринг Род.
E-mail: sunita.shri45@gmail.com

On the cover: The destructed surface of a brazed joint of a hard alloy with steel with excess silicon in the brazing alloy. Authors of the photo: I.N. Pashkov, Doctor of Sciences (Engineering), professor of Chair No.1101 (Moscow Aviation Institute, Moscow, Russia), T.A. Bazlova, PhD (Engineering), assistant professor of Chair “Foundry Technologies and Material Art Working” (University of Science and Technology MISIS, Moscow, Russia).

На обложке: Поверхность разрушения паяного соединения твердого сплава со сталью при избытке кремния в припое. Авторы фото: И.Н. Пашков, доктор технических наук, профессор кафедры 1101 (Московский авиационный институт, Москва, Россия), Т.А. Базлова, кандидат технических наук, доцент кафедры «Литейные технологии и художественная обработка материалов» (Университет науки и технологий МИСИС, Москва, Россия).